



The
University
Of
Sheffield.

**The corrosion behaviour of equiatomic CoCrFeNi
and the high entropy alloys CoCrFeNiX
(X=Al, Cu, Sn)**

Piyanut Muangtong

Supervisor: Prof. Russell Goodall and Prof. Iain Todd

A Thesis submitted for the degree of Doctor of Philosophy

Department of Materials Science and Engineering

Faculty of Engineering

The University of Sheffield

May 2023

DECLARATION

I would like to declare that all of the content of this thesis, entitled "The corrosion behaviour of equiatomic CoCrFeNi and the high entropy alloys CoCrFeNiX (X=Al, Cu, Sn)", has been written by myself. All data for this PhD project shown in this thesis was generated by my own experimental work, except where the contribution of collaborators is acknowledged. In addition, this dissertation has not been previously submitted, accepted, or published in any other examination or dissertation.

CONFERENCES

My attendance for presentation in international conferences is summarized below:

- “The Corrosion Resistance of CoCrFeNi High Entropy Alloys in Chloride Solution”, 10th International Conference on Materials Science and Technology (10th MSAT), 6-7 September 2018, Thailand. (In the section of poster presentation: Received the best poster award).
- “The Effect of Alloying Elements on the Improvement in Hardness of CoCrFeNi-X High Entropy Alloys”, 18th International Conference on Applied Science and Engineering (18th ICASE), 7-8 April 2019, Singapore. (In the section of oral presentation: Received an excellent paper award).

PUBLICATIONS

Work from this thesis has been published in the scientific literature as follows:

- P. Muangtong, A. Rodchanarowan, D. Chaysuwan, N. Chanlek, and R. Goodall, “The Corrosion Behaviour of CoCrFeNi-X (X = Cu, Al, Sn) High Entropy Alloy Systems in Chloride Solution”, *Corros. Sci.*, 2020, 172, 1-11.
- P. Muangtong, R.M. Namus, and R. Goodall, “Improved Tribocorrosion Resistance by Addition of Sn to CrFeCoNi High Entropy Alloy”, *Metals*, 2021, 11(13), 1-14.

ACKNOWLEDGEMENTS

For my PhD journey, a four-year period of study time is a warm and special duration to open my mind to gain new knowledge, new experiences, new friends, and new personal connections to drive me to graduate a PhD program. I would like to acknowledge everybody who supports me by giving encouragement and advice for passing the problems as below;

Prof Russell Goodall is the best supervisor in my heart to push and support me in everything for the whole study period. Assoc.Prof Aphichart Rodchanarowan, Dr Narong Chanlek, and Dr Righdan M Namus are great research collaborators for supporting the analytical instruments in this project. The researchers, Dr Zhao Y Leong and Dr Phillip Mahoney, and the technical staff in the Department of Materials Science and Engineering and Sorby centre, Dr Le Ma, Dr Cheryl Shaw, and Dawn Bussey, who give me training and advice on the experimental research, including sharing their working experiences for problem-solving during experimental works or using machine.

In addition, I would also like to thank my parents, my younger brother, and my new friends, Luis F Romano Acosta and Shaiful A Ismail, for all their support and encouragement in both the good and bad days of my PhD life. It contributes to healing my mind and feeling to make me successful in this program.

ABSTRACT

Currently, High Entropy Alloys (HEAs) are attracting interest from many researchers for alloy design and the development of alloy properties, by creating and exploring alloys made with multiple metallic elements. Many HEA systems thus far reported reveal various outstanding material properties, such as mechanical properties, corrosion properties, electrical properties, etc., which could potentially support current and future applications. Furthermore, the unexpected microstructure of HEAs is a great motivation for further research to identify their properties leading to the selection of appropriate applications in industry.

In corrosion studies, most of the work that has been reported has been carried out on HEAs based on the CoCrFeNi system, with additional alloying elements. This system was selected as the main alloy system for study here, with additions of inexpensive metallic elements, Al, Cu, and Sn. The CoCrFeNi-based alloy and three equiatomic HEA alloys, CoCrFeNiAl, CoCrFeNiCu, and CoCrFeNiSn, were produced by vacuum arc melting. Corrosion behaviour has been assessed in three different solutions representing different conditions and pH; 0.6 M NaCl, 0.6 M H₂SO₄, and 0.6 M NaAlO₂ solutions. Chloride solution was also used to observe tribocorrosion resistance. In addition, phase composition, chemical composition, microstructure, hardness, and density were examined.

These results indicate that the alloying elements have an effect on the microstructure of the CoCrFeNi system. The addition of a fifth alloying element, Al, Cu, or Sn, can transform the structure from a single FCC phase to dual phase. The second phase, Al-Ni-rich, Cu-rich, and Ni-Sn-rich phases respectively, is formed in each HEA system. In the study of corrosion behaviour, CoCrFeNiSn shows the highest passivity of all the tested specimens in 0.6 M NaCl solution, stemming from Cr₂O₃ and SnO₂ based oxide films. In acidic and alkaline solutions, the best corrosion properties with the highest corrosion and transpassive potentials, E_{corr} and E_t , which decrease the corrosion sensitivity are observed in CoCrFeNiSn for 0.6 M H₂SO₄ solution and CoCrFeNiCu for 0.6 M NaAlO₂ solution, in both cases occurring as a consequence of the high quantity of protective Cr₂O₃ film covered on the alloy surfaces. In addition, it can be found that CoCrFeNiAl has the widest passive region under both acidic and alkaline solutions, resulting from the formation of Al₂O₃ or a mixed (Cr, Al)₂O₃ film on the sample surface. CoCrFeNiSn has higher hardness than CoCrFeNi, resulting from the dual phase structure, with high hardness in the Ni-Sn-rich phase, but also ductility in the CoCrFeNi phase which provides a degree of toughness improvement and seems to resist crack propagation,

perhaps contributing to CoCrFeNiSn having better tribocorrosion resistance than CoCrFeNi in chloride conditions. From all the results outlined above, the creation of high entropy CoCrFeNiX alloys with inexpensive metallic elements (X) such as Al, Cu, and especially Sn, reveals a positive effect on the development of corrosion properties in various solutions. These finding can be a significant spur to drive further development of these materials for diverse industries in the future.

TABLE OF CONTENTS

CHAPTER 1-INTRODUCTION	1
CHAPTER 2-LITERATURE REVIEW	5
2.1 High entropy alloys.....	5
2.1.1 The discovery of HEAs.....	5
2.1.2 Phase composition in HEA systems.....	7
2.1.3 Production routes for HEAs.....	12
2.1.4 HEA in structural and functional applications.....	17
2.1.5 The CoCrFeNi-base alloy of many HEA systems	21
2.2 Structural properties of HEAs and conventional alloys.....	35
2.2.1 Hardness.....	35
2.2.2 Corrosion properties.....	42
2.2.3 Tribocorrosion properties.....	67
CHAPTER 3-RESEARCH METHODOLOGY	75
3.1 An overview of the approach.....	75
3.2 Selection and interpretation of HEA systems	76
3.3 Raw material and solution preparation.....	79
3.3.1 Raw material preparation.....	79
3.3.2 Solution preparation.....	80
3.4 Vacuum arc melting.....	80
3.5 HEA sample preparation.....	83
3.5.1 Corrosion samples.....	83
3.5.2 Tribocorrosion samples.....	83
3.6 Property characterization.....	85
3.6.1 Physical analysis.....	85
3.6.1.1 Microstructure analysis by SEM.....	85
3.6.1.2 Density balance.....	86
3.6.1.3 Micro-indentation.....	86
3.6.1.4 Nano-indentation.....	87
3.6.2 Chemical analysis.....	87
3.6.2.1 EDS-SEM.....	87
3.6.2.2 Oxide and chemical composition investigation by XPS.....	88

3.6.3	Phase analysis.....	88
3.6.3.1	XRD.....	88
3.6.3.2	Image analysis by ImageJ software.....	89
3.6.4	Corrosion analysis.....	89
3.6.5	Tribocorrosion analysis.....	92
CHAPTER 4-RESULTS AND DISCUSSION.....		94
4.1	Results: characterization of as-cast CoCrFeNi and HEA samples	94
4.1.1	Phase composition analysis	94
4.1.2	Microstructure and chemical composition observation.....	96
4.1.3	Interpretation of phase formation.....	100
4.1.4	The chemical composition of oxide film on the sample surface.....	101
4.1.5	Hardness measurements.....	108
4.2	Discussion: characterization of as-cast CoCrFeNi and HEA samples	110
4.2.1	Effect of alloying elements on the microstructure and phase evolution of as-cast samples.....	110
4.2.2	Effect of alloying elements on the hardness of CoCrFeNi and HEA samples.....	115
4.3	Results: characterization of CoCrFeNi and HEA samples after corrosion testing.....	117
4.3.1	Corrosion analysis in 0.6 M NaCl solution.....	117
4.3.2	Post-corrosion alloy microstructure and composition (0.6 M NaCl solution).....	120
4.3.3	Post-corrosion surface analysis (0.6 M NaCl solution).....	131
4.3.4	Corrosion analysis in 0.6 M H ₂ SO ₄ solution.....	137
4.3.5	Post-corrosion microstructure and surface analysis (0.6 M H ₂ SO ₄ solution).....	139
4.3.6	Corrosion analysis in 0.6 M NaAlO ₂ solution.....	148
4.3.7	Post-corrosion microstructure and surface analysis (0.6 M NaAlO ₂ solution).....	150
4.4	Discussion: characterization of CoCrFeNi and HEA samples after corrosion testing	159
4.4.1	Effect of alloying element on the corrosion properties of alloy samples in 0.6 M NaCl solution.....	159

4.4.2	Effect of alloying element on the corrosion properties of alloy samples in 0.6 M H ₂ SO ₄ solution.....	162
4.4.3	Effect of alloying element on the corrosion properties of alloy samples in 0.6 M NaAlO ₂ solution.....	165
4.5	Results: characterization of CoCrFeNi and CoCrFeNiSn after tribocorrosion testing in 0.6 M NaCl solution.....	167
4.5.1	Hardness observation.....	168
4.5.2	Corrosion analysis in 0.6 M NaCl solution.....	169
4.5.3	Tribocorrosion analysis in 0.6 M NaCl solution.....	174
4.6	Discussion: characterization of CoCrFeNi and CoCrFeNiSn after tribocorrosion testing in 0.6 M NaCl solution	179
4.6.1	Effect of the Sn addition on the tribocorrosion properties of CoCrFeNiSn testing in 0.6 M NaCl solution.....	179
	CHAPTER 5-OVERALL CONCLUSIONS AND RECOMMENDATIONS.....	181
5.1	Overall conclusions.....	181
5.2	Recommendations.....	182
	REFERENCES.....	184
	APPENDIX A.....	201
	APPENDIX B.....	212
	APPENDIX C.....	213
	APPENDIX D.....	217

LIST OF FIGURES

Figure 1.1	Schematic diagram of the PhD research plan	4
Figure 2.1	A diagram associating material evolution with historical periods	5
Figure 2.2	A schematic diagram of the general concept of multiple equiatomic alloys; a) before mixing (representing a relatively low configurational entropy situation) and b) the formation of random solid solution structure (with an increased degree of configurational entropy) after mixing	6
Figure 2.3	The relationship of the number of elements and the mixing entropy for equiatomic alloys during the state of random solubility	8
Figure 2.4	The processing routes of HEAs as classified by the mixing states	12
Figure 2.5	The number of scientific papers published regarding HEAs between the years 2002 and 2020 (data generated using the Web of Science on April 17th, 2023, for publications using the term "high entropy alloys")	13
Figure 2.6	An arc melter and a casting set with a copper casting mould and a copper hearth	14
Figure 2.7	XRD results showing a) CoCrFeNi (AM) produced by arc melting and b) CoCrFeNi (SPS [^]) produced by spark plasma sintering	15
Figure 2.8	The effect of the different processing methods on corrosion potential (E_{corr}) and pitting potential (E_{pit}) of CoCrFeNi alloys in chloride solution (3.5 wt.%) at ambient temperature; spark plasma sintering (SPS [^]) and arc melting (AM)	15
Figure 2.9	The impact of technological advance in HEAs and their manufacturing processes on the diverse applications	17
Figure 2.10	A SEM image showing a wear track in an AlCoCrFeNiTi coating on a S235 steel substrate	18
Figure 2.11	The relationship between temperature and electrical resistivity in superconductors and normal, non-superconducting metals	19
Figure 2.12	The superconducting transition temperature (T_c) in the (NbTa) _{0.67} (HfTiZr) _{0.33} system over an applied pressure range of 0 to 190.6 GPa	19
Figure 2.13	The classification of alloys based on the calculation of mixing entropy	21
Figure 2.14	a) The SEM micrograph of CoCrFeNi and b) The XRD pattern of CoCrFeNi (FCC: face-centered cubic phase, and IM: intermetallic phase)	21
Figure 2.15	The binary equilibrium phase diagram of Co-Cr	22
Figure 2.16	The binary equilibrium phase diagram of Co-Fe	23
Figure 2.17	The binary equilibrium phase diagram of Co-Ni	23
Figure 2.18	The binary equilibrium phase diagram of Cr-Fe	24
Figure 2.19	The binary equilibrium phase diagram of Cr-Ni	24
Figure 2.20	The binary equilibrium phase diagram of Fe-Ni	25
Figure 2.21	SEM images showing the microstructure of CoCrFeNiAl forming; a) a single-phase and b) a multiple-phase structure	26

Figure 2.22	The binary equilibrium phase diagram of Al-Co	27
Figure 2.23	The binary equilibrium phase diagram of Al-Cr	27
Figure 2.24	The binary equilibrium phase diagram of Al-Fe	28
Figure 2.25	The binary equilibrium phase diagram of Al-Ni	28
Figure 2.26	EDS images showing the Cu segregation on the CoCrFeNiCu surface; a) a SEM image of CoCrFeNiCu, b) EDS mapping of Cr, c) EDS mapping of Fe, d) EDS mapping of Co, e) EDS mapping of Ni, and f) EDS mapping of Cu	29
Figure 2.27	The binary equilibrium phase diagram of Co-Cu	30
Figure 2.28	The binary equilibrium phase diagram of Cr-Cu	30
Figure 2.29	The binary equilibrium phase diagram of Cu-Fe	31
Figure 2.30	The binary equilibrium phase diagram of Cu-Ni	31
Figure 2.31	SEM images showing the microstructure of CoCrFeNiSn	32
Figure 2.32	The binary equilibrium phase diagram of Co-Sn	33
Figure 2.33	The binary equilibrium phase diagram of Cr-Sn	33
Figure 2.34	The binary equilibrium phase diagram of Fe-Sn	34
Figure 2.35	The binary equilibrium phase diagram of Ni-Sn	34
Figure 2.36	A schematic diagram of a compressive stress-strain curve in solid materials	35
Figure 2.37	Comparison of three indent scales for hardness testing in polycrystalline materials; a) macroscale, b) microscale, and c) nanoscale indentations	36
Figure 2.38	The difference of micro-indent shape between Knoop and Vickers	37
Figure 2.39	The hardness measurement operated with the micro-Vickers indentation	37
Figure 2.40	The influence of Al addition on the phase transformation and hardness in the $Al_xCoCrFeNi$ system	41
Figure 2.41	a) XRD patterns of as-cast HEA samples and Linear polarization curves of HEAs after corrosion testing in b) 3.5 wt.% NaCl solution and c) 0.5 NaOH solution	44
Figure 2.42	Three regions on the polarization curve during the corrosion measurement	45
Figure 2.43	The analysis of Tafel slopes to calculate E_{corr} and i_{corr}	45
Figure 2.44	The Evans diagram for a mixed electrode state in the system of iron electrode and acidic solution	47
Figure 2.45	The comparison of an Evans diagram and experimental polarization curves in the system of an iron electrode and acidic solution	48
Figure 2.46	The simplified potential-pH equilibrium diagram in the system of the iron and water	49
Figure 2.47	The potential-pH equilibrium diagram for a) water, b) copper, c) iron, and d) aluminium at 25 °C containing; white region (immunity), grey region (passivity), and dark region (activity)	50

Figure 2.48	The potential-pH equilibrium diagram for cobalt and water at 25 °C	51
Figure 2.49	The potential-pH equilibrium diagram for chromium and water at 25 °C	51
Figure 2.50	The potential-pH equilibrium diagram for nickel and water at 25 °C	52
Figure 2.51	The potential-pH equilibrium diagram for tin and water at 25 °C	52
Figure 2.52	Several corrosion forms in metals	54
Figure 2.53	Steel tubes in the boiler-feedwater system undergoing general corrosion	55
Figure 2.54	The formation of galvanic corrosion is found in a ray lamp of a distillation column which occurred at the interface between a stainless steel AISI 410 plate in contact with a carbon steel bolt in an environment with hydrocarbons contaminated with salts	56
Figure 2.55	The galvanic corrosion from a couple of steel and broken mill scale	56
Figure 2.56	Pitting corrosion formed on AISI 316 stainless steel in 3.5 wt.% NaCl solution	57
Figure 2.57	An etched cross-sectional image of Cu-Zn alloy showing the dezincification	58
Figure 2.58	The corrosion mechanism of Al _{0.5-0.7} CoCrFeNi in 0.6 M NaCl solution at room temperature	63
Figure 2.59	SEM images of a) CuCr ₂ Fe ₂ Ni ₂ Mn ₂ and b) Cu ₂ CrFe ₂ NiMn ₂ alloy after corrosion testing in 1 M H ₂ SO ₄ solution at room temperature	66
Figure 2.60	The application relating with tribocorrosion properties	67
Figure 2.61	Five contact modes for tribocorrosion tests	68
Figure 2.62	The common components of tribocorrosion experimental setups	69
Figure 2.63	The diagram showing a comparison of tribocorrosion properties between coating with and without AlCoCrFe on the Al substrate	72
Figure 2.64	The comparison of tribocorrosion properties between coating with and without AlFeCrNiMo on the SS 304 substrate; a) COF vs time and b) wear volume loss	73
Figure 3.1	Schematic diagram of whole PhD research experimentation	76
Figure 3.2	Schematic diagram of the sample fabrication by vacuum arc melting technique	82
Figure 3.3	The process of corrosion sample preparation and the final samples used	84
Figure 3.4	The process of tribocorrosion sample preparation and the final samples used	84
Figure 3.5	A cross-sectional SEM image of CoCrFeNiSn prepared using the FIB-SEM technique	85
Figure 3.6	The approach used to determine the Tafel slopes	90
Figure 4.1	The XRD patterns of the four as-cast samples examined	94
Figure 4.2	Rietveld refinement of as-cast CoCrFeNiSn sample	95

Figure 4.3	BSE-SEM micrographs of as-cast samples; (a) CoCrFeNi, (b) CoCrFeNiAl, (c) CoCrFeNiCu, and (d) CoCrFeNiSn alloys	96
Figure 4.4	BSE-SEM micrographs showing EDS spots of the as-cast CrFeCoNiSn sample with unetched condition	98
Figure 4.5	EDS elemental maps showing as-cast samples; CoCrFeNi, CoCrFeNiAl, CoCrFeNiCu, and CoCrFeNiSn	99
Figure 4.6	The XPS spectra of as-cast samples showing the metal and metal-oxide regions of; a,c,f,i) Cr 2p, d) Al 2p, g) Cu 2p _{3/2} , j) Sn 3d, and b,e,h,k) O 1s peak	107
Figure 4.7	Hardness of as-cast samples and conventional alloys at HV0.5	108
Figure 4.8	SE-SEM micrographs of as-cast sample indents; (a) CoCrFeNi, (b) CoCrFeNiAl, (c) CoCrFeNiCu, and (d) CoCrFeNiSn alloys	109
Figure 4.9	The XPS spectra of CoCrFeNi showing the main peak overlapping in Co, Fe, and Ni elements between 710 eV-714 eV	114
Figure 4.10	EDS analysis showing the chemical composition of CoCrFeNiSn indent	116
Figure 4.11	Linear polarization curves of four alloy and two stainless steel samples immersed in 0.6 M NaCl solution at room temperature	117
Figure 4.12	E_{corr} and E_p of CoCrFeNiSn immersed in 0.6 M NaCl solution at room temperature plotted on the E-pH diagram of water at room temperature	119
Figure 4.13	BSE images of the surface of HEAs samples after immersion in 0.6 M NaCl solution at room temperature; a) CoCrFeNi, b) CoCrFeNiAl, c) CoCrFeNiCu, and d) CoCrFeNiSn	120
Figure 4.14	EDS mapping images of the surface of HEAs samples after immersion in 0.6 M NaCl solution at room temperature; a) CoCrFeNi, b) CoCrFeNiAl, c) CoCrFeNiCu, and d) CoCrFeNiSn (The contrast and sharpness of these images have been adjusted manually to aid visualization and analysis)	124
Figure 4.15	Cross-sectional SEM images of FIB cross sections through features observed on the surface of HEA samples immersed in 0.6 M NaCl solution at room temperature; a-b) CoCrFeNiAl, c-d) CoCrFeNiCu, and e-f) CoCrFeNiSn	126
Figure 4.16	EDS mapping images of cross-sectional CoCrFeNiAl immersed in 0.6 M NaCl solution at room temperature	127
Figure 4.17	EDS mapping images of a cross-section through CoCrFeNiAl at high resolution showing in a porous Co-Cr-Fe-rich structure after corrosion testing in 0.6 M NaCl solution at room temperature	128
Figure 4.18	EDS mapping images of a cross-section through CoCrFeNiAl at high resolution showing in both the dense and porous regions after corrosion testing in 0.6 M NaCl solution at room temperature	129
Figure 4.19	A chemical composition comparing dense and porous regions from the EDS data of Figure 4.18	130

Figure 4.20	a) XPS survey spectra and b) high resolution XPS spectra in the binding energies range of 40-70 eV of alloy samples after corrosion testing	133
Figure 4.21	High resolution XPS spectra in the; a,c,f,i) Cr 2p, d) Al 2p, g) Cu 2p _{3/2} , j) Sn 3d, and b,e,h,k) O 1s peak regions of CoCrFeNi and three HEA samples after corrosion testing in 0.6 NaCl solution	136
Figure 4.22	Corrosion behaviour of four alloy and two stainless steel samples immersion in 0.6 M H ₂ SO ₄ solution	138
Figure 4.23	BSE micrographs on the corroded surface of four alloy samples after immersion in 0.6 M H ₂ SO ₄ solution	140
Figure 4.24	The XPS spectra of alloys analysed post-corrosion testing in 0.6 M H ₂ SO ₄ solution to present the metal and metal-oxide regions of; a,c,f,i) Cr 2p, d) Al 2p, g) Cu 2p _{3/2} , j) Sn 3d, and b,e,h,k) O 1s peaks	144
Figure 4.25	The comparison of the extent of oxidation at the sample surface, assessed via the ratio of metal oxide to metal in four alloys in pre- and post-corrosion testing in 0.6 M H ₂ SO ₄ solution (BC refers to before corrosion testing, and AC means after corrosion testing)	147
Figure 4.26	Corrosion behaviour of four alloy and two stainless steel samples immersion in 0.6 M NaAlO ₂ solution	149
Figure 4.27	BSE micrographs on the corroded surface of four alloy samples after immersion in 0.6 M NaAlO ₂ solution	151
Figure 4.28	The XPS spectra of alloys analysed post-corrosion testing in 0.6 M NaAlO ₂ solution to present the metal and metal-oxide regions of; a,c,f,i) Cr 2p, d) Al 2p, g) Cu 2p _{3/2} , j) Sn 3d, and b,e,h,k) O 1s peaks	155
Figure 4.29	The comparison of the extent of oxidation at the sample surface, assessed via the ratio of metal oxide to metal in four alloys in pre- and post-corrosion testing in 0.6 M NaAlO ₂ solution (BC refers to before corrosion testing, and AC means after corrosion testing)	157
Figure 4.30	A schematic diagram of the proposed processes occurring during the corrosion of three HEA samples examined in this work when tested in 0.6 M NaCl solution at room temperature; a-c) CoCrFeNiAl, d-f) CoCrFeNiCu, and g-i) CoCrFeNiSn	161
Figure 4.31	Load-displacement curves for nanoindentation testing in CoCrFeNiSn showing a different indentation deformation behaviour between FCC CoCrFeNi and Ni-Sn-rich hexagonal phases	169
Figure 4.32	The potentiodynamic curves of CoCrFeNi and CoCrFeNiSn alloys in 0.6 M NaCl solution at ambient temperature	171
Figure 4.33	The Nyquist plots of CoCrFeNi and CoCrFeNiSn alloys in 0.6 M NaCl solution at ambient temperature	172
Figure 4.34	a) The Bode plots and b) Bode phase plots of CoCrFeNi and CoCrFeNiSn alloys in 0.6 M NaCl solution at ambient temperature	173
Figure 4.35	The equivalent circuit model of alloys for fitting in 0.6 M NaCl solution at ambient temperature	174

Figure 4.36	Sliding potential for CoCrFeNi and CoCrFeNiSn alloys tested in 0.6 M NaCl solution at ambient temperature	175
Figure 4.37	Cathodic current flowing in tribocorrosion testing for CoCrFeNi and CoCrFeNiSn alloys tested in 0.6 M NaCl solution at ambient temperature	176
Figure 4.38	Tribocorrosion testing parameters for CoCrFeNi and CoCrFeNiSn tested in 0.6 M NaCl solution at ambient temperature	177
Figure 4.39	SEM micrographs showing the wear morphology after tribocorrosion testing of (a) CoCrFeNi and (b) CoCrFeNiSn	179

LIST OF TABLES

Table 2.1	The values of mixing entropy in equiatomic alloys with additional elements up to 13	8
Table 2.2	Various criteria introduced for the interpretation of HEA systems	11
Table 2.3	A summary table of some of the reported CoCrFeNi properties	22
Table 2.4	The ISO 14577-1 standard for the scales of hardness tests	37
Table 2.5	The hardness values of conventional alloys collected from previous research	39
Table 2.6	The hardness values of HEAs collected from previous research	40
Table 2.7	The effect of volume fraction of Laves phase on hardness and plastic strain in the CoCrFeNiTa _x system	42
Table 2.8	The corrosion properties of conventional alloys in chloride solution at room temperature	59
Table 2.9	The corrosion properties of conventional alloys in acidic solution at room temperature	60
Table 2.10	The corrosion properties of conventional alloys in alkaline solution at room temperature	60
Table 2.11	The corrosion properties of HEAs in chloride solution at room temperature	62
Table 2.12	The corrosion properties of HEAs in acidic solution at room temperature	62
Table 2.13	The corrosion properties of HEAs in alkaline solution at room temperature	63
Table 2.14	The criteria for considering dominant mechanism in tribocorrosion testing	70
Table 2.15	The summary of detected volume loss of SS 304 in 0.5 M NaCl solution	71
Table 3.1	The chemical composition of four alloy systems (compositions were selected in atomic percent ratios, and the conversion to weight percentage was calculated using the atomic masses; 26.98 (Al), 58.93 (Co), 52.00 (Cr), 63.55 (Cu), 55.85 (Fe), 58.69 (Ni), and 118.71 (Sn))	77
Table 3.2	The fundamental variables to calculate the five thermodynamic variables for HEA systems	78
Table 3.3	The values of mixing enthalpy of different atomic couples (kJ/mol) for HEA systems	78
Table 3.4	The calculation of five thermodynamic variables for the interpretation of HEA systems	79
Table 3.5	The fundamental data of raw materials and conventional alloys	79
Table 3.6	The fundamental data of chemicals used in the electrochemical experiments	80
Table 3.7	The set parameters for SEM analysis	85

Table 4.1	Refined structural parameters of as-cast CoCrFeNiSn sample	95
Table 4.2	The quantitative chemical composition (at.%) of as-cast samples as analyzed through the EDS technique from a previously published work [172]	97
Table 4.3	The chemical compositions in atomic percent (at.%) of CrFeCoNiSn alloys phase via EDS analysis determined here, and the phase composition (phase composition identification from previous research [172])	98
Table 4.4	The relative atomic concentration (at.%) at the as-cast sample surfaces; CoCrFeNi, CoCrFeNiAl, CoCrFeNiCu, and CoCrFeNiSn alloys	103
Table 4.5	The relative surface atomic concentration (at.%) of each analysed element at the as-cast sample surface in metallic and ionized form (taken to indicate the relative involvement of the atoms in either the alloy in metallic form or as metal oxides)	104
Table 4.6	The stable metal-oxide reaction and the standard Gibbs free energy change of all elements (Al, Co, Cr, Cu, Fe, Ni and Sn) in this work	113
Table 4.7	The corrosion properties of four alloy and two stainless steel samples immersed in 0.6 M NaCl solution at room temperature	118
Table 4.8	The results of phase fraction analysis via ImageJ software and the general observation of surface characteristics. Results are for the CoCrFeNi and three HEA surfaces after corrosion testing, with an additional test of CoCrFeNiSn before corrosion testing, which was conducted to better understand the phase makeup of this novel alloy, and whether the apparent dominance of the hexagonal phase seen in the corroded samples was an effect of large changes in visible phases due to the corrosion process.	122
Table 4.9	The chemical composition on the sample surfaces after corrosion testing in 0.6 M NaCl solution	132
Table 4.10	The relative atomic proportion of metal oxides and metals (referred to atomic percentage of the total content of the element at the surface) on the sample surfaces after corrosion testing in 0.6 M NaCl solution	134
Table 4.11	The analytical corrosion data of four alloy and two stainless steel samples in 0.6 M H ₂ SO ₄ solution at room temperature	139
Table 4.12	The relative atomic concentration (at.%) at the sample surfaces for the alloys under study post-corrosion testing in 0.6 M H ₂ SO ₄ solution	142
Table 4.13	The relative surface atomic concentration (at.%) of each analysed element at the surface post-corrosion testing in 0.6 M H ₂ SO ₄ solution in metallic and ionized form (taken to indicate the relative involvement of the atoms in either the alloy in metallic form or as metal oxides)	146
Table 4.14	The analytical corrosion data of four alloy and two stainless steel samples in 0.6 M NaAlO ₂ solution at room temperature	150
Table 4.15	The relative atomic concentration (at.%) at the sample surfaces for the alloys under study post-corrosion testing in 0.6 M NaAlO ₂ solution	152

Table 4.16	The relative surface atomic concentration (at.%) of each analysed element at the surface post-corrosion testing in 0.6 M NaAlO ₂ solution in metallic and ionized form (taken to indicate the relative involvement of the atoms in either the alloy in metallic form or as metal oxides)	156
Table 4.17	The mechanical properties, hardness and modulus, and contact depth during nanoindentation testing of two phases in the CoCrFeNiSn alloy	169
Table 4.18	The corrosion parameters, obtained via the electrochemical analysis of CoCrFeNi and CoCrFeNiSn alloys in 0.6 M NaCl solution at ambient temperature	170
Table 4.19	EIS model parameters for CoCrFeNi and CoCrFeNiSn alloys in 0.6 M NaCl solution at ambient temperature	178
Table 4.20	Tribological and tribocorrosion parameters for CoCrFeNi and CoCrFeNiSn alloys tested in 0.6 M NaCl solution at ambient temperature	178

CHAPTER 1

INTRODUCTION

Recently, much attention has been paid to the design of new alloys using the concept of high entropy alloys (HEAs). This route can inspire new discoveries and allow the development of material properties for use in several application areas, for example automotive, aerospace, renewable energy, biomaterials, coating materials, and construction [1-4]. In these areas materials may be sought which offer improved strength, ductility or toughness, higher temperature capability or resistance to corrosion or wear, for example; all of which can be offered by HEAs [1-3]. The class of alloys was first defined by Yeh et al. [5] in the 1990s. HEAs have been widely known since 2004, when the first research papers on such alloys were published, with perhaps some work predating this (for example, in his book [5], Yeh claims to have been working on such alloys since 1995). It shows the combination of many metallic elements in equiatomic and also non-equiatomic (but still relatively similar) ratios to form single or multiple phase alloys [1-4,6]. Because of this perhaps unexpected behavior, and the intriguing properties shown, there has been increasing research in both the design of new alloys and to identify and understand material properties shown by these new HEA systems.

Currently, the issue of material damage resulting from corrosion attack is still of interest to many scientists, who search for both the solution to and prevention of this problem. Corrosion in materials leads not only to risk to human life during the working operation, but also is the cause of economic harm in the industrial sector [7]. In 1978, the first assessment of the economic impact caused by corrosion in the United States estimated that the cost was \$300 billion a year. By 1995 this had been reduced to \$139 billion, stemming from technological changes brought about with greater understanding of the corrosion process [7]. However, the corrosion cost rapidly jumped from an estimated \$276 billion in 1998 to \$1,000 billion in 2013, due to the increase in both direct and indirect costs of corrosion in the industrial and domestic sectors. For example, the cost of research and technology required for corrosion control are direct costs, and the indirect costs are related corrosion management, for example by inspection and maintenance, or the damage caused by corrosion itself [8,9]. As a result of this, corrosion has been a major topic in materials research and development for a considerable time. More recently this study has encompassed HEAs, in the hope that these alloys may provide an alternative way to solve current corrosion issues.

Many HEA systems have been explored to some extent and reported in the literature. One particularly common set of examples are those involving the 3d transition elements, in particular based on the CoCrFeNi system. In its quaternary equiatomic form, it forms a single solid-solution phase with FCC structure [10,11] and can display some attractive properties, such as relatively high levels of ductility, strength, and corrosion resistance [10,11]. This system therefore is suitable as a base system for the development of enhanced corrosion properties by the addition of further alloying elements. In the previous research, there have been a number of studies that attempt to do this, and report the effect of various alloying elements on the corrosion properties in the main CoCrFeNi alloy. The addition of noble metallic elements and high-passivating metallic elements, such as Al, Cu, Mo, and Ti, has been found to affect the corrosion properties and oxide films formed in this system [1,2,12,13]. Some of these, Mo and Ti, have shown a positive effect on the corrosion resistance in chloride solution, as a consequence of the efficiency of oxide films that are formed in resisting such attack [1,2,12,13]. Other elements, Al and Cu, have poor capability to resist chloride. This comes about as the passive films formed are unstable or thin (nanoscale) [1,2]. In addition to the effect on corrosion, the inclusion of these other elements will also change other properties of CoCrFeNi. For example, the addition of equiatomic Al (forming CoCrFeNiAl) leads to a rise in the hardness and compressive strength, due to the change of stable phase from FCC to BCC and the increased solid solution strengthening that takes place [14]. As another case, CoCrFeNiTi has both good corrosion resistance in chloride-containing solution and high tensile strength, resulting from the homogeneous precipitation of Ni-Ti intermetallic phases which form nanoparticles [12,13].

From such studies, it is clear that it is possible to form both good mechanical and corrosion properties by using HEAs (though it is also clear it is equally possible to fail to reach good properties in both these respects). In general, these materials may allow an increase in the corrosion resistance, hardness, and tribocorrosion properties, and it is clear that the route of adding different fifth elements to equiatomic CoCrFeNi permits many variations in structure, microstructure and chemical properties to be probed, while maintaining some consistency in the systems under study, and avoiding highly exotic (and expensive) elements which would make such alloys a less attractive solution for industry.

This work began with the intention to explore porous structures made from High Entropy Alloys, to seek to exploit their mechanical behavior in different ways. A base 4 component alloy, CoCrFeNi was chosen as this features in many reported HEAs, and has been

studied in its own right. Additions to this were made of aluminium, as this changes the FCC structure of the base alloy to BCC, or copper, as this results in two phase FCC material, and of Sn as the limited information available suggested that it would produce an intermetallic [1-4,10,11,14]. The range of alloys would therefore be expected to show different behaviours due to the different structures. Processing of porous metals is complex however, and one route requires a “space holder” material to retain the pore spaces. High temperature soluble space holders are rare, with an example being sodium aluminate (NaAlO_2), which dissolves in water under alkaline conditions, and work was commenced on the effect of high pH environments on various HEAs based on the CoCrFeNi system, as a well-known base for many HEA compositions. It was soon found however that infiltration into the space holder at the required temperatures was not possible with available equipment, and, as the behaviour revealed under NaAlO_2 solution was seen to be interesting, the focus of the work was shifted to study the corrosion behaviour of the alloys specifically in more detail, with examination under NaCl and H_2SO_4 solutions to provide complementary pH information to that gained with sodium aluminate study.

The aims of the work presented in this thesis therefore are to investigate the changes in corrosion resistance, hardness, and tribocorrosion properties of the main equiatomic CoCrFeNi alloy and three component HEA systems derived from this, by taking equiatomic CoCrFeNi and adding different fifth alloying elements, Al, Cu, and Sn, in equiatomic ratio. The objectives are as below:

- To verify the reported high corrosion resistance of high entropy alloys, over a range of example systems and corrosion conditions in the different solutions; NaCl-neutral solution, H_2SO_4 -acidic solution, and NaAlO_2 -alkaline solution.
- To understand the origin of these effects in terms of desirable formulations and microstructures, leading to low-corrosion alloys.
- To observe the effect of pH (both strong acid and high alkaline solutions) on the passivity of oxide films during uniform corrosion of the main HEA and with the addition of alloying elements Al, Cu, and Sn.
- By characterizing the corrosion properties, microstructural and hardness changes induced by the added elements, and their behaviour under tribocorrosion, to evaluate their potential for applications exposed to mechanical wear in the presence of corrosive environment with chloride attack.

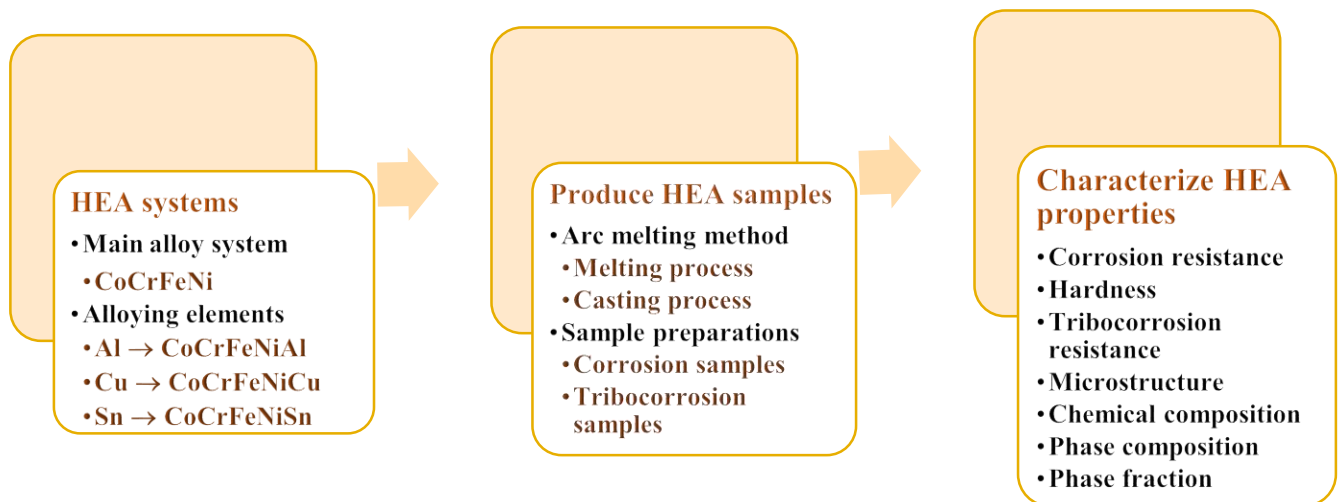


Figure 1.1: Schematic diagram of the PhD research plan.

Overall this thesis consists of five chapters. The introduction is presented first in the chapter one to outline the background and aims of this PhD research. Chapter two discusses recent research relevant to the study, with special attention paid to, corrosion, hardness, and tribocorrosion, of high entropy alloys and conventional alloys. After that, the research methodology is shown in chapter three, which is divided into two sections; materials and experiments. Details are given regarding raw materials, sample preparation methods, and the experimental techniques (listed, in Figure 1.1). The experimental results are presented and discussed in chapter four. Chapter four consists of three sections; firstly, the physical and chemical characteristics of main alloys, CoCrFeNi, CoCrFeNiAl, CoCrFeNiCu, and CoCrFeNiSn, in as-cast form. These includes chemical composition, phase composition, microstructure, and hardness. The second section discusses the corrosion properties of these alloys in several aqueous solutions, NaCl, H₂SO₄, and NaAlO₂ solutions, at room temperature. This section is based on two research papers; “the corrosion behaviour of CoCrFeNi-x (x = Cu, Al, Sn) high entropy alloy systems in chloride solution”, published in *Corrosion Science* and another, “The corrosion resistance of CoCrFeNi-x (x = Al, Cu, Sn) high entropy alloys in different solutions (H₂SO₄ and NaAlO₂ solutions)”, which is to be submitted. The last section discusses the “improved tribocorrosion resistance by addition of Sn to CrFeCoNi high entropy alloy”, a paper published in *Metals*. Finally, the overall conclusion is summarized in chapter five, giving the outcome of this research, including suggestions for relevant future work that could be pursued to take these investigations further.

CHAPTER 2

LITERATURE REVIEW

2.1 High entropy alloys

2.1.1 The discovery of HEAs

As the historical timeline of material evolution in Figure 2.1 suggests, metals have been continuously developed from ancient times to the modern era [15]. Pure metals, gold and copper, were first used, since at least 10,000 BC. Alloys were probably accidentally formed involving Cu, such as Cu-As, Cu-Zn, and Cu-Sn alloys in the Bronze Age. In later times, mechanical properties have been the initial demand behind the development of many alloys for example, steels, super alloys, Ti alloys, Zr alloys, etc.

Subsequently, the concept of multiple component alloys was introduced; generally highlighting that some alloys with multiple components do not produce as many phases as would be allowed for the degrees of freedom they represent under the Gibbs phase rule [15].

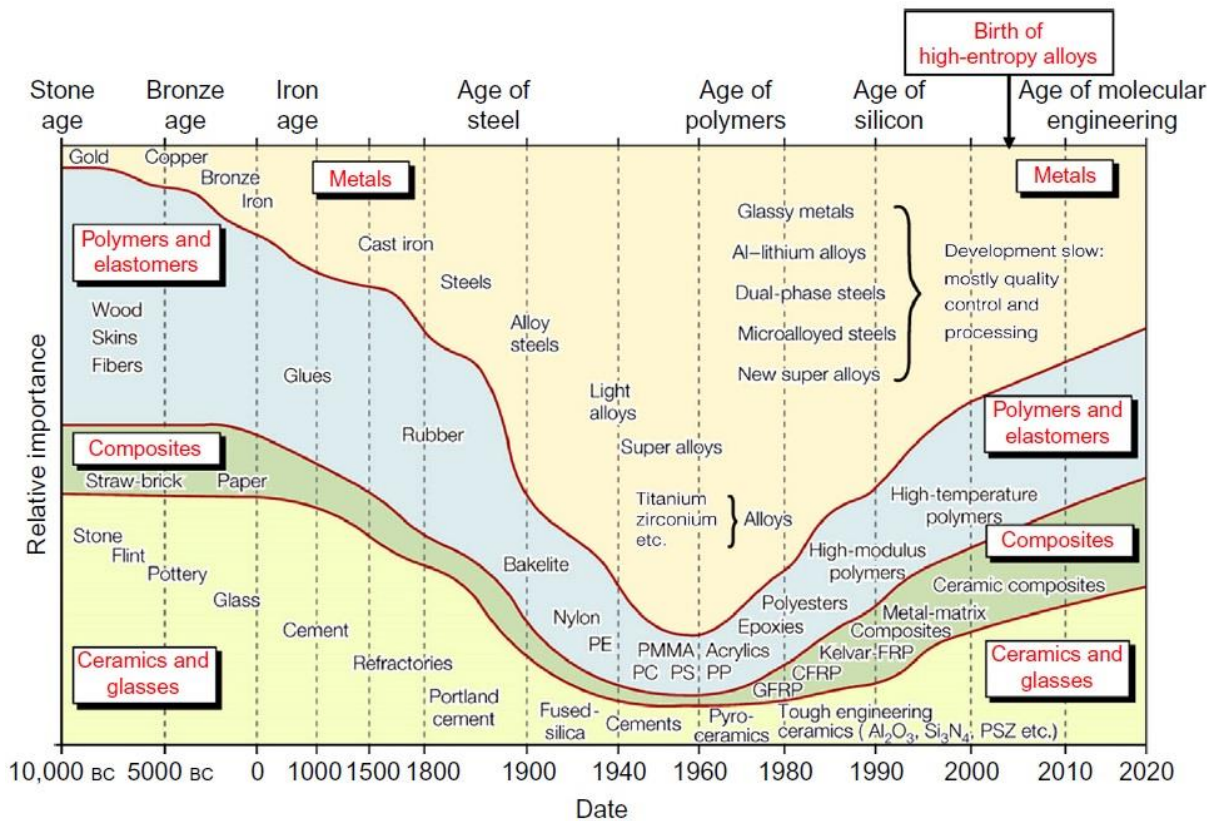


Figure 2.1: A diagram associating material evolution with historical periods [15].

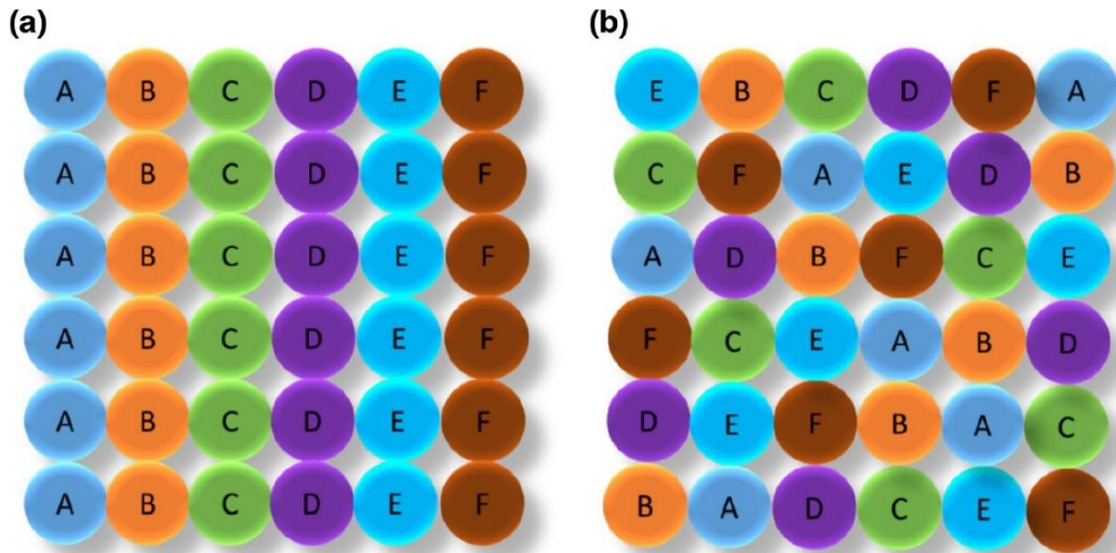


Figure 2.2: A schematic diagram of the general concept of multiple equiatomic alloys; a) before mixing (representing a relatively low configurational entropy situation) and b) the formation of random solid solution structure (with an increased degree of configurational entropy) after mixing [16].

Although the discovery and naming of HEAs took place in recent years, multi-metallic element alloys without a clear main element were first studied by Achard in the 18th Century [5]. As mentioned by Yeh et al. [5], the German scientist Franz Carl Achard reputedly also worked on such alloys, though direct publications arising from his work have only one book on the record (*Recherches sur les propriétés des alliages métalliques*, published in 1788). Many scientists have more recently attempted to define a class of alloys of this type in many different ways. One of the most well-known examples is Yeh et al. in 2004 giving the definition that it requires mixing of a minimum of five elements in equimolar or near-equimolar ratios (5-35 at% of each) to form solid solutions [5,17,18], Cantor et al. in 2004 referred to the formation of equiatomic multicomponent alloys from six to nine metallic elements with a resulting high mixing entropy [5, 17,18], and Miracle et al. in 2014 proposed that the definition of HEAs should be based on the change of mixing entropy relative to a random solid solution as it follows the ideal concept of mixing entropy [5]. Currently, there are several popular terms for referring to multiple element alloys such as ‘high entropy alloys’ (HEAs) and ‘multi-principal element alloys’ (MPEAs), as found in the current publications [18,19], with others such as Complex Concentrated Alloys (CCAs) used [18]. In this thesis the definition of Yeh is used when describing alloys as high entropy alloys. It revealed that equimass multi-element alloys could form from the combination of five to seven elements. The interest in multiple element

alloys was reawakened by the discoveries of Yeh and Huang in the 1990s [5,20], who introduced the term *high entropy alloys* [15]. Subsequently, the term HEAs as Yeh's concept has come to be used for referring to alloys which are formed by mixing five or more metallic elements in either equiatomic/near-equiatomic ratios or in amounts ranging between 5 to 35 at.% [15,16,21]. This can lead to the formation of unique structures, with a single solid-solution phase (as in Figure 2.2) or multiple phases. In either case there can be unusual properties, for instance, magnetic and electric properties, mechanical properties, wear properties, corrosion properties, and lightweight [6,21] which of course could promote the use of such alloys in several applications, for example, areas including biomaterials, electronic devices, vehicle components, energy storage devices, and turbine blades have all been suggested as possible application areas for HEAs [1,15,21]. Thus, the determination of HEA systems in this work was applied as follows Yeh's concept.

2.1.2 Phase composition in HEA systems

The initial approach taken to interpret HEAs made reference to thermodynamics. As described through thermodynamic theory, the phase composition in HEA structures can be interpreted by reference to thermodynamic variables. The constituent phases in the HEA structures were initially interpreted with a focus on the mixing entropy (ΔS_m) [6,15]. This variable relates to how the level of disorder is increased in a multi-component system when transitioning from a fully demixed or partitioned to an ideally mixed state. The calculation of mixing entropy can be made by a relatively simple and well-known equation [22,23].

$$\Delta S_m = -R \sum_{i=1}^n X_i \ln X_i \quad \text{Equation 1}$$

where ΔS_m is the mixing entropy of the system (J/K mol), n is the number of elements, R is the gas constant (8.314 J/K mol), and X_i is the mole fraction of the X_i component. It is noteworthy that this equation is however applicable to two component systems of ideal gases, and it may not therefore be suited to multicomponent solid alloys.

Yeh's report in 2004 [6] used the fact that ΔS_m will increase in alloys with additional elements to interpret the ΔS_m value as the vital parameter in the evolution of constituent phases in HEA structures, as shown in Figure 2.3 and Table 2.1 [15,20]. Increased entropy of mixing under the random arrangement of multi-element alloys affects the formation of phases in the HEA structures and could possibly cause the enhancement of HEA properties. Applying Equation 1 to the mixing of five elements in the solid state, would give a ΔS_m value of 13.37

J/K.mol, and in Yeh’s interpretation this is taken as the lowest requirement to create HEAs. The theory states that in such a case the entropy of mixing is sufficiently high to counterbalance the enthalpy of mixing in most alloy systems and hence lead to favourable Gibbs free energy change for generating single-phase solid solutions. Since being put forward by Yeh et al., this has widely been used to refer to the component-based definition of HEA systems [18,20].

Further to the formation of a single phase, mutual solid solubility in multi-metallic elements may increase the probability of creating unique phases, not discovered before. This also applies to alloys that form multiple phases, and unique phases could arise which are either ordered or disordered; solid solution phases, body-centered cubic (BCC), face-centered cubic (FCC), and hexagonal closed-packed (HCP) structures [15].

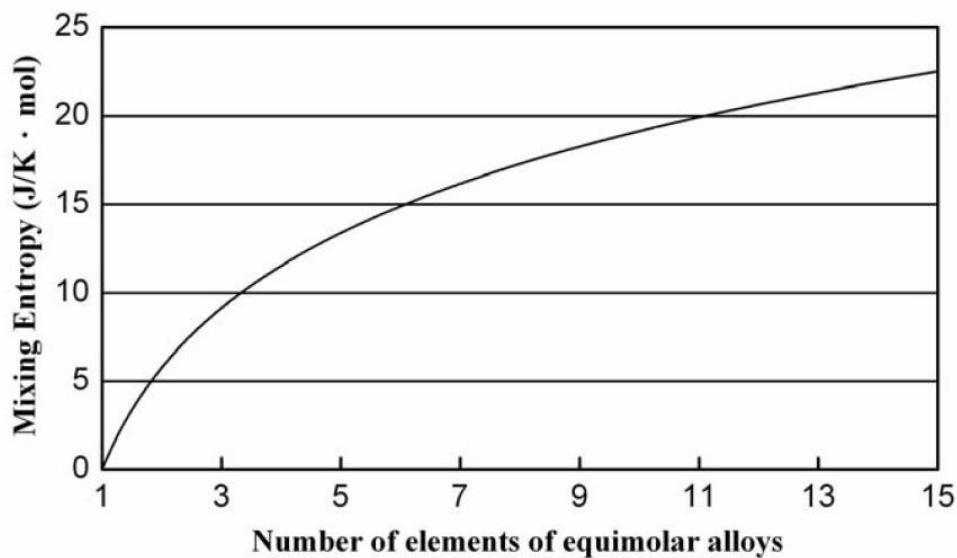


Figure 2.3: The relationship of the number of elements and the mixing entropy for equiatomic alloys during the state of random solubility [20].

Table 2.1: The values of mixing entropy in equiatomic alloys with additional elements up to 13 [15].

N	1	2	3	4	5	6	7	8	9	10	11	12	13
ΔS_m	0	0.69R	1.1R	1.39R	1.61R	1.79R	1.95R	2.08R	2.2R	2.3R	2.4R	2.29R	2.57R

As a corollary to this effect, increase in entropy of mixing could contribute to decreasing the probability of forming complex structures or intermetallic compounds, and thus increasing the probability of generating solid-solution alloys for HEAs as compared with conventional alloys, according to the Gibbs phase rule and the Gibbs free energy of mixing (ΔG_m) [2,15]. The number of phases seen in HEAs is often less than the estimation arrived at by the Gibbs phase rule. This is suggested to stem from high mutual solubility of most metallic

elements in the liquid state with the increased entropy of mixing. This can reduce the number of phase components in the process of formation, specially considering the effect of the suggested low diffusivities of multiple elements in HEA systems [15]. Thus, as a high mixing entropy may prevent intermetallic phases forming [8] this variable has been used for the assessment of phase composition in HEA systems.

$$P + F = C + 1 \quad \text{Equation 2}$$

$$\Delta G_m = \Delta H_m - T\Delta S_m \quad \text{Equation 3}$$

where P is the number of phases, C is the number of components at constant pressure in an equilibrium system, F is the number of degrees of freedom, ΔG_m is the Gibbs free energy of mixing (kJ/mol), T is the absolute temperature (K), ΔH_m is the mixing enthalpy (kJ/mol), and ΔS_m is the mixing entropy (kJ/K mol).

As well as the entropy of mixing (ΔS_m) [24-28], there are four other variables that are also commonly used, consisting of the enthalpy of mixing (ΔH_m) [24-28], the atomic size difference (δ) [24-28], the electronegativity difference ($\Delta\chi$) [15,29], and the valence electron concentration (VEC) [22,27-30], calculated as in the equations below.

$$\Delta H_m = 4 \sum_{i=1, j \neq i}^n \Delta H_{ij}^m X_i X_j \quad \text{Equation 4}$$

$$\delta = 100 \sqrt{\sum_{i=1}^n c_i (1 - r_i/\bar{r})^2} \quad \text{Equation 5}$$

$$\Delta\chi = \sqrt{\sum_{i=1}^n c_i (x_i - \bar{x})^2} \quad \text{Equation 6}$$

$$VEC = \sum_{i=1}^n c_i (VEC)_i \quad \text{Equation 7}$$

where n is the number of elements, X_i is the mole fraction of the X_i component, and X_j is the mole fraction of the X_j component, ΔH_m is the mixing enthalpy of the system (kJ/mol), $\Delta H_{m,ij}$ is the mixing enthalpy of atomic couples (kJ/mol), δ is the atomic size difference (%), c_i is the molar ratio, r_i is the atomic radius of the i th element, \bar{r} is the average atomic radius, $\Delta\chi$ is the electronegativity difference (%), x_i is the Pauling electronegativity of the i th element, \bar{x} is the average electronegativity, VEC is the valence electron concentration, $(VEC)_i$ is the valence electron concentration of the i th element.

As reported by Liang and Fetzer [29], these parameters can be divided into two groups. The first group of δ , $\Delta\chi$, and VEC are three parameters indicated by the Hume-Rothery Rules, which are intended to identify solid solubility by looking for similarity in crystal structure,

valence electrons, atomic size difference, and electronegativity in binary alloys [15,29]. The second group of ΔH_m and ΔS_m are two parameters calculated from thermodynamics [29]. Each parameter has been used to try to explain phase formation in HEA systems as follows. ΔS_m is an initial thermodynamic parameter calculated under the concept of the high mixing entropy for creating equiatomic alloys with 5 or more elements [29]. Increased mixing entropy may restrain the formation of intermetallic phases, and is thus included in the assessment of the stability of disordered solid-solution phases in HEA systems [15,29]. ΔH_m indicates the favourability of mixing, which is required to form a disordered solid solution [29]. δ can be used to evaluate the formation of a solid solution in binary alloy systems, and is extended to the formation of disordered solid-solution phase in HEA systems, and $\Delta\chi$ is also used in this way [29]. The *VEC* value can be related to the crystallographic structure that forms in a HEA system [22,29]. In addition, recent work by Calvo-Dahlborg and Brown [19] highlights two variables developed from the Hume-Rothery rules; the ratio of itinerant electrons to atoms (e/a) and the average radius, with which they followed the approach of creating a self-organizing map. These parameters are used to identify the region where alloys are stable, and make predictions of properties and phases in the HEA system. This work found that e/a has higher accuracy than *VEC* for estimating the phase composition, due to the impact on pseudogap formation through the interference phenomenon, as reported by Mizutani and Sato [31]. However, the limitation of the e/a approach is that the method required to accurately calculate this value for a multicomponent alloy is complicated. It may require a first-principles full-potential linearized augmented plane wave (FLAPW)-Fourier calculation [31].

Once these parameters have been calculated there are several criteria which can be applied, those introduced by Zhang et al. [24,32], Guo et al. [25,26,30], Ren et al. [33], and Chen et al. [27] as summarised in Table 2.2. These criteria can be used to make predictions and attempt to design alloys, and to interpret the microstructures observed in HEAs. However, these criteria do not give exact results which can explain correctly the observations in all reported HEA systems. Other complicating factors include the processing method, the mutual solubility of particular components of the alloys, etc.

Table 2.2: Various criteria introduced for the interpretation of HEA systems.

Reference	Criteria for evaluation	Phase prediction
Zhang et al. (2008) [24]	$-20 \leq \Delta H_m \leq 5$ $12 \leq \Delta S_m \leq 17.5$ $\delta \leq 6.4$	Simple solid solution phases
	$\Delta H_m \geq -15$ $\delta \leq 4.6$	Disordered solid solution phases
Guo and Liu (2011) [25]	$-22 \leq \Delta H_m \leq 7$ $11 \leq \Delta S_m \leq 19.5$ $0 \leq \delta \leq 8.5$	Solid solution phases
	$-49 \leq \Delta H_m \leq -5.5$ $7 \leq \Delta S_m \leq 16$ $\delta \geq 9$	Bulk metallic glasses
Guo et al. (2011) [30]	$VEC \geq 8$	FCC phases
	$6.87 \leq VEC < 8$	FCC+BCC phases
	$VEC < 6.87$	BCC phases
Guo et al. (2013) [27]	$-11.6 < \Delta H_m < 3.2$ $\delta \leq 6.6$	Solid solution phases
	$\Delta H_m < -12.2$ $\delta > 6.4$	Amorphous phases
	Out of these rules	Intermetallic phases
Ren et al. (2013) [33]	$\Delta H_m \geq -8.8$ $\delta \leq 2.77$	Solid solution phases
Chen et al. (2019) [27]	$\Delta \chi < 10$	Solid solution phases
	$\Delta \chi \geq 10$	Compound phases
Calvo-Dahlborg et al. (2021) [31]	$e/a < 1.53$	FCC or HCP phases
	$e/a > 1.88$	BCC phases
	$1.53 < e/a < 1.88$	FCC+BCC phases or intermetallic phases

2.1.3 Production routes for HEAs

HEAs can be produced by a wide range of methods, as reported in previous literature. This diversity stems from the development of new HEA formulations, which uses many processing methods, such as vacuum arc melting (e.g. for CoCrFeNiAl, CoCrFeNiCu, and CoCrFeNiMn [28,34]), spark plasma sintering (SPS) (for CoCrFeNiMn [35]), and laser cladding of AlCoCrFeNiSi_x-HEA coatings [36].

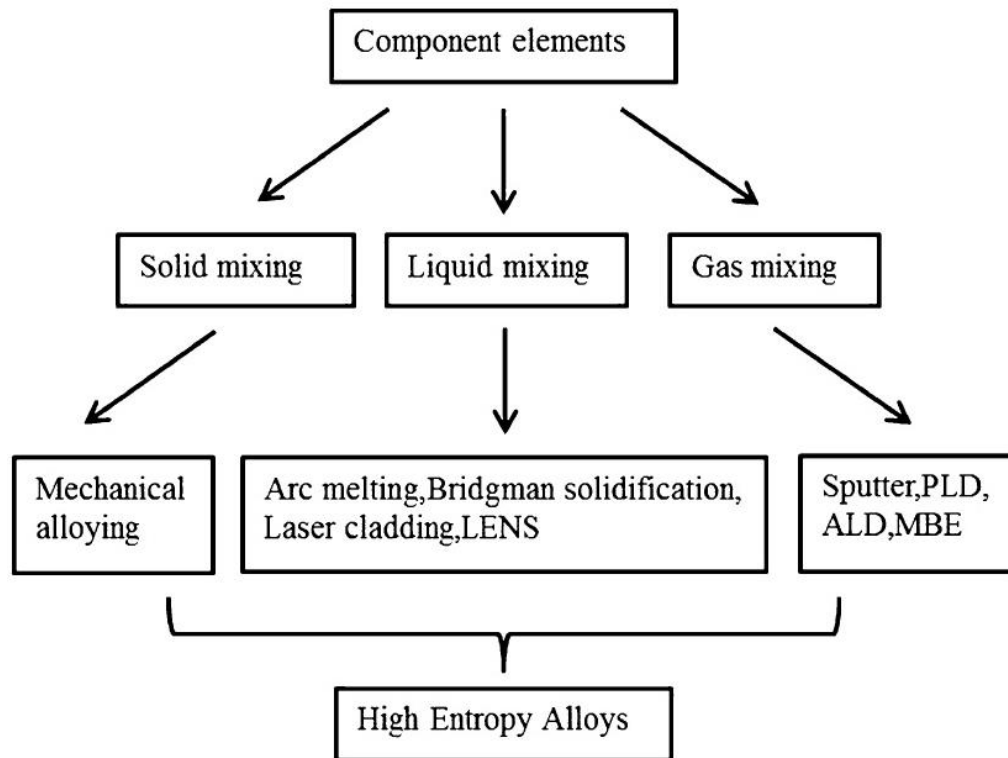


Figure 2.4: The processing routes of HEAs as classified by the mixing states [37].

As classified by Zhang et al. in Figure 2.4 [37], HEA manufacturing methods can be organized by the mixing states during the HEA fabrication operation. They can be divided into three groups; solid state mixing, liquid state mixing, and gas state mixing [37]. Firstly, solid state mixing refers to the processing techniques where elements are mixed in solid form to form HEAs, for example, mechanical alloying. Such HEAs are then formed into bulk samples by using mechanical forces such as forging and compacting [37]. Secondly, liquid state mixing is the formation of HEAs via the combination of metallic elements in the liquid state. For most alloys when all elements are melted at high temperature, each element can be mixed together to form a homogeneous alloy. Examples of this group of methods include vacuum arc melting, Laser Enhanced Net Shape (LENS), Bridgman solidification, and laser cladding [37]. Lastly, gas state mixing is the group of fabrication routes with the mixing of metallic elements in

vapour state, such as sputter deposition, atomic layer deposition (ALD), and pulse laser deposition (PLD) [37].

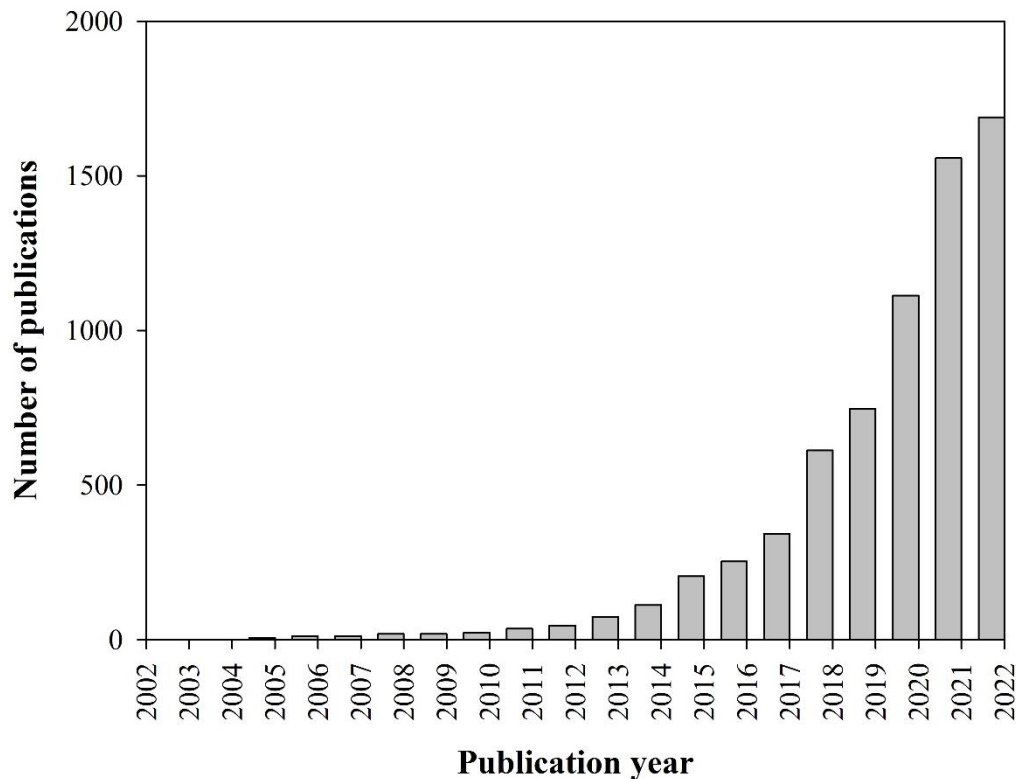


Figure 2.5: The number of scientific papers published regarding HEAs between the years 2002 and 2020 (data generated using the Web of Science on April 17th, 2023, for publications using the term "high entropy alloys") [38].

Figure 2.5 shows the number of scientific papers published regarding HEAs produced by different methods in the last twenty years (2002–2020) in peer-reviewed journals, using the data generated from the Web of Science [38]. It revealed a rising trend in the amount of scientific papers published on HEA research each year, from 2 papers in 2002 to 1,689 papers in 2022 [38]. It has been caused by the materials development in terms of technology, manufacturing process, etc. for supporting the emergence and growth of various industries. In the HEA production routes, Yeh et al. (2004) initially used sputtered film deposition to produce HEAs [6]. However, melting and casting methods are most popularly used for the formation of HEAs. Murty et al. [15] report that approximately 75% of scientific papers, published from 2004 to 2013, used melting and casting for forming bulk alloys. It is also observed that there is a trend for increase in the HEA fabrication by casting route each year [15], possibly reflecting some scaling up investigations on these alloys.

Arc melting is a conventional method, and is the most popular of the methods in the scientific literature for preparing bulk HEA samples [15,37]. Figure 2.6 shows the main components of an arc melter which consists of a melter, a casting mould, and a casting hearth [37]. HEA samples are melted and homogeneously mixed in the liquid state with re-melting five or more times [15,37,39,40]. The temperature may be up to 3,000 °C during the heating step [1,15,41], and this is followed by rapid cooling under the argon environment (this inert gas used to restrict oxidation on the sample surface [39,42]).

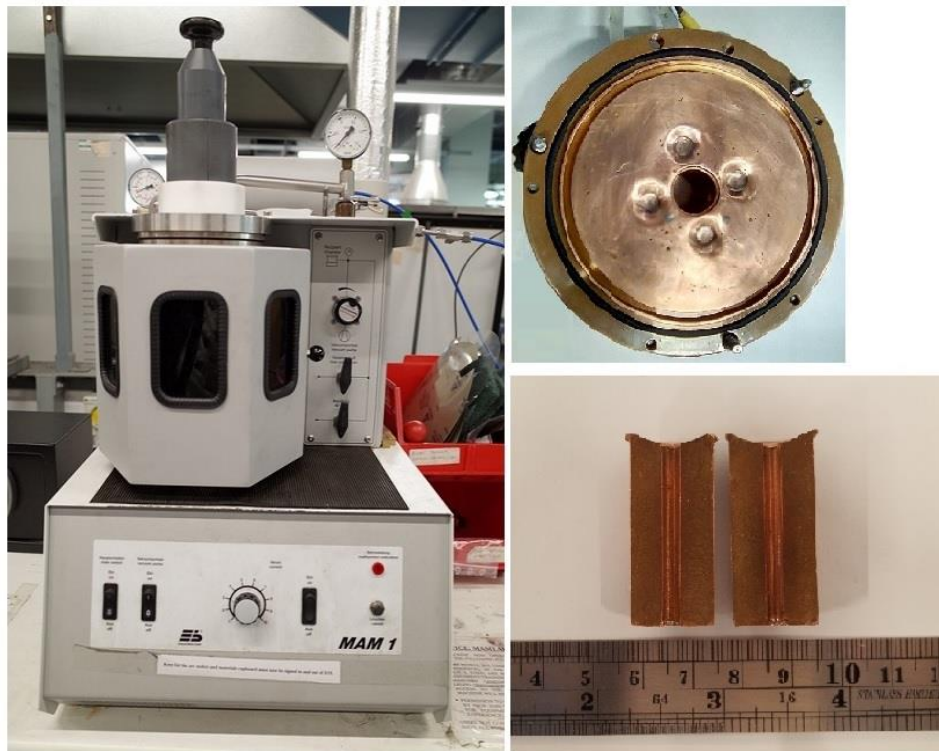


Figure 2.6: An arc melter and a casting set with a copper casting mould and a copper hearth.

Arc melting involves rapid solidification, and this can restrain the process of secondary-phase precipitation, and thus (if samples are observed in the as-cast state) it may increase the chances of observation of single solid-solution phase alloys [15,37], even if these are not the stable phase. The technique also has limitations, such as not being suitable to form alloy systems which contain high vapour pressure elements, for example Mg, Mn, and Zn. The evaporation of these elements can lead to change of chemical composition [1,15,41].

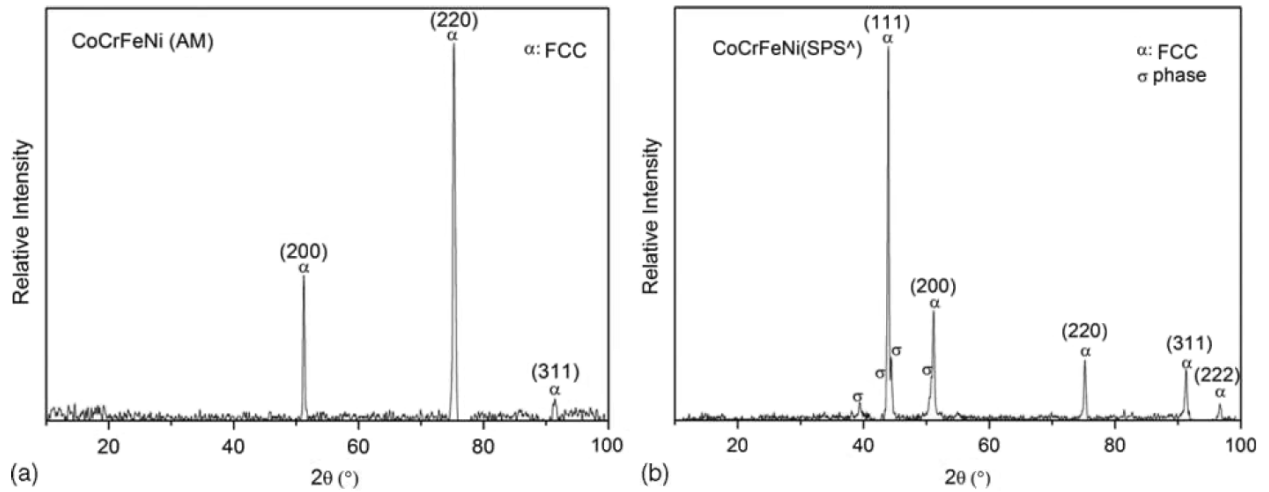


Figure 2.7: XRD results showing a) CoCrFeNi (AM) produced by arc melting and b) CoCrFeNi (SPS^A) produced by spark plasma sintering [43].

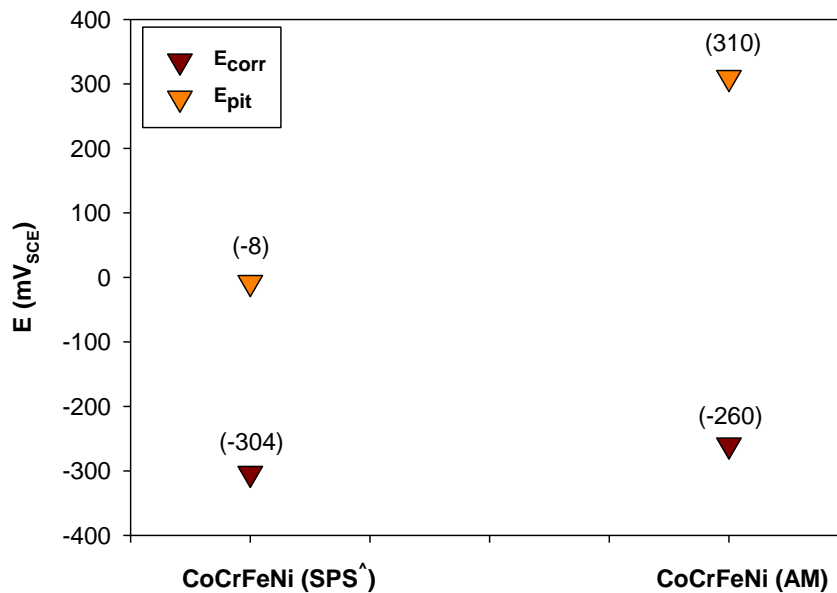


Figure 2.8: The effect of the different processing methods on corrosion potential (E_{corr}) and pitting potential (E_{pit}) of CoCrFeNi alloys in chloride solution (3.5 wt.%) at ambient temperature; spark plasma sintering (SPS^A) and arc melting (AM) [11,43,44].

Another significant aspect of the choice of processing method used to form HEAs is the impact it will have on the HEA properties. Each fabrication method affects the phase components and the HEA microstructures, which will affect both chemical and physical properties. For example, the use of spark plasma sintering and arc melting to form CoCrFeNi have been shown to affect the phase structures and corrosion properties as shown in Figures 2.7 and 2.8 [11,43,44]. The CoCrFeNi samples from arc-melting contain a single CoCrFeNi FCC phase, while samples which were produced by spark plasma sintering consist of two

phases, the major FCC phase and minor Cr- σ intermetallic phase in a structure of complex tetragonal form, as presented in Figure 2.7 [43]. This difference between the two processing routes can result in dissimilar properties, for example the corrosion values of the corrosion parameters, E_{corr} and E_{pit} (the corrosion potential and the pitting potential). The CoCrFeNi alloy produced by arc melting has been found to have higher values of E_{corr} and E_{pit} than nominally the same alloy formed by spark plasma sintering due to the formation of Cr- σ phases in the CoCrFeNi structure in the latter [43]. This phase leads to a decrease in the quantity of Cr in the major CoCrFeNi FCC phase produced by SPS, which affects the capability of the protective Cr₂O₃ film to inhibit the corrosion attack [2,43]. Therefore, the loss of Cr from the major CoCrFeNi phase is a vital reason for poorer corrosion properties in this alloy.

2.1.4 HEA in structural and functional applications

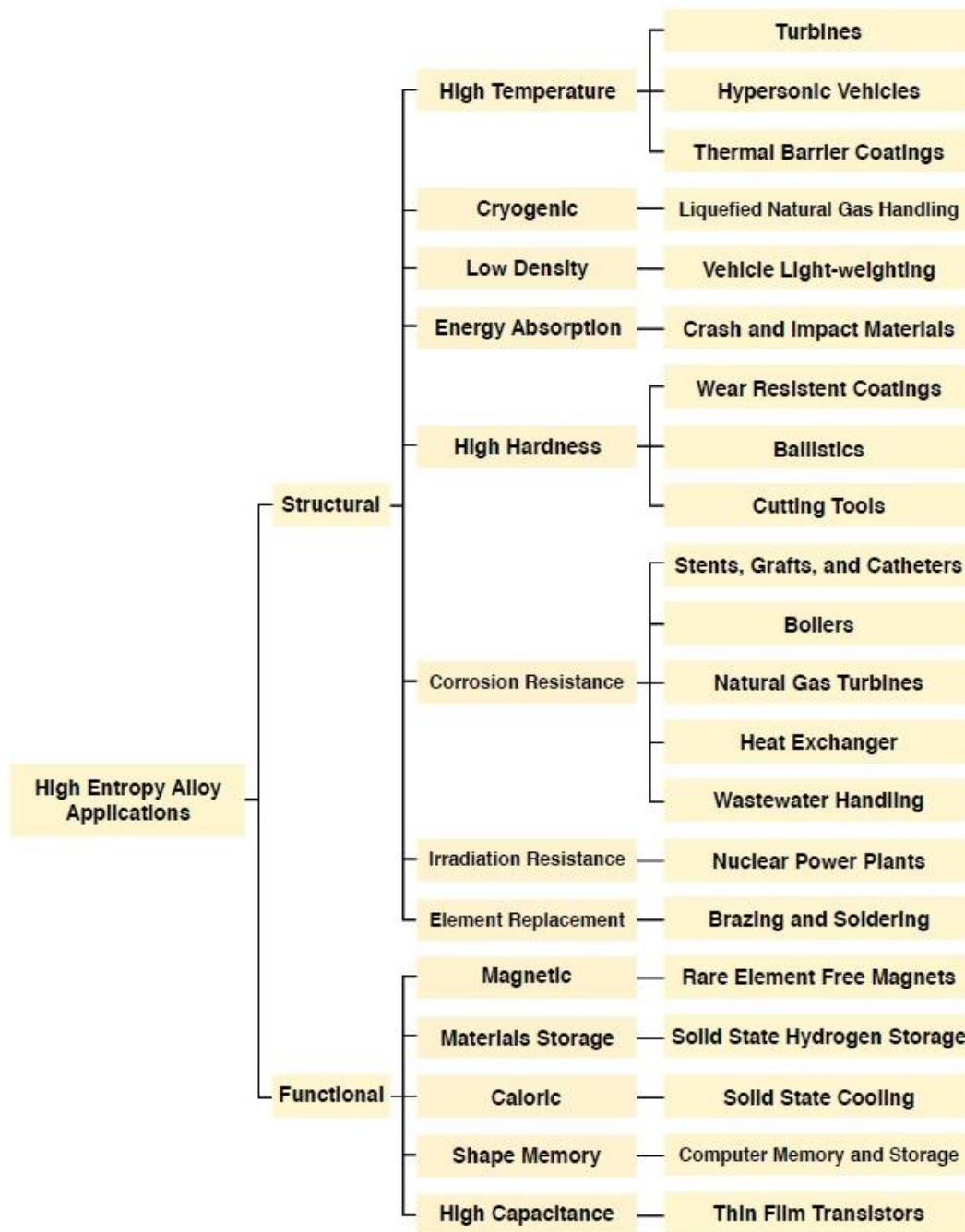


Figure 2.9: The impact of technological advance in HEAs and their manufacturing processes on the diverse applications [45].

Currently, many HEA systems have been explored to improve their properties and overcome the limitations of conventional alloys for use in several applications, for example in automotive, aerospace, defense, energy, electronics components, and medical devices [45]. Figure 2.9 shows the classification of suggested fields for HEA applications which consists of two root categories; structural and functional approaches.

For structural applications for HEAs the focus is for development of alloy structures and defects to increase the properties, such as mechanical behavior at high temperature, cryogenic temperatures, high hardness, and also associated properties such as low density, corrosion resistance, etc. [45,46]. Success with these goals could lead to the substitution of some traditional alloys by HEAs. Design of alloys to have the correct microstructures is done by calculating data related to phase transformations, phase equilibria, phase stability, and other thermodynamic data [47]. An example of such development for a structural application is equiatomic AlCoCrFeNiTi which has relatively high ductility, hardness, strength, and wear resistance [45,48]. This has been used as a coating on S235 steel substrate approximately 210 μm in thick, deposited by thermal spraying. This HEA consists of a matrix phase of ordered B2/BCC structure and two minor phases of disordered A2/BCC and A12/centred cluster structures. The substrate hardness of S235 steel is not reported in this paper, but the hardness value of this grade of steel was found to be about 183 (HV0.1) in Liu and Janssen's report [49]. An increase in the microhardness of samples coated with AlCoCrFeNiTi of approximately 730 (HV0.1) was observed, without any cracks resulting from the brittle behaviour being seen on the wear tracks after wear testing under different tribological tests; ball-on-disk, oscillating wear, and scratch tests, as shown in Figure 2.10 [48]. Thus, this alloy may be suitable for ballistics, cutting tools, and wear-resistant coatings [45,48].

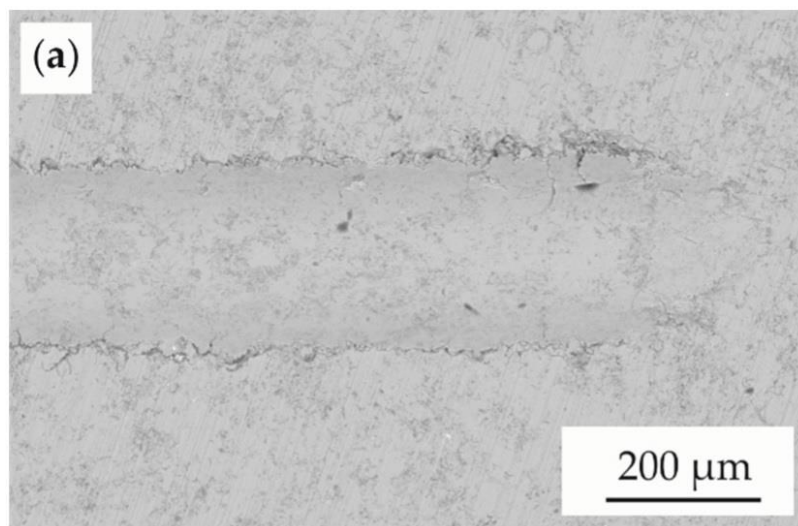


Figure 2.10: A SEM image showing a wear track in an AlCoCrFeNiTi coating on a S235 steel substrate [48].

In the functional application of HEAs, many HEA systems have unique properties, such as high capacitance, magnetic behaviour, superconductivity, and shape memory behavior. These could prove useful in, for example, computer memory and storage, solid state hydrogen

storage, thin film transistors, and superconductors [45,50]. $(\text{NbTa})_{0.67}(\text{HfTiZr})_{0.33}$ is an example of a HEA for a functional application, as it presents superconductivity under pressure [50]. Generally, the characteristic of superconductors is an appearance of zero electrical resistance below a critical transition temperature (T_c), Figure 2.11 [51,52]. $(\text{NbTa})_{0.67}(\text{HfTiZr})_{0.33}$, which contained a BCC phase, can increase T_c for the transition to superconducting state as pressure is applied. T_c is at a temperature of 7.7 K at ambient pressure and 10 K at a pressure of approximately 60 GPa. Further increases of pressure saw T_c slowly drop, reaching 9 K at a 190.6 GPa, Figure 2.12 [50,51]. This may stem from unusual electronic states in HEAs [50,51].

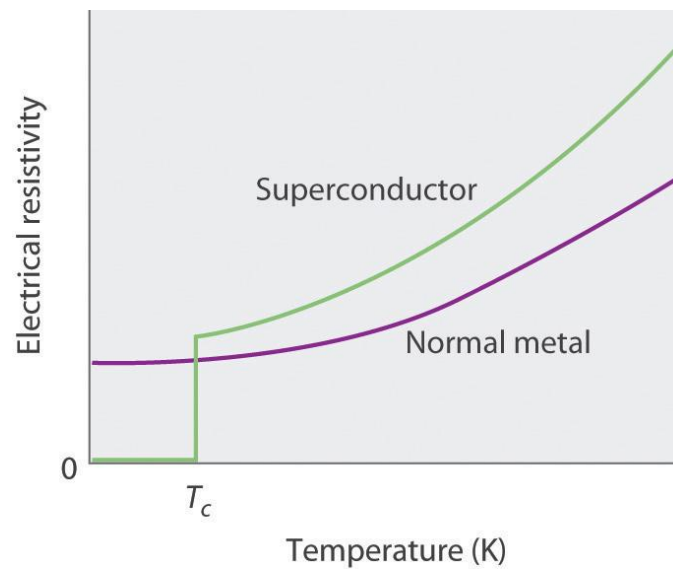


Figure 2.11: The relationship between temperature and electrical resistivity in superconductors and normal, non-superconducting metals [52].

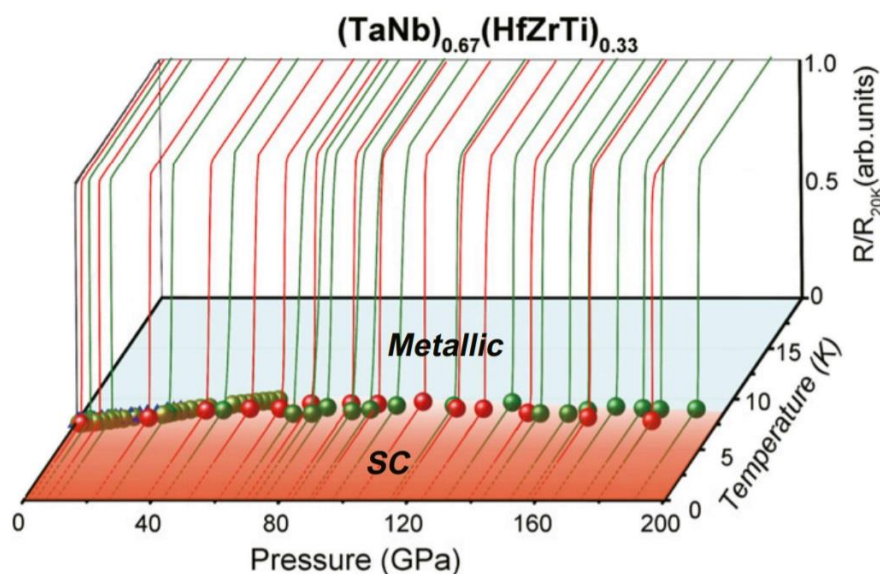


Figure 2.12: The superconducting transition temperature (T_c) in the $(\text{NbTa})_{0.67}(\text{HfTiZr})_{0.33}$ system over an applied pressure range of 0 to 190.6 GPa [51].

HEAs have been explored in research for potential applications in different fields, as shown above. Some HEA systems may be focused for the replacement of current conventional alloys in specific industrial sectors, such as in biomaterial applications [53], for example dental and orthopedic implants. These components are conventionally materials like stainless steel, shape-memory alloys, CoCrMo alloys, Ti alloys, and Mn alloys [53,54]. Ti-6Al-4V and Ti-6Al-7Nb alloys are particularly applied as implant biomaterials due to their high strength and good corrosion resistance. However, some of the alloying elements, Al and V, may cause toxic effects on living tissues and organs in humans [53]. Ti-based HEAs may allow the required properties to be achieved with alternative alloying elements.

Examples of candidate alloys include $(\text{MoTa})_{0.2}\text{NbTiZr}$, which has good mechanical properties with high strength and ductility, and when tested in a mouse model, toxic effects on the surrounding muscle tissue were not found [55]. TiZrHfNbTa has good bio-corrosion behavior with a low corrosion rate of 10^{-4} mm/year in Hank's solution and excellent biocompatibility in vitro examinations with good cell viability, adhesion, and proliferation of the pre-osteoblasts (MC3T3-E1) [56]. $\text{Ti}_{40}\text{Zr}_{20}\text{Hf}_{10}\text{Nb}_{20}\text{Ta}_{10}$ has good mechanical properties for hard tissue implants, as the Young's modulus is low (which brings it closer to the bone) and it has high strength and ductility. It also has good biocompatibility in tests with human gingival fibroblasts with excellent cell adhesion, proliferation, and low toxicity [57].

Such research demonstrates the capacity for consideration of HEAs to lead to new alloys as candidates for different applications. As with all alloys though, the pathway to industrial adoption is long, and in the biomaterial field there is currently a lack of clinical tests of these alloys for actual applications. Experiments in both in vivo and in vitro conditions will be required before use on an industrial scale will be considered [53,54].

2.1.5 The CoCrFeNi-base alloy of many HEA systems

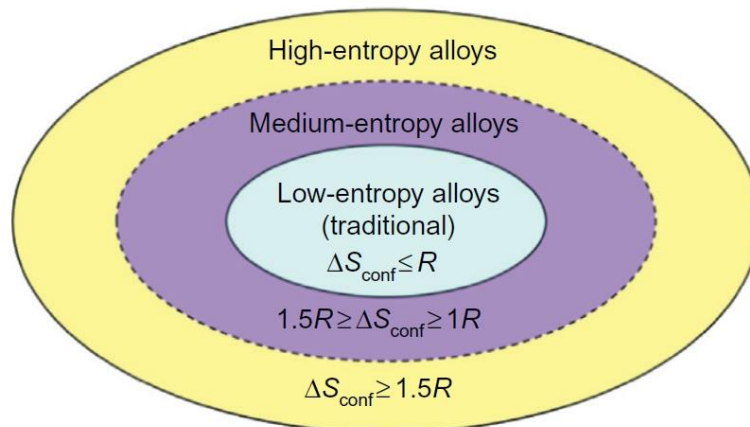


Figure 2.13: The classification of alloys based on the calculation of mixing entropy [15].

There are many discovered HEA systems up to now. Equiatomic CoCrFeNi is one of the most popular systems, used as four-component base alloy to produce HEA systems when mixed with other alloying elements, such as Al, Cu, Mo, Mn, and Ti, to investigate the development of HEA structures and properties [58]. As the criterion of Yeh in Figure 2.13 [15,59], CoCrFeNi, which has an ΔS_{mix} value of $1.39R$, is classified in the group of medium entropy alloys by mixing Co, Cr, Fe, and Ni together. Most frequently, this alloy is produced by arc melting to form a single solid-solution phase of CoCrFeNi with FCC structure, shown by XRD analysis giving a pattern consistent with an FCC structure, and SEM micrographs showing a uniform structure, Figure 2.14 [44,60]. In addition, this alloy has also shown many good materials properties, especially mechanical and corrosion properties, due to a single phase composition and a uniform structure [10,61,62]. The reported CoCrFeNi properties are summarised in Table 2.3.

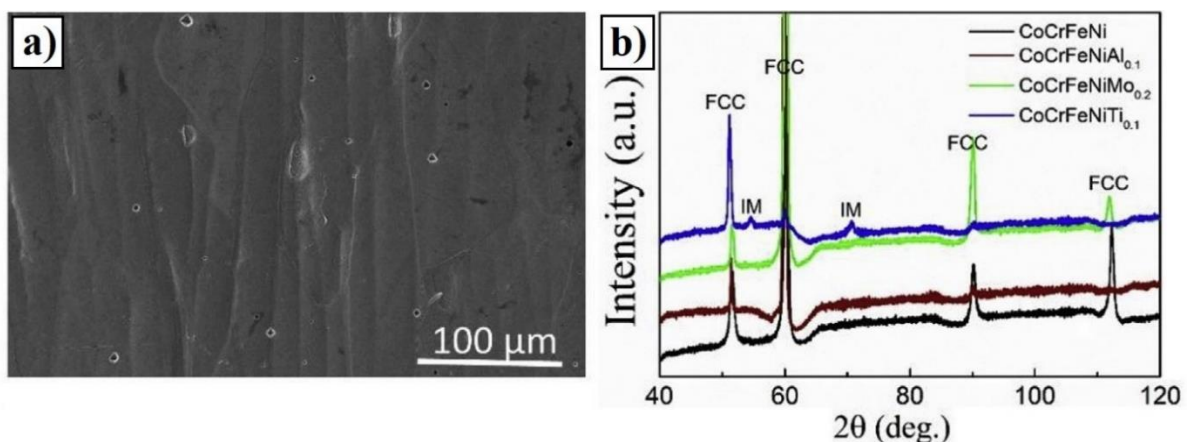


Figure 2.14: a) The SEM micrograph of CoCrFeNi and b) The XRD pattern of CoCrFeNi (FCC: face-centered cubic phase, and IM: intermetallic phase) [60].

Table 2.3: A summary table of some of the reported CoCrFeNi properties.

Materials properties	The measured value as reported in previous works	References
Micro-hardness	150 HV for an as-cast sample 272 HV at an undercooling temperature of 300 K	[61]
Yield strength	155 MPa	[62]
Ultimate tensile strength	472 MPa	
Elongation	59%	
Corrosion resistance (0.6 NaCl solution)	-0.46 V _{SHE} (E _{corr}), 0.035 μA/cm ² (i _{corr}), and 0.31 V _{SHE} (E _{pit})	[11]
Corrosion resistance (0.5 H ₂ SO ₄ solution)	-0.081 V _{SHE} (E _{corr}), 15.8 μA/cm ² (i _{corr}), and 1.017 V _{SHE} (E _t)	[10]

Many researchers have selected CoCrFeNi-based alloys to explore the microstructural changes on addition of a fifth metallic element. The microstructure of the equiatomic CoCrFeNi alloy, created by arc melting, is a single FCC solid solution phase. To help understand this, the binary equilibrium phase diagrams of the elemental pairs in CoCrFeNi alloys can be considered: Co-Cr, Co-Fe, Co-Ni, Cr-Fe, Cr-Ni, and Fe-Ni, Figures 2.15-2.20.

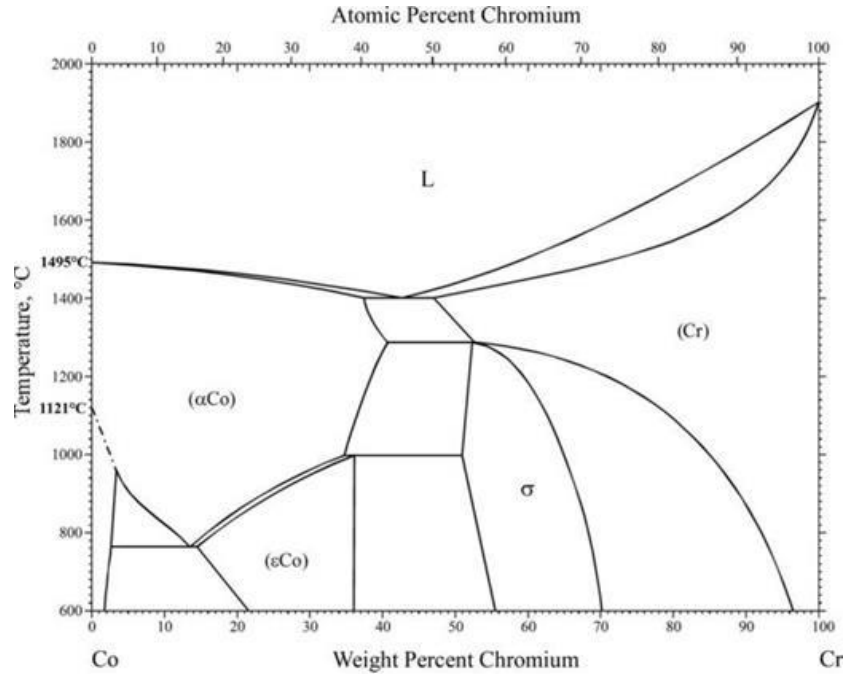


Figure 2.15: The binary equilibrium phase diagram of Co-Cr [63].

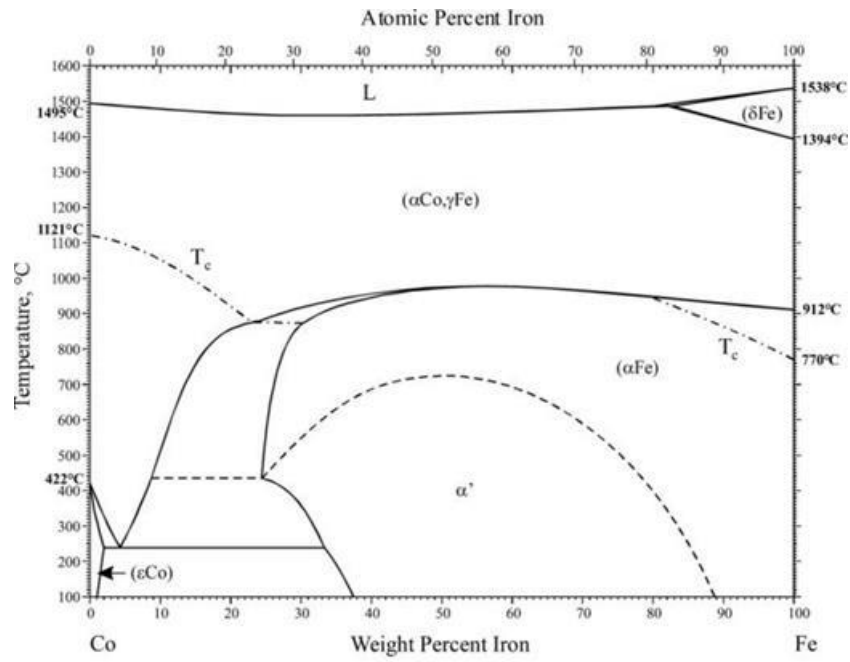


Figure 2.16: The binary equilibrium phase diagram of Co-Fe [63].

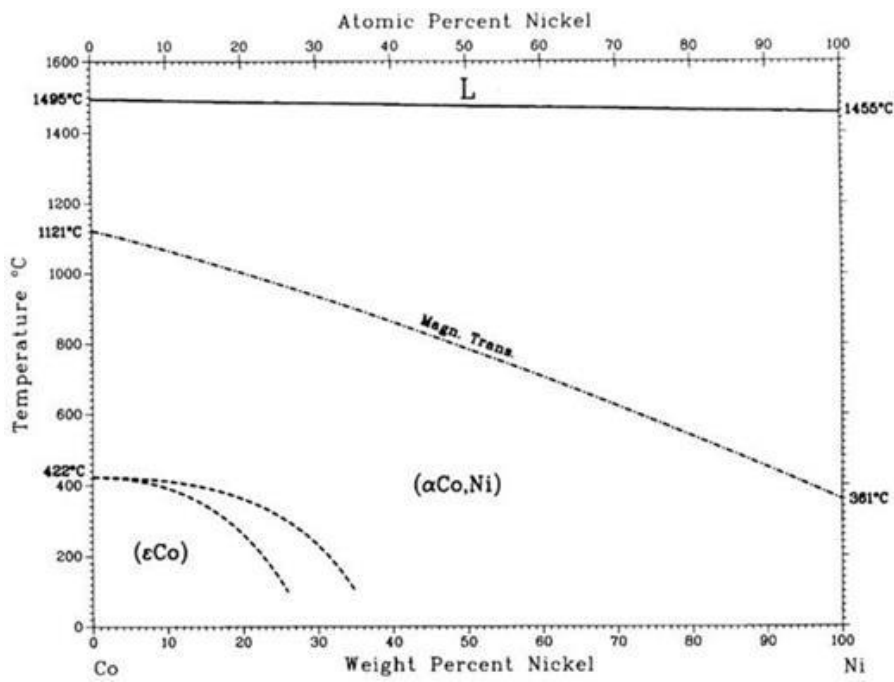


Figure 2.17: The binary equilibrium phase diagram of Co-Ni [63].

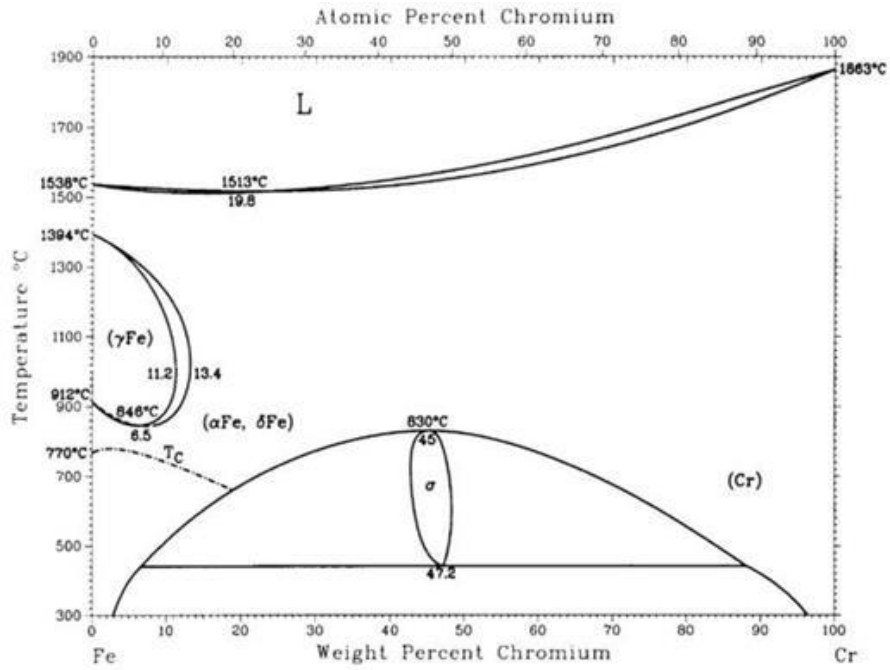


Figure 2.18: The binary equilibrium phase diagram of Cr-Fe [63].

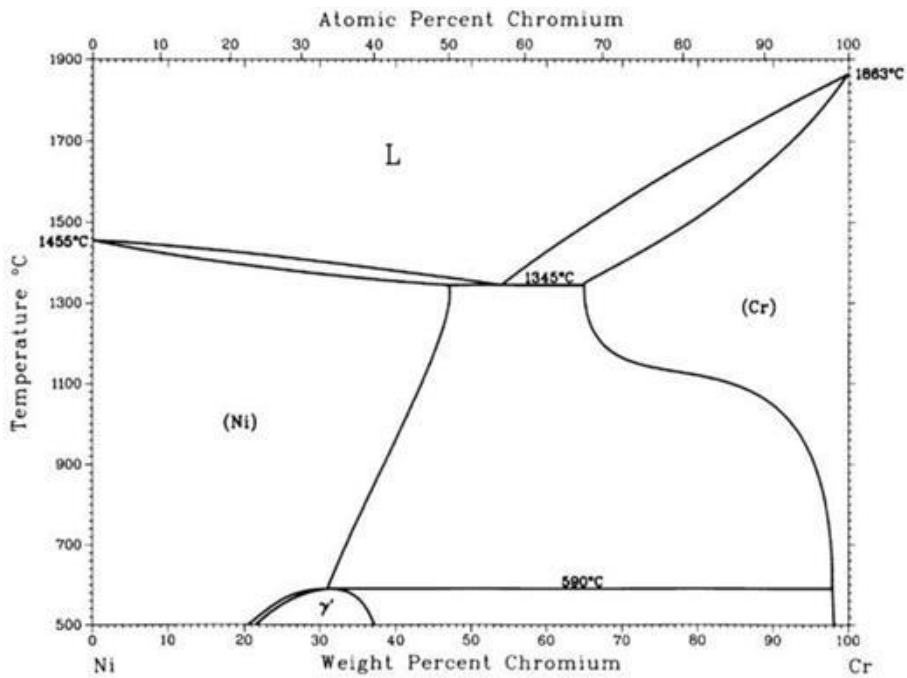


Figure 2.19: The binary equilibrium phase diagram of Cr-Ni [63].

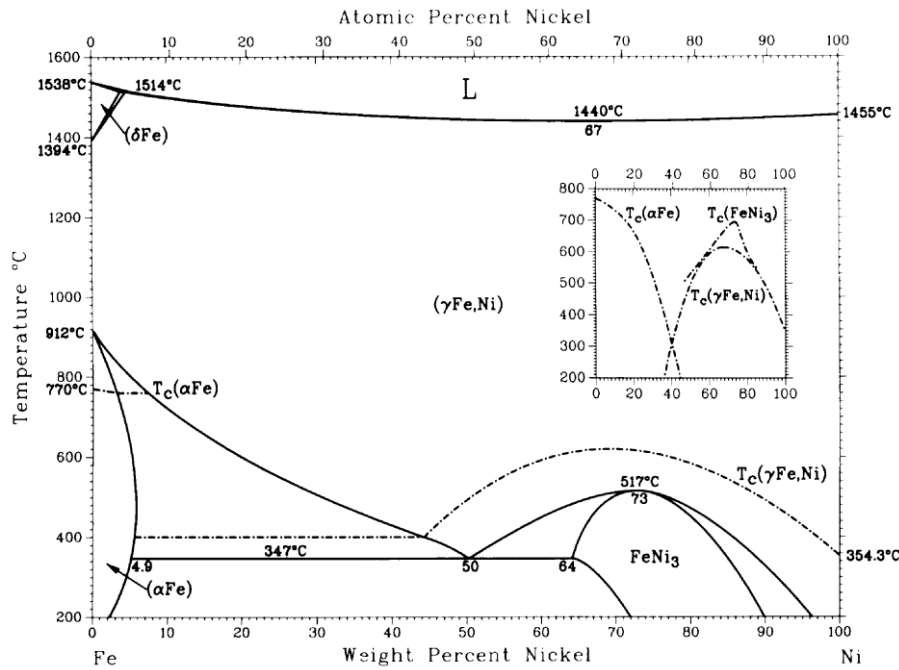


Figure 2.20: The binary equilibrium phase diagram of Fe-Ni [63].

While the binary phase diagrams alone do not reveal all the potential interactions that can occur in multicomponent alloys, they can be a useful guide to what phases could be expected. The phase diagrams in Figures 2.15-2.20, reveal the possible formation of six different phases when the binary systems are considered at an equal atomic ratio (50:50) of the two metallic elements. Notably, while some correspond to single phase solid solutions, this is not the case in all of the systems. The expected phases at the 50:50 atomic ratio are;

- **Co-Cr system:** a mixture of ϵ Co phase (hexagonal $P6_3/mmc$ space group) and σ phase (tetragonal $P4_2/mnm$ space group), found at a temperature below approximately 1000 °C (Figure 2.15).
- **Co-Fe system:** α' phase (cubic $Pm\bar{3}m$ space group), found at a temperature below approximately 740 °C (Figure 2.16).
- **Co-Ni system:** $(\alpha\text{Co,Ni})$ phase (cubic $Fm\bar{3}m$ space group), found at a temperature below approximately 800 °C (Figure 2.17).
- **Cr-Fe system:** $(\alpha\text{Fe,Cr})$ phase (cubic $Im\bar{3}m$ space group), found at a temperature below approximately 440 °C (Figure 2.18).
- **Cr-Ni system:** a mixture of γ' phase (orthorhombic $Immm$ space group) and (Cr) phase (cubic $Im\bar{3}m$ space group), found at a temperature below approximately 590 °C (Figure 2.19).

- **Fe-Ni system:** a mixture of (α Fe) phase (cubic $Im\bar{3}m$ space group) and $FeNi_3$ phase (cubic $Pm\bar{3}m$ space group), found at a temperature below approximately 347 °C (Figure 2.20).

Evidently, some alloying to form solid solutions is possible in this system, and all of the elements display some (often quite significant) solid solubility. It is not the case however that there is complete solid solubility across the whole system, while the observations of the phase structure of CoCrFeNi suggest that a single phase solid solution involving all elements is formed.

As well as being interesting in its own right, CoCrFeNi is frequently used as a precursor for observing phase transformation or microstructure change in HEAs when adding the fifth element into the HEA system. Many CoCrFeNi-based HEA systems have been studied such as CoCrFeNiAl, CoCrFeNiCu, CoCrFeNiSn, among other examples, and these will be introduced next.

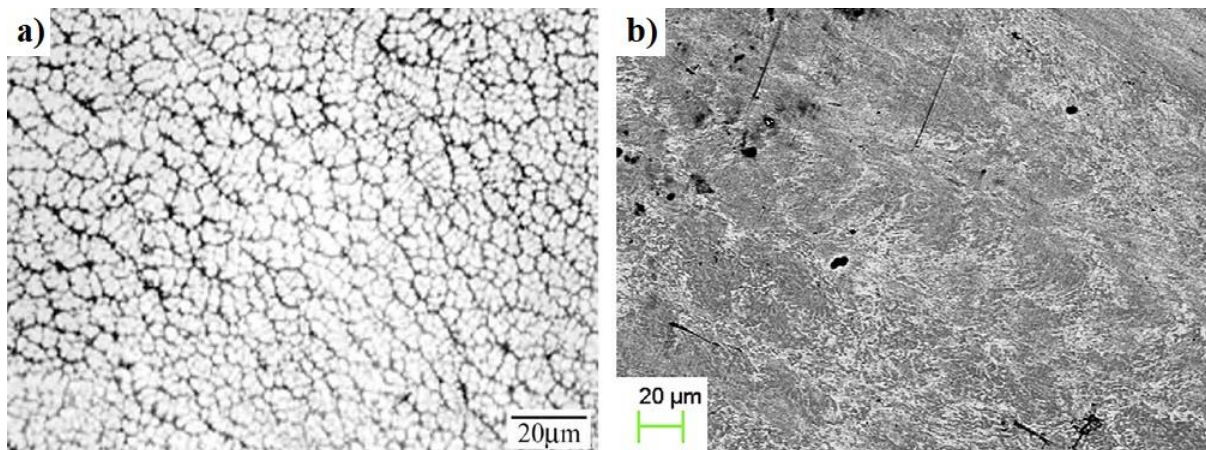


Figure 2.21: SEM images showing the microstructure of CoCrFeNiAl forming; a) a single-phase [64] and b) a multiple-phase structure [65].

Figure 2.21 shows arc melted CoCrFeNiAl. The two reports shown here indicate different microstructures which have been seen, single multiple-phase structures. When a single phase is seen, it has an ordered BCC-structure (B2), Figure 2.21a, as observed in [42] and [64]. In some studies however, SEM-EDS analysis at a high resolution at the surface of a cast ingot (where the cooling rate would be expected to be more rapid) reveals a complicated microstructure consisting of an Al-Ni-rich phase formed as dendrites with Cr-Fe-rich phases in the interdendritic region and at grain boundaries [42], Figure 2.21b. Hsu et al. [66] reported that this is a combination of a major BCC-phase and a minor B2-phase while a main FCC-phase and a minor B2-phase are found by Kao et al. [67]. Overall, it seems that the addition of

Al promotes an increase of BCC phase, and possible second phase formation, as compared to the CoCrFeNi alloy.

We can again explore the binary phase diagrams to attempt to account for this. Below the additional binary equilibrium phase diagrams required for the addition of Al are given, Figures 2.22-2.25.

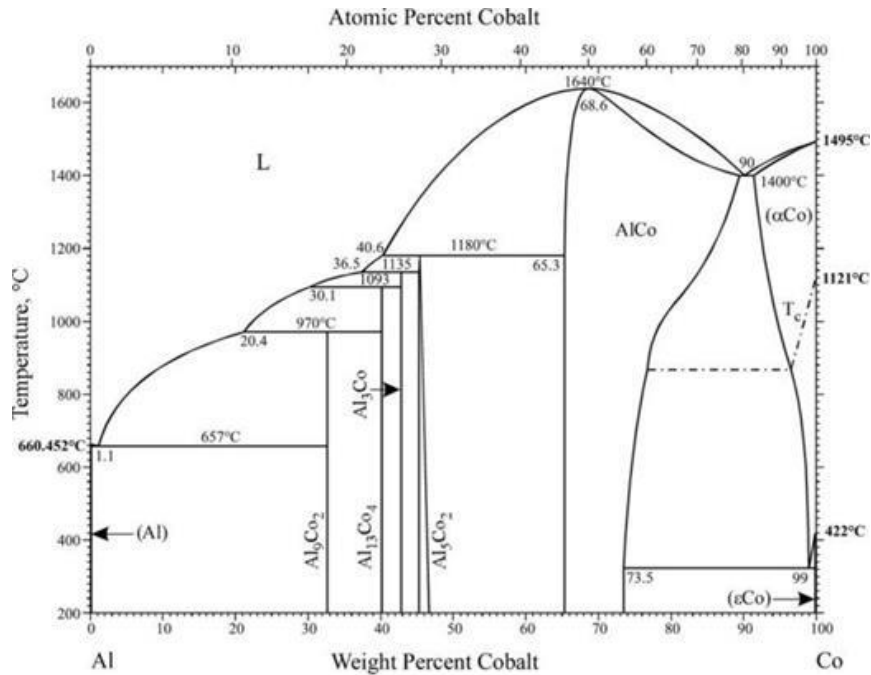


Figure 2.22: The binary equilibrium phase diagram of Al-Co [63].

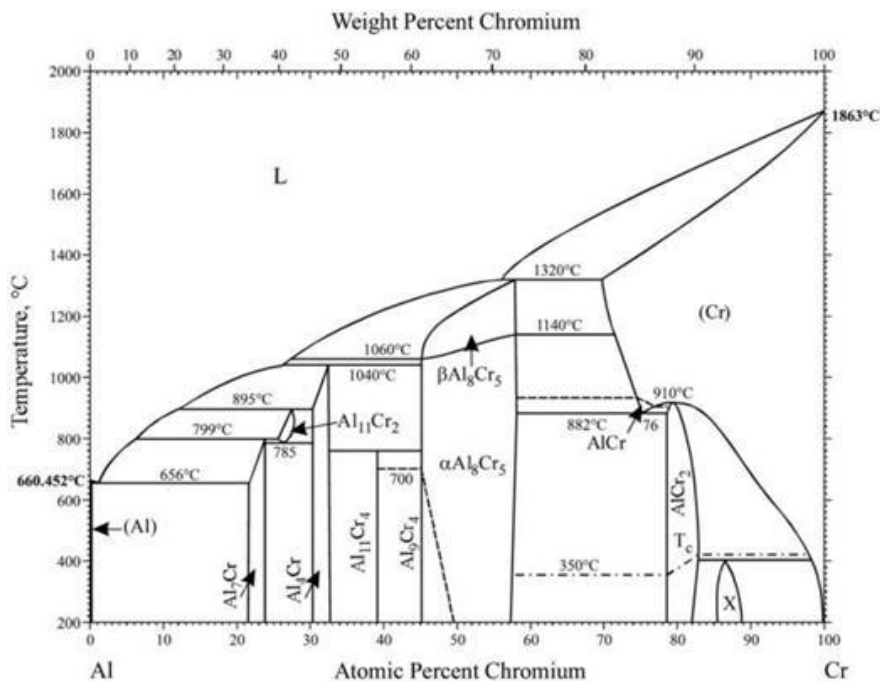


Figure 2.23: The binary equilibrium phase diagram of Al-Cr [63].

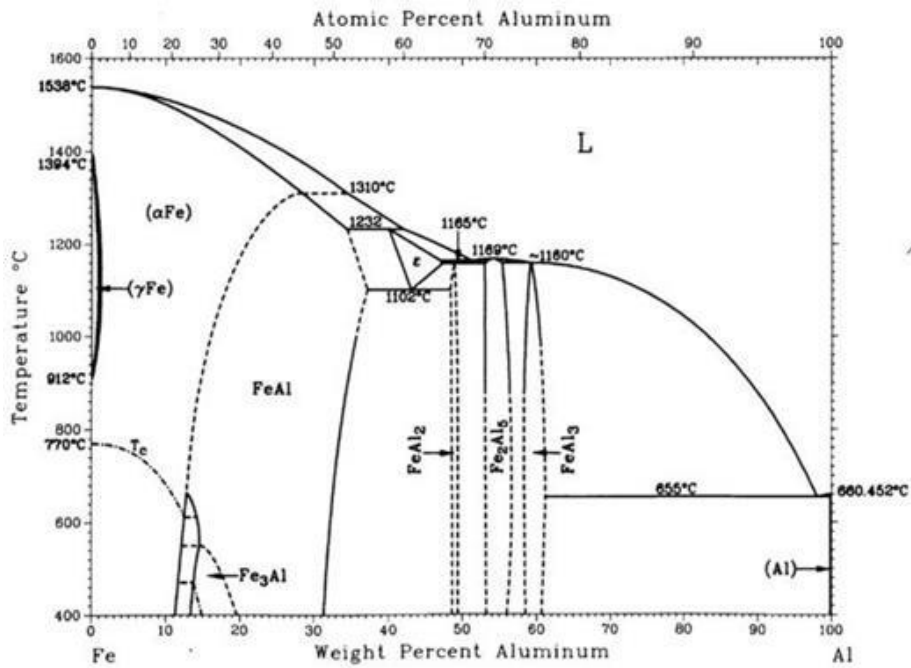


Figure 2.24: The binary equilibrium phase diagram of Al-Fe [63].

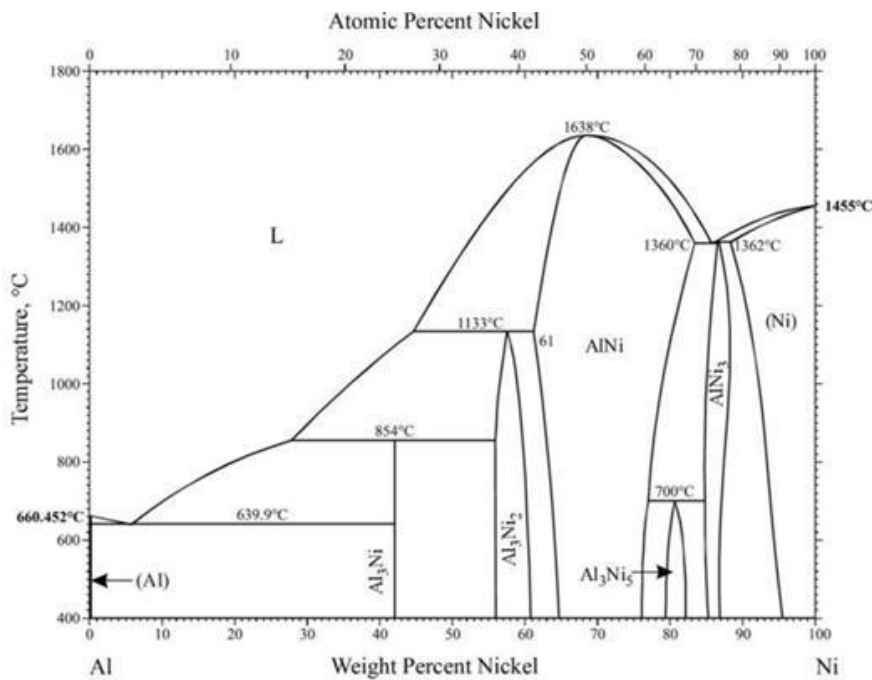


Figure 2.25: The binary equilibrium phase diagram of Al-Ni [63].

These diagrams indicate the possibility of forming four additional phases at the equiatomic ratios for binaries in the CoCrFeNiAl system. The expected phases at the 50:50 atomic ratio are;

- **Al-Co system:** AlCo phase (cubic $Pm\bar{3}m$ space group), found at a temperature below approximately 1640 °C (Figure 2.22).

- **Al-Cr system:** $\alpha\text{Al}_8\text{Cr}_5$ phase (trigonal $R\bar{3}m$ space group), found at a temperature below approximately 1080 °C (Figure 2.23).
- **Al-Fe system:** a mixture of FeAl phase (cubic $Pm\bar{3}m$ space group) and FeAl_2 phase (triclinic $P1$ space group), found at a temperature below approximately 700 °C (Figure 2.24).
- **Al-Ni system:** AlNi phase (cubic $Pm\bar{3}m$ space group), found at a temperature below approximately 1638 °C (Figure 2.25).

These observations show a greater likelihood of the formation of intermetallic compounds between these elements and aluminium, though solid solution to some extent is still possible in all of the systems (notably however the other elements have little solubility in Al). It therefore appears logical that the addition of Al may disturb the CoCrFeNi alloy, and lead to the formation of a second phase.

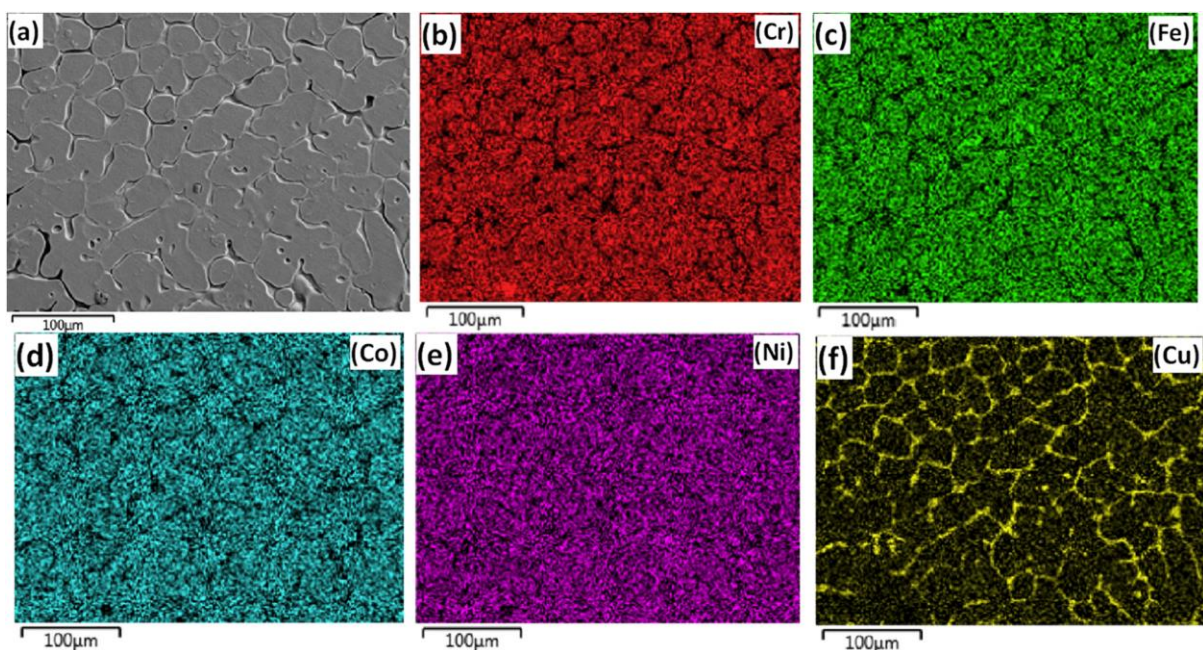


Figure 2.26: EDS images showing the Cu segregation on the CoCrFeNiCu surface; a) a SEM image of CoCrFeNiCu, b) EDS mapping of Cr, c) EDS mapping of Fe, d) EDS mapping of Co, e) EDS mapping of Ni, and f) EDS mapping of Cu [68].

Figure 2.26 shows the arc-melted CoCrFeNiCu microstructure, which consists of two phases, a minor Cu-rich phase of FCC structure, along the interdendritic regions and a major phase, also of FCC structure, mostly consisting of CoCrFeNi [68]. Once again the binary phase diagrams with copper can be observed, Figures 2.27-2.30.

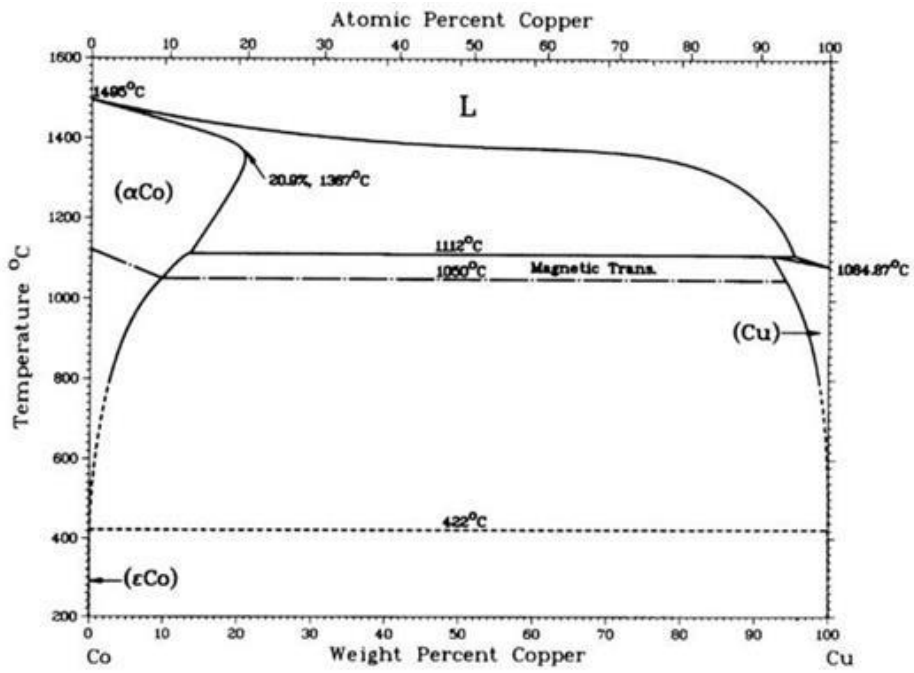


Figure 2.27: The binary equilibrium phase diagram of Co-Cu [63].

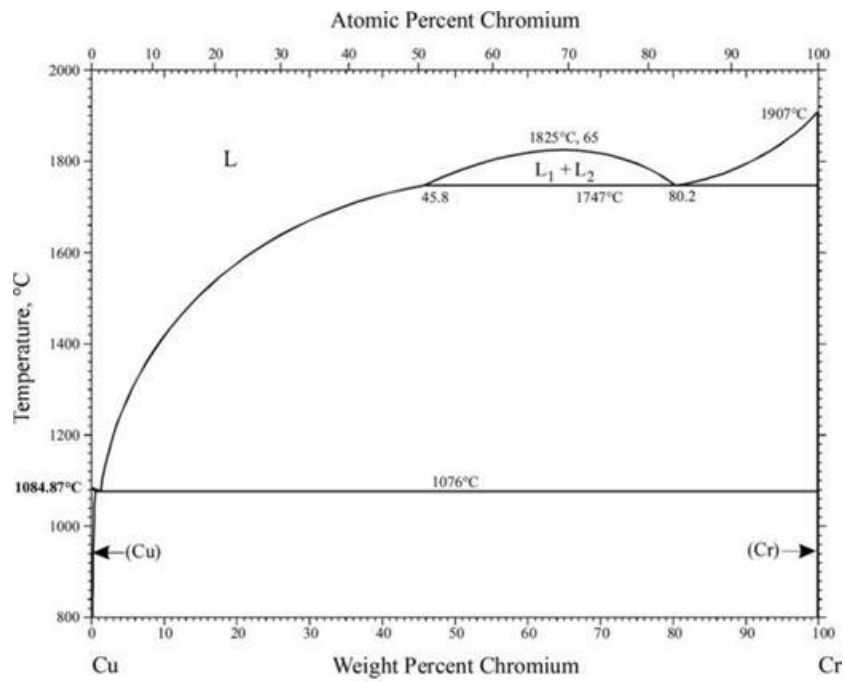


Figure 2.28: The binary equilibrium phase diagram of Cr-Cu [63].

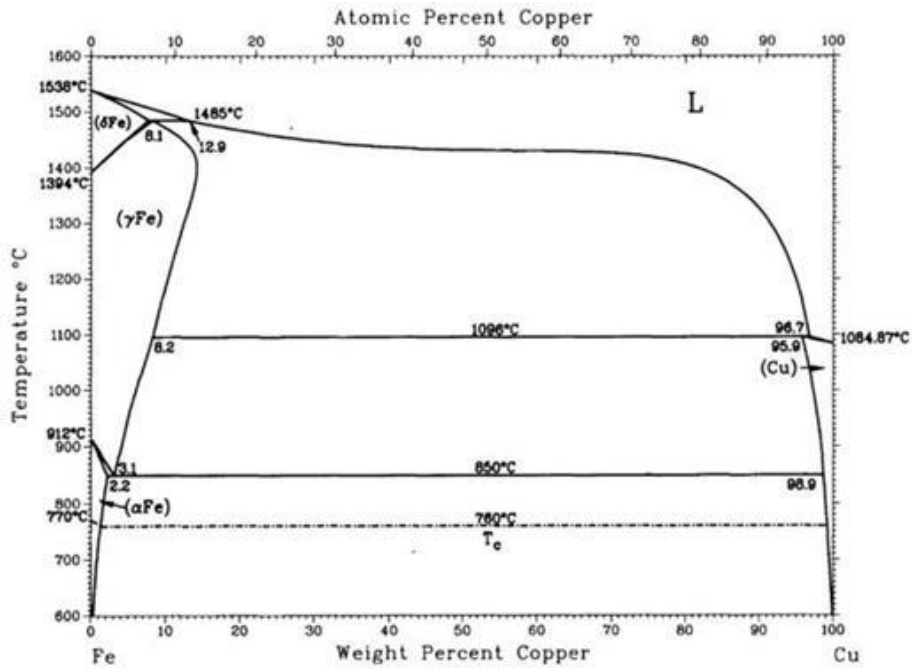


Figure 2.29: The binary equilibrium phase diagram of Cu-Fe [63].

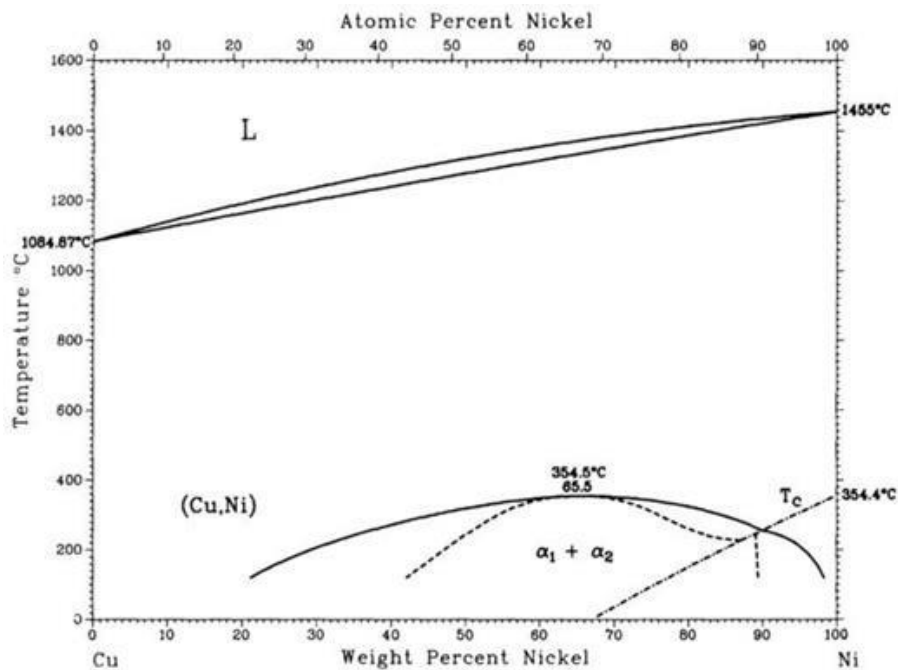


Figure 2.30: The binary equilibrium phase diagram of Cu-Ni [63].

These diagrams show the possibility to form four additional phases in the equiatomic pairs from the CoCrFeNiCu system. The expected phases at the 50:50 atomic ratio are;

- **Co-Cu system:** a mixture of (ϵ Co) phase (hexagonal $P6_3/mmc$ space group) and (Cu) phase (cubic $Fm\bar{3}m$ space group), found at a temperature below approximately 422 °C (Figure 2.27).

- **Cr-Cu system:** a mixture of (Cu) phase (cubic $Fm\bar{3}m$ space group) and (Cr) phase (cubic $Im\bar{3}m$ space group), found at a temperature below approximately 1076 °C (Figure 2.28).
- **Cu-Fe system:** a mixture of (α Fe) phase (cubic $Im\bar{3}m$ space group) and (Cu) phase (cubic $Fm\bar{3}m$ space group), found at a temperature below approximately 760 °C (Figure 2.29).
- **Cu-Ni system:** (Cu,Ni) phase (cubic $Fm\bar{3}m$ space group), found at a temperature below approximately 1270 °C (Figure 2.30).

Here it is noteworthy that in most cases multiple phases have formed, and indeed for all of the constituents except for Ni, there is extremely limited solid solubility with Cu. It is therefore reasonable that the microstructure seen in two phase, with the copper the dominant element in the second phase.

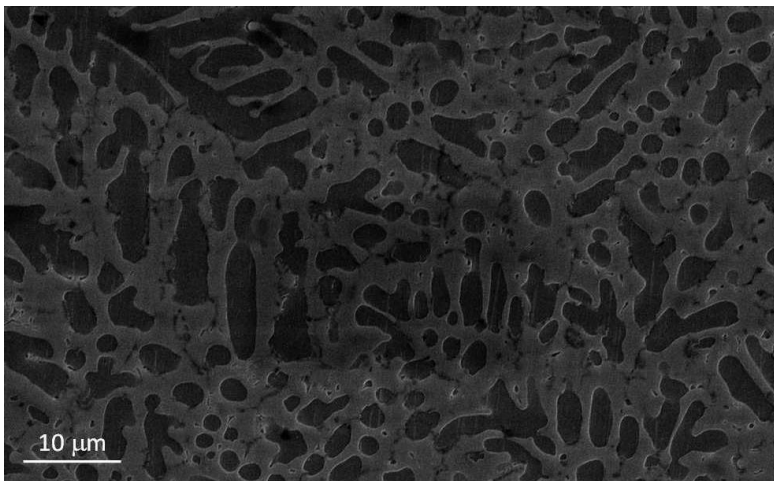


Figure 2.31: SEM images showing the microstructure of CoCrFeNiSn [69].

Figure 2.31 presents the microstructure of arc-melted CoCrFeNiSn. There is a dendritic structure, consisting of an FCC CoCrFeNi phase (enriched in Co, Cr and Fe) and an orthorhombic Ni-Sn-rich phase [69]. The binary equilibrium phase diagrams to describe this system are shown in Figures 2.32-2.35.

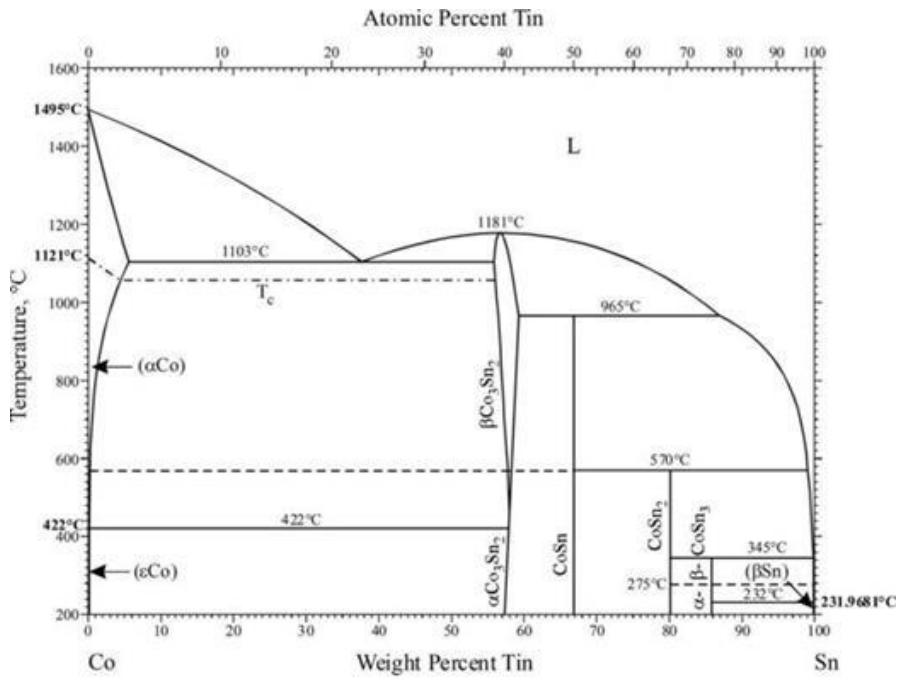


Figure 2.32: The binary equilibrium phase diagram of Co-Sn [63].

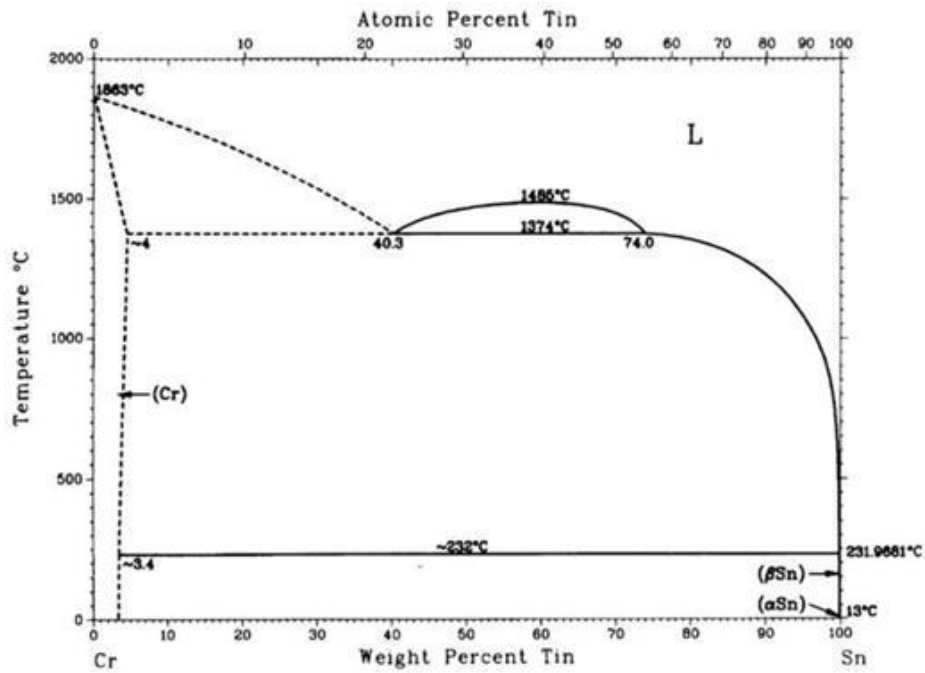


Figure 2.33: The binary equilibrium phase diagram of Cr-Sn [63].

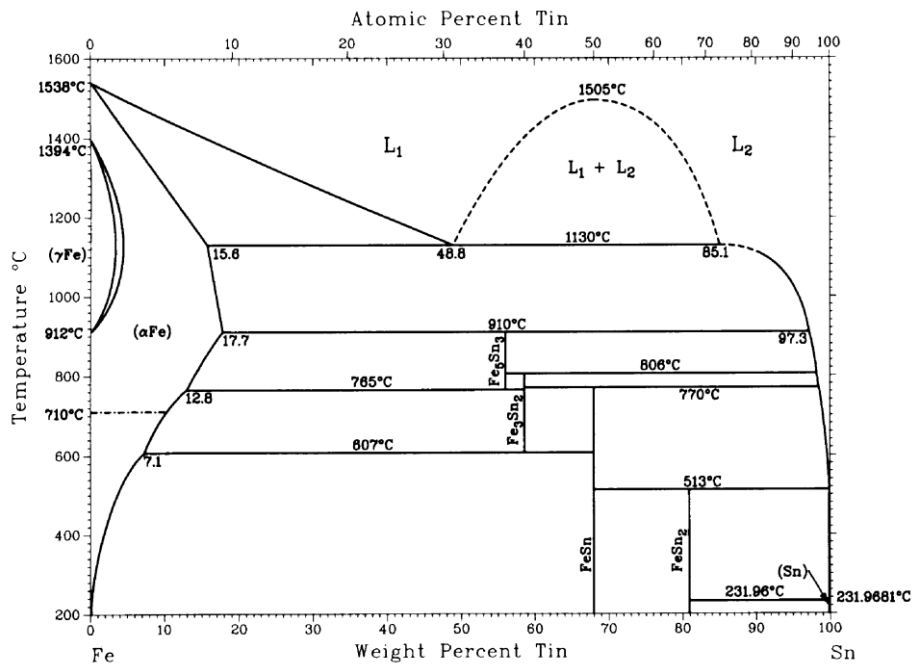


Figure 2.34: The binary equilibrium phase diagram of Fe-Sn [63].

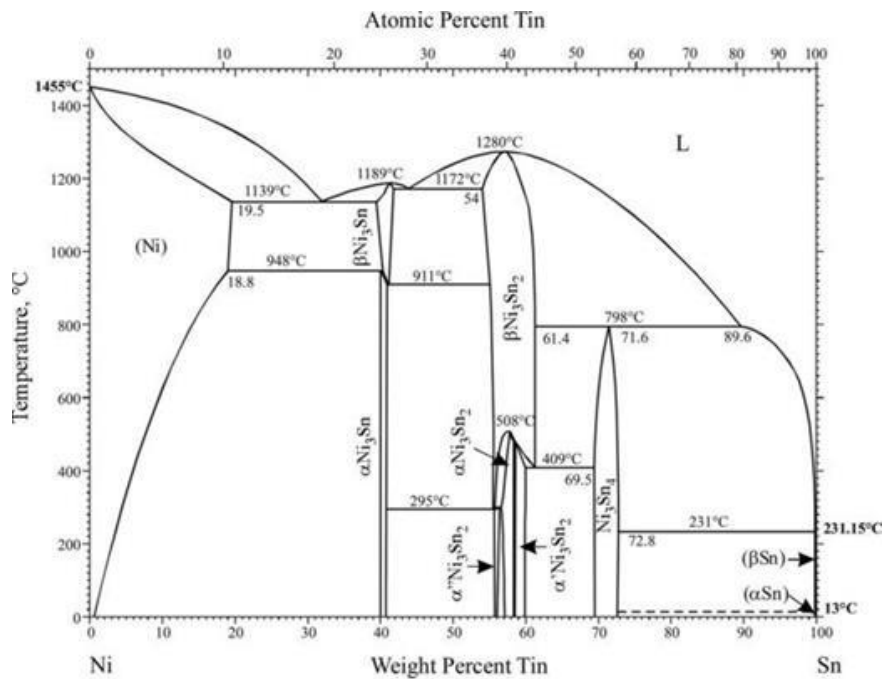


Figure 2.35 The binary equilibrium phase diagram of Ni-Sn [63].

The phase diagrams show the possibility to forming four additional phases in the equiatomic binaries of the CoCrFeNiSn system. The expected phases at the 50:50 atomic ratio are;

- **Co-Sn system:** CoSn phase (hexagonal $P6/mmm$ space group), found at a temperature below approximately 965 °C (Figure 2.32).

- **Cr-Sn system:** a mixture of (Cr) phase (cubic $Im\bar{3}m$ space group) and (β Sn) phase (tetragonal $I4_1/amd$ space group), found at a temperature below approximately 232 °C (Figure 2.33).
- **Fe-Sn system:** FeSn phase (hexagonal $P6/mmm$ space group), found at a temperature below approximately 607 °C (Figure 2.34).
- **Ni-Sn system:** a mixture of α' Ni₃Sn₂ phase (orthorhombic $Cmcm$ space group) and Ni₃Sn₄ phase (monoclinic $C2/m$ space group), found at a temperature below approximately 409 °C (Figure 2.35).

This shows that the interaction with tin is likely to produce additional phases in the system, as there are a number of intermetallics that can form, and limited solid solubility. Of the available phases which can form there are monoclinic, orthorhombic and hexagonal structures (and other intermetallic phases exist in some of the phase diagrams away from the equiatomic composition).

2.2 Structural properties of HEAs and conventional alloys

This part of thesis will focus on literature regarding three particular properties of HEAs and relevant conventional alloys; the hardness, corrosion, and tribocorrosion properties. Knowledge and advanced data on these are used in other chapters, especially in designing and planning the experimental work, and the results and discussion parts.

2.2.1 Hardness

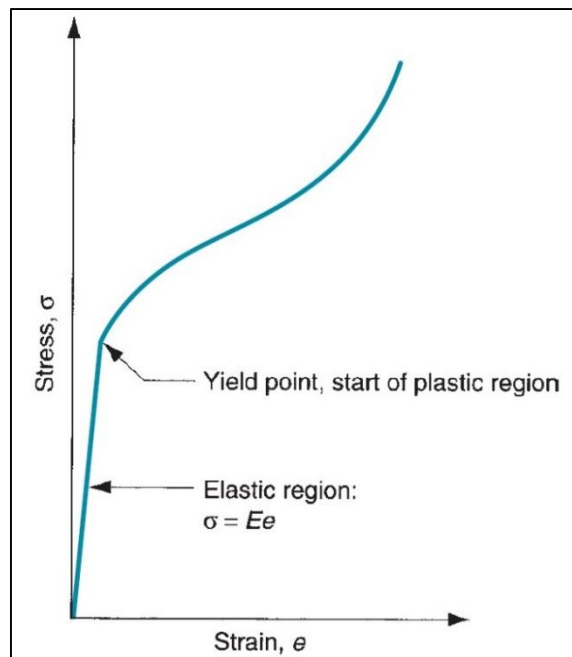


Figure 2.36: A schematic diagram of a compressive stress-strain curve in solid materials [70].

Hardness is one of structural properties of solid materials which refers to its ability to resist plastic deformation (permanent shape change), as in Figure 2.36 [70], when load is applied to the material's surface [71,72]. It also affects the tribological behaviour and can be related to other mechanical properties, such as ductility, fatigue resistance, and strength [71,72]. Thus, this is an essential, and easily accessible, property to consider for material design and use in a diverse range of applications in both industrial and domestic sectors.

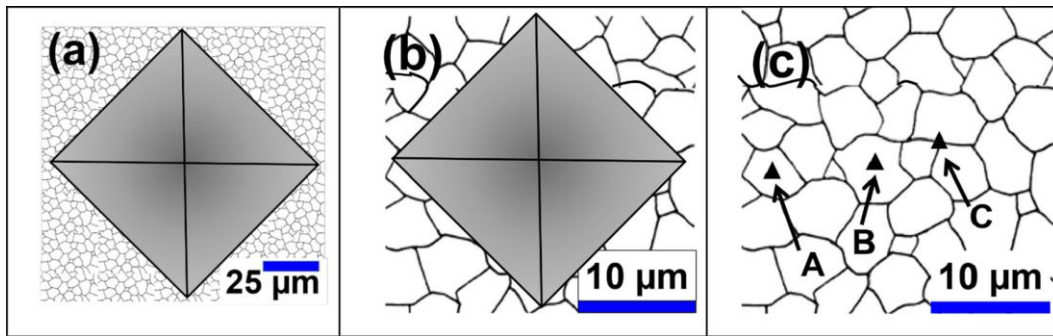


Figure 2.37: Comparison of three indent scales for hardness testing in polycrystalline materials; a) macroscale, b) microscale, and c) nanoscale indentations [71].

In the hardness measurement, there are typically three scales for the hardness indentation, macro-, micro-, and nanoscale tests, Figure 2.37. It is determined with the ISO 14577-1 standard under the consideration of load range as in Table 2.4 [71,73]. Macro-indentation hardness testing is examined by the applied load to the indenter between $2 \text{ N} < L < 30,000 \text{ N}$ [73]. Six methods, Meyer, Brinell, Rockwell, Vickers, the International Rubber Hardness (IRHD), and Shore Durometer, are commonly used for macro-hardness testing in research and industry, with different methods preferred for different material types [71]. Micro-indentation hardness testing consists of two hardness tests, micro-Vickers and micro-Knoop, and it is operated under a lower applied load than 2 N and generally has an indent depth down to $0.2 \text{ }\mu\text{m}$. A diamond indenter can penetrate the sample surface with a pyramid shape in Figure 2.38 [71]. The other methods of micro-hardness testing are Buchholz and Micro-IRHD tests [71]. Lastly, nano-indentation hardness testing is not at a specified load range but its indent depth should be less than $0.2 \text{ }\mu\text{m}$ [71]. The two main methods for nanoscale hardness tests use either a Berkovich pyramid or a cube corner indent shape. The projected area of a Berkovich indent is the same as the Vickers indent, while the cube-corner indent shows the shape of three-sided pyramid with a centreline-to-face angle of 34.3° , the same shape as the corner of a cube [71].

Table 2.4: The ISO 14577-1 standard for the scales of hardness tests [73].

Testing scale	Load range; L (N)	Penetration range; h (μm)	Sample size
Macroscale testing	$2 < L < 30,000$	Not specified	Large
Microscale testing	$L < 2$	$h > 0.2$	Medium
Nanoscale testing	Not specified	$h < 0.2$	Small

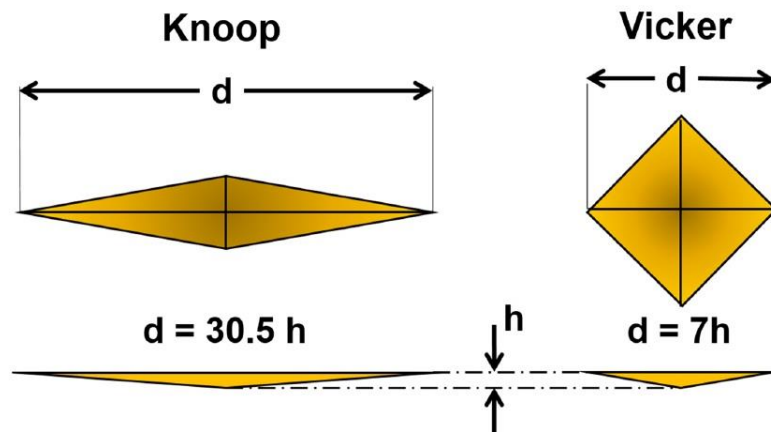


Figure 2.38: The difference of micro-indent shape between Knoop and Vickers [71].

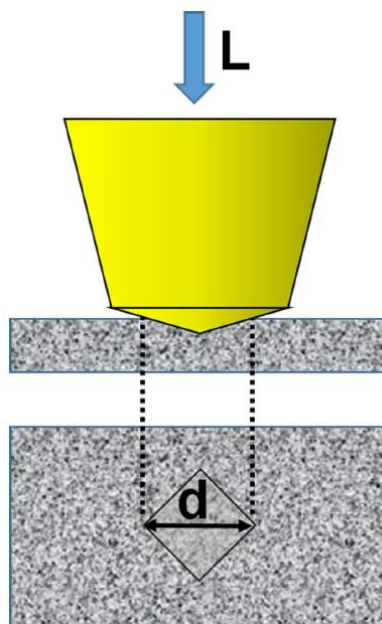


Figure 2.39: The hardness measurement operated with the micro-Vickers indentation [71].

Shown in Figure 2.39 [71], the micro-hardness Vickers test is probably the most popular method on a laboratory scale. The size of indent produced under load of a pyramidal diamond indenter is used for calculating the hardness value by the equation below [71]. The testing condition of micro-Vickers indentation is $L < 2 \text{ N}$ (the load range), $h > 0.2 \mu\text{m}$ (the penetration range), $t \sim 2\text{-}8 \text{ s}$ (the time for the initial test force), and $t \sim 10\text{-}15 \text{ s}$ (the dwell time for the maintained test force) [71,73].

$$HV = \frac{L}{A} = \frac{2L}{d^2} \sin \frac{136^\circ}{2} = 1.8544 \frac{L}{d^2} (kgf \cdot mm^{-2}) = 0.1891 \frac{L}{d^2} (N \cdot mm^{-2}) \quad \text{Equation 8}$$

where HV is the micro-hardness Vickers values; $kgf \cdot mm^{-2}$, L is the indenter load applied on the sample surface; kgf , A is the indented surface area; mm^2 , d is the length of diagonal distance determined from a corner point to an opposite corner point on the surface area of actual indent; mm . If the applied load is in the unit of N , the number of 9.8065 should be used to divide for this equation and HV can be reported in the unit of $N \cdot mm^{-2}$ or MPa . However, like all indentation based methods, there are concerns with the indentation size effect (ISE). It has been found that different test loads give different values of hardness in Vickers tests [74,75], due to the different size of indent produced. There are two types of ISE; normal ISE and reversed ISE. Firstly, normal ISE is a lower hardness value with increasing load, which particularly occurs in brittle materials. Secondly, reversed ISE is an increasing hardness value with load, that more frequently is seen in ductile materials [74,75].

A collection of typical hardness results from several alloys is shown in Table 2.5. Conventional alloys, such as Al, Fe, Ni, Ti alloys and stainless steels, reveal a wide range of hardness values from 111 HV to 800 HV, reflecting the diverse range of microstructures and deformation characteristics in these systems [76]. For example, the Al 2024 sample has the lowest hardness value (111 HV) in Table 2.5 as its main phase is FCC structured, allowing many slip systems and relatively easy deformation. On the other hand, the highest measured hardness value (800 HV) in the same table is the M2 steel which has several hard and brittle secondary phases such as the martensite phase, austenite phase, and fine-scale carbides. Where similar materials display a range of reported hardness values, this is likely to be due to microstructural differences arising from different thermomechanical histories; the amount, size and distribution of structural elements like second phases and grain boundaries, as well as other dislocations and point defects, will all affect dislocation mobility and the hardness value determined.

Table 2.5: The hardness values of conventional alloys collected from previous research.

Alloy	Grade	Phase composition	Hardness (HV)	Reference
Al alloys	AlSi10Mg	FCC phase	114 HV0.3	[77]
	Al-12Si	Major dendritic FCC phase Minor eutectic phases	135 HV0.1	[78]
	Al 2024	FCC phase	111 HV0.2	[79]
Fe alloys	H13	Major ferrite phase Minor austenite phase	581 HV0.5	[80]
	M2 steel	Martensite phase Austenite phase Fine-grain carbides	800 HV0.05	[81]
	420 SS	Major martensite phase Minor austenite phase	515-688 HV0.5	[82]
Ni alloys	IN625	Matrix FCC phase Carbides (NbC, TiC) Hexagonal NiCrNb phase	316 HV0.1	[83]
	IN718	FCC- γ phase	365 HV0.1	[84]
	IN939	FCC- γ phase	450 HV0.5	[85]
Ti alloys	Ti-6Al-4V	$\beta + \alpha$ phase	335 HV0.2	[86]
	Ti-24Nb-4Zr-8Sn	BCC- β phase	219 HV5	[87]
Stainless steels	SS 304	Major austenite phase Minor ferrite phase	168 HV0.5	[88]
	SS 316L	Matrix austenite phase	176-213 HV5	[89]

Table 2.6 shows the hardness of a range of reported HEA systems. This also shows the influence of alloying elements, such as Al, Cu, Nb, Mo, Ta, and Ti, on hardness where these are added to the main CoCrFeNi system on which many explored HEAs are based. It shows a wide range of hardness values from 120 HV to 747 HV caused by the significant changes in microstructure that occur with different alloying elements (CoCrFeNi, Al_x CoCrFeNi, CoCrFeNiCu_x, CoCrFeNiNb_xMo_y, CoCrFeNiTa_x, CoCrFeNiTi_x, CoCrFeNiMn, CoCrFeNiV, and AlCoCrFeNb_xNi). Without these additions, an as-cast CoCrFeNi sample, produced with the arc melting technique, has a relatively low hardness value of 120 HV. It consists of a single solid-solution phase of FCC structure with significant ductility [90,91]. However, its hardness can be improved by the addition of other metallic elements as reported previous research in Table 2.6.

Table 2.6: The hardness values of HEAs collected from previous research.

HEA	Phase composition	Hardness (HV)	Reference
CoCrFeNi	FCC phase	120 HV5	[90]
Al _{0.9} CoCrFeNi	BCC phase	527 HV5	
CoCrFeNiCu	Major FCC phase Minor FCC Cu-rich phase	169 HV0.3	[68]
CrFeCoNiNb	FCC phase HCP phase Nb-rich precipitate	652 HV10	[92]
CrFeCoNiMo	SC phase FCC phase	604 HV10	
CoCrFeNiTa _{0.75}	FCC phase Co ₂ Ta/ Laves phase	550 HV0.5	[91]
CoCrFeNiTi _{0.5}	FCC phase (Ni,Ti)-rich phase (R phase) (Cr,Fe)-rich phase (σ phase) (Ti,Co)-rich/ Laves phase	515 HV1	[93]
CoCrFeNiMn	FCC phase	170 HV0.25	[94]
CoCrFeNiV	Disordered FCC phase σ -Tetragonal phase	524 HV0.25	
CoCrFeNiAl _{0.5} Ti _{0.5}	FeCr BCC phase Al-Ni-Ti BCC phase σ -Tetragonal phase	601 HV0.05	[95]
CrFeCoNiNb _{0.5} Mo _{0.5}	FCC phase HCP phase	533 HV10	[92]
Al _{0.5} CoCrFe _{0.5} NiTi _{0.5}	BCC phase FCC phase σ phase Ordered BCC phase	730 HV1	[96]
Al _{0.5} CoCrFe _{1.5} NiTi _{0.5}	BCC phase FCC phase Ordered BCC phase	430 HV1	
AlCoCrFeNb _{0.5} Ni	BCC phase (CoCr)Nb/ Laves phase	747 HV0.5	[97]
AlCoCrFeNiV	BCC phase	649 HV1	[98]
CoCrFeNiMnV	Disordered FCC phase σ -Tetragonal intermetallic phase	650 HV0.25	[94]
CoFeNiVMo	FCC phase CoMo ₂ Ni intermetallic phase	625 HV1	[99]

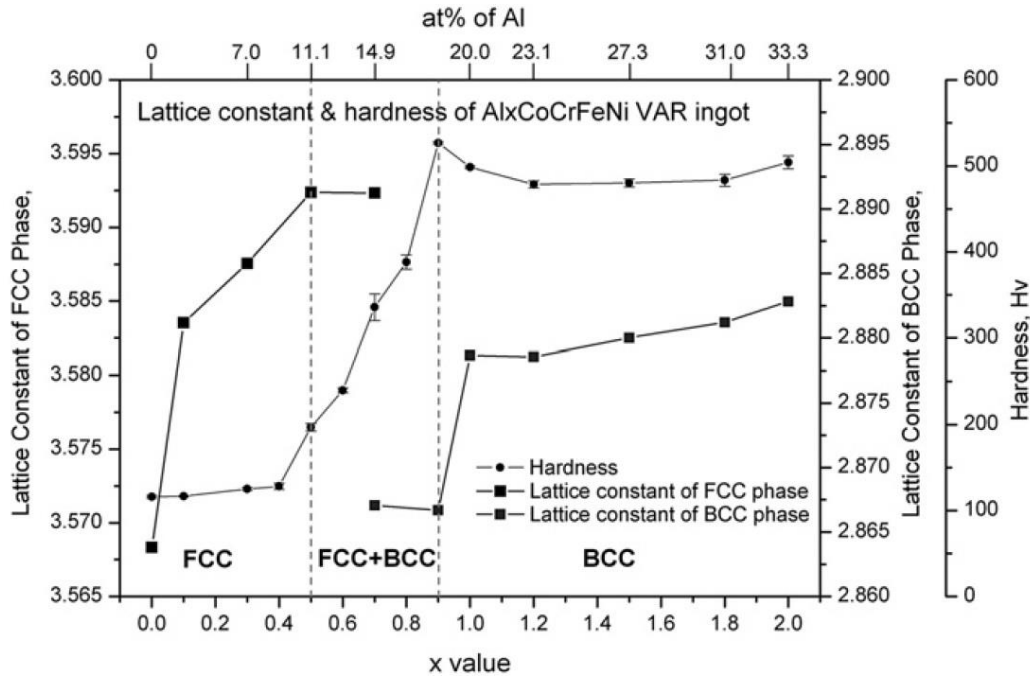


Figure 2.40: The influence of Al addition on the phase transformation and hardness in the $\text{Al}_x\text{CoCrFeNi}$ system [90].

For the addition of Al, the $\text{Al}_{0.9}\text{CoCrFeNi}$ system with Al at a molar ratio of 0.9, shows the highest hardness [90]. The transformation of phase structure from FCC phase to BCC phase in $\text{Al}_x\text{CoCrFeNi}$ occurs with increase of Al content, Figure 2.40 [90]. In addition, it is found that the formation of BCC phase, which contains the spinodal structure with alternating interconnected phases, may be an important reason for the increase in hardness for this HEA [90]. In the case of the Cu addition, increasing Cu content ($x = 0-1.0$ at.%) in the as-arc melted and cast CoCrFeNiCu_x system leads to increase in the measured hardness values from 136 HV-169 HV. This may be caused by an increase in the amount of the second Cu-rich phase, and a grain size reduction as a result, although this hypothesis has not been tested with experimental data from the alloy [68]. For the mixing of Nb and Mo elements, both of them added in the CoCrFeNi-x system can lead to a higher hardness [92]. The as-arc melted CoCrFeNiNb sample has higher hardness value than the CoCrFeNiMo sample, resulting from a greater volume fraction of the dendritic CoCrFeNiNb structure [92]. In contrast, the simultaneous addition of Nb and Mo elements into the $\text{CrFeCoNiNb}_{0.5}\text{Mo}_{0.5}$ system leads to a decrease in hardness due to the decrease in volume fraction of the dendritic structure [92].

As reported by Jiang et al. [91], hardness can be enhanced (and ductility reduced, as commonly results) with Ta addition. As-cast CoCrFeNiTa_x samples have microstructures which change from an initial phase of FCC structure to a multiple phase of FCC and Co_2Ta -

Laves phases in the hypereutectic microstructure when the molar ratio of Ta is 0.5 and 0.75 [91]. Consequently, the increase of Laves phases in HEA structures can result in increasing hardness and reduction of ductility, Table 2.7 [91].

Table 2.7: The effect of volume fraction of Laves phase on hardness and plastic strain in the CoCrFeNiTa_x system [91].

Alloys	Plastic strain ϵ_p (%)	Vickers hardness (HV)	Volume fraction of Laves phase (%)
Ta00	>50	141	0
Ta01	>50	180	3.1
Ta02	>50	277	16.5
Ta03	30	365	34.7
Ta04	22.6	492	37.5
Ta05	19.7	498	55
Ta075	0	550	59

For the impact of Ti on the as-arc melted CoCrFeNiTi_x samples, a higher hardness and a lower ductility occurs with increasing Ti content [93]. The formation of solid-solution strengthening in the matrix phase of FCC structure and three hard secondary phases, which consist of σ , R, and Laves phases, can contribute to this [93]. By the addition of Mn and V to the main CoCrFeNi system, two HEAs, CoCrFeNiMn and CoCrFeNiV, were formed by arc melting. Mn does not increase the hardness but it gives a better ductility due to its structure as a single FCC phase alloy [94]. On the other hand, V can lead to a higher hardness resulting from the formation of σ -Tetragonal phase, but this leads to brittle behaviour [94].

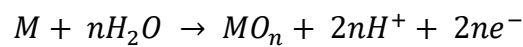
2.2.2 Corrosion properties

Corrosion is currently one of the major material problems, occurring under natural or man-made conditions and leading in the worst cases to the loss of human life and economic damage. Corrosion resistance as a property can refer to the electrochemical ability of materials, especially metals, and the products which are the results of interactions between their surfaces and other species they encounter, to resist corrosion attack in different solutions or environments [2]. The electrochemical system during the corrosion process of metals contains half-cell reactions regarding the electron transfer [100]. A transfer of metal electrons into the electrolyte occurs at the interface between the metal surface and solution (the anodic site) when it is dissolved in the media. The anodic reaction relates to the oxidation of metal, leading to the flow of its ions into an electrolyte, while the cathodic reaction involves the reduction of species

at the cathodic side. Electrons liberated from the anodic reaction are consumed at the cathode surface, as summarized in the equations below [100].



These reactions are important for the formation of protective passive film through the oxidation reaction at the interface. The metal surface (M) interacts with oxygen to generate a metal oxide layer (MO_n) on its surface. This nano-film directly affects the corrosion resistance of metals, as shown in an equation below [100].



There are two major parameters (internal and external parameters), which have an effect on the assessment of the corrosion resistance of metals. The former is an influence of the metal itself, such as the phase composition in the metal structures, in that a single phase usually has better corrosion resistance. For example, this effect of different phase structures has been seen in $Al_xCoCrFeNiTi_{1-x}$ ($x = 1, 0.8, 0.5$) exploring the corrosion behavior when immersed in 3.5 wt.% NaCl solution [101]. $AlCoCrFeNi$ ($x = 1$, E_{corr} ; -0.27 V) contains a single BCC phase, and has higher corrosion potential (E_{corr}) in 3.5 wt.% NaCl solution than the two other alloys tested in this system, $Al_{0.8}CoCrFeNiTi_{0.2}$ (E_{corr} ; -0.69 V) and $Al_{0.5}CoCrFeNiTi_{0.5}$ (E_{corr} ; -0.32 V), which both consist of FCC and BCC phases, Figure 2.41 [101]. This shows the influence of phase composition in HEA systems on corrosion properties. External parameters on the other hand are factors such as the specific solutions, the concentration of those solutions, and the environmental temperature [2]. An example of the effect of this is the observation of corrosion resistance of $Al_{0.8}CoCrFeNiTi_{0.2}$ alloy under different test solutions; 3.5 wt.% NaCl solution and 0.5 NaOH solution [101]. This HEA has high corrosion resistance (E_{corr} ; -0.27 V) in 0.5 NaOH solution while the corrosion properties are poor (E_{corr} ; -0.69 V) in 3.5 wt.% NaCl solution, Figure 2.41 [101]. This effect shows that the specific solution (an external parameter) is extremely important for corrosion properties.

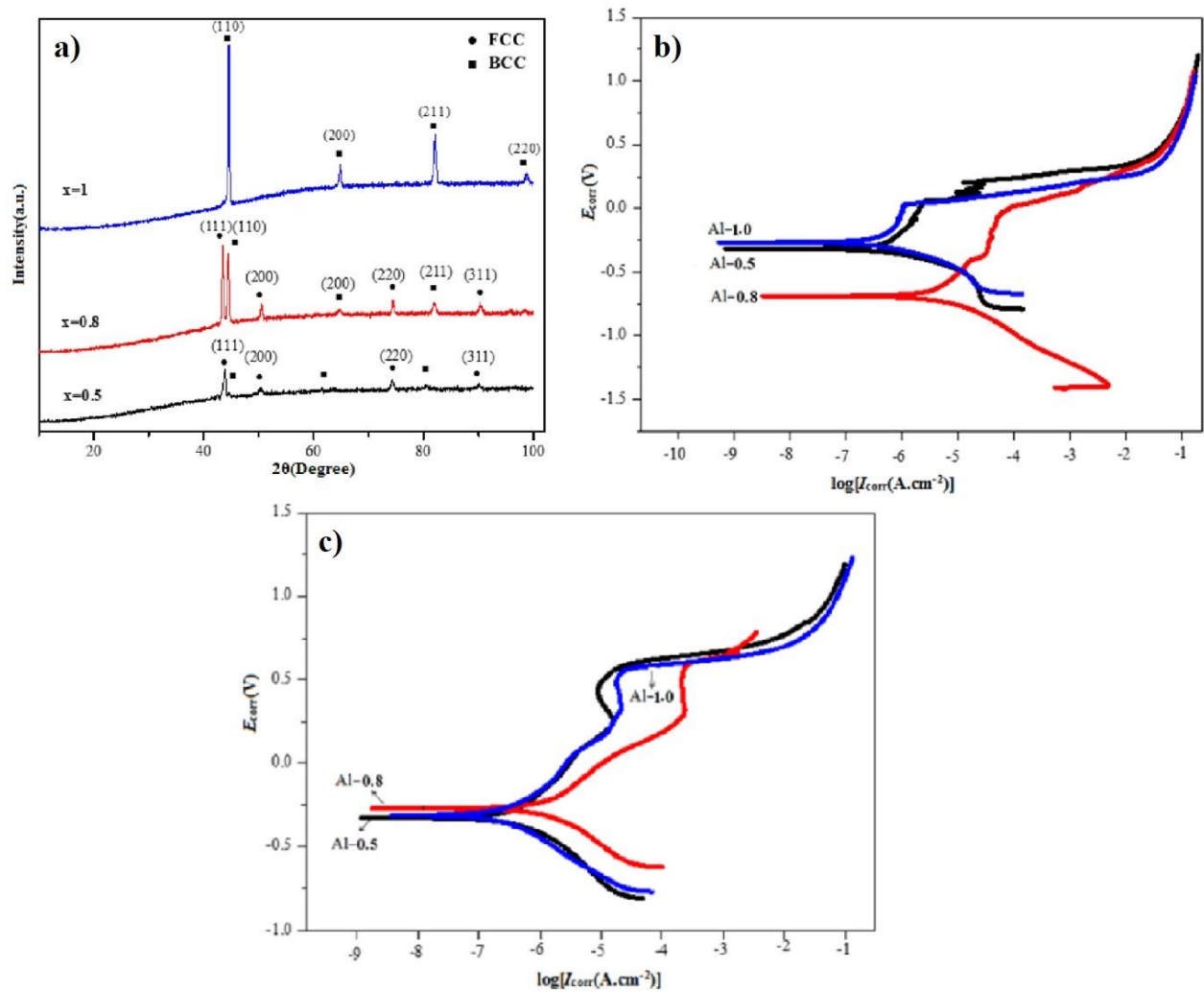


Figure 2.41: a) XRD patterns of as-cast HEA samples and Linear polarization curves of HEAs after corrosion testing in b) 3.5 wt.% NaCl solution and c) 0.5 NaOH solution [101].

The most common way to measure the corrosion behaviour is by the electrochemical Potentiostat technique. This induces a corrosion reaction between samples and testing solutions, and then measures the corrosion parameters such as E_{corr} , i_{corr} , Polarization resistance (R_p), and corrosion rate (CR) [2]. The polarization curve shows the relationship of applied electrode potential (E) and detected current density (i) in Figure 2.42. Three regions are usually found in the corrosion measurement which are: i) the active region, ii) the passive region, and iii) the transpassive region [102].

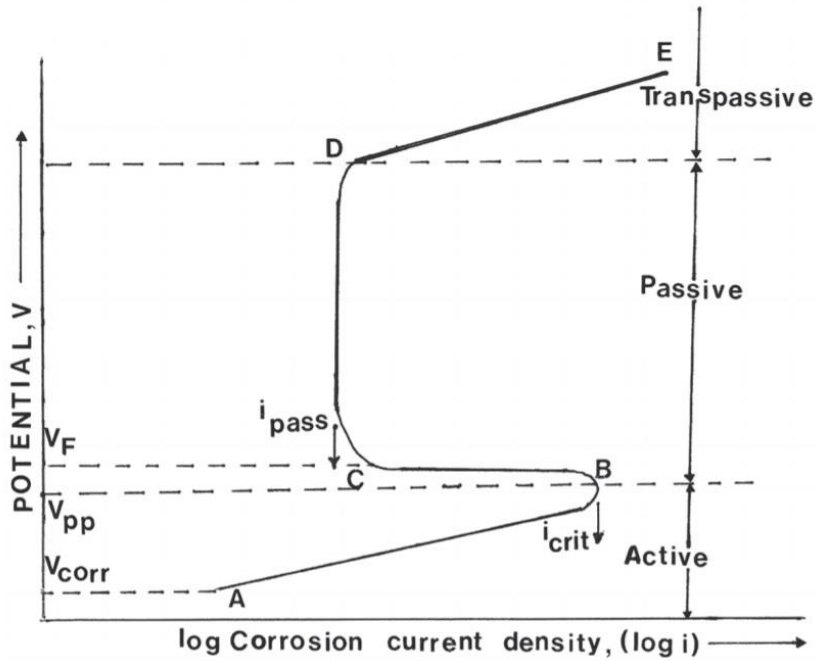


Figure 2.42: Three regions on the polarization curve during the corrosion measurement [102].

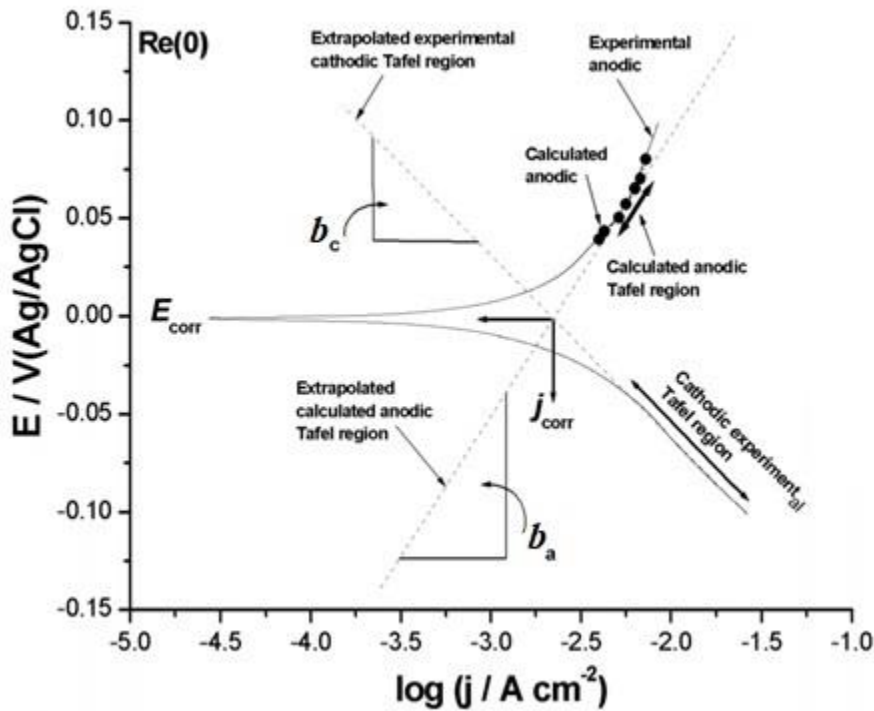


Figure 2.43: The analysis of Tafel slopes to calculate E_{corr} and i_{corr} [103].

Firstly, the active region describes the conditions under which a corrosion cell operates when the metal surface contacts the solution. The anodic and cathodic reactions begin at the interface. It can be referred to as uniform corrosion, when metals are dissolved in an electrolyte [102]. As in Figure 2.43 [103], both anodic and cathodic current densities are measurable with

the increase of potential values. Tafel slopes are measured to lead to the calculation of i_{corr} in A/cm² using the Stern-Geary equation [102,104].

$$B = \frac{b_a \cdot |b_c|}{2.303(b_a + |b_c|)} \quad \text{Equation 9}$$

$$i_{corr} = \frac{B}{R_p} \quad \text{Equation 10}$$

where B is the Stern-Geary constant; V, b_a is the anodic Tafel slope; V/decade, b_c is the cathodic Tafel slope; V/decade, i_{corr} is the corrosion current density; $\mu\text{A}/\text{cm}^2$, and R_p is the polarization resistance; $\Omega \cdot \text{cm}^2$.

From the equations above, the value of i_{corr} is used to calculate the corrosion rate (CR), according to the ASTM G102-89 standard [104].

$$CR = 3.27 \times 10^{-3} \frac{i_{corr}}{\rho} EW \quad \text{Equation 11}$$

where CR is the corrosion rate; mm/y, ρ is the density; g/cm³, and EW is the equivalent weight.

Figure 2.43 presents schematically the analysis of E_{corr} and i_{corr} on the diagram of potential (E) against current density (i); the well-known Evans diagram [105]. The graph links to theories such as the mixed potential and electrochemical polarization to obtain the value of E_{corr} and i_{corr} .

During the 1930s, the mixed potential theory was proposed by Wagner and Traud [105]. This theory consists of two simple assumptions; firstly, any electrochemical reaction can form with two or more partial oxidation and reduction reactions at the anode and cathode. Secondly, electric charges cannot accumulate while an electrochemical reaction progresses. This means that spontaneous electric-charge accumulation will not occur in the metal immersed in an electrolyte. This requirement leads to the outcome that the total rate of oxidation and reduction reactions must be equal during corrosion in the system of electrically separated metals [105]. The concepts of this theory can be used to predict the corrosion tendency and describe many materials and a diversity of environmental effects on the corrosion behaviour observed [105,106].

An example in Figure 2.44 [107] is the Evans diagram for an iron electrode immersed in an acidic solution. Shifting the potentials of both anodic and cathodic reactions by i_{corr} can lead to E_{corr} being obtained, with the possible anodic and cathodic reactions as below. This

graph presents a non-equilibrium system in which the corrosion current is produced and maintained by dynamic reactions [107].

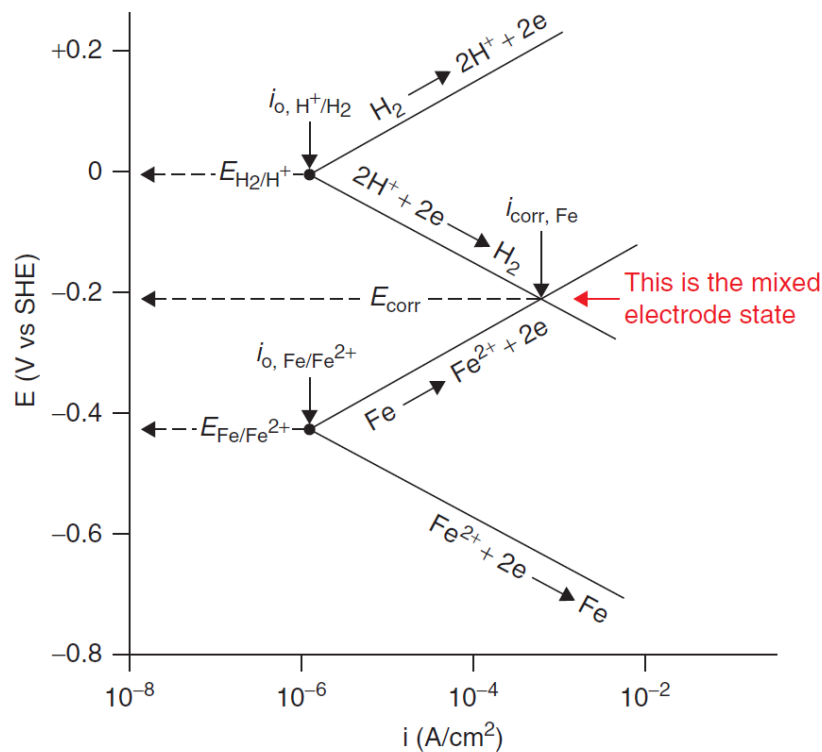
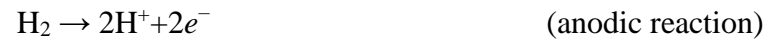


Figure 2.44: The Evans diagram for a mixed electrode state in the system of iron electrode and acidic solution [107].

In addition, measured data can link a corroding electrode and i_{corr} values by determining i_{corr} with a perturbation signal on the electrode in an electrochemical polarization experiment. In this measurement, an electrode is polarized from its steady-state mixed potential E_{corr} (which is not the equilibrium potential), to a new electrode potential (E) using a potentiostat. A response to the current applied is found in the overpotential in Equation 12 [107]. This can be modified to any value desired. The measured data between potential and current (or $\log i$) are generally displayed as polarization curves, as in Figure 2.45. This shows the electrochemical polarization experiment in the system of the iron electrode in an acidic solution, including a comparison between the experimental polarization diagram and the Evans diagram [107].

$$\eta = E - E_{corr}$$

Equation 12

where η is the overpotential; V , E is the new electrode potential; V , and E_{corr} is the corrosion potential; V .

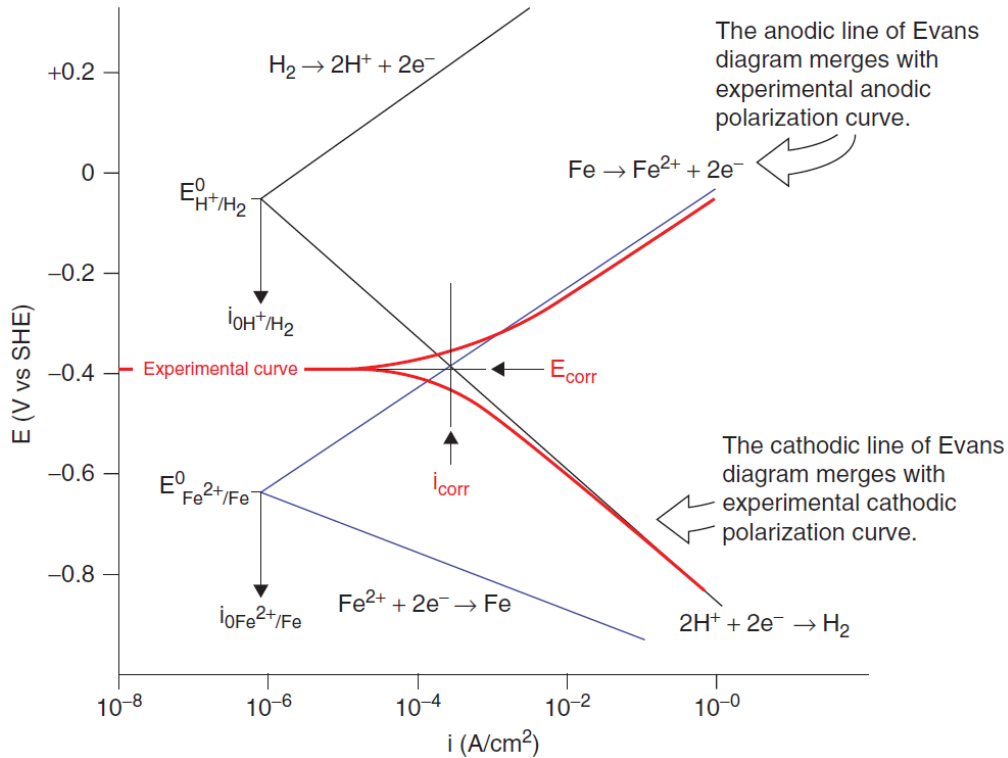


Figure 2.45: The comparison of an Evans diagram and experimental polarization curves in the system of an iron electrode and acidic solution [107].

Both the polarization curve and the Evans diagram can be used to explain the process of metal corrosion in mixed electrodes. The two diagrams are related but different. In Figure 2.45, it is the Evans diagram with simplified plots between the anodic and cathodic reaction curves in an electrochemical system of metals and acid. On the other hand, the behaviour between potential and current density of the applied current or potential in an electrochemical experiment is described following the polarization curves. The combination of the polarization curves in the anodic and cathodic reactions with the Evans diagram under a relatively high-polarization region is generally known as the Tafel region [107]. This is related to the Tafel technique where the extrapolation of the polarization curve can determine the values of E_{corr} and i_{corr} . Besides, Tafel slopes lead to the calculation of i_{corr} following the Stern-Geary equation in Equations 9 and 10.

Secondly, the passive region indicates the ability of oxide film, forming at the metal surface, to resist the corrosion attack (passivity) [102]. It shows a range, the passive zone,

before this protective film will break down. The applied potential increases through this zone but the current density remains constant. In addition, many metals, such as aluminum, chromium, copper, iron, nickel, tin, titanium, etc., can form an oxide or passive film on the metal surface to protect against corrosive attack. This protective behaviour in passive layers stems from the phenomenon of passivity [108,109].

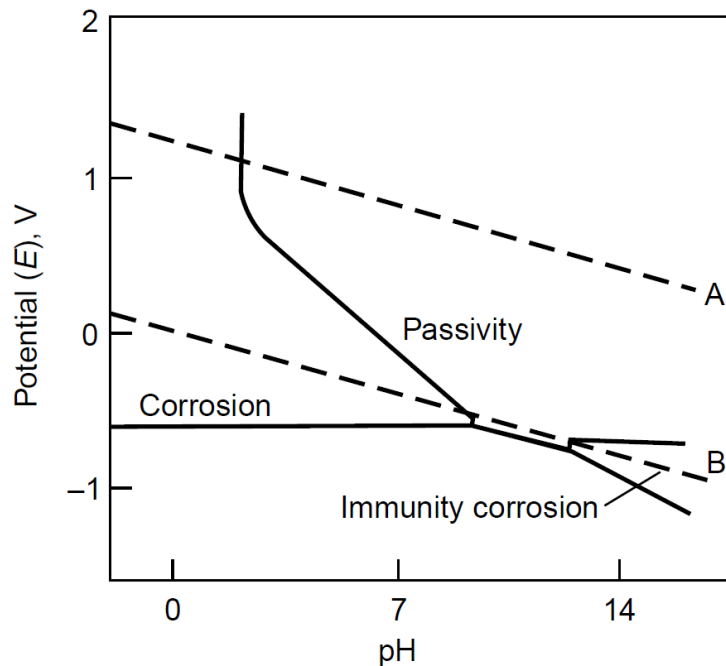


Figure 2.46: The simplified potential-pH equilibrium diagram in the system of the iron and water [108].

In previous research in the 1920s, the study of passivity in metals was used to promote the advance in engineering materials, especially the improvement of stainless steel, to understand the essential role of alloying elements and composition ratios in the determining properties of passive layers in metals and alloys [108]. In the thermodynamic approach, passivity can be seen in the equilibrium potential-pH (Pourbaix) diagram in Figure 2.46 [108]. Such a diagram can estimate the stable and unstable states of metals, ions, and oxides. These are separated by the chemical property of solution with pH values and electrochemical property of metals with potential values [109]. This diagram consists of three regions, corrosion, immunity, and passivation, in aqueous solutions. It is similar to the equilibrium phase diagrams in terms of indicating the expected thermodynamic outcome under certain conditions [108,109]. The immunity zone refers to where the material remains in the original form and corrosion will not occur, Gibbs free energy change (ΔG) > 0. The principle of cathodic protection is to create potential conditions such that metal remains in the immunity region.

Secondly, the corrosion or active area is where the material is corroded, $\Delta G < 0$. Thirdly, the passivity region is the area where the material is sealed by corrosion products or passive films. These can resist the progress of the corrosion reaction, $\Delta G < 0$ [109].

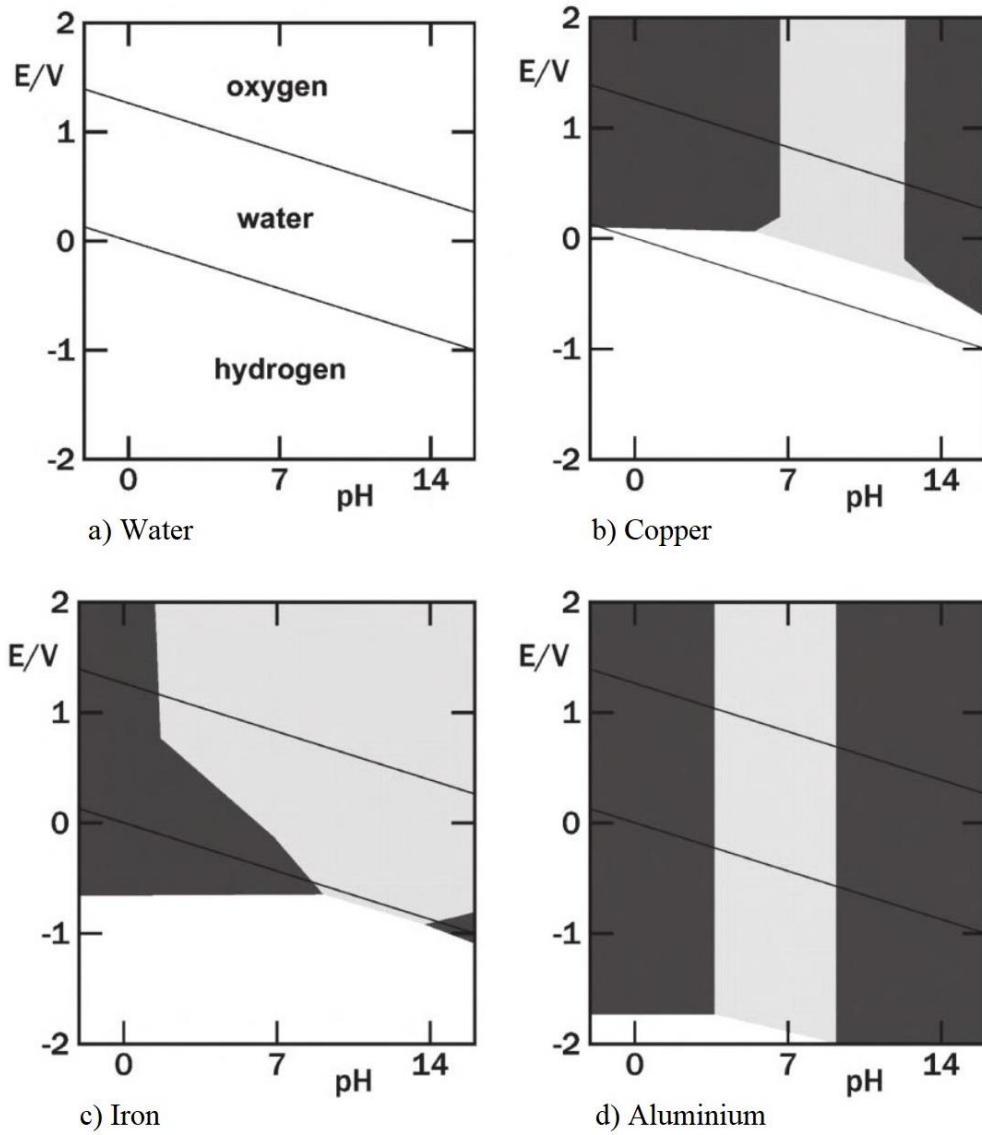


Figure 2.47: The potential-pH equilibrium diagram for a) water, b) copper, c) iron, and d) aluminium at 25 °C containing; white region (immunity), grey region (passivity), and dark region (activity) [110].

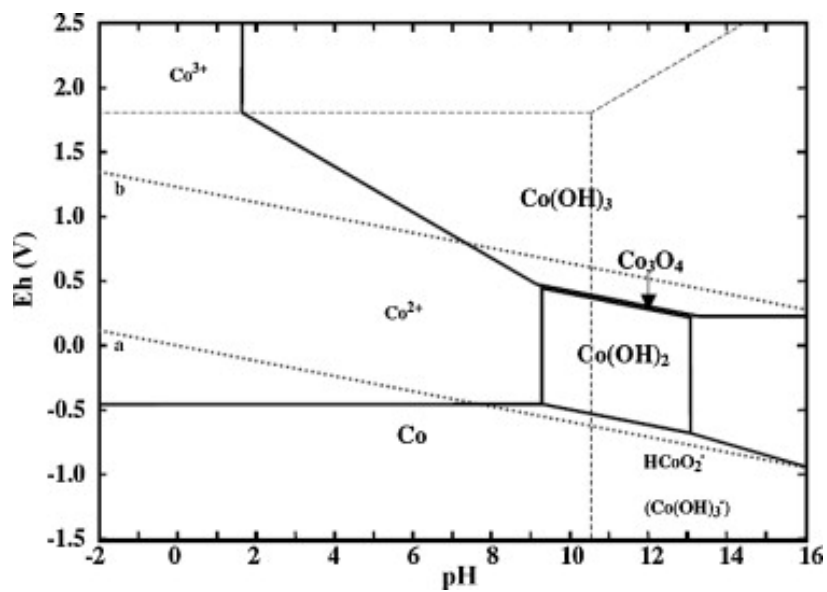


Figure 2.48: The potential-pH equilibrium diagram for cobalt and water at 25 °C [111].

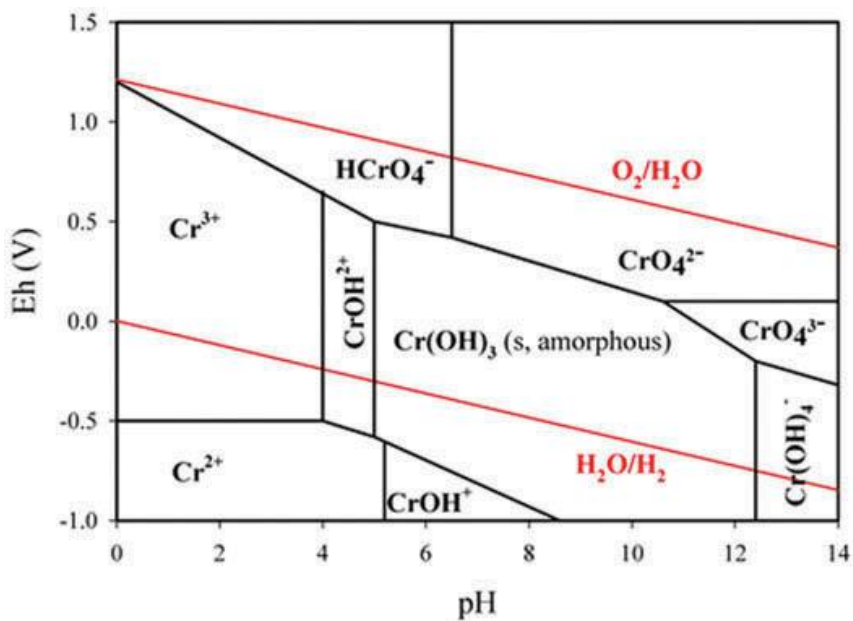


Figure 2.49: The potential-pH equilibrium diagram for chromium and water at 25 °C [112].

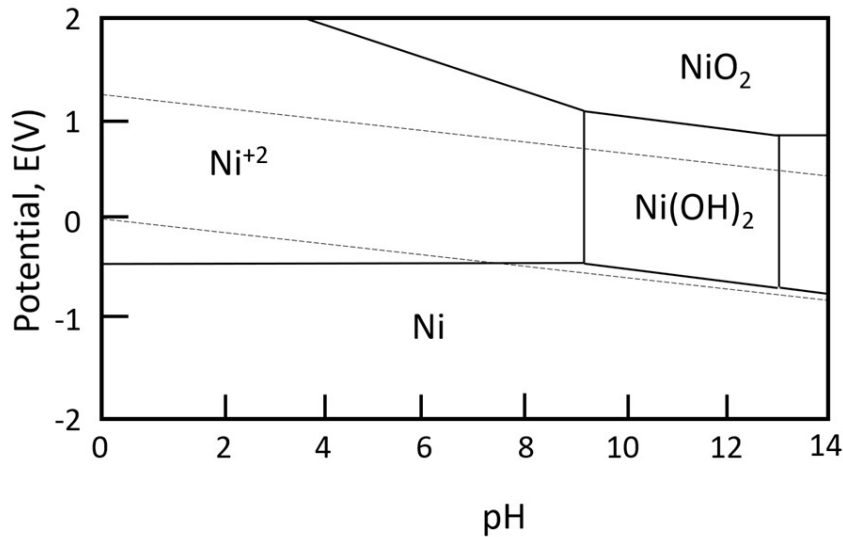


Figure 2.50: The potential-pH equilibrium diagram for nickel and water at 25 °C [113].

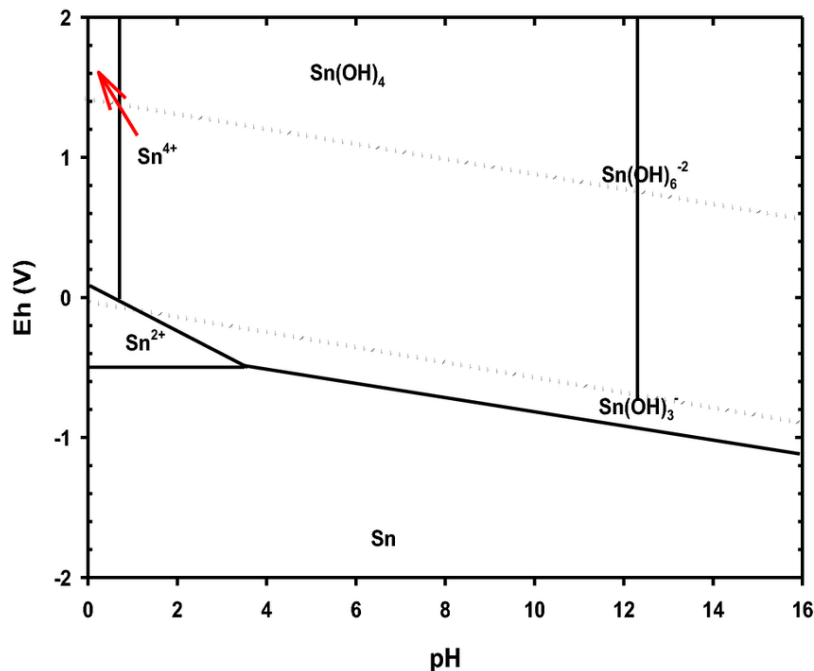


Figure 2.51: The potential-pH equilibrium diagram for tin and water at 25 °C [114].

The Pourbaix diagram of water consists of three areas; the first zone is the reduction to form hydrogen gas, the second zone is water stability, and the third zone is the decomposition of water to become oxygen gas. This diagram is used to consider the stable and unstable areas of metals immersed in the aqueous solution, as how the water behaves has a great effect on possible corrosion processes [110].

An example is that the water stability region is used to overlay with the potential-pH of metals in Figures 2.47-2.51 [110-114]. Overlaying of two areas containing stabilities of water and metal is under the condition that water would not rather spontaneously decompose during

the contact of the metal surface and solution. Figure 2.47b shows the narrow area of copper stability, Cu_2O and CuO , in aqueous solution (approximately pH 7-pH 13). This metal can be oxidized easily in acid (approximately pH<7) and reduced in strongly alkaline solutions (approximately pH>13) [110]. In the case of iron, it is sensitive to acid (approximately pH <8), while it has high corrosion resistance in alkaline solution (approximately pH>8), Figure 2.47c [110]. Figure 2.47d presents the narrow region of aluminium stability forming Al_2O_3 in the aqueous solution (approximately pH 4-pH 9) [110], similar to the stability of cobalt which has a narrow region to form $\text{Co}(\text{OH})_2$ and Co_3O_4 (approximately pH 9-pH 13) in Figure 2.48 [111]. The chromium stability in $\text{Cr}(\text{OH})_3$ or Cr_2O_3 form has a large area in aqueous solution (approximately pH 5-pH 12). It is unstable in acids below pH 5, Figure 2.49 [112]. Nickel is highly sensitive to acids below pH 9, and there is a narrow region of metal stability, $\text{Ni}(\text{OH})_2$ or NiO , in aqueous solution (approximately pH 9-pH 13), Figure 2.50 [113]. The tin stability has a large region at an approximate pH value of 1 to 12 in aqueous solution. $\text{Sn}(\text{OH})_4$ or SnO_2 can form in this area. In contrast, tin is unstable in the strongly acidic and alkaline solutions (approximately pH<1 and pH>12), Figure 2.51 [114].

As above, it indicates that tin has the most stability when in contact with aqueous solution out of these example metals (iron, chromium aluminium, cobalt, copper, and nickel), indicated by the largest area of metal stability of those discussed above.

Thirdly, the transpassive region refers to an initial point for the breakdown of oxide films. The transpassive potential (E_t) is measured at the change point of current density when a consistent value turns to a high value rapidly. It means that the protective film has lost the ability to resist the corrosion attack with the breakdown of passive film [80]. It may correspond to the breakdown potential of water or the pitting potential (E_p). E_p can refer to the potential at which a sudden increase in the current density occurs, as a result of a passive-film breakdown on the metal surface in the anodic area [105].

The electrochemical reaction between the metal and its environment leads to corrosion. This can cause failure of metal parts or increase the sensitivity to damage by other mechanisms. There are many different corrosion types with unique corrosion forms in Figure 2.52 [115]. For example, general corrosion, intergranular corrosion, pitting corrosion, stress-corrosion cracking, selective leaching corrosion, crevice corrosion, etc. These can be classified by the nature of the metallic corrodents, corrosion mechanism, and the surface appearance of the corroded metallic region [2,115,116]. Some corrosion forms relevant to this work are

presented, for example, general corrosion, galvanic corrosion, pitting corrosion, and selective leaching corrosion.

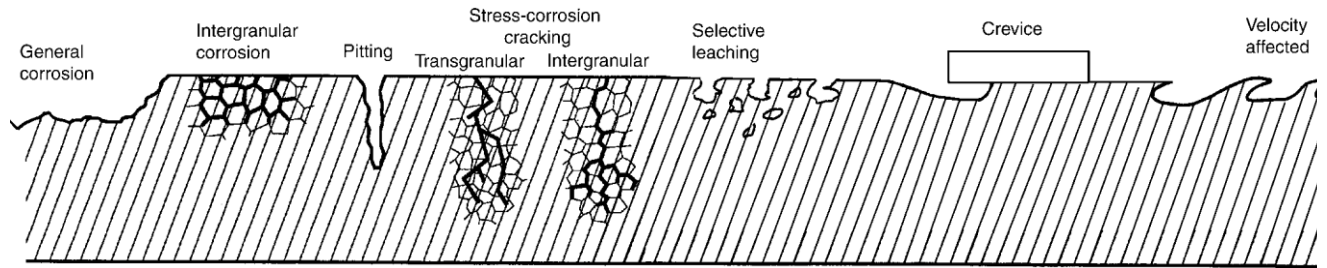


Figure 2.52: Several corrosion forms in metals [115].

General (or uniform) corrosion refers to a corrosion process with a relatively uniform thinning on the metal surface, without an appearance of localized attack, Figure 2.53 [115]. This form is the most common type of corrosion in metals due to the uniform chemical attack. It can occur in solutions, the atmosphere, soil, and during service under normal conditions. Corrosion is seen as a single penetration. In contrast, uniformly thinned traces after a corrosion attack can be observed by cross-section tests [115,116]. A familiar example is the formation of rust on steel under the air. The change in the environment can also lead to an increase in corrosion attack. Examples of conventional alloys exhibiting uniform corrosion are many steels, Cu alloys, Mg alloys, and Zn alloys [115]. Generally, this corrosion type can form on the metal surface with uniform microstructures and homogeneous chemical compositions. Its corrosion process proceeds on the metal surface by environmental attack unrestrictedly and uniformly. The corrosion interaction can change the mode of metallic deterioration away from general corrosion [115].

In addition, the mechanism of general corrosion at the microlevel is the electrochemical reaction between adjacent, closely spaced micro-cathodic and micro-anodic areas. Thus, general corrosion may be considered a type of localized electrolytic attack arising consistently over the metal surface. It can be found in a binary alloy system having phases with different corrosion potential. One phase will become anodic to the other phase. Hence an electrolytic cell is produced when a suitable electrolyte is present [115].

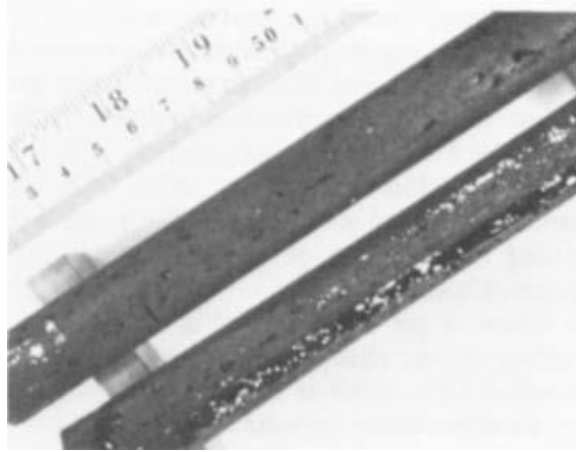


Figure 2.53: Steel tubes in the boiler-feedwater system undergoing general corrosion [115].

Galvanic corrosion, Figure 2.54, is one form of corrosion type occurring when two dissimilar materials (metallic or non-metallic types) are in electrical contact with each other and exposed to the environment [115,116]. It generally stems from the contact between two dissimilar conducting materials immersed in an electrolyte which is a conducting fluid, or it may be caused by similar conducting materials in contact with dissimilar electrolytes.

The mechanism of galvanic corrosion is the reaction of a galvanic cell with an anode and cathode, and the electrically coupled system, to create a galvanic current which flows at the interface reaction due to different potential between the two materials [115]. The galvanic couple contains an anodic site, which is a corroded material to release electrons dissolving in the electrolyte or forming metal oxides, and a cathodic site which gains electrons and releases hydrogen to the electrolyte to reduce oxides. Both reactions at the contacting area must proceed simultaneously to create galvanic corrosion. The anodic reaction with dissolution or oxidation in metals leads to the flow of electrical current from the more anodic site to the other more cathodic site via the electrolyte, like a galvanic couple of steel in the anode and broken mill scale in the cathode, Figure 2.55 [115].



Figure 2.54: The formation of galvanic corrosion is found in a ray lamp of a distillation column which occurred at the interface between a stainless steel AISI 410 plate in contact with a carbon steel bolt in an environment with hydrocarbons contaminated with salts [116].

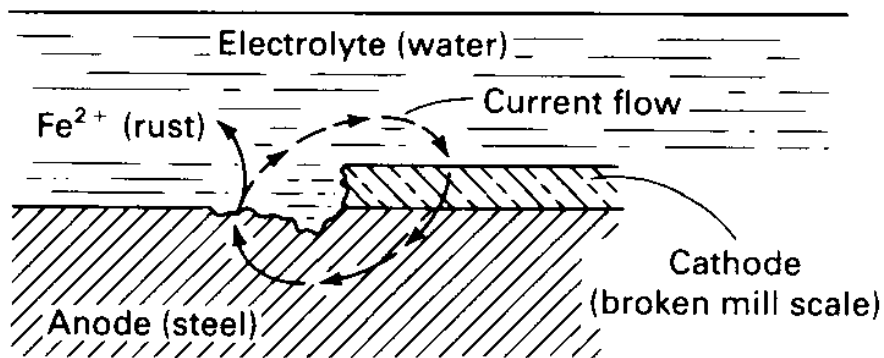


Figure 2.55: The galvanic corrosion from a couple of steel and broken mill scale [115].

Pitting corrosion, Figure 2.56 [116], is one form of localized corrosion that is an important cause of metallic damage with corrosion attack on the passivated protected area in the metal surface [115]. It can stem from specific anions in the electrolytes. For instance, chloride ions attack the oxide film at microscopic scale [116]. An example of other causes of pitting corrosion are a locally inhomogeneous metallic surface, locally losing passivity, a rupture of protective oxide films, and discontinuous organic coating [115]. This is one of the most dangerous corrosion forms characterized by holes, also called pits. Metal failure stems from perforation by a pitting attack. Pitting is not only difficult to detect but also can form rapidly on the metal surface. These factors can lead to unpredicted loss of function in metals [115].

All conventional engineering metals or alloys are sensitive to pitting corrosion. The pitting mechanism proceeds when the anodic site forms on the local surface of metals with a remaining area on the metal surface as the cathode site following highly localized changes in the contacting area leading to an accelerated localized attack [115]. The initiation of a passive-film breakdown or the local breakdown of inhibitor-produced protection in the pitting form usually occurs on clean metallic surfaces. The propagation of pits starts at small and widely separated sites which have proceeded with little or no general corrosion, as a high ratio of the cathode-to-anode region. Subsequently, the penetration step progresses more rapidly than when pits are formed with numerous amounts and close together, as an increase in the anode area [115].

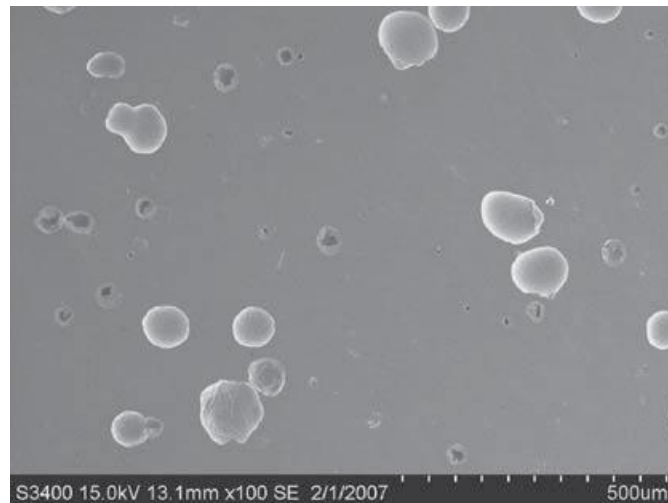
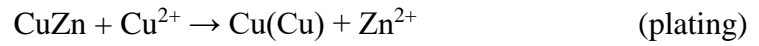


Figure 2.56: Pitting corrosion formed on AISI 316 stainless steel in 3.5 wt.% NaCl solution [116].

Selective leaching corrosion is also known as dealloying or parting when applied to noble metals. It occurs with the removal of one element or a phase with less noble elements from the alloy, which has different electrochemical potentials from other alloy components, caused by a corrosion reaction under a corrosive environment [115,116]. This corrosion form can lead to microstructural change of the original alloy. A porous structure can be observed on the alloy surface when removing an element or phase from the initial alloy surface, Figure 2.46 [115]. There are many types of selective leaching corrosion, such as dezincification in Cu-Zn alloys, denickelification in Cu-Ni alloys, and graphitic corrosion in cast iron [115,116].

Selective leaching corrosion has several theories regarding its mechanism. There are two prominent mechanisms. Firstly, an alloy containing two elements or phases can dissolve, and then a dissolved element re-plates on the alloy surface. Secondly, one element or phase selectively dissolving from an initial alloy and releasing the more noble elements with higher

potentials in a porous metallic form [115]. An example of selective leaching observed in Cu-Zn alloys is dezincification. The proposed reaction mechanisms of dezincification are given below.



Initially, both Cu and Zn elements are dissolved in the dissolution step. Subsequently, Cu (ii) ions move to deposit on the alloy surface, replacing Zn. It results in a porous structure containing a Cu-rich phase on the surface with depleting Zn [116].

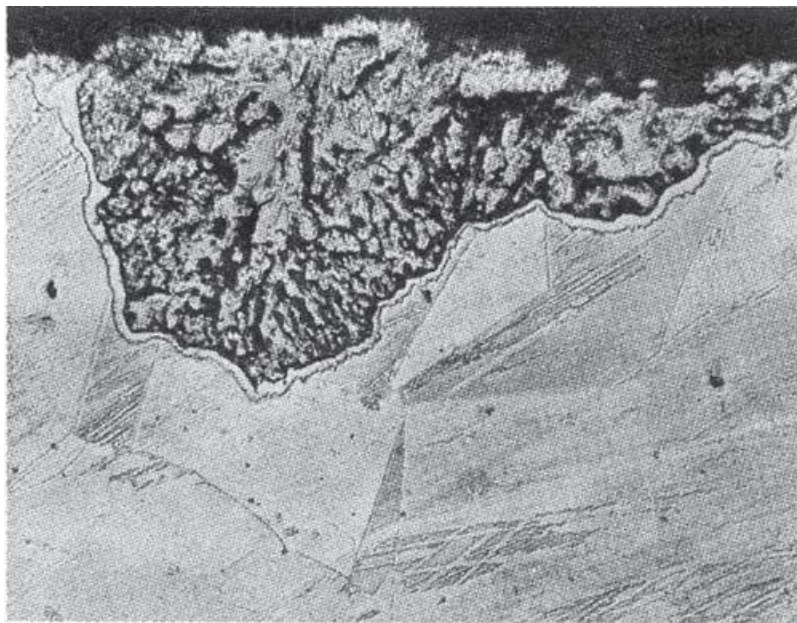


Figure 2.57: An etched cross-sectional image of Cu-Zn alloy showing the dezincification [116].

Corrosion is a specific electrochemical reaction between metals and electrolytes. This work pays attention to the diversity of the general test electrolytes, such as NaCl solution, H₂SO₄ solution, and NaOH solution. NaOH data was used to replace the NaAlO₂ data (NaAlO₂ being considered as a possible leachable space holder phase for porous metal production; in this route the high surface area porous metal must survive extended periods in concentrated solutions during processing) due to a lack of information on corrosion testing of the relevant metals/alloys in NaAlO₂ solution. It also includes different types of metallic samples such as pure metals, conventional alloys, and HEAs. The corrosion properties of some elements or alloys in several test solutions are presented in Tables 2.8-2.13.

Table 2.8: The corrosion properties of conventional alloys in chloride solution at room temperature.

Alloy	Grade	NaCl concentration	E_{corr} (V _{Ag/AgCl})	i_{corr} ($\mu\text{A}/\text{cm}^2$)	E_t/E_p (V _{Ag/AgCl})	Reference
Al	Pure grade	0.6 M	-0.87 (V _{SCE})	11.16	-	[117]
Cu			-0.24 (V _{SCE})	7.84	-	[118]
Sn		0.35 M	-0.59 (V _{SCE})	0.29	-	[119]
Cu alloys	Cu5wt.%Ni	0.6 M	-0.21	15.80	-	[120]
	Cu10wt.%Ni		-0.27	18.31	-	[121]
Ni alloys	Ni7wt.%Mo		-0.59	0.52	-	[122]
	Ni15wt.%Mo		-0.55	0.14	-	
	Ni20wt.%Mo		-0.59	0.58	-	
	Ni25wt.%Mo		-0.56	0.82	-	
Ti alloys	Ti-6Al-4V		-0.21	2.57	1.19	[123]
Steels	AISI 1045		-0.71	3.07	-	[124]
	A36		-0.54	2.92	-0.45	[125]
Stainless steels	SS 304		-0.06	0.11	0.66	
	SS 316L		-0.27	0.21	0.47	[126]

Table 2.9: The corrosion properties of conventional alloys in acidic solution at room temperature.

Alloy	Grade	H ₂ SO ₄ concentration	E_{corr} (V _{Ag/AgCl})	i_{corr} (μ A/cm ²)	E_t/E_p (V _{Ag/AgCl})	Reference
Al	Pure grade	1 M	-0.68 (V _{SCE})	56	-	[127]
Cu			-0.12 (V _{SCE})	2.5	-	
Ni alloys	Ni3at.%Mo	1 M	-0.20	69.00	1.01	[128]
	Ni5at.%Mo		-0.27	78.00	1.01	
	Ni6at.%Mo		-0.20	220.00	1.01	
	Ni9at.%Mo		-0.23	642.00	1.01	
Ti alloys	Ti-6Al-4V	0.5 M	-0.65	3.02	0.48	[123]
Steels	AISI 1018		-0.46	300.00	-	[129]
	A36		-0.25	204.00	1.60	[125]
Stainless steels	SS 304		-0.10	11.60	1.17	
	SS 316L		-0.39	380.00	-	[130]

Table 2.10: The corrosion properties of conventional alloys in alkaline solution at room temperature.

Alloy	Grade	NaOH concentration	E_{corr} (V _{Ag/AgCl})	i_{corr} (μ A/cm ²)	E_t/E_p (V _{Ag/AgCl})	Reference
Al	Pure grade	0.1 M	-1.55 (V _{SCE})	435.4	-	[50]
Cu		0.1 M	-0.48 (V _{SCE})	34.4	-	[51]
Ni alloys	Ni11wt.%Mo	0.5 M	-0.39	708.00	-	[131]
	Ni15wt.%Mo		-0.43	406.00	-	
	Ni23wt.%Mo		-0.38	493.00	-	
Ti alloys	Ti-6Al-4V	1 M	-0.17	0.17	1.28	[123]
Steels	Q235	1 M	-0.88	0.67	-	[132]
Stainless steels	SS 304	1.5 M	-0.43	0.46	-	[133]

Tables 2.8-2.10 show examples of corrosion properties for several conventional alloys. Some of these alloys, such as steels, stainless steels, Cu alloys, Ni alloys, and Ti alloys, are reported in three solutions, chloride, acidic, and alkaline solutions. Each alloy has specific corrosion properties depending on the type of solution as reported in the results in these summary tables. For example, SS 304 which is one of most popular alloys for use in applications subject to corrosion is reported for all three solutions. As in Table 2.8, this alloy has the highest corrosion resistance in 0.6 M NaCl solution with high E_{corr} (-0.06 V_{Ag/AgCl}) and low i_{corr} (0.11 $\mu\text{A}/\text{cm}^2$), while poorer corrosion properties are found in both 0.5 M H₂SO₄ solution from a low E_{corr} value (-0.10 V_{Ag/AgCl}) and the highest i_{corr} value (11.60 $\mu\text{A}/\text{cm}^2$), and 1.5 M NaOH solution from the lowest E_{corr} value (-0.43 V_{Ag/AgCl}) and a high i_{corr} value (0.46 $\mu\text{A}/\text{cm}^2$) [125,133] in Tables 2.9 and 2.10. These results indicate that the Cr₂O₃ formed on the surface of this alloy is a stable layer for inhibiting the chloride attack, but its stability decreases in acidic and alkaline solutions. The corrosion behaviour of SS 316L in NaCl and H₂SO₄ solutions is similar to SS 304. It has good corrosion resistance in chloride solution, while poor corrosion properties are detected in acidic solution. The corrosion properties of this alloy depend on the ability of protective Cr₂O₃ film [126,130].

In addition, a difference in chemical composition between SS 316 and SS 304 affects their properties. SS 316 consists of 16% Cr, 10% Ni, and 2% Mo while SS 304 contains 18% Cr and 8% Ni. The Mo addition promotes more corrosion resistance in the chloride environment. It can form the passive film in the repassivation process to resist pitting corrosion. It is likely to decrease the critical passivation current and the number of pitting holes, as well as increase pitting potential [134,135]. The Ni content in stainless steel can lead to an increase in formability and weldability due to changing to an austenitic structure. SS 316 has high Mo and Ni contents, resulting in better properties with high corrosion resistance, formability, and weldability than SS 304. In contrast, it is more expensive than SS304 [125,126,130,133]. As mentioned above, SS 304 immersed in a solution containing chloride has the highest corrosion resistance in Table 2.8. It has a high corrosion potential and low corrosion current density leading to high efficiency in resisting the chloride attack. This result is similar to Table 2.9 in acidic solution, while Ti-6Al-4V alloy tested in alkaline solution has the highest corrosion resistance with the highest E_{corr} value (-0.17 V_{Ag/AgCl}) and the lowest i_{corr} value (0.17 $\mu\text{A}/\text{cm}^2$) in Table 2.10 [122].

Table 2.11: The corrosion properties of HEAs in chloride solution at room temperature.

HEA	NaCl concentration	E_{corr} (V _{Ag/AgCl})	i_{corr} ($\mu\text{A}/\text{cm}^2$)	E_t/E_p (V _{Ag/AgCl})	Reference
Al _{0.3} CoCrFeNi	0.6 M	-0.15	0.08	0.51	[136]
Al _{0.5} CoCrFeNi		-0.18	0.25	0.43	
Al _{0.7} CoCrFeNi		-0.23	0.43	0.10	
FeCoNiCr		-0.22	0.03	0.36	[11]
FeCoNiCrCu _{0.5}		-0.25	0.72	0.14	
FeCoNiCrCu		-0.29	1.32	0.13	
CrMnFeCoNi		-0.30	0.11	0.02	[125]
(CoCrFeNi) ₉₉ Mo ₁		-0.15	0.40	1.04	[137]
(CoCrFeNi) ₉₈ Mo ₂		-0.23	0.24	1.01	
(CoCrFeNi) ₉₇ Mo ₃		-0.45	6.61	1.10	

Table 2.12: The corrosion properties of HEAs in acidic solution at room temperature.

HEA	H ₂ SO ₄ concentration	E_{corr} (V _{Ag/AgCl})	i_{corr} ($\mu\text{A}/\text{cm}^2$)	E_t/E_p (V _{Ag/AgCl})	Reference
CoCrFeNi	0.5 M	-0.08	15.8	-	[10]
Al _{0.25} CoCrFeNi		-0.10	16.7	-	
Al _{0.5} CoCrFeNi		-0.08	13.4	-	
AlCoCrFeNi		-0.09	13.1	-	
CuCr ₂ Fe ₂ Ni ₂ Mn ₂	1 M	-0.93	2.09	-	[138]
Cu ₂ CrFe ₂ NiMn ₂		-1.10	40.20	-	
CrMnFeCoNi	0.5 M	-0.33	8.96	0.91	[125]
(CoCrFeNi) ₉₉ Mo ₁		-0.25	34.10	0.41	[137]
(CoCrFeNi) ₉₈ Mo ₂		-0.25	28.00	0.44	
(CoCrFeNi) ₉₇ Mo ₃		-0.23	15.40	0.52	

Table 2.13: The corrosion properties of HEAs in alkaline solution at room temperature.

HEA	NaOH concentration	E_{corr} (V _{Ag/AgCl})	i_{corr} (μA/cm ²)	E_t/E_p (V _{Ag/AgCl})	Reference
Al ₂ CrFeCuNiTi	1 M	-0.82	0.12	-	[132]
Al ₂ CrFeCo _{0.5} CuNiTi		-0.82	0.13	-	
Al ₂ CrFeCo _{1.0} CuNiTi		-0.61	0.0003	-	
Al ₂ CrFeCo _{1.5} CuNiTi		-0.85	0.20	-	
Al ₂ CrFeCo _{2.0} CuNiTi		-0.83	0.03	-	
Co _{1.5} CrFeNi _{1.5} Ti _{0.5}		-0.75	0.09	0.45	[139]
Co _{1.5} CrFeNi _{1.5} Ti _{0.5} Mo _{0.1}		-0.59	0.11	0.45	
Co _{1.5} CrFeNi _{1.5} Ti _{0.5} Mo _{0.5}		-0.87	0.16	0.45	
Co _{1.5} CrFeNi _{1.5} Ti _{0.5} Mo _{0.8}		-0.80	0.25	0.45	

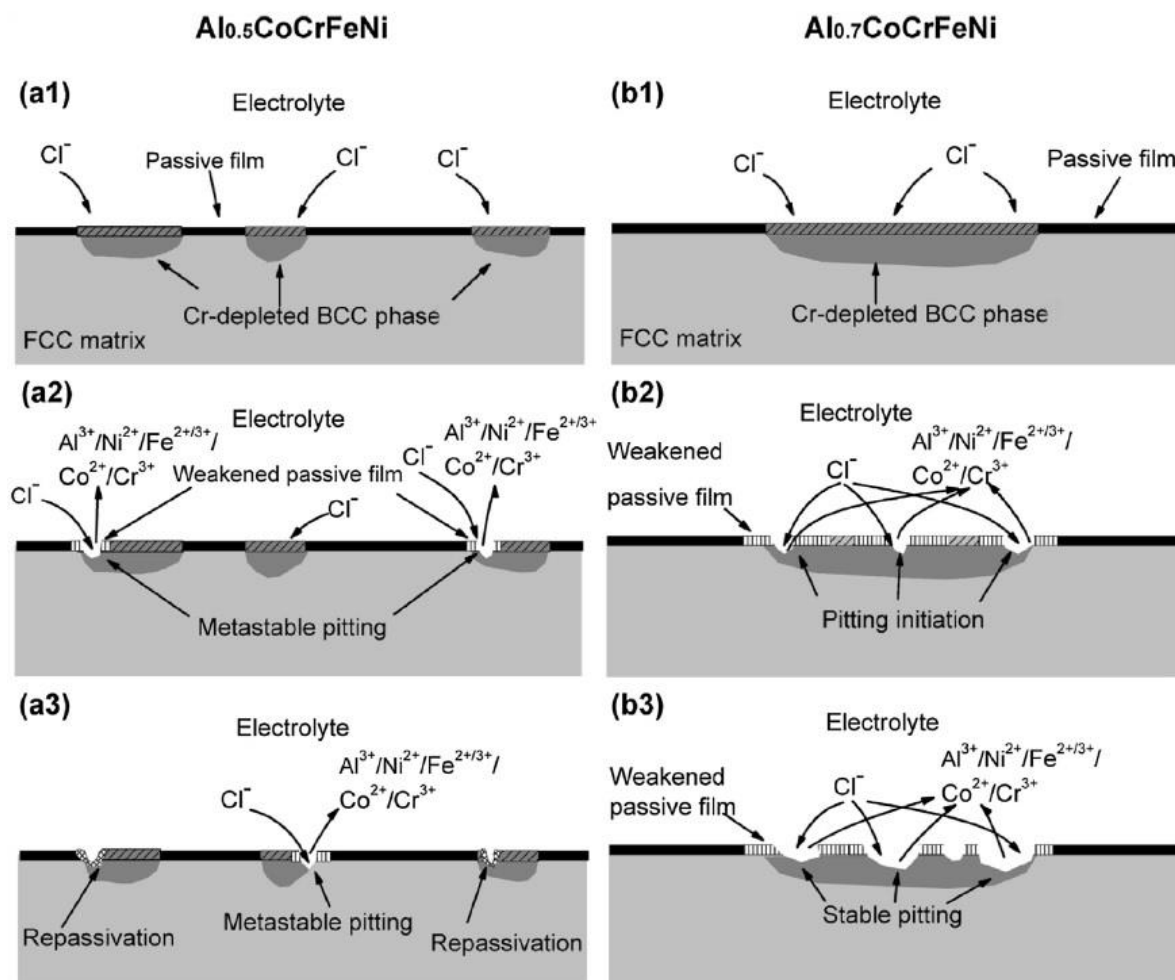


Figure 2.58: The corrosion mechanism of Al_{0.5-0.7}CoCrFeNi in 0.6 M NaCl solution at room temperature [136].

Some measurements have been made of the corrosion properties of HEAs, presented in Tables 2.11-2.13. These are again examined in the different solutions, chloride, acidic, alkaline solutions, at room temperature. The effect of alloying elements on corrosion properties of HEAs is observed. As in Table 2.11, Al, Cu, Mn, and Mo are alloying elements added to the main CoCrFeNi systems for the investigation of corrosion behaviour in chloride solution [11,125,136,137]. The additions of Al and Cu have a negative effect on the development of corrosion properties in the CoCrFeNi system. The increase of Al in $Al_xCoCrFeNi$ leads to a decrease in corrosion resistance with lower E_{corr} and E_p values, and higher i_{corr} values. This stems from the loss Cr proportion in the BCC phase leading to the reduction of protective Cr_2O_3 film formation under the medium chloride condition as in Figure 2.58 [136]. In the case of Cu addition, the corrosion resistance of $CoCrFeNiCu_x$ is poorer when the Cu content is higher. A high Cu proportion can give rise to the formation of Cu segregation at the interdendritic region. An unstable oxide film is formed on the Cu-rich region and, being two phases, it is easy to corrode by galvanic corrosion [11]. On the other hand, Mn and Mo additions in the main CoCrFeNi system lead to an increase in the corrosion properties [125,137]. CrMnFeCoNi coated on the substrate provides higher corrosion resistance, especially the region of uniform corrosion, with high E_{corr} ($-0.30 V_{Ag/AgCl}$) and low i_{corr} ($0.11 \mu A/cm^2$). However, it has been found that a coating of CrMnFeCoNi has a narrow passive region and it is sensitive to pitting corrosion [125]. For the addition of Mo, the passivity of $(CoCrFeNi)_{100-x}Mo_x$ alloys increases with Mo content, with a large passive zone. Nevertheless, the highest Mo ratio in $(CoCrFeNi)_{97}Mo_3$ decreased corrosion resistance with low E_{corr} ($-0.45 V_{Ag/AgCl}$) and high i_{corr} ($6.61 \mu A/cm^2$). The loss of Cr content from the matrix FCC phase occurs, due to the formation of σ phase with Cr-Mo structure in the interdendritic region, including two phases in HEA structures which easily undergo galvanic corrosion [137]. In addition, it is also found that an increase in the Mo content can promote higher hardness and strength in HEAs due to the formation of BCC phase containing high Mo and Cr. It indicates that the Mo addition, as a BCC stabilizer, can improve the mechanical properties in the CoCrFeNi-based HEA, while corrosion properties can be decreased when the Mo content is above 3 wt.% [137]. As shown in Table 2.11, $Al_{0.3}CoCrFeNi$ tested in 0.6 M NaCl solution is the most corrosion-resistant of all HEAs in Table 2.11, with high corrosion potential and low corrosion current density.

Table 2.12 shows the corrosion behaviour of HEAs in acidic solution. The influence of alloying elements, Al, Cu, Mn, and Mo, is observed. The Al addition to $Al_xCoCrFeNi$ alloys has no observable effect on the region of uniform corrosion. The E_{corr} and i_{corr} of all HEA

systems have similar values. However, the increase of passive current density (i_{pass}) is detected with increased Al content, resulting from the formation of porous Al-oxide film on the HEA surfaces [10]. In the Cu addition to $\text{CuCr}_2\text{Fe}_2\text{Ni}_2\text{Mn}_2$ and $\text{Cu}_2\text{CrFe}_2\text{NiMn}_2$ alloys, high Cu content leads to the phase formation changing from a single FCC phase to a dual phase (BCC+FCC). A difference in phase content between interdendritic regions and the dendrites can give rise to poor corrosion properties due to galvanic corrosion, Figure 2.59 [138]. An addition of Mn was attempted, for A36 steel coated with 2 mm thick CrMnFeCoNi. This led to an increase in corrosion resistance, with higher E_{corr} ($-0.33 \text{ V}_{\text{Ag}/\text{AgCl}}$) and lower i_{corr} ($8.96 \mu\text{A}/\text{cm}^2$), due to the formation of an oxide film during the immersion in acidic solution [125]. In addition, the increase in the Mo content in $(\text{CoCrFeNi})_{100-x}\text{Mo}_x$ alloys leads to the enhancement of corrosion resistance. High E_{corr} ($-0.23 \text{ V}_{\text{Ag}/\text{AgCl}}$) and E_t ($-0.52 \text{ V}_{\text{Ag}/\text{AgCl}}$), and low i_{corr} ($15.40 \mu\text{A}/\text{cm}^2$) were found with more Mo in $(\text{CoCrFeNi})_{97}\text{Mo}_3$, due to the formation of stable Cr and Mo oxides, reducing the dissolution rate in active zones. [137]. It is also found that the extensive passive zone with high Mo content may be caused by Molybdate anions, MoO_4^{2-} , promoting the re-passivation of oxide films, similar to SS 316 [130,137]. For Table 2.12, $\text{Al}_{0.5}\text{CoCrFeNi}$ is the best HEA system to inhibit corrosion attack in 0.5 M H_2SO_4 solution, comparing all HEAs in this table.

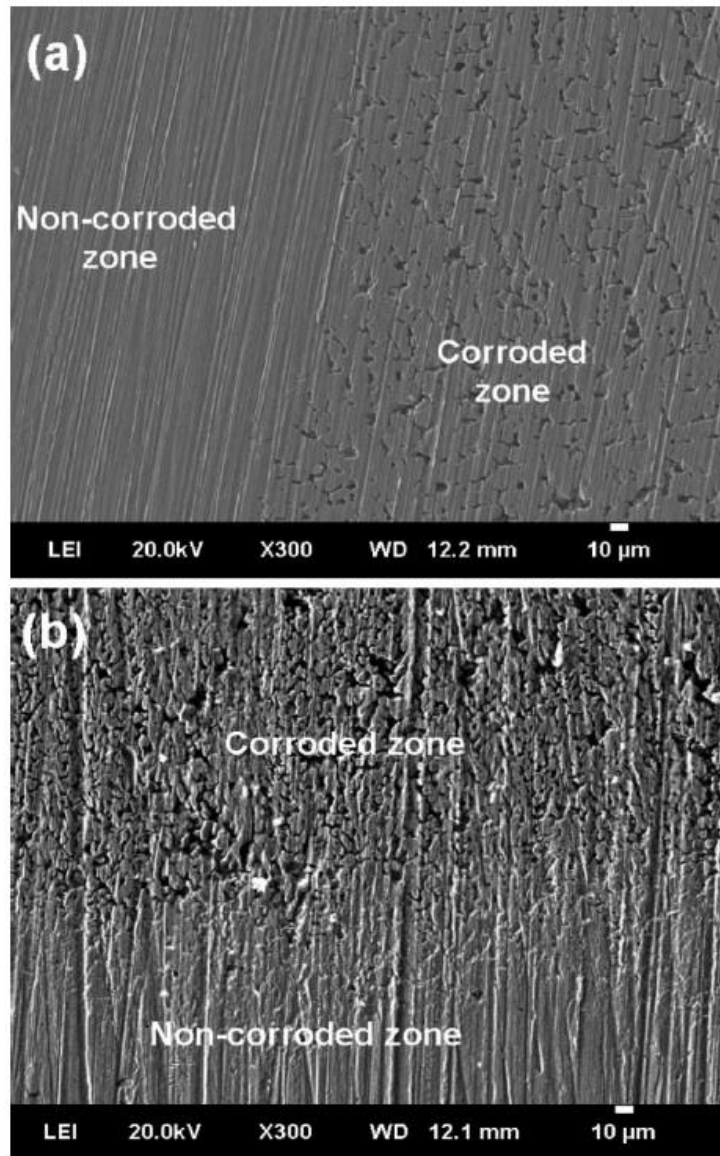


Figure 2.59: SEM images of a) $\text{CuCr}_2\text{Fe}_2\text{Ni}_2\text{Mn}_2$ and b) $\text{Cu}_2\text{CrFe}_2\text{NiMn}_2$ alloy after corrosion testing in 1 M H_2SO_4 solution at room temperature [138].

Lastly, the corrosion resistance of HEAs in alkaline solution is shown in Table 2.13. The impact of Co and Mo additions on the corrosion properties of HEAs has been investigated. $\text{Al}_2\text{CrFeCo}_x\text{CuNiTi}$ alloys have been used as coatings on the surface of Q235 steel. This steel is a commercial grade for plain-carbon steel with approximately 0.2 wt.% of carbon content. It is mostly used in engineering structures and infrastructure construction, stemming from good weldability, good forming ability, and also good mechanical properties [132]. $\text{Al}_2\text{CrFeCo}_x\text{CuNiTi}$ shows better corrosion properties than pure Q235 steels with reduced i_{corr} value from $0.12 \mu\text{A}/\text{cm}^2$ in $\text{Al}_2\text{CrFeCuNiTi}$ to $0.03 \mu\text{A}/\text{cm}^2$ in $\text{Al}_2\text{CrFeCo}_{2.0}\text{CuNiTi}$. Three elements, Cr, Co, and Ni, show good ability to form a dense layer of metal oxides, inhibiting

the acidic corrosion attack [132]. For the Mo addition to $\text{Co}_{1.5}\text{CrFeNi}_{1.5}\text{Ti}_{0.5}\text{Mo}_x$ alloys, the Mo content affects the decrease in corrosion properties compared the same system without Mo. High i_{corr} ($0.25 \mu\text{A}/\text{cm}^2$) and low E_{corr} ($-0.80 \text{ V}_{\text{Ag}/\text{AgCl}}$) values are found in the system with Mo ($\text{Co}_{1.5}\text{CrFeNi}_{1.5}\text{Ti}_{0.5}\text{Mo}_{0.8}$), resulting from the decrease in dominant elements, Co, Ni, and Ti, which play a vital role in the creating protective oxide films [139]. As mentioned above, it can be concluded that the highest corrosion resistance immersed in 1 M NaOH solution in Table 2.13 is found with $\text{Co}_{1.5}\text{CrFeNi}_{1.5}\text{Ti}_{0.5}\text{Mo}_{0.1}$ with low corrosion current density ($0.11 \mu\text{A}/\text{cm}^2$) and high corrosion potential ($-0.59 \text{ V}_{\text{Ag}/\text{AgCl}}$).

2.2.3 Tribocorrosion properties

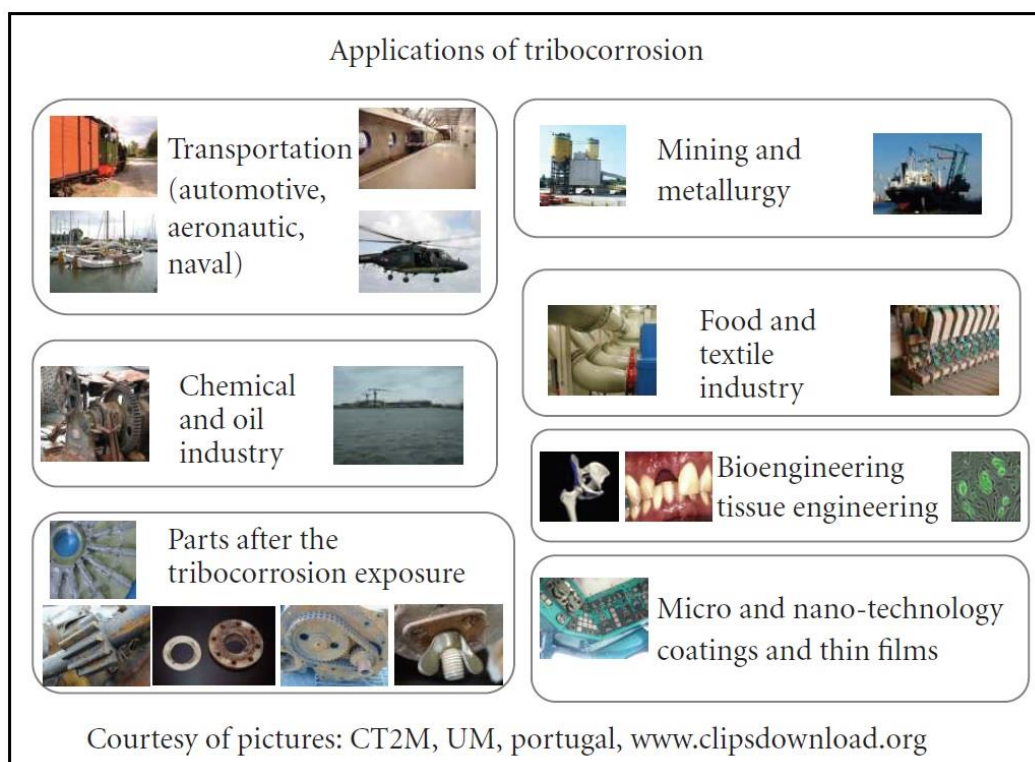


Figure 2.60: The application relating with tribocorrosion properties [140].

Under conditions of high wear and aggressive environment, such as under submarine and fluid conditions, severe material degradation may occur [141]. In such situations tribocorrosion properties (the resistance to wear and corrosion combined) will be important. It can refer to several mechanisms of surface deterioration of materials, such as abrasion, erosion, and friction as wear parameters, and chemical reaction and electrochemical effects at the interface between materials and electrolyte solution [140,142]. As in Figure 2.60, this property needs to be considered for diverse industrial applications, for example, biomaterials, transportation, chemical processing, gas and oil, etc. [140,142].

Contact mode	Schematic
Sliding <ul style="list-style-type: none"> • Unidirectional • Reciprocating Corrosive wear Chemo-mechanical polishing	
Fretting Dentistry Body joints (hip and knee)	
Rolling Dentistry Body joints (hip and knee)	
Microabrasion Rolling Grooving	
Impingement Erosion corrosion Impingement attack	

Figure 2.61: Five contact modes for tribocorrosion tests [140].

In tribocorrosion tests, the interaction between the sample surface and the media surface directly affects the degradation behaviour of materials. The selection of contact modes for testing needs to be correct [140]. There are five contact modes, Figure 2.61, which link with corrosion on the sample surface and lead to the formation of tribocorrosion. For example, a fretting mode is a reciprocating movement of a certain amplitude below 500 μm . A rolling mode is found in ball bearings (where tribocorrosion often occurs). Lastly, an impingement mode occurs with small particle contact, which can result in the formation of erosion corrosion in fluid [140].

Tribocorrosion tests operate with two systems; wear and corrosion. In addition, other complementary instruments are used to analyse the tests, such as electrochemical impedance

spectroscopy (EIS), to identify the tribocorrosion mechanism between passive layers on the contact surface, including oxide-film properties or characteristics formed on the engagement region. These tests are carried out before and after the wear or sliding step to observe the change of oxide-film properties [140].

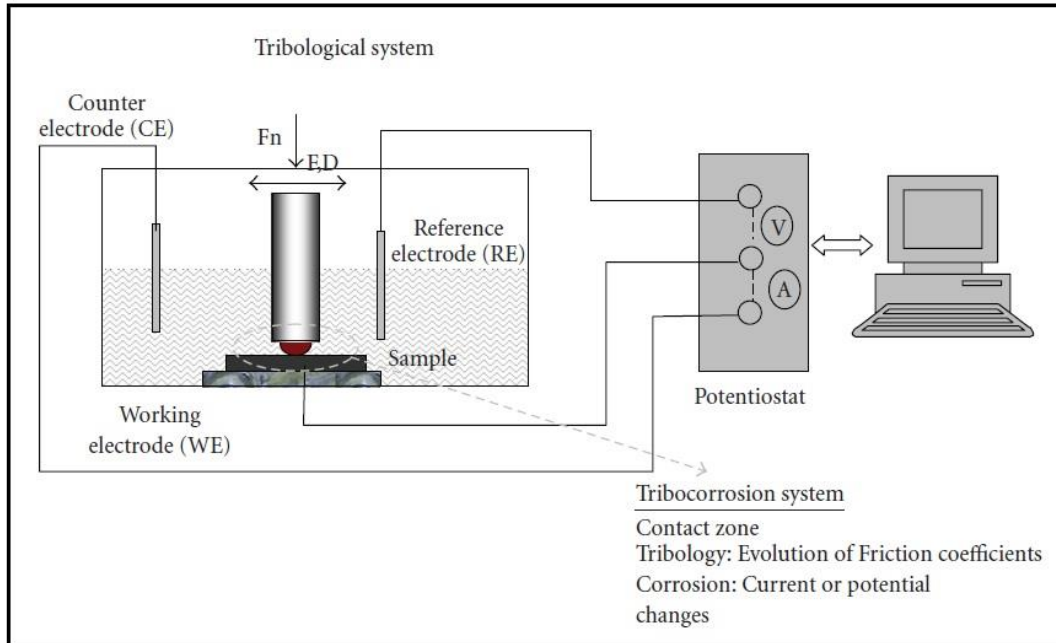


Figure 2.62: The common components of tribocorrosion experimental setups [140].

In the operation of a tribocorrosion system, the temperature is controlled and recorded, as are the main tribocorrosion parameters, the normal force (F_z), friction force (F_x) and the value of coefficient of friction (COF). The cell consists of three electrodes; a reference electrode; such as standard calomel electrode (SCE) and Ag/AgCl electrode, a counter electrode; a platinum wire, and a working electrode; testing samples as in Figure 2.62 [140,142]. Subsequently, tribocorrosion parameters, such as COF , current, and potential, can be calculated using the equations below [143-145].

$$W_C = W_0 + \Delta W_C \quad \text{Equation 13}$$

$$C_W = C_0 + \Delta C_W \quad \text{Equation 14}$$

$$T = W_C + C_W \quad \text{Equation 15}$$

or

$$T = W_0 + \Delta W_C + \Delta C_W \quad \text{Equation 16}$$

where T is the total material loss rate; mm/year, W_C and C_W are the total material loss due to mechanical wear and corrosion respectively, W_0 is the mechanical wear in absence of corrosion

calculated from wear tests at cathodic potential, C_0 is the corrosion material loss rate in the absence of wear, which is normally treated as being negligible for passive metals and alloys, ΔW_c is the change in wear rate due to corrosion; mm/year, and ΔC_w is the change in corrosion rate due to wear; mm/year.

In addition, the change in corrosion rate (ΔC_w), the wear rate in mm/year, and the specific wear rate (K) can be calculated from Equations 17-19:

$$\Delta C_w = k \frac{i_{wt}}{\rho} M \quad \text{Equation 17}$$

where i_{wt} is the flowing current from wear track during abrasion; $\mu\text{A}/\text{cm}^2$, k is a constant (3.27×10^{-3}); $\text{mm}\cdot\text{g}/\mu\text{A}\cdot\text{cm}\cdot\text{year}$, M is the equivalent weight; g/mol , and ρ is the density; g/cm^3 .

$$\text{Wear rate (mm/year)} = \frac{8760 V}{t A} \quad \text{Equation 18}$$

$$K = \frac{V}{dL} \quad \text{Equation 19}$$

where A is the surface area of the wear track, t is the test time, K is the specific wear rate; $\text{mm}^3/\text{N}\cdot\text{m}$, V is the wear volume of material loss; mm^3 , L is normal load; N , and d is the total sliding distance; m .

In addition, the identification of the dominant tribocorrosion parameter between wear and corrosion effects, is calculated from the ratio of $\Delta C_w/\Delta W_c$, following the standard ASTM G119-09, Table 2.14 [143].

Table 2.14: The criteria for considering dominant mechanism in tribocorrosion testing [143].

Condition	Dominant mechanism
$\Delta C_w/\Delta W_c < 0.1$	Corrosion effect
$0.1 \leq \Delta C_w/\Delta W_c < 1$	Both effects of corrosion and wear
$\Delta C_w/\Delta W_c \geq 1$	Wear effect

There are examples of previous work regarding the tribocorrosion properties of both conventional alloys and HEAs. Several conventional alloys have been studied for tribocorrosion performance, for example, stainless steels, Co alloys, and Ti alloys. SS 304 shows the typical effect of applied potential on total material loss (V_t) in 0.5 M NaCl solution.

High applied potential during tribocorrosion testing induces an increase in V_t as in Table 2.15. It stems from the increase of applied potential leading to weakening of passive films and easy pitting corrosion. The increase of pitting products induces a higher volume loss during wear. However, a decrease of COF is found with increasing applied potential, probably due to the lubricating effect of oxide on the sample surface. The oxide film formation during contact intervals can potentially resist the weight loss of material with mechanical wear [146].

Table 2.15: The summary of detected volume loss of SS 304 in 0.5 M NaCl solution [146].

Applied potential (mV(SCE))	Measured total volume loss V_T (mm ³)	Pure mechanical wear V_w (mm ³)	Wear-induced corrosion ΔV_c (mm ³)	Corrosion-induced wear ΔV_w (mm ³)
-550	0.01766	0.01766	0	0
OCP (-458)	0.022733	0.01766	0.0053	-0.000227
-320	0.03698	0.01766	0.0250	-0.00568
-200	0.06017	0.01766	0.0351	0.00741

In the example of Co alloys, CoCrMo is one of the most popular alloys to use for biomedical implant materials. CoCrMo alloys exist with different carbon contents, either low carbon (LC) CoCrMo alloy or high carbon (HC) CoCrMo alloy. These have both been tested and compared with SS 316L for corrosion behaviour. For the concentration of 0.36 wt.% in NaCl solution at 37°C, LC CoCrMo alloy has the lowest average coefficient of friction (COF) in all alloys at 0.65, while SS 316 and HC CoCrMo alloy have higher COF values at 0.77 (SS 316) and 0.79 (HC CoCrMo). Ion release measured by ICP shows that LC CoCrMo alloy has the lowest Cr ion release. This shows that this alloy may form a strong passive layer in this solution [147]. Furthermore, Ti6Al4V alloy is also popular to examine in artificial seawater and pure water. In order to investigate the tribocorrosion behaviour of Ti6Al4V alloy and SS 316, an experiment was carried out by using a pin-on-disk test rig under different test solutions with artificial seawater and pure water. It was found that both Ti6Al4V alloy and SS 316 have lower wear loss in seawater than in pure water. Wear weight loss due to corrosion is accelerated. It is considered that stress corrosion cracks may form due to chloride attack acting with wear processes to promote micro-crack propagation on the sample surfaces. In addition, Ti6Al4V alloy is more highly resistant to wear damage than SS 316 [148].

Tribocorrosion resistance in HEAs has recently received attention, and is appearing in published scientific papers. An example is an AlCoCrFe coating on the surface of Al substrate by the laser additive manufacturing method, which was assessed in 0.6 M NaCl solution. The effect of one of the laser processing parameters, the laser fluence, was investigated over a range of 17.0, 19.1, 21.2 J/mm². Coating with AlCoCrFe shows an increase in tribocorrosion

properties [149]. The coated sample produced with a laser fluence of 19.1 J/mm^2 can reduce the wear volume loss from 0.11 mm^3 to 0.01 mm^3 compared with pure Al substrates, as in Figure 2.63. This is suggested to be due to a high level of phase stability achieved with the correct ratio of HEA phase to intermetallic phase [150], although the fundamental benefit of the coating must also come from increased mechanical properties and chemical resistance over the pure Al substrate.

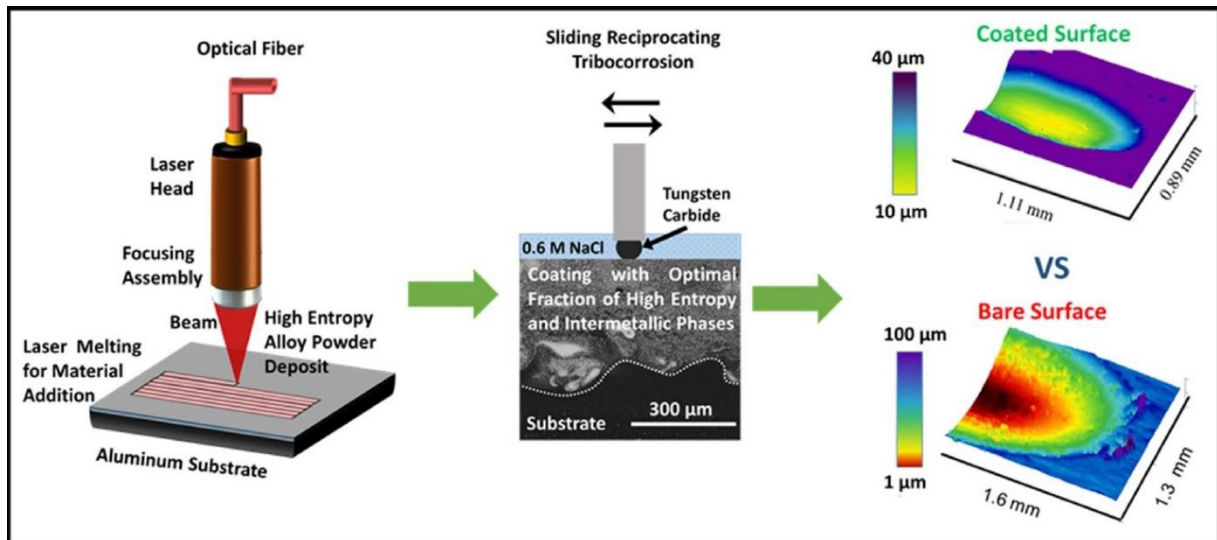


Figure 2.63: The diagram showing a comparison of tribocorrosion properties between coating with and without AlCoCrFe on the Al substrate [150].

It is also found that another HEA has good tribocorrosion properties when used as a coating. An SS 304 substrate was coated by AlFeCrNiMo and tested in artificial seawater. This coating shows a decreased COF which is lower than pure SS 304. Low friction in the HEA coating is consistent with low volume loss as observed in wear tracks in Figure 2.64. The formation of BCC phase leads to increase in tribocorrosion resistance with solid solution strengthening, including the passive film formed on the HEA surface [151].

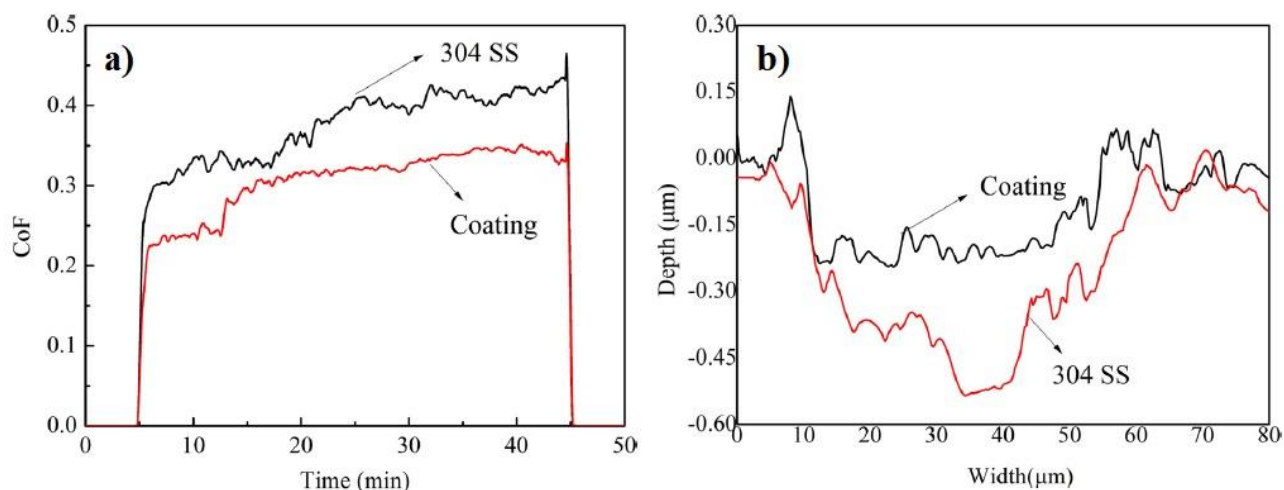


Figure 2.64: The comparison of tribocorrosion properties between coating with and without AlFeCrNiMo on the SS 304 substrate; a) *COF* vs time and b) wear volume loss [151].

In addition, VAlTiCrCu was produced as films deposited on a SS 304 substrate. Tribocorrosion properties of this coating are examined in three solutions, 0.6 M NaCl, 0.5 M H₂SO₄, and 1 M NaOH solutions, at room temperature. The HEA coating has the best tribocorrosion resistance in alkaline solution with the lowest *COF*, resulting from the formation of stable oxide film and the inhibition of pitting corrosion from SO₄²⁻ ions. In contrast, this alloy shows poor tribocorrosion properties in both chloride and acidic solutions due to the unstable oxide film leading to oxide removal during the wear process [27].

In summary, the type of materials that have here been described under the term “HEAs” are potentially attractive alloys, covering undoubtedly many alloys not yet discovered, and the full properties of many reported alloys not known. This chapter has summarised vital information on the theories, fundamental knowledge, and related research publications to design the experiments and provide the supporting evidence for the work that will be described in the results and discussion chapters. It can be concluded that;

- As reported in previous research, the alloying elements affect the alloy phase and microstructures, which in turn alter properties such as hardness, corrosion properties, and tribocorrosion resistance. As particular examples, Al, Cu, and Sn can make different such alterations to the base structure of the four component system CoCrFeNi, and are inexpensive metallic elements, applied in a wide range of industries. This makes them attractive candidates for further study.
- The formation of different phase composition in HEAs can be interpreted by several criteria, without there being a universally applied method for this. Common criteria are

parameters from thermodynamics and the Hume-Rothery Rules, which are easily applied in a wide range of different HEA systems.

- Some HEA systems which were previously studied, CoCrFeNiAl, CoCrFeNiCu, and CoCrFeNiSn will require further investigation, to cover the details of the corrosion mechanisms and also the species of oxide film formed, as this is often the critical part in determining the behaviour with regard to these corrosion and wear properties.
 - CoCrFeNiSn has less existing information than CoCrFeNiAl and CoCrFeNiCu. The one previous publication providing data regarding the microstructure and phase composition suggests its properties are interesting to explore.
 - CoCrFeNiAl and CoCrFeNiCu have been studied for properties including hardness and corrosion, but have not been explored in a range of test solutions.
- There are several methods for producing alloys like HEAs. Arc melting is indicated as an efficient method to form a homogeneous mixture sample and is easy to use to create basic sample shapes by casting.

The literature reported here is an essential knowledge basis for the experimental design and investigation of new or existing HEA systems to determine new properties. It is noteworthy that tribocorrosion properties of HEAs are currently very little explored.

CHAPTER 3

RESEARCH METHODOLOGY

3.1 An overview of the approach

This PhD project aims to explore the corrosion, tribocorrosion, and hardness properties of a series of different HEAs; the alloys under investigation have been chosen to display different types of microstructure sometimes present in these alloys, which will be described in more detail later on. As shown in Figure 3.1, the whole PhD experimental process can be divided into three experimental investigations. The work of these will be described, and then the operation of each technique will be described in detail.

In the first period, the main equiatomic system and metallic elements that could be added to this were selected from a suitable HEA system, which was anticipated to have good corrosion properties. Previous research indicates that the CoCrFeNi alloy has high corrosion resistance, and can act as the main system, while Al, Cu, and Sn are inexpensive metals, which have high passivation tendency, forming stable oxide films [152-154]. Four alloy systems are therefore addressed in this project; CoCrFeNi (as the main system), CoCrFeNiAl (adding Al), CoCrFeNiCu (adding Cu), and CoCrFeNiSn (adding Sn). All samples were produced by vacuum arc melting to melt and cast, with the density analyzed between these steps. In addition, there also are two commercial grades of stainless steel, SS304 and SS316, which were selected to be compared with HEA samples.

In the second period, HEA ingots were prepared for corrosion and other tests. Before corrosion testing, the prepared sample surfaces were analyzed by X-Ray Diffraction (XRD), Scanning Electron Microscopy (SEM), and Energy Dispersive x-ray Spectroscopy (EDS). After that, corrosion samples were made and the corrosion behaviour of the samples in NaCl, H₂SO₄, NaAlO₂ solutions was analyzed by the Potentiostat technique, before being retested with SEM, cross-sectional SEM, EDS, and X-ray Photoelectron Spectroscopy (XPS).

In the final stage, samples were prepared for hardness and tribocorrosion testing. Firstly, the phase fraction of multiphase samples and the hardness were measured. Then the best performing HEA system, with high hardness and good corrosion resistance, was selected for tribocorrosion testing under 0.6 M NaCl solution. Post-testing, samples were evaluated via SEM, EDS, and Stylus profilometry which was used for wear volume measurement.

The experimental methods are discussed in detail below, under the four categories; selection and interpretation of HEA systems, raw material and solution preparation, HEA sample preparation, and HEA properties characterization.

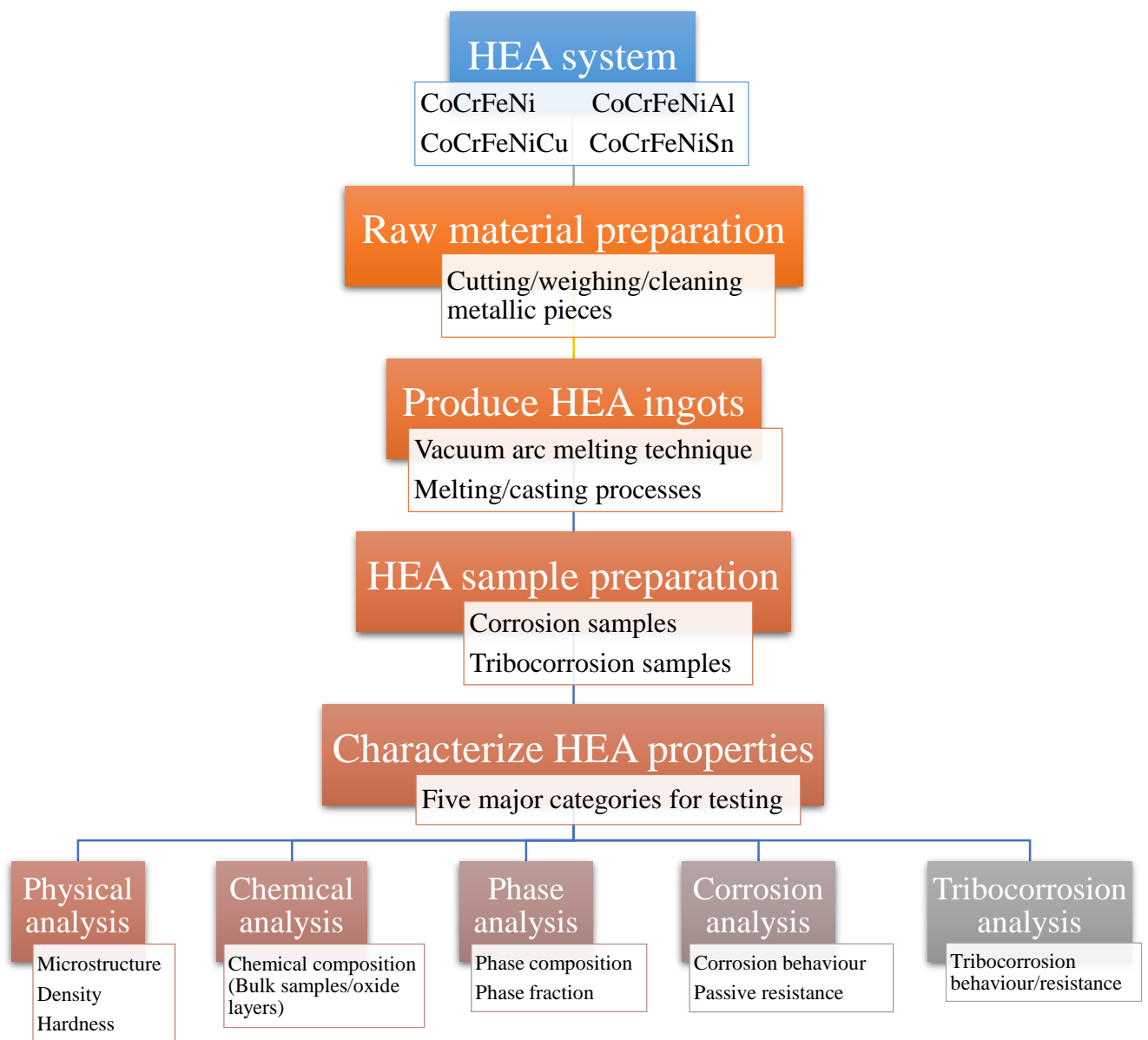


Figure 3.1: Schematic diagram of whole PhD research experimentation.

3.2 Selection and interpretation of HEA systems

From information regarding HEAs in the literature, the 4-element system, Co, Cr, Fe, and Ni, was selected as the main HEA system, stemming from having good corrosion resistance and single phase character. Three alloying elements, Al, Cu, and Sn, which are inexpensive elements and have good passive film formation, are added into the system as a dependent

variable to observe the development of HEA properties, such as corrosion behaviour, hardness, and tribocorrosion resistance. As the main HEA system was determined to be only one phase, this aim is to observe clearly the impact of alloying elements on the microstructure change, and the effect of this on the properties.

Subsequently, Table 3.1 shows the alloy specification for four alloy systems; CoCrFeNi, CoCrFeNiAl, CoCrFeNiCu, and CoCrFeNiSn alloys. These are at equiatomic ratios with 25:25:25:25 for the four elements of CoCrFeNi and 20:20:20:20:20 for the five elements of CoCrFeNiAl, CoCrFeNiCu, and CoCrFeNiSn. The equivalent weight percentage, which was used to calculate quantities by weighing in alloy production, is also given.

Table 3.1: The chemical composition of four alloy systems (compositions were selected in atomic percent ratios, and the conversion to weight percentage was calculated using the atomic masses; 26.98 (Al), 58.93 (Co), 52.00 (Cr), 63.55 (Cu), 55.85 (Fe), 58.69 (Ni), and 118.71 (Sn)).

Alloy systems	Units	Elements						
		Co	Cr	Fe	Ni	Al	Cu	Sn
CoCrFeNi	at%	25	25	25	25			
	wt%	26.14	23.06	24.77	26.03			
CoCrFeNiAl	at%	20	20	20	20	20		
	wt%	23.34	20.60	22.12	23.25	10.69		
CoCrFeNiCu	at%	20	20	20	20		20	
	wt%	20.39	17.99	19.32	20.31		21.99	
CoCrFeNiSn	at%	20	20	20	20			20
	wt%	17.12	15.11	16.23	17.05			34.49

There are five thermodynamic variables which are commonly used in reports in the literature for initial HEA system design. These consist of the enthalpy of mixing (ΔH_m), the entropy of mixing (ΔS_m), the atomic size difference (δ), the electronegativity difference ($\Delta\chi$), and the valence electron concentration (VEC). Here these are used not for alloy design, but as a means to interpret and rationalise the phase composition observed in the alloys explored. The parameters can be calculated by Equations 1 and 4-7. δ , $\Delta\chi$, and the VEC are three indicators, featuring in the Hume-Rothery rules for binary solution formation, which identify solid solubility by looking for similarity in the crystal structure, valence electrons, atomic size difference, and electronegativity. ΔH_m and ΔS_m are two further thermodynamic parameters

which have gained particular attention for the explanation of phase formation in HEA systems. These were discussed in the literature review, and the relevant parameters for the alloys of interest here were calculated and are summarised in Tables 3.2-3.4.

Table 3.2: The fundamental variables to calculate the five thermodynamic variables for HEA systems [30,155,156].

Metallic elements	Atomic radius (Å)	Electronegativity	Valence electron concentration
Co	1.25	1.88	9
Cr	1.25	1.66	6
Fe	1.24	1.83	8
Ni	1.25	1.91	10
Al	1.43	1.61	3
Cu	1.28	1.90	11
B7Sn	1.41	1.96	4

Table 3.3: The values of mixing enthalpy of different atomic couples (kJ/mol) for HEA systems [155].

Metallic Elements	Co	Cr	Fe	Ni	Al	Cu	Sn
Co	0	-4	-1	0	-19	6	0
Cr		0	-1	-7	-10	12	10
Fe			0	-2	-11	13	11
Ni				0	-22	4	-4
Al					0	-	-
Cu						0	-
Sn							0

Table 3.4: The calculation of five thermodynamic variables for the interpretation of HEA systems.

HEA systems	ΔH_m (kJ/mol)	ΔS_m (J/K mol)	δ (%)	$\Delta\chi$ (%)	VEC
CoCrFeNi	-3.75	11.53	0.35	9.67	8.25
CoCrFeNiAl	-12.32	13.38	5.69	12.06	7.20
CoCrFeNiCu	3.20	13.38	1.08	9.22	8.80
CoCrFeNiSn	0.32	13.38	5.69	10.30	7.40

3.3 Raw material and solution preparation

3.3.1 Raw material preparation

Table 3.5: The fundamental data of raw materials and conventional alloys.

Metals	Metal types	Commercial forms	Manufacturing companies	Purity (%)
Co	Element	Cobalt foil	Alfa Aesar, UK	99.95
Cr	Element	Chromium cube	Alfa Aesar, UK	99.95
Fe	Element	Iron slug	Alfa Aesar, UK	99.95
Ni	Element	Nickel foil	Advent Research Materials, UK	99.95
Al	Element	Aluminum rod	Goodfellow, UK	99.95
Cu	Element	Copper foil	Alfa Aesar, UK	99.95
Sn	Element	Tin foil	Advent Research Materials, UK	99.95
SS304	Alloy	SS304 rod	Advent Research Materials, UK	-
SS316	Alloy	SS316 rod	Advent Research Materials, UK	-

For the selection of HEA systems, seven metallic elements were required for producing the samples, and two conventional alloys were needed for comparison in the corrosion experiment. Raw materials were composed of Al, Co, Cr, Cu, Fe, Ni, and Sn at 99.95% purity or better, as shown in Table 3.5. All metallic elements were prepared for 8 g of the total weight of HEA compositions, by cutting, grinding by grit paper, weighing, and ultrasonic cleaning

with isopropanol solution for 10 min. Furthermore, two conventional pre-alloyed samples of stainless steel grade 304 and 316 (SS304 and SS316), shown in Table 3.5 were prepared by the same steps for use as a comparison in corrosion testing.

3.3.2 Solution preparation

Table 3.6: The fundamental data of chemicals used in the electrochemical experiments.

Chemicals	Chemical formula	Commercial forms	Manufacturing companies	Concentration
Sodium aluminate	NaAlO ₂	Powder	Sigma-Aldrich, UK	Technical grade
Sodium chloride	NaCl	Powder	Ajax Finechem, Australia	99.5% (Purity)
Sulfuric acid	H ₂ SO ₄	Solution	Ajax Finechem, Australia	98%

In this work, three types of solution were prepared for the corrosion experiment and one solution for tribocorrosion testing. As presented in Table 3.6, three chemicals were obtained for the electrochemical experiments. Firstly, 0.6 M NaCl solution was prepared for both corrosion and tribocorrosion experiments. Sodium chloride powder, which was a solute, was weighed to 7.02 g and poured into a volumetric flask. Deionized water was poured to obtain 200 ml of solution. Then this solution was stirred by a magnetic stirrer until fully dissolved. Secondly, 0.6 M H₂SO₄ solution was prepared from the initial solution of 2.5 M sulfuric acid. 48 ml of initial sulfuric solution was diluted by mixing with deionized water to a final solution volume of 200 ml. Lastly, 0.6 M NaAlO₂ solution was prepared in the same way as the chloride solution, but with a different weight of solute. 9.84 g of sodium aluminate was dissolved in deionized water to make 200 ml of solution. In addition, the pH values of all solutions were measured using a Bench pH Meter (STARTER 3000, OHAUS, USA) after the preparation step.

3.4 Vacuum arc melting

Arc melting was used to create samples (MAM1 arc melter, Edmund Buehler, Germany), in Figure 3.2. There are four main systems in the melter; the heating system to melt or cast metals, the vacuum system to achieve low pressure and feed argon gas, the water cooling system to cool down after the heating process, and the suction system which is an extra part

required for the casting process. This technique can be divided into two steps; melting and casting, and this affects the type of hearths used.

In the melting process, all components to be placed inside the chamber and melting hearth were cleaned by isopropanol and vacuumed to remove any contaminants on the equipment surface. Vacuum cleaning was a suitable way to eliminate small metal fragments and other particles which cannot be cleaned completely by wiping with isopropanol. After cleaning, weighed out pieces of the required metallic elements were placed on the copper melting hearth with the lowest melting point element placed first, and the highest melting point element on the top. A Ti getter was used to trap further contaminants (especially oxygen) during melting, and was placed in the central hole of hearth; this would be melted first in the alloying operation. The cooling system and vacuum system were connected to the melter. The vacuum chamber was prepared by evacuating air three times, each followed by feeding argon to 3×10^3 Pa pressure, then the pressure was reduced from approximately 20 Pa (1.5×10^{-1} torr) to below approximately 8×10^{-3} Pa (6.0×10^{-5} torr), and the cooling water system turned on, while increasing argon pressure to 7×10^3 Pa. Subsequently, the Ti getter was melted to eliminate residual oxygen gas inside the vacuum chamber and the contents of each hole in the hearth were rapidly melted. All metallic elements were combined together in this process, flipped and re-melted five times to improve homogeneity. Finally, the ingot was cooled down for 5 min, removed from the chamber, cleaned with isopropanol in an ultrasonic bath and weighed.

For the casting process, the alloyed ingot was placed on the central hearth which contained a cylindrical copper mould of 0.6 cm of diameter. This hearth was connected with a casting tube to the suction system. However, due to good flowability of the alloys, the application of a partial pressure environment was not required to cause the mould to be filled, and all steps of the casting process were the same as the melting process.

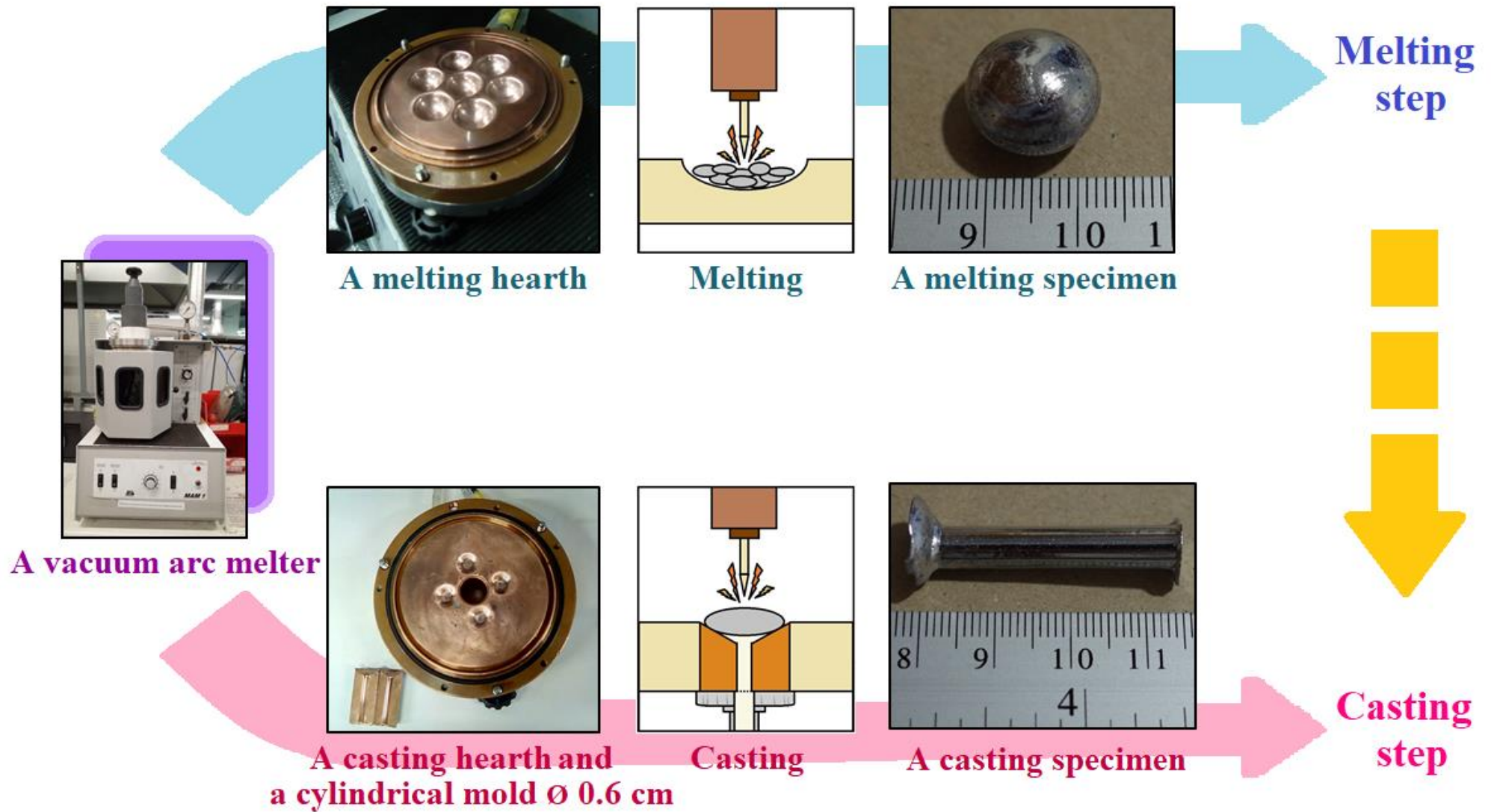


Figure 3.2: Schematic diagram of the sample fabrication by vacuum arc melting technique.

3.5 HEA sample preparation

3.5.1 Corrosion samples

All corrosion samples were prepared according to Figure 3.3. The specimens were cut as cylinders 0.6 cm in diameter \times 1 cm height. The sample surface was prepared by grinding from a low number of grit paper down to a high number of grit paper; P280, P400, P800, P1200, and P2500, then polishing with 1 μ m diamond suspension. After ultrasonic cleaning with isopropanol, corrosion specimens were electrically connected by a copper wire inserted in a glass tube and later cold mounted by epoxy resin (Struers Ltd., Canada) in cubic silicone moulds 2 cm width \times 2 cm length \times 2 cm height [157]. The exposed area of 0.28 cm² was the location of any interaction between the sample surface and the electrolyte.

3.5.2 Tribocorrosion samples

Figure 3.4 shows the process of tribocorrosion sample preparation. Cylindrical HEA samples were cut to approximately 1 cm height and mounted with epoxy resin (Struers Ltd., Canada) in cylindrical silicone moulds of 4 cm diameter. Subsequently, the upper and lower sample surfaces were ground with grit papers, P280, P400, P800, P1200, P2500 and P4000 respectively, and finely polished by using 1 μ m grain-size diamond suspension to produce a final specimen height of 0.6 cm. Before the last step for ultrasonic cleaning with isopropanol, the epoxy mount of the samples was reshaped by re-grinding from cylinders to cuboids of 2 cm width \times 2 cm length. The exposed area of the sample to the solution was 0.28 cm² in each case. These samples were also reused for tribocorrosion, by re-grinding and polishing, to reduce the sample size down to 3 mm in height. This was required so that they would be the right size to place in the tribocorrosion cell.

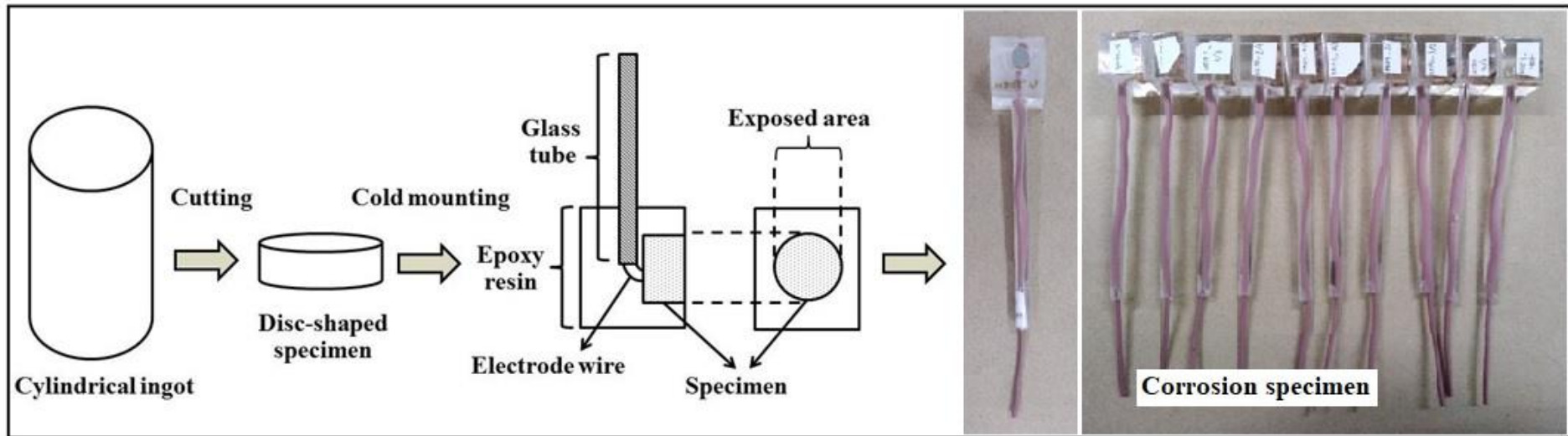


Figure 3.3: The process of corrosion sample preparation and the final samples used.

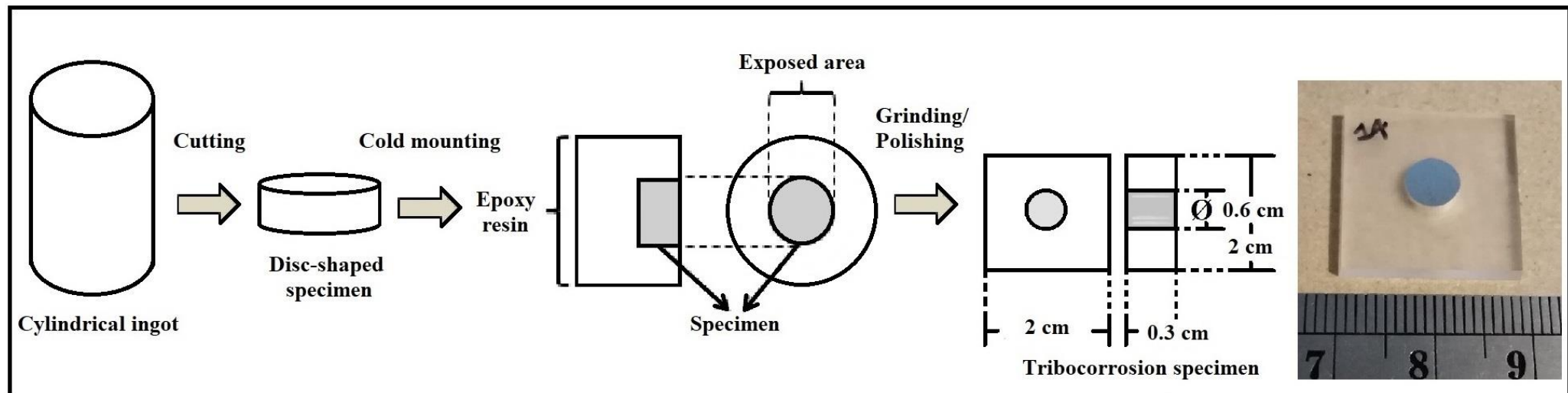


Figure 3.4: The process of tribocorrosion sample preparation and the final samples used.

3.6 Property characterization

3.6.1 Physical analysis

3.6.1.1 Microstructure analysis by SEM

The sample microstructure was monitored using SEM (Inspect F50, FEI, USA) in both secondary electron (SE) and backscattered electron (BSE) modes. Before SEM analysis, all samples in the as-cast and prepared for testing conditions were cleaned by isopropanol in an ultrasonic bath for 10 min and dried in air. The parameters shown in Table 3.7 were used. The choice of different values of accelerating electron voltage depended on the analytical mode used in SEM. The SE mode was applied to analyze topography with a surface signal. The analysis of atomic number and topographical information showing phase differences was carried out by the BSE mode with a bulk signal. For this reason, the BSE mode needed higher energy electrons than the SE mode, and was thus set with a higher value of accelerating electron voltage than the SE mode.

Table 3.7: The set parameters for SEM analysis.

SEM modes	Accelerating electron voltage (kV)	Spot size	Working distance (mm)
SE	5	3.5-4.0	9.5-10.8
BSE	20	3.5-4.0	9.5-10.8

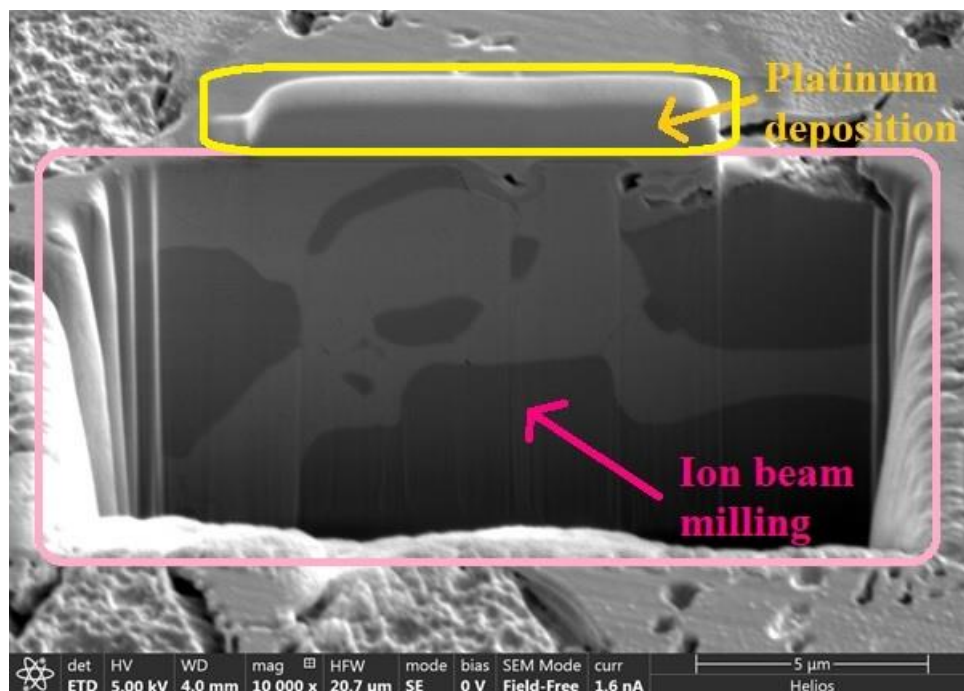


Figure 3.5: A cross-sectional SEM image of CoCrFeNiSn prepared using the FIB-SEM technique.

In addition, samples were also analyzed to determine the cross-sectional microstructure following the formation of a section by Focused Ion Beam milling (FIB; Helios NanoLab G3 UC, FEI, USA), as shown in Figure 3.5. This technique permits site-specific imaging of the sub-surface morphology in samples, by removing material allowing a plane at right angles to the polished surface to be examined. It can provide vital information relevant to corrosion, such as the direction of corrosion in relation to the microstructure, the corrosion depth, and information useful in determining the corrosion mechanism. This work was carried out by Dr Le Ma, Dept. Materials Science & Engineering, the University of Sheffield, UK. Initially, the sample surface was prepared by sputtering (Q150T ES, Quorum, UK) a gold coating of 10 nm thickness. In the chamber, corrosion-related features were identified for further exploration, and platinum was deposited where milling was not wanted on the sample surface. To perform milling, Ga⁺ ions with beam current of 0.8 nA-1.6 nA were used. HEA samples were fixed on a stage and tilted to an angle of 52 degrees between ion beam and plane surface of the samples. Finally, the cross-sectional microstructure made visible by the milling process was imaged by SEM.

3.6.1.2 Density balance

As-melted samples were cleaned by an ultrasonic bath with isopropanol and dried in air, and the density was measured using density balance equipment (MS104S/01 NewClassic MF, Mettler Toledo, Switzerland). The density was assessed at room temperature using Archimedes' principle. Each alloy was assessed three times with different samples. Density was calculated as the equation below [158];

$$\rho_{sample} = \frac{A}{A-B} (\rho_{liquid} - \rho_{air}) + \rho_{air} \quad \text{Equation 20}$$

where ρ_{sample} is the density of the sample; g/cm³, ρ_{liquid} is the density of the liquid used which was water; g/cm³, ρ_{air} is the density of air; 0.0012 g/cm³, A is the sample's weight in air; g, and B is the sample's weight in liquid; g.

3.6.1.3 Micro-indentation

As-cast samples were cold mounted with epoxy resin (Struers Ltd., Canada) and surface prepared by grinding with grit papers from P280 up to P2500 and polishing by using 1 μm diamond suspension. The surfaces were cleaned by isopropanol in an ultrasonic bath for 10 min and dried in air. They were hardness tested by using a Vickers micro-indentation hardness indenter (DuraScan 70, emco-TEST, Struers, Austria). Indents were performed under HV0.5

(500 gf) for dwell time of 15 s in the series measurement testing mode. Each sample was measured by at least 10 indents.

3.6.1.4 Nano-indentation

As-cast CoCrFeNiSn samples contained two phases; FCC-CoCrFeNi and hexagonal-NixSny phases. The hardness of the CoCrFeNiSn sample was measured over small volumes by Nano-indentation (Hysitron, TI Premier, USA), in order to analyze the hardness of each phase separately. Samples not exceeding 10 mm height were prepared during the same step as the micro-indentation testing with the cold mounting method, and followed the same protocols. The resulting sample was stuck to an aluminum sample stub with adhesive and laid on a sample holder platform inside a chamber. A Berkovich pyramid diamond indenter was placed in contact with the sample surface and loaded, with the depth of penetration sensed carefully, and used to deduce the contact area at a given load and thus measure the local hardness. Before testing, the calibration of the area profile of the indenter tip was performed with different loads on fused quartz (as a standard material with well-defined characteristics), fitting an area function to produce the correct hardness value across the different loads, and therefore depths. A polycarbonate sample was used for calibration of the X-Y sample platform and the optical resolution, to ensure indents were placed in the regions identified by the in-built optical microscope. Single-indent mode was selected to test the local hardness of different phases, by positioning the indents well within the visible regions of each phase. Ten indents in total were recorded for each phase, with a load of 2,000 μN applied for a dwell time of 10 sec./indent. The collected data are fitted with a function by the Hysitron software, which calculates the hardness and Young's modulus values.

3.6.2 Chemical analysis

3.6.2.1 EDS-SEM

The chemical composition of samples was analysed by using SEM (Inspect F50, FEI, USA) combined with an EDS detector (Oxford Instruments, UK). Samples were monitored in BSE mode and linked to EDS system under the operation of AZtec software for chemical analysis. A beam spot size of 1 μm and an accelerating electron voltage of 20 kV were used, for both point and area measurements. The point mode gave a quantitative assessment of the relative amounts of different elements, whereas the area measurements were carried out in a mapping mode, producing images for each element of interest showing its distribution.

3.6.2.2 Oxide and chemical composition investigation by XPS

XPS (PHI5000 Versa Probe II, Ulvac-PHI, Japan) was used for the chemical analysis of any oxide film on the sample surfaces in each system after the corrosion properties were tested. This work was supported by Dr Narong Chanlek, a beamline scientist at the Synchrotron Light Research Institute, Thailand. Before the operation, the sample surface was cleaned using Ar sputtering, controlled not to exceed 10 nm in depth for removing any contamination present, such as a carbon layer or dust on the sample surface [159]. An X-ray beam size of 100 μm diameter was set on the analysis area. The XPS data were analyzed following procedures specified in the ULVAC PHI PHI5000 VersaProbe manual [160] and the database for fitting curves was taken from the Handbook of X-ray Photoelectron Spectroscopy [161]. In addition, the relative atomic concentration of each element at the surface was analyzed by this technique, calculated as below [136,162].

$$X_i = 100 \frac{A_i}{\sum_{i=1}^n A_i} \quad \text{Equation 21}$$

$$A_i = \frac{J_i}{S_i K} \quad \text{Equation 22}$$

where X_i is the atomic percent of each element, A_i is the adjusted elemental intensities, J_i is the measured intensity of each elemental composition, K is the kinetic energy, S_i is the relative sensitivity which is determined from the XPS measurement, i is each element, and n is the amount of elements.

3.6.3 Phase analysis

3.6.3.1 XRD

The phase composition of HEAs was characterized via XRD (D2 PHASER, Bruker, USA). The X-ray source used was Cu-K α 1 with the wavelength of 1.54060 \AA . As-cast samples were first prepared by grinding with grit papers from P280 up to P2500 and polishing with 1 μm diamond suspension. The surfaces were cleaned by isopropanol in an ultrasonic bath for 10 min and dried in air. Samples were placed on the sample holder and set into the XRD chamber, then scanned over a range of 2θ angles from 20° to 100° at a scan rate of $2^\circ/\text{min}$ and a step size of $0.02^\circ/\text{step}$. Subsequently, the XRD data was exported, as a RAW V4 text *.txt file to analyzed by EVA software in the ICDD PDF-4+ database.

Furthermore, additional data (phase fraction, space group, and lattice parameter) of the diffraction pattern peaks attributed to the Ni-Sn and FCC phases in the CoCrFeNiSn system were determined by the Rietveld refinement method. This analysis was carried out on the XRD peaks via GSAS software combined with the EXPGUI interface. This analysis was conducted by Dr Zhao Y Leong, Dept. Materials Science & Engineering, the University of Sheffield, UK.

3.6.3.2 Image analysis by ImageJ software

BSE images which were recorded by SEM were analysed to determine the phase fraction in each system by using ImageJ software over a number of images. This is a public domain image processing program based on Java, which can be downloaded from <https://fiji.sc/>. Initially, images of size approximately $100\ \mu\text{m} \times 86\ \mu\text{m}$ were recorded at a resolution of 1023×884 pixels. Images were set a scale according to the true scale bar. The brightness and contrast of images were adjusted with the Fast Fourier Transform (FFT) and Threshold functions in the software, and then the phase fraction was measured using the Analyze Particles algorithm. This average value was calculated from five randomly-positioned images, recorded for each HEA system under investigation.

3.6.4 Corrosion analysis

The corrosion testing in this work was divided into two parts; the first was performed during a research visit at the Department of Materials Engineering, Faculty of Engineering, Kasetsart University, Thailand, and the second was carried out at Department of Materials Science and Engineering, Faculty of Engineering, the University of Sheffield, UK.

In the first part, the corrosion behaviour of samples was studied by electrochemical analysis (PGSTAT302N Autolab, Metrohm Autolab, the Netherlands). All of the HEA samples and the conventional alloys used for comparison were analysed by the Linear polarization curve technique with three electrolytes, NaCl solution, H₂SO₄ solution, and NaAlO₂ solution, all of 0.6 M concentration. Testing was carried out at room temperature and each alloy was tested at least three times [136]. Three electrode cells were used for the corrosion study. The working (WE), counter (CE) and reference electrodes (RE) were the prepared specimen, a platinum electrode, and Ag/AgCl reference electrode, respectively. The Open Circuit Potential (OCP) was set up for operation for 30 min before the next step. The scan rate used for the linear polarization was 1 mV/s [43] and the potential was scanned from -0.9 V to +1.3 V with respect to the OCP obtaining a stable value [163]. The range of applied potential for corrosion testing

in this work was adapted and modified from [164,165], where it was used to study CoCrFeNi and CoCrFeNiAl in 0.6 M NaCl solution. This potential range for corrosion testing was used for all samples examined here; CoCrFeNi-based alloy, three HEA systems, and two grades of stainless steel. The corrosion parameters were analyzed after data collection by Nova 1.11.2 software according to the method detailed in Appendix A. As shown in Figure 3.6, the systematic approach was used to obtain precise value for the Tafel slopes (b_a and b_c) by using several data points at around ± 100 mV away from the value of E_{corr} . In addition, Electrochemical Impedance Spectroscopy (EIS) was employed to investigate the status of the oxide layer and the polarization resistance (R_p) of the sample surfaces. HEA samples were tested with three electrolytes using the same Linear polarization curve technique. The frequency was scanned from 100 kHz to 0.01 Hz with a perturbation amplitude of 10 mV and then EIS data were analyzed by Nova 1.11.2 software.

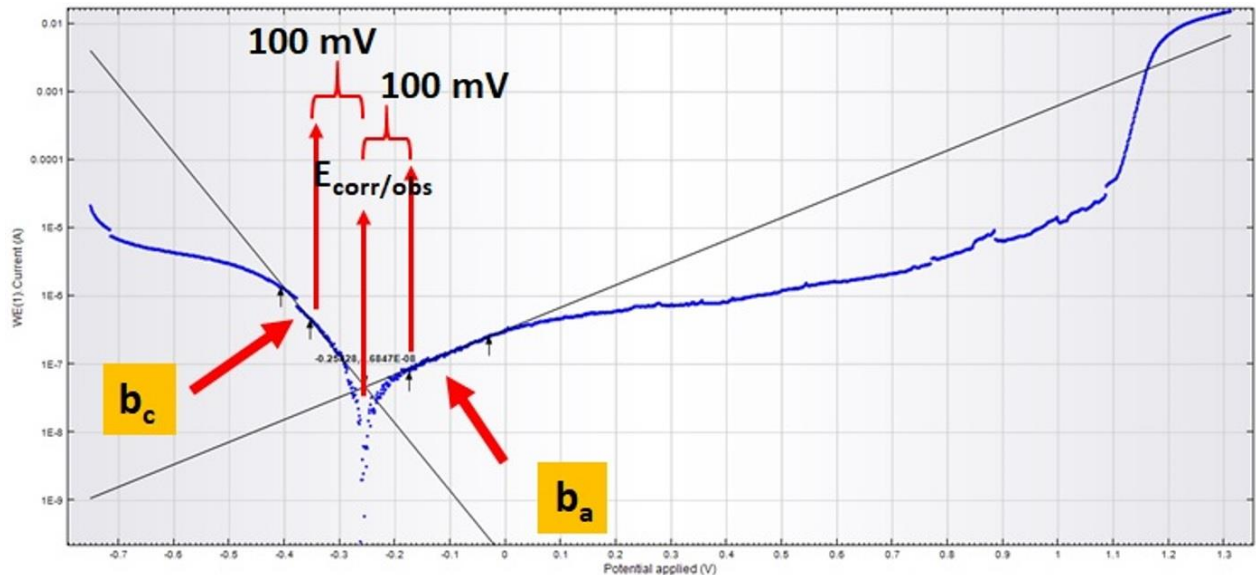


Figure 3.6: The approach used to determine the Tafel slopes.

In the second part, CoCrFeNi and CoCrFeNiSn alloys were analyzed for corrosion resistance in freshly prepared 0.6 M NaCl solution by using a VersaSTAT 3F Potentiostat Galvanostat (Princeton Applied Research, USA) to control the potential for corrosion testing. The corrosion cell included three electrodes; a Saturated Calomel Electrode (SCE) as a reference electrode, a platinum wire as a counter electrode, and the sample being tested as a working electrode. The volume of solution in the cell container was approximately 100 mL. The Potentiodynamic curves, which were repeated twice, were measured from -0.25 V to 1.3 V with respect to the OCP at a scan rate of 0.5 mV/s. This potential range for corrosion testing was used for the two HEA systems which were examined using this method; CoCrFeNi and

CoCrFeNiSn. Corrosion parameters were calculated by using CView software. Meanwhile, Electrical Impedance Spectroscopy (EIS) was used to evaluate the electrical resistance at the interface between an exposed metal surface and solution over the range of low to high frequency values. These EIS results can determine the polarization resistance in the low-frequency range, solution resistance in the high-frequency range, and the capacitance of the double layer. These are essential parameters to identify the tribocorrosion mechanism between passive layers on the contact surface and oxide-film properties formed on the interface. Polarization resistance can be referred to as a polarizing electrode. When a specimen (electrode) is polarized, it can lead to the flow of current through electrochemical reactions occurring on the specimen surface. It corresponds with the protective ability of oxide films in alloys. High polarization resistance can cause superior corrosion resistance, while poor corrosion resistance stems from inferior polarization resistance in alloys [166]. Solution resistance (electrolyte resistance) is an essential factor in the EIS technique. It occurs when voltage is passed from the working electrode to the reference electrode in the electrolyte solution. Ions in the solution perform as resistors to impede electron flow. The resulting voltage is recorded by the reference electrode. This electrode is used to measure the solution resistance with a comparison of the input and output voltages. However, solution resistance can be calculated by fitting experimental EIS data to an equivalent circuit [166]. Double layer capacitance can be defined as the polarization of ionic charge at the specimen surface in the EIS system. It is formed as ions from the solution adsorb onto the specimen surface, occurring at the interface between the specimen and its surrounding electrolyte solution. An insulating space acts to separate the charged electrode from the charged ions on the order of angstroms. A capacitor can be formed by charges being separated. Because of this, an uncovered metal immersed in an electrolyte solution will act like a capacitor [166]. The corrosion rate was then calculated from the value of polarization resistance as Equations 10 and 11. All samples were tested with the same solution at room temperature. The frequency range was 100 kHz to 15 mHz with a perturbation amplitude of 10 mV at 10 points per frequency decade. The ZView software was used to model the data with an appropriate equivalent circuit. The equivalent circuit model in this work is properly selected using an analysis of passive metallic materials, as discussed in section 4.5.2.

According to the ASTM G102-89 standard [104], the vital corrosion parameters of HEAs were calculated as Equations 9-11.

3.6.5 Tribocorrosion analysis

The tribocorrosion experiment was assisted by Dr Righdan Mohsen Namus, Department of Materials Science and Engineering, Faculty of Engineering, the University of Sheffield, UK. HEA samples were analyzed for tribocorrosion properties in freshly prepared 0.6 M NaCl solution, using a tribocorrosion cell in a TriboLab multifunctional wear test equipment (Bruker, USA). This controls the temperature and records the main tribocorrosion parameters, the normal force (F_z), friction force (F_x) and the value of coefficient of friction (COF). The cell consisted of three electrodes; a SCE as a reference electrode, a platinum wire as a counter electrode, and the HEA sample as a working electrode. The volume of the cell was approximately 100 mL for containing testing solution.

Reciprocating sliding wear tests were carried out using a ball on plate configuration, which conformed to ASTM G133. The counterpart was an alumina ball with 4 mm diameter and 99% purity (Oakwase Ltd., UK), loaded at 0.5 N. Tribocorrosion tests were carried out at room temperature with 5 Hz sliding speed and 2 mm stroke length, giving 20 mm/s linear sliding speed. The testing time was 3 h, to give in total 108,000 strokes and 216 m sliding distance. Tests further used either -0.9 V cathodic potential or OCP. In both conditions, 30 minutes was allowed in the solution under the test conditions before wear began, a time which was found to be sufficient to allow the OCP to stabilize. All tests were repeated twice and showed high reproducibility.

After tribocorrosion testing, the wear volume of the sample surface was determined by using Stylus profilometry (Dektak 150, Veeco, USA). A series of cross section profiles along the wear track were taken and the cross section area was measured. The volume of the wear track (V_{total}) was then calculated by multiplying the average cross section area by the stroke length. Other tribocorrosion parameters were calculated using the standard formula as Equations 13-19 [143,144].

The driving force for this material loss is the galvanic couple that forms between the depassivated surface (wear track) and the still passivated one (the rest of the surface). Espallargas et al. [167] suggested a new experimental setup to calculate this effect using a zero-resistance ammeter (ZRA), though here we have used the galvanic coupling model suggested by Vieira et al. [168], which has been applied to different materials by Papageorgiou and Mischler [169], to calculate the current flowing from the wear track ($i_{\omega t}$) as the following:

$$\log i_{\omega t} = \frac{(E_{corr} - E_{\omega t} + a_c - b_c \log(\frac{A_{wt}}{A_p}))}{b_c} \quad \text{Equation 23}$$

where: $E_{\omega t}$ is sliding potential, a_c and b_c are Tafel constants calculated from the cathodic branch of the potentiodynamic curve [170]. A_{wt} and A_p are the surface area of the wear track and the passive surface respectively.

CHAPTER 4

Results and Discussion

4.1 Results: characterization of as-cast CoCrFeNi and HEA samples

4.1.1 Phase composition analysis

To understand the phase composition, XRD analysis was conducted, Figure 4.1.

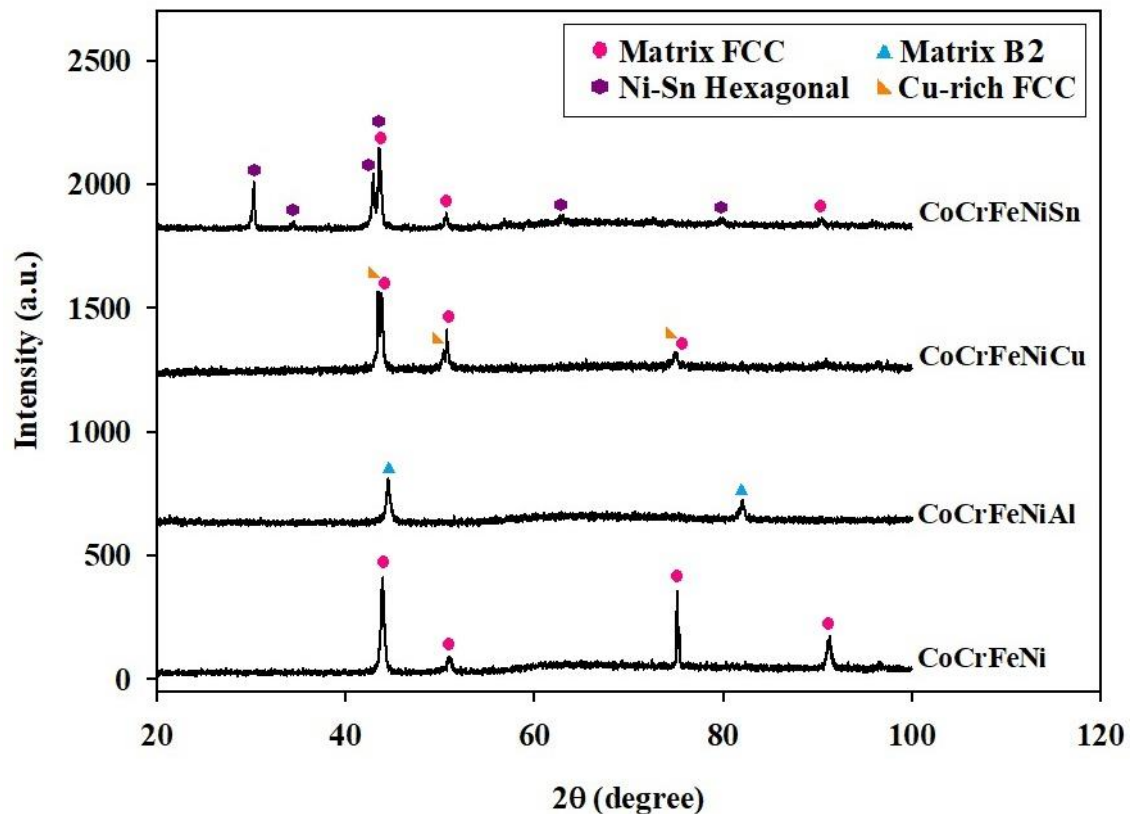


Figure 4.1: The XRD patterns of the four as-cast samples examined.

As shown in Figure 4.1, the analysis of the XRD results indicates that the CoCrFeNi alloy consists of a single solid solution FCC phase, with, as expected, peaks consistent with $\text{Cr}_{0.25}\text{Fe}_{0.25}\text{Co}_{0.25}\text{Ni}_{0.25}$ (ICDD card number: 04-018-7506). The addition of a fifth alloying element either leads to the evolution of a second phase or unresolved nano-precipitates, resulting in a multiphase structure where the phases have different crystal structures. In the first HEA system, the Al addition transforms the crystallographic phase structure from FCC to BCC (ICDD card number: 04-018-5047). CoCrFeNiAl can form the B2-ordered BCC phase as the major phase in this alloy. Another phase that could be present is the Al-Ni-rich (BCC) phase as a minor phase, possibly an intermetallic compound present as fine particles [42,171]. These

nano-precipitates with Al and Ni richness can be detected in the dendritic segregation region [42]. The XRD technique does not detect this phase, which could be due to the low volume fraction and fine nanoparticles. Most probably, particles only a few nanometers in size may make it difficult to resolve from the Cu-K α radiation wavelength via XRD analysis. However, EDS analysis at high resolution can show a structure consistent with an Al-Ni-rich phase present after corrosion testing in 0.6 M NaCl solution (section 4.3.2). For the second and third HEA systems, Cu and Sn additions lead to the formation of a two phase structure; CoCrFeNiCu shows segregation of elemental Cu (ICDD card number: 04-009-2090) from the major FCC phase present in CoCrFeNi, and CoCrFeNiSn retains the FCC structure of CoCrFeNi and introduces a secondary hexagonal phase with similar XRD peak positions to Ni_{1.5-1.63}Sn (ICDD card number: 04-017-6375 and 04-016-8768).

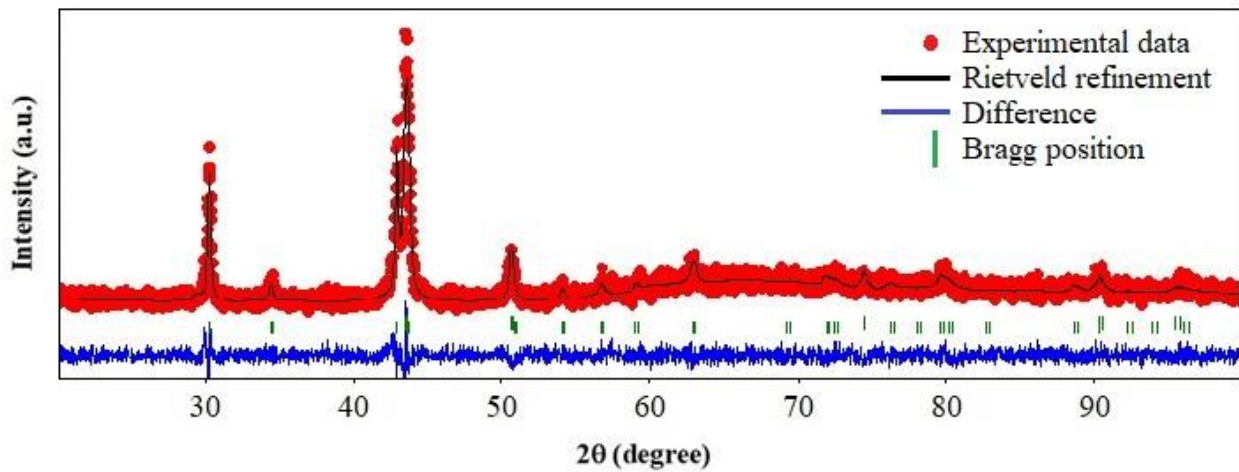


Figure 4.2: Rietveld refinement of as-cast CoCrFeNiSn sample.

Table 4.1: Refined structural parameters of as-cast CoCrFeNiSn sample.

Phase	Space group	Crystal structure	Lattice parameter (Å)	Phase fraction (%)
FCC	$Fm\bar{3}m$ (No.225)	Cubic	3.602	38
NiSn	$P6_3/mmc$ (No.194)	Hexagonal	4.142 (a,b) 5.205 (c)	62

In addition, Rietveld refinement analysis of the pattern from CoCrFeNiSn, Figure 4.2, is consistent with it being composed of two phases, as shown in Table 4.1. A major phase, 62% of the phase fraction, is a hexagonally structured Ni-Sn rich phase with $P6_3/mmc$ space group. A minor phase, 38% of the phase fraction, is a cubic (FCC) structure with $Fm\bar{3}m$ space group.

4.1.2 Microstructure and chemical composition observation

To understand the microstructure and chemical composition, SEM and EDS were conducted (Figures 4.3–4.5 and Tables 4.2–4.3).

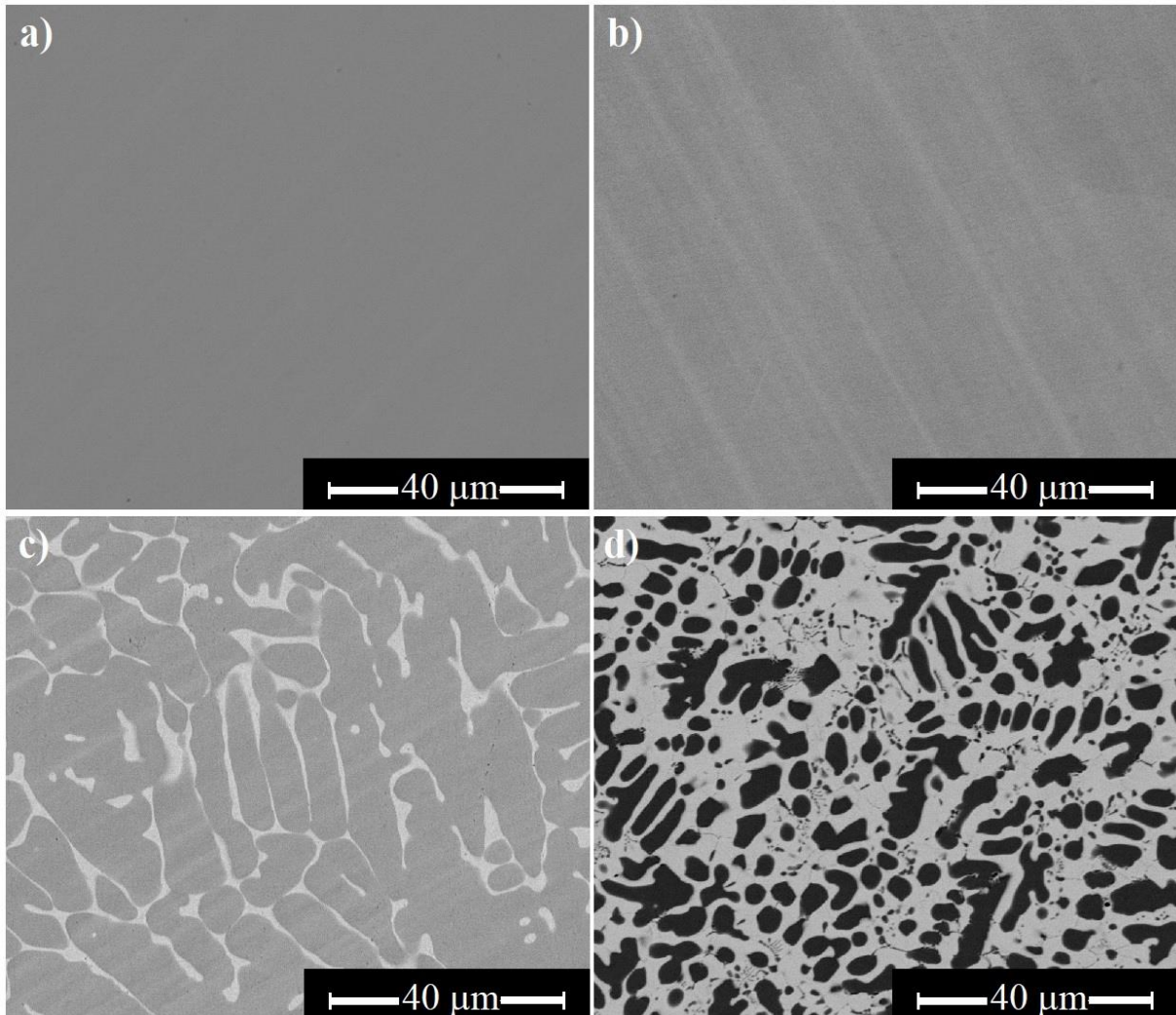


Figure 4.3: BSE-SEM micrographs of as-cast samples; (a) CoCrFeNi, (b) CoCrFeNiAl, (c) CoCrFeNiCu, and (d) CoCrFeNiSn alloys.

BSE-SEM images showing the microstructures of all as-cast samples are given in Figure 4.3. As-cast CoCrFeNi and CoCrFeNiAl samples, Figures 4.3a and 4.3b, do not show any secondary phase. Both microstructures at the scale observed are homogeneous and uniform throughout the observed section. However, while no other phases are found in CoCrFeNi, an Al-Ni rich phase (possibly an intermetallic compound), is found by EDS at high resolution in the CoCrFeNiAl system. This observation is described in section 4.3.2. This suggests that CoCrFeNiAl has a secondary Al-Ni phase as well as the ordered B2 phase. Figure 4.3c presents the dendritic as-cast microstructure of the CoCrFeNiCu alloy. The dendritic structure forms as

a matrix phase, and Cu segregation is found in the interdendritic regions. Lastly, the Sn addition, Figure 4.3d, forming CoCrFeNiSn can transform the microstructure from a solid solution phase to a dendritic CoCrFe-rich phase and an interdendritic Ni-Sn-rich phase. The interdendritic Ni-Sn region in the CoCrFeNiSn alloy is larger in scale than the interdendritic Cu-rich region in the CoCrFeNiCu alloy. In addition, the elemental location in each alloy is confirmed by the EDS analysis below.

Table 4.2: The quantitative chemical composition (at.%) of as-cast samples as analyzed through the EDS technique from a previously published work [172].

HEAs	Co	Cr	Fe	Ni	Al	Cu	Sn
CoCrFeNi	25.5	25.1	25.2	24.2	-	-	-
CoCrFeNiAl	20.7	20.5	20.5	19.9	18.4	-	-
CoCrFeNiCu	19.9	20.6	19.9	19.8	-	19.8	-
CoCrFeNiSn	20.7	18.7	20.3	19.8	-	-	20.4

The chemical compositions of the as-cast samples used in this work were determined previously [172] by EDS and are summarized in Table 4.2. They correspond to the nominal equiatomic compositions within an error of ± 2 at.% (The % error is found by calculating the difference between measured values of the quantitative chemical composition by EDS and the nominal equiatomic composition, which this value being given as a percentage of the measured value). This result shows that the actual chemical compositions in each as-cast sample are close to the nominal equiatomic compositions at 25 at.% of each element in the CoCrFeNi alloy and 20 at.% of each component in CoCrFeNiAl, CoCrFeNiCu, and CoCrFeNiSn alloys.

Table 4.3 shows the composition of distinguishable phases in CrFeCoNiSn, determined by EDS. It reveals that CrFeCoNiSn (within an experimental error of ± 1 at.%) forms a dual phase structures; shown previously by XRD to be CrFeCoNi FCC phase and Ni_{1.5-1.63}Sn hexagonal phase [172]. A BSE micrograph of the HEA sample gathered here, Figure 4.4, corresponds with these earlier results. In the unetched condition under BSE imaging, the morphology of CrFeCoNiSn includes two phases; the matrix phase of Ni-Sn with high Sn (38.57 at.%) and Ni (28.68 at.%), and the minor phase of CrFeCoNi with high Fe (30.64 at.%), Co (28.70 at.%), Cr (26.67 at.%), and Ni (11.14 at.%) respectively. It should be noted that, chemical composition analysis via EDS technique may give low-accuracy results caused by scanning with a spot size of a few microns, and relatively few assessment points made. While area scans can be more accurate, there is also the difficulty of obtaining signal from different

phases in the subsurface region. Better results could be obtained at higher magnification, for example in a TEM. This compositional uncertainty should be especially considered when attempting to analyse unknown phases for example the Ni-Sn phase.

Table 4.3: The chemical compositions in atomic percent (at.%) of CrFeCoNiSn alloys phase via EDS analysis determined here, and the phase composition (phase composition identification from previous research [172]).

HEA system	Phase composition	Chemical composition (at.%)				
		Co	Cr	Fe	Ni	Sn
	The whole surface area (An area scan)	20.7	18.7	20.3	19.8	20.4
CoCrFeNiSn	Ni-Sn Hexagonal	14.1	8.7	9.9	28.7	38.6
	CoCrFeNi FCC (A point scan)	28.7	26.7	30.6	11.1	2.9

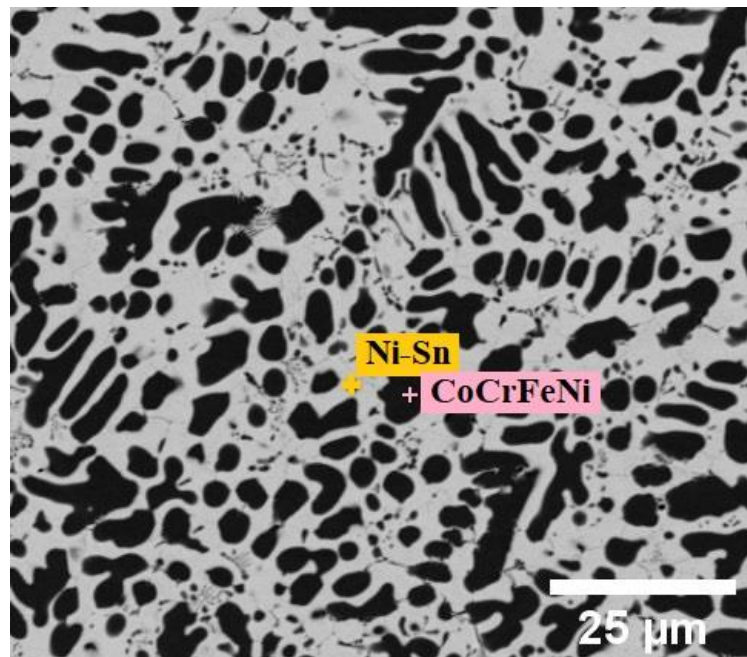


Figure 4.4: BSE-SEM micrographs showing EDS spots of the as-cast CrFeCoNiSn sample with unetched condition.

The result above on these alloys indicates that the main alloy system, CoCrFeNi, has a single phase FCC crystal structure. The three alloying elements, Al, Cu, and Sn, lead to the formation of new phases; a major B2 and minor Al-Ni-rich phase in CoCrFeNiAl [4,42], a major CoCrFeNi FCC and minor Cu FCC phases in CoCrFeNiCu [11,173], and Ni_{1.5-1.63}Sn hexagonal and CoCrFeNi FCC phases in CoCrFeNiSn [69,172]. These results are consistent

with the EDS mapping reported here which show the elemental distribution in the microstructure of as-cast samples, Figure 4.5. This shows that both CoCrFeNi and CoCrFeNiAl alloys appear to have a uniform elemental distribution, consistent with the formation of a single phase. However, CoCrFeNiAl is not single phase. It also contains a minor Al-Ni-rich phase observed when this sample is examined following polarisation in chloride solution. The formation of two phases has been observed in the CoCrFeNiCu and CoCrFeNiSn systems. Cu segregates from the major phase of CoCrFeNi in the elemental map of CoCrFeNiCu while the Sn addition to CoCrFeNiSn alloy leads to Ni and Sn being found in the same area, consistent with the formation of the Ni-Sn hexagonal structure. Both Cu-rich phases and hexagonal phases containing Ni and Sn occur in the interdendritic region.

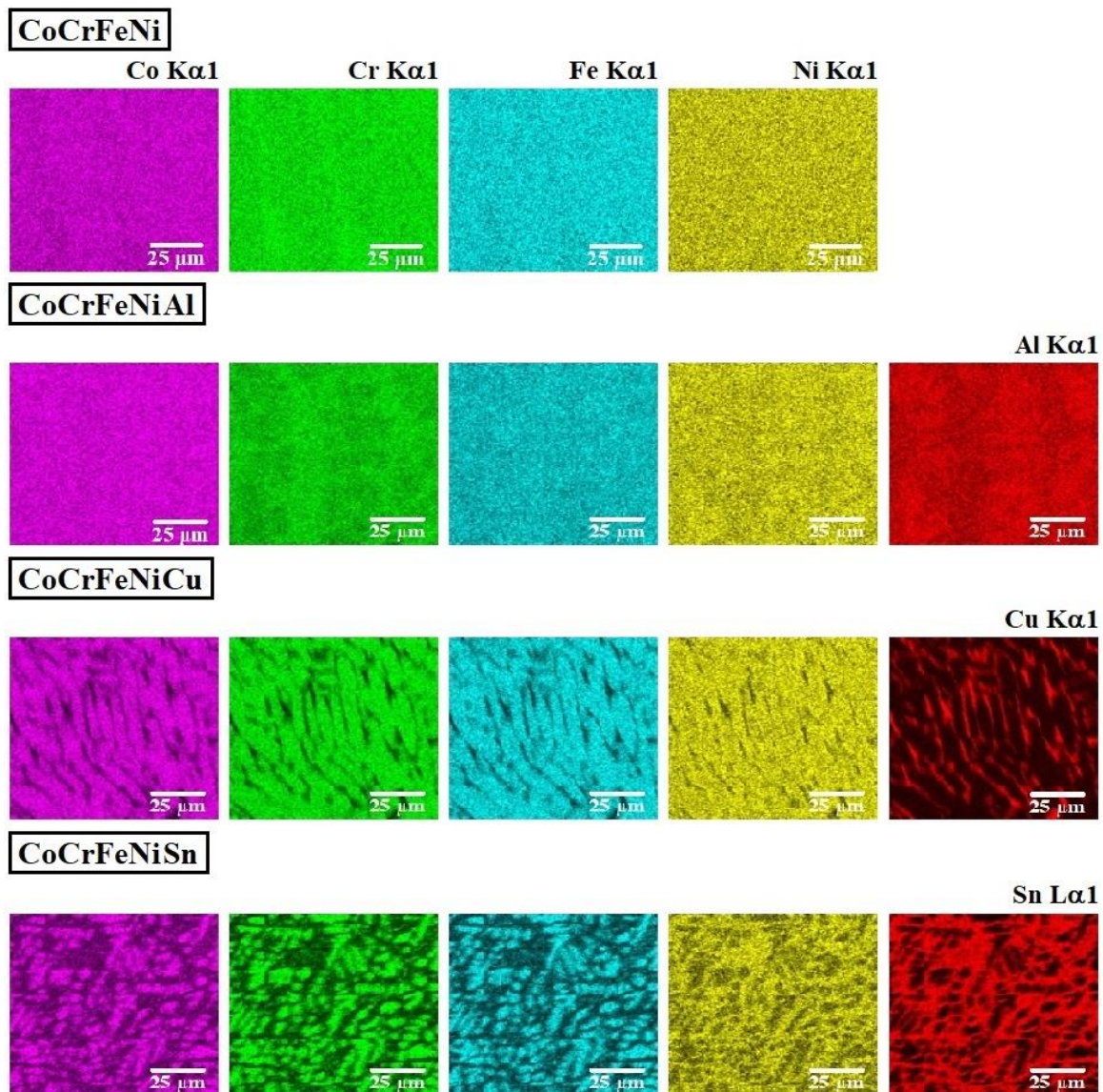


Figure 4.5: EDS elemental maps showing as-cast samples; CoCrFeNi, CoCrFeNiAl, CoCrFeNiCu, and CoCrFeNiSn.

4.1.3 Interpretation of phase formation

In thermodynamic and fundamental solid solutions theories, there are five variables which are commonly used in the interpretation of HEA system, which we can also employ to understand why the alloys under study in this work form the phases observed. These common variables are the enthalpy of mixing (ΔH_m) [24,32-36], the entropy of mixing (ΔS_m) [24,32-36], the atomic size difference (δ) [24,32-36], the electronegativity difference ($\Delta\chi$) [28], and the valence electron concentration (VEC) [35-37], calculated as in Equations 1 and 4-7 (discussed in section 2.1.2). Other parameters of similar type exist, and have been indicated to be effective in rationalising the phases formed. One such example is the electrons per atom (e/a ratio). This parameter is not used in this work however as the determination of an accurate value is difficult for multicomponent alloys.

The relevant parameters for the alloys of interest here were calculated and are summarised in Tables 3.2-3.4 (presented in section 3.2). Tables 3.2 and 3.3 show the essential variables used to calculate the base thermodynamic parameters for each alloy, which are shown in Table 3.4. These values for the CoCrFeNi-based alloy and three HEA systems investigated are compared to the criteria for HEA formation introduced by Guo et al. [33,34,37], Chen et al. [35] and the Gibbs free energy of mixing [34], as summarised in Table 2.2 (presented in section 2.1.2). These criteria can be used to interpret the microstructures observed in these alloys.

It was found that the criteria indicate CoCrFeNi would be expected to form as a solid solution phase, having a negative ΔH_m value (-3.75 kJ/mol) and a low δ value (0.35%), including a low $\Delta\chi$ value (9.67%). Formation of FCC phase is also indicated as VEC is high (8.25). From the results gathered here, this alloy does indeed seem to show these characteristics in the as-cast form examined. Intermetallic compound formation is feasible in the CoCrFeNiAl alloy, resulting from the impact of the Al content leading to a large negative value of ΔH_m (-12.32 kJ/mol) and a large $\Delta\chi$ value (12.06%). From the results found here, there is a clear indication of an additional phase meaning the alloy consists of a major B2 phase and an Al-Ni rich phase, possibly an intermetallic compound given the propensity for these elements to react and form this, as shown by the binary phase diagrams given earlier. This intermetallic phase can form as fine particles distributed in the matrix B2 phase, and structures consistent with this are seen after attack by chloride ions. The CoCrFeNiCu alloy shows Cu segregation, which the criteria suggest stems from the positive value of ΔH_m (3.20 kJ/mol) and positive ΔH_m values of all the Cu-A couples (A is Co, Cr, Fe, and Ni), indicating that these bonds are not preferred

compared to those between other elements in the CoCrFeNiCu alloy. The high VEC value (8.80) indicated that FCC phase may be expected, and indeed this is seen, although it is across two phases, the FCC Cu phase and the CoCrFeNi phase, so the alloy-level VEC value probably does not apply to either of these phases exactly. From Guo et al.'s criteria [33,34], CoCrFeNiSn can form a compound phase. Considering Chen et al.'s criteria [27], $\Delta\chi$ (10.30%) indicates the formation of compound phases (as is actually observed in the alloy, where a primary FCC CoCrFeNi phase and a secondary hexagonal Ni-Sn-rich phase are seen). Furthermore, the strong bonding of the Ni-Sn couple, with the most negative ΔH_m of the atomic couples of the elements (-4 kJ/mol) present and Sn, leads to the segregation of the Ni-Sn hexagonal phase from the other phase present.

To sum up, the previous criteria for HEA-system interpretation do not give an exact criterion which can explain correctly the observations in all of the HEA systems studied here, though seeking the most common result of multiple criteria seems to be correct for the small number of alloys studied. In this, it should be noted that the alloys in the present study are examined in the as cast state, and it may be that some of the observed phase compositions are not the final equilibrium structures which could be arrived at.

4.1.4 The chemical composition of oxide film on the sample surface

Generally, HEA samples consisting of multiple metallic components can form several kinds of nanoscale-metallic oxide films on the surface during reaction with oxygen [174]. For example, Cr_2O_3 , Fe_2O_3 , Co_3O_4 , and NiO were observed to have formed on the surface of CoCrFeNi [175], and CoCrFeNiAl_{0.3-0.9} showed that Cr_2O_3 , Fe_2O_3 , Co_3O_4 , NiO, and Al_2O_3 formed on its surface [175]. This work focuses on the investigation of the corrosion behavior of alloys in different testing solutions. The analysis of passive films on the as-cast sample surface (the original surface) is essential to understand the corrosion mechanism in each alloy with the different testing solutions, as it is these films that will first experience the effects of the conditions. XPS testing was carried out on sample surfaces to evaluate nanoscale-metallic oxide films forming in a natural environment. This method typically is sensitive to approximately 5-10 nm in depth when used in this way [136], and will reveal information about the oxidation state of the elements at the surface, from which inferences about possible oxides can be made. This is important as not all oxide films are good at resisting corrosive attack. In order to identify the oxide film, and thus to assess the corrosion properties, we investigate here the formation of what is likely to be the main protective oxide film, Cr_2O_3 , and also the

formation of minor passive films, Al_2O_3 , Cu_2O , and SnO_2 , the oxides of the elements added to the main CoCrFeNi system here. The chemical composition of these films, which were original oxide films formed on the as-cast samples after surface preparation (sectioning and polishing) and then exposure to air, was evaluated via surface analysis by XPS.

The relative atomic concentration of the elements in Table 4.4 present at the as-cast sample surfaces was first explored by XPS analysis (the composition has been assessed for the bulk alloy pre-corrosion testing to be in all cases relatively close to equiatomic, Table 4.2 and [172] at least when the content of oxygen and carbon are not taken into account, see section 4.1.2). This indicates that the proportion of Cr detected at the surface is the highest (without considering the oxygen and carbon contents, but examining the main elements (Co, Cr, Fe, and Ni) and the fifth additional element (Al, Cu, and Sn)) in all alloy systems explored; 16.4 at.% in CoCrFeNi, 14.8 at.% in CoCrFeNiAl, 17.1 at.% in CoCrFeNiCu, and 16.7 at.% in CoCrFeNiSn alloy. The amount of Cr at the surface can be linked to the capability for Cr-oxide formation on the sample surface. A sample surface with high Cr content (such as CoCrFeNiCu) has the potential to produce a high amount of Cr_2O_3 films (which typically performs well in resisting corrosive attack) while a sample surface with low Cr content (such as CoCrFeNiAl) seems to generate a lower amount of Cr_2O_3 film. Actually, not only the consideration of Cr content can indicate the ability to form Cr_2O_3 films, but also the amount of oxygen, as a precursor, that reacts with metals to generate passive films. It corresponds with the measured surface oxygen concentration of CoCrFeNiAl, which is the highest of all in Table 4.4. In practice, Cr_2O_3 and Al_2O_3 tend to be isostructural, easily forming a mixed-cation $(\text{Cr,Al})_2\text{O}_3$ oxide, which is discussed in 4.3.5. It is thus highly likely that the Al content will promote the formation of a thicker, more durable Al-containing Cr_2O_3 surface oxide layer. As mentioned above, it can indicate that the lower measured Cr surface concentration is misleading to form a lower amount of Cr_2O_3 film since it is likely due to the strong segregation of both Cr and Al into the surface oxide layer formed, as found in the very high Al^{3+} and low Al-metallic signals in Table 4.5. In addition, the amount of detected oxygen is important for metal-oxide formation, as this is available at the surface to interact with metallic elements. Oxygen amounts are shown in Table 4.4 below, in large amounts 43.8-56.6 at.%. In addition, unexpectedly high carbon contamination can be found in Appendix B. Carbon contamination on the sample surface which gives rise to a signal in the XPS data is also reported in several previous papers [176,177]. XPS is a highly sensitive technique for detecting chemical species on a surface [160], and it is relatively easy for surfaces to pick up contamination, including carbon, which might occur during handling, or in

this case the shipping that was required to transport the samples for testing. However, these carbon contents are not expected to affect the formation of metal oxides, as the sample-surface preparation and testing are carried out under aerated conditions in a natural environment, and there is an ample supply of oxygen from the atmosphere, which will preferentially react with the metals. The carbon peaks are also not expected to obscure the peaks of the metallic elements of interest, being at very different energy ranges, and therefore, while it indicates that improved laboratory practice would be desirable to reduce contamination in general, it is not expected to alter the validity of the findings with respect to the relative oxidation of the different elements at the surface.

Table 4.4: The relative atomic concentration (at.%) at the as-cast sample surfaces; CoCrFeNi, CoCrFeNiAl, CoCrFeNiCu, and CoCrFeNiSn alloys.

Alloys	Relative atomic concentration (at.%)							
	Co	Cr	Fe	Ni	Al	Cu	Sn	O
CoCrFeNi	10.77	16.39	12.36	14.62	-	-	-	45.86
CoCrFeNiAl	5.39	14.79	8.14	4.37	10.74	-	-	56.57
CoCrFeNiCu	5.87	17.10	9.77	6.05	-	10.03	-	51.16
CoCrFeNiSn	8.08	16.65	8.06	10.84	-	-	12.55	43.82

Figure 4.6 displays XPS spectra for high resolution monitoring of the samples in an as-cast condition. Five elemental XPS spectra; Al 2p, Cr 2p, Cu 2p_{3/2}, O1s and Sn 3d, are used to assess the chemical state of the corresponding atomic species (and thus indicate whether these atoms tend to be present in the metallic form or as compounds; likely to be oxides) at the sample surfaces. The results are consistent with a main protective film of Cr₂O₃ formed by the interaction between Cr³⁺ and O²⁻. Cr 2p spin-orbit coupling consisting of Cr 2p_{3/2} and Cr 2p_{1/2} is detected in all alloys analysed. The deconvoluted Cr 2p_{3/2} peak can be found at the binding energies of 574.30 eV (Cr metal) and 576.38 eV (Cr oxide). The form of the oxygen absorption on the sample surface analyzed by XPS can be identified to be one of two types; metal oxide and chemisorbed oxygen. The metal oxide form is the result of reaction between oxygen and metallic elements (Al, Co, Cr, Cu, Fe, Ni, and Sn in this case) on the substrate to form metal oxides such as Al₂O₃, Cr₂O₃, Cu₂O, and SnO₂. The chemisorbed form of oxygen covers the absorption of oxygen and oxygen-containing contaminants (which do not involve metallic elements from the samples, such as H₂O) on the sample surface, comprising any species containing bonds such as C-O, C=O, and O-H [178]. The O 1s peak can be detected at the

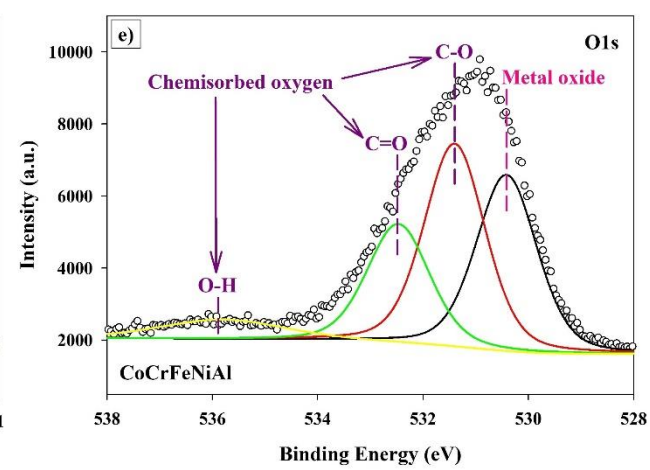
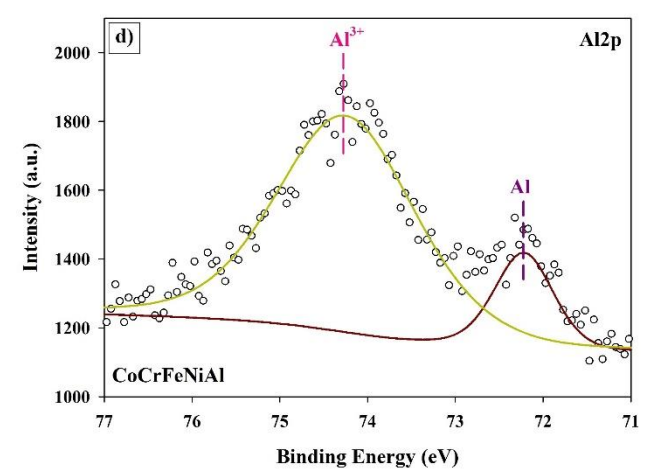
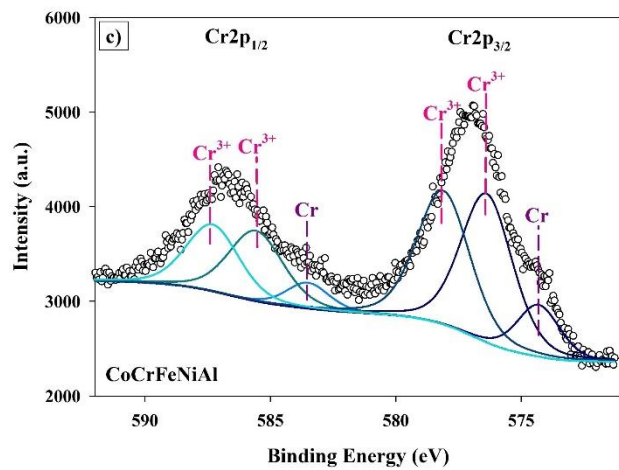
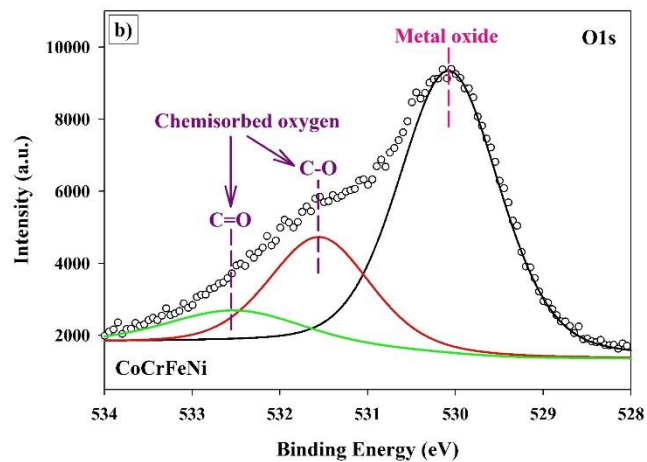
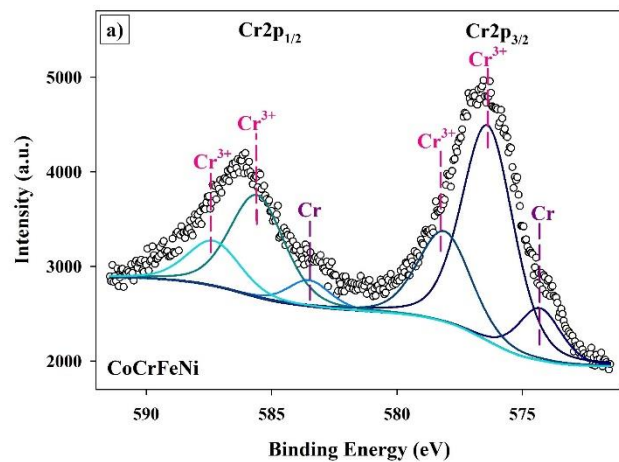
binding energies of 530.07 eV-530.41 eV (metal oxide) and 531.40 eV-535.79 eV (chemisorbed oxygen). For the three alloying elements which distinguish the samples here (Al, Cu and Sn), the formation of Al₂O₃ with Al³⁺ in the CoCrFeNiAl system was indicated by two peaks of Al 2p spectra at the binding energies of 72.22 eV (Al metal) and 74.25 eV (Al oxide). The Cu 2p_{3/2} peak suggesting the creation of Cu₂O from Cu¹⁺ in the CoCrFeNiCu system was detected from two peaks at the binding energies of 932.82 eV (Cu metal) and 933.91 eV (Cu oxide). Two spin orbitals can be detected in the Sn 3d spectrum; Sn 3d_{5/2} and Sn 3d_{3/2} for the formation of SnO₂ with Sn⁴⁺. The Sn 3d_{5/2} peak can be found at the binding energies of 484.89 eV (Sn metal) and 486.43 eV (Sn oxide).

Table 4.5: The relative surface atomic concentration (at.%) of each analysed element at the as-cast sample surface in metallic and ionized form (taken to indicate the relative involvement of the atoms in either the alloy in metallic form or as metal oxides).

Alloys	Cr (Cr at.%)		Al (Al at.%)		Cu (Cu at.%)		Sn (Sn at.%)	
	Cr	Cr ³⁺	Al	Al ³⁺	Cu	Cu ¹⁺	Sn	Sn ⁴⁺
CoCrFeNi	12.27	87.73	-	-	-	-	-	-
CoCrFeNiAl	13.02	86.98	16.03	83.97	-	-	-	-
CoCrFeNiCu	8.43	91.57	-	-	71.08	28.92	-	-
CoCrFeNiSn	8.15	91.85	-	-	-	-	33.89	66.11

Table 4.5 presents the calculated proportions for each of the analysed elements between the metallic form and as ions (taken to represent oxides) on the as-cast sample surface of CoCrFeNi and the three HEA systems examined here. With the assumption that the reaction of these elements has occurred with oxygen, rather than any other species, these values indicate the amount of the passive-film present. This is a useful indication in interpreting corrosion behavior as metal oxides are generally quite stable, and are likely to affect the performance in resisting corrosion attack. The addition of the further alloying elements to the main four component HEA system affects the oxide formation on the specimen surface. The extra elements all reduce the proportion of the Cr in a state that suggests it may be participating in oxide. The reduction is least with Sn addition, where CoCrFeNiSn has 91.9 at.% of the Cr in the oxidized form (versus 87.7 at.% in CoCrFeNi), CoCrFeNiAl contains 87.0 at.% of the Cr in the oxidized form, and CoCrFeNiCu has 91.6 at.% of the Cr is oxidized. In addition, on the surface of CoCrFeNiAl 84.0 at.% of the Al is oxidized, but only 29.0 at.% of the Cu on the surface of CoCrFeNiCu. The as-cast CoCrFeNiSn surface contains 66.1 at.% of the Sn is

oxidized, as in Table 4.5. In relation to Cr, which may be the optimum oxide to form, CoCrFeNiSn has the highest ability to generate the Cr oxide with 91.9 at.% of this element at its surface. However, if oxide films from both Cr and alloying elements (Al, Sn, and Cu) are considered, CoCrFeNiAl may be an attractive candidate. It stems from the fact that this alloy can form a mixed-cation (Cr,Al)₂O₃ oxide with high amounts of Cr₂O₃ and Al₂O₃ films.



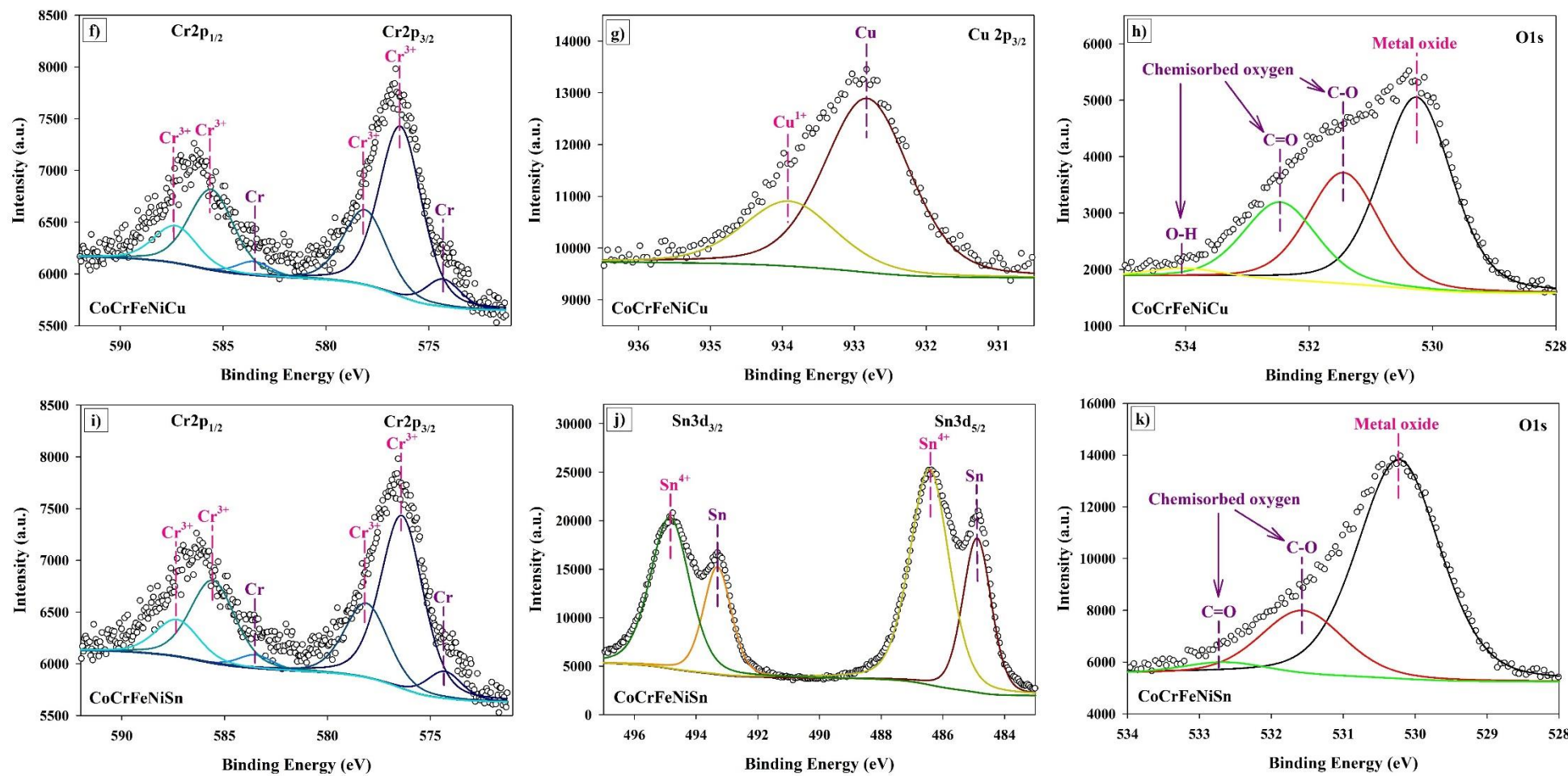


Figure 4.6: The XPS spectra of as-cast samples showing the metal and metal-oxide regions of;
a,c,f,i) Cr 2p, d) Al 2p, g) Cu 2p_{3/2}, j) Sn 3d, and b,e,h,k) O 1s peak

4.1.5 Hardness measurements

To understand the hardness, a Vickers micro-indentation hardness indenter was conducted, Figure 4.7.

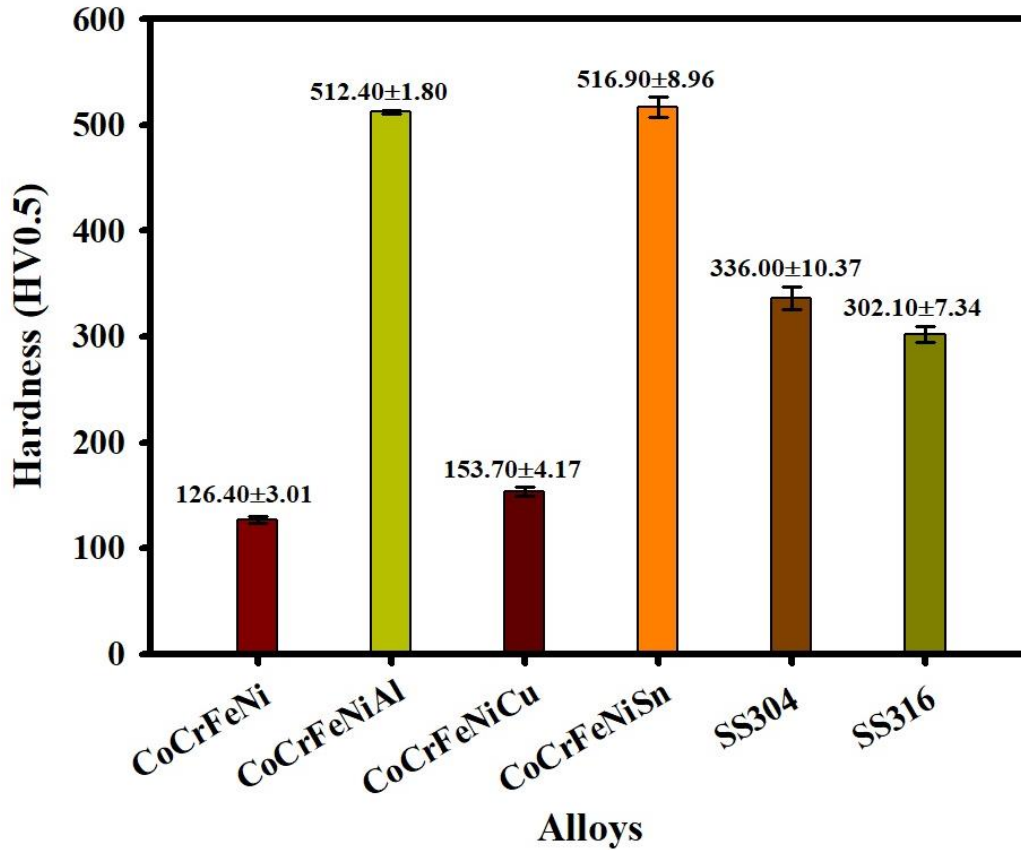


Figure 4.7: Hardness of as-cast samples and conventional alloys at HV0.5.

As shown in Figure 4.7, the hardness values of all as-cast samples are compared with two conventional alloys (also in as-cast form, following the same processing route), grades 304 and 316 stainless steel. The hardness value of SS316 is lower than SS304, 302 HV0.5 (2.96 GPa) and 336 HV0.5 (2.30 GPa) respectively, which would be the reverse of what is usually expected. However, these alloys being the as cast state will not have their usual, optimized microstructure, due to the thermal histories [179]. The comparison between as-cast samples from this work and the conventional alloys indicates that the hardness values of both SS304 and SS316 are lower than CoCrFeNiSn (517 HV0.5; 5.07 GPa) and CoCrFeNiAl (512 HV0.5; 5.03 GPa), though they are harder than CoCrFeNi (126 HV0.5; 1.24 GPa) and CoCrFeNiCu (154 HV0.5; 1.51 GPa); recalling that none of the samples will be microstructurally optimized for hardness. The highest hardness value is found in CoCrFeNiSn, while CoCrFeNi has the lowest hardness of the samples explored here.

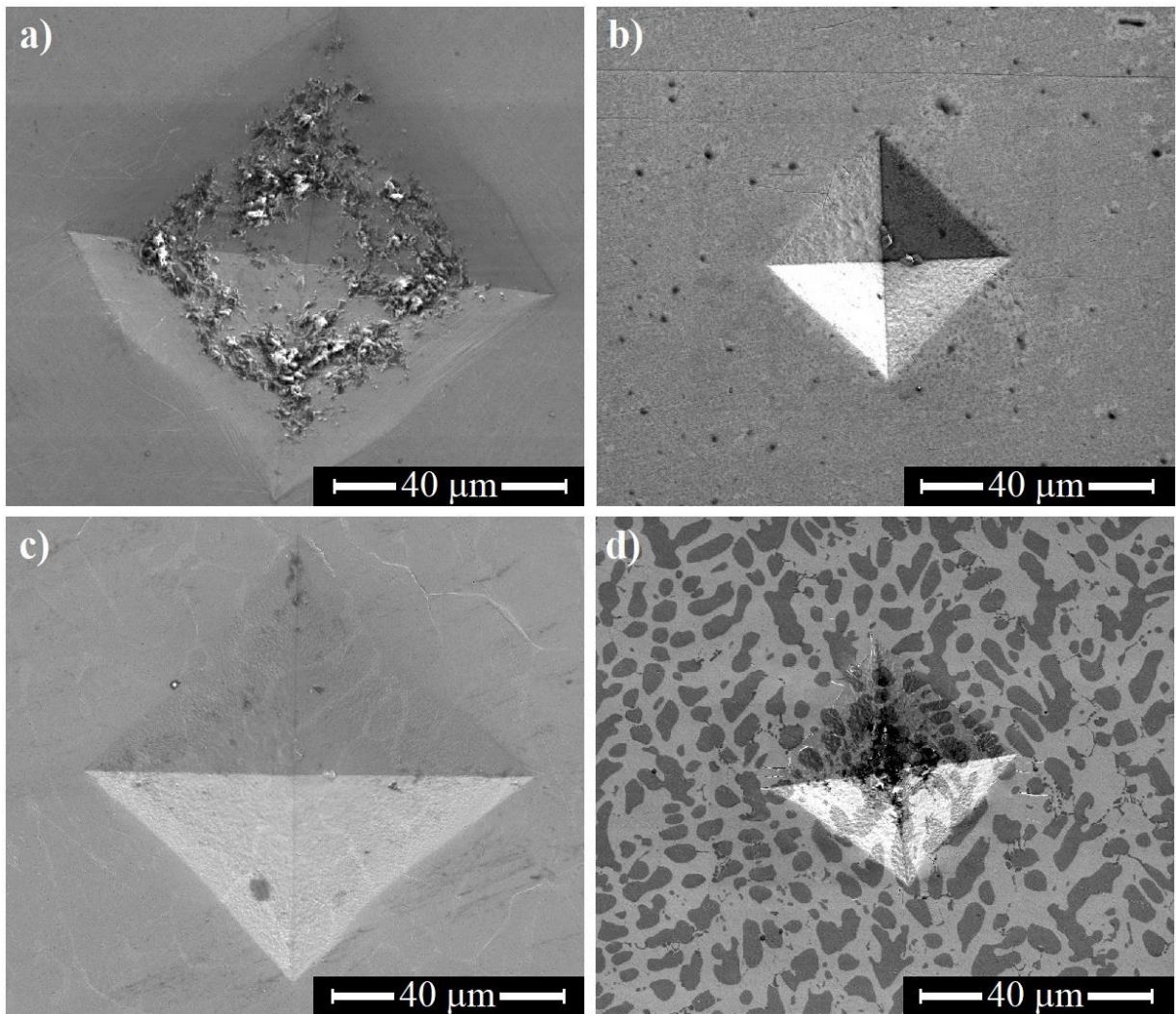


Figure 4.8: SE-SEM micrographs of as-cast sample indents; (a) CoCrFeNi, (b) CoCrFeNiAl, (c) CoCrFeNiCu, and (d) CoCrFeNiSn alloys.

SEM images of the indents in all as-cast alloys after hardness testing are shown in Figure 4.8. As well as the difference in dimensions due to the change in hardness value, indents in CoCrFeNi, Figure 4.8a, show bowed edges with no observable cracks on the sample surface, suggesting ductility. Wang et al. [180] have shown that CoCrFeNi can undergo plastic deformation to high strains, with deformation by dislocation motion, and the operation of work hardening mechanisms at a significant rate, stemming from the low stacking fault energy [181] (approximately 30 mJ/m^2 despite the content of Ni [60]). This result is similar to CoCrFeNiCu in Figure 4.8c. The appearance of the indent in this alloy is like that in CoCrFeNi with slightly bowed edges. After indentation cracks were seen in the interdendritic region in CoCrFeNiCu, while CoCrFeNi showed no cracking. The indent size in both CoCrFeNiAl and CoCrFeNiSn is smaller than that in CoCrFeNi and CoCrFeNiCu, reflecting the hardness differences, Figures 4.8b and 4.8d. As some of these indents are small, there could be some error in the dimensional

measurement in the hardness testing system, meaning the values may not be precise, but the trends in hardness are clear. The structural changes brought about by the Al and Sn additions increase the hardness value of the alloys, with the Sn-containing alloy showing cracking around indents, Figure 4.8d, with it being particularly noteworthy that these occur in the Ni-Sn phase (the lighter contrast phase in the image) only.

4.2 Discussion: characterization of as-cast CoCrFeNi and HEA samples

4.2.1 Effect of alloying elements on the microstructure and phase evolution of as-cast samples

The results presented above confirm that the alloying elements have a clear effect on the phase structure in the systems under observation in this work. The CoCrFeNi alloy has its single FCC phase microstructure converted to various dual phase structures by the addition of different fifth elements, Al, Cu, and Sn. Most of the observations made are in accord with previous literature where this exists [4,28,42,69,136,182], as described below.

Firstly, the Al addition seems to form one or two phases in CoCrFeNiAl. There is clear observation of a major, ordered B2 phase and also some evidence of what could be a minor Al-Ni intermetallic phase. The former is detected by the XRD analysis shown in section 4.1.1. Al is a BCC stabilizer in this system, leading the formation of the BCC phase when combined with CoCrFeNi [183]. An increase in the ratio of Al content is known to correlate with a rise in the amount of BCC phase in CoCrFeNi alloy [90]. Much research suggests that the phase structure of CoCrFeNiAl alloys stems from the difference in atomic size between the elements of the CoCrFeNi system and Al, which is larger [4,90,136], though more comprehensive descriptions of alloys would use the relative energies of the electronic structure of different systems as a means to discriminate between different structures. Further detail of the structure is observed by EDS at high resolution on samples after corrosion testing in chloride solution, section 4.3.2. Fine particles, which could be a minor Al-Ni intermetallic phase are found distributed in the matrix phase. Similar observations in other work have shown that such particles do exist, with the area around these possible Al-Ni phases consists of a CoCrFe-rich phase due to Al and Ni being depleted from it [28,42]. These phases are present at only small volume fractions, and therefore do not give an observable signal in XRD; TEM observation would be required to give a definitive answer. If it does occur, formation of the Al-Ni intermetallic phase may be due to the mixing enthalpy of the different atomic pairs ($\Delta H_{mix, <ij>}$) in the system. The $\Delta H_{mix, <ij>}$ of the Al-Ni pair has the lowest value (-22 kJ/mol) of all the pairs

in the CoCrFeNiAl system, suggesting that a phase consisting of these two elements strongly bonded would be most likely to form. This is also seen in the binary equilibrium phase diagram of the Al-Ni system [63] in section 2.1.5, where intermetallic phases occur. The expected phases between Al-Ni at 50:50 atomic ratio is a cubic $Pm\bar{3}m$ space group phase at a temperature below approximately 1638 °C [63].

Secondly, CoCrFeNiCu shows Cu segregation from the major FCC phase. A minor Cu-rich FCC phase and a major FCC CoCrFeNi phase can be found by the XRD technique, section 4.1.1, while the phase location is confirmed via the EDS elemental map, section 4.1.2, which also shows that the segregation of Cu occurs in the interdendritic region along grain boundaries. The dendritic region itself contains high Co, Cr, Fe, and Ni. This segregation can be understood from the large positive values of the mixing enthalpy between Cu and the other elements in the system; with Co (6 kJ/mol), Cr (12 kJ/mol), Fe (13 kJ/mol), and Ni (4 kJ/mol) [28], as in Table 3.3. As pointed out before, these values would suggest that copper is unlikely to mix with the other constituents [28]. The experimental observation of two FCC phases in CoCrFeNiCu in this work is consistent in the phase composition analysis in previous research [11,28,68].

Thirdly, the addition of Sn as an alloying element leads to the formation of two phases in CoCrFeNiSn. XRD analysis indicates the alloy contains an FCC phase (CoCrFeNi) and a Ni-Sn-rich hexagonal phase (which also contains significant amounts of the other elements), which is consistent with Rietveld refinement for this structure, section 4.1.1. The EDS mapping indicates phase positions in the structure of CoCrFeNiSn, section 4.1.2. The dendritic zone has the elements that make up the FCC phase, while the elements corresponding to the Ni-Sn-rich hexagonal phase appear in the interdendritic zone. The formation of the Ni-Sn-rich hexagonal phase is likely to be caused by $\Delta H_{mix,<ij>}$ for element pairs in the system. The $\Delta H_{mix,<ij>}$ of the Ni-Sn couple (-4 kJ/mol) has the most negative value, including strong bonding between these being preferred, and leading to the formation of Ni-Sn phase. Other possible couples (Co, Cr and Fe) with Sn have a positive $\Delta H_{mix,<ij>}$ value, indicating that these elements will not preferentially interact with the tin [69,182], although it is clear from the EDS spot analysis that they are present at significant levels in this phase, with the interaction perhaps mediated by the presence of the Ni.

The identification of the second phase as a hexagonal structure is in contrast to previous reports suggesting that the Ni-Sn orthorhombic structure will be formed in CoCrFeNiSn [69]. Orthorhombic is a feasible structure, as there are three phases of this type according to the

binary equilibrium phase diagram of Ni-Sn; α -Ni₃Sn₂ (orthorhombic *Cmcm* space group), α 'Ni₃Sn₂ (orthorhombic *Pnma* space group), and α ''Ni₃Sn₂ (orthorhombic *Cmcm* space group) in the compositional range of 55.7 to 60.1 wt.% Sn [63]. An orthorhombic phase is therefore consistent with the expected phases in the Ni-Sn system around a 50:50 atomic ratio, which would be a mixture of α 'Ni₃Sn₂ phase (orthorhombic *Cmcm* space group) and Ni₃Sn₄ phase (monoclinic *C2/m* space group), at a temperature below approximately 409 °C, (Figure 2.35) [63]. The best match from the pattern database for the phase seen in this work is the hexagonal structure of Ni_{1.5-1.63}Sn phase with *P6₃/mmc* space group. Although not identified specifically in the binary phase diagram, this structure matches with that of the β Ni₃Sn₂ structure found at 54 to 61.4 wt.% Sn, although it cannot be exactly this phase as the ratio of the elements is different, and there are additional elements present. There could therefore be a prototype for the Ni-Sn-rich hexagonal phase in the binary diagram, though its presence may indicate formation under non-equilibrium phase conditions. This could occur in the processing of the samples used here; the casting process used with a small sample size will lead to rapid cooling, for example, [184], and may also result in the loss of some elements during the casting operation (though elemental characterization does not show a large departure from the nominal levels). There are other differences between the work here and that reported in previous research, such as the number of remelting steps used [69]; samples in this work were remelted at least five times, while previous research remelted at least four times [69]. While this difference would probably be small, it could have resulted in better homogeneity in the current work and more representative material being examined.

The different alloying elements present are also seen to give different oxidation states in the as-cast samples, and are therefore likely to have an effect on the formation of passive films. The different fifth elements added (Al, Cu, and Sn) all appear to interact with oxygen in this way, with Cr also being a significant element. These oxidation states were detected by XPS analysis in section 4.1.4. The large amount of Cr present in all alloys (nominally 25 at.% Cr and 20 at.% Cr in CoCrFeNi and the three five component systems, respectively), means that they are likely to form high quantities of Cr₂O₃ film (approximately 87.0-91.9 at.% of the Cr at the surface is in the appropriate oxidation state, Table 4.5). The standard Gibbs free energy change (ΔG°) for the formation of Cr₂O₃ is low (-1,058.1 kJ/mol), meaning it is likely to form and be stable. CoCrFeNiAl, an isostructural mixed (Cr,Al)₂O₃ oxide, is likely to separate Cr₂O₃/Al₂O₃ phases. These films are unlikely to coexist on the CoCrFeNiAl surface. It can

detect Al₂O₃ at the surface (84.0 at.% of the surface Al in the correct oxidation state), Cu₂O may be forming on CoCrFeNiCu (29.0 at.% of the Cu at the surface in the right oxidation state) and CoCrFeNiSn is likely to have some SnO₂ present at the surface (66.1 % of the surface Sn in the appropriate oxidation state). These tendencies in oxide formation are consistent with the relevant ΔG° values. The Gibbs Free Energies of formation (standard temperature and pressure) for these oxides are shown in Table 4.6, determined from the Ellingham diagram [185,186].

Table 4.6: The stable metal-oxide reaction and the standard Gibbs free energy change of all elements (Al, Co, Cr, Cu, Fe, Ni and Sn) in this work [185-188].

Element	The stable metal-oxide reaction	ΔG° (kJ/mol)
Al	$\frac{4}{3}Al + O_2 = \frac{2}{3}Al_2O_3$	-1,582.3
Co	$\frac{3}{2}Co + O_2 = \frac{1}{2}Co_3O_4$	-774.0
Cr	$\frac{4}{3}Cr + O_2 = \frac{2}{3}Cr_2O_3$	-1,058.1
Cu	$4Cu + O_2 = 2Cu_2O$	-146.0
Fe	$\frac{4}{3}Fe + O_2 = \frac{2}{3}Fe_2O_3$	-742.2
Ni	$2Ni + O_2 = 2NiO$	-211.7
Sn	$Sn + O_2 = SnO_2$	-519.6

The standard Gibbs free energy change at 25 °C and 1 atm can indicate the possibility of metal oxide formation and stability [187]. As the values for formation of Al₂O₃, Cr₂O₃, Cu₂O and SnO₂ are all negative, they can form spontaneously, with the Al₂O₃ film most likely to form and be stable as it has the most negative ΔG° (-1,582 kJ/mol) while the least negative ΔG° of Cu₂O (-146 kJ/mol) indicates a low potential for forming an oxide film. To investigate the predominant passive films in each alloy in this work, the ΔG° values of all metallic elements in each phase within the alloys need to be taken into consideration, as in Table 4.6. The FCC CoCrFeNi phase is observed in all as-cast samples, CoCrFeNi, CoCrFeNiAl, CoCrFeNiCu,

and CoCrFeNiSn, and the ΔG° of Cr (-1,058 kJ/mol) has the most negative value in this phase. It indicates that it is more likely for Cr to be oxidized than Co, Fe, and Ni, and the oxide would be expected to have a higher participation of Cr. For the secondary phases, the Al-Ni rich phase in CoCrFeNiAl is likely to form an oxide dominated by aluminium with the highly negative ΔG° of Al (-1,582 kJ/mol). Tin-rich oxide can form on the surface of the Ni-Sn-rich hexagonal phase in CoCrFeNiSn due to a more negative ΔG° value of Sn (-520 kJ/mol) than Ni (-212 kJ/mol), though Co, Cr and Fe, which all seem to be present in the phase in some content would be predicted to be more likely to oxidise, and so an oxide of mixed cations may be most likely. A minor Cu-rich FCC phase is likely to create Cu₂O in the region of the Cu segregation, the ΔG° of Cu (-146 kJ/mol). In addition, the interpretation of possible oxide formation from ΔG° is consistent with the XPS analysis in section 4.1.4.

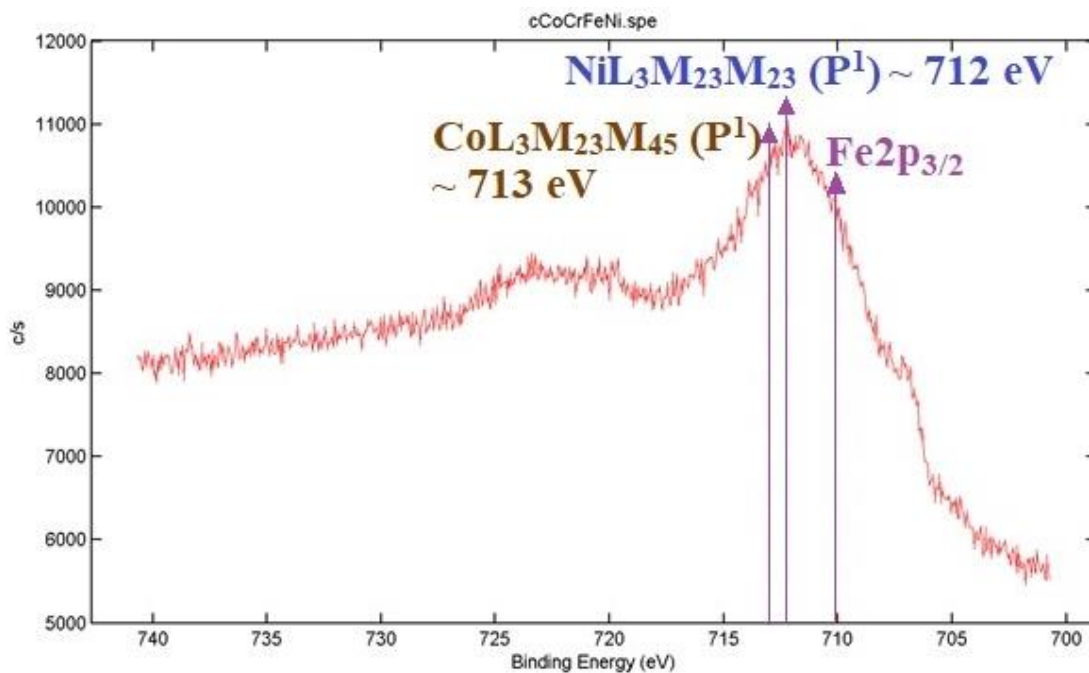


Figure 4.9: The XPS spectra of CoCrFeNi showing the main peak overlapping in Co, Fe, and Ni elements between 710 eV-714 eV.

It is important to note that some of the metals that could be oxidized and participate in an oxide film in the samples examined cannot be clearly distinguished by the XPS technique. This is particularly the case for the transition metals (Fe, Co, Ni here). This is because the main peaks for Co, Fe, and Ni overlap (see the overlapping peaks in the binding energy range of 710 eV-714 eV in Figure 4.9). In addition, XPS identifies the oxidation state of the atomic species, and can indicate if it has been oxidized, but not if it is part of a mixed-metal oxide film generated by several transition metals, due to the capability of transition metals to adopt

multiple oxidation states. Data analysis is difficult where there is peak overlapping and this may introduce some error into the absolute amounts. Nevertheless, the examination of the energies of formation of the oxides suggests that it is those examined in this study that would be the most likely ones to form, albeit that the oxides are not likely to be pure versions of any one oxide. High resolution investigation, for example by TEM, would be needed to obtain further information on the oxide structure and composition.

In order to analyse metal oxide film thickness via XPS, specific determination with either of these two techniques, an angle XPS technique or angle resolved X-ray photoelectron spectroscopy (ARXPS), is required. For example, to achieve such measurements of film thickness by using the ARXPS technique, the surface depth profile was acquired at 6 different angles of emission (α) ($0^\circ < \alpha \leq 90^\circ$) in [189]. In contrast, the XPS analysis in this work only aims to detect chemical composition on the sample surface, and only one angle of emission was measured. Hence, XPS data from this work is insufficient to investigate the thickness of metallic oxide films.

4.2.2 Effect of alloying elements on the hardness of CoCrFeNi and HEA samples

As shown in section 4.1.4, alloying elements affect the microstructure, and this will have an impact on the hardness value of the alloys [68,90], although the precise values will be very dependent on the thermal history, which has not been optimized for mechanical properties in this work (the samples all being examined in the as-cast state). The Al addition is known to increase the hardness value of CoCrFeNiAl due to the formation of two BCC phases; the main ordered B2 phase and the minor Al-Ni intermetallic phase [90]. The hardness value of CoCrFeNiAl as tested here rises from 126 HV0.5 (CoCrFeNi) to 512 HV0.5 (CoCrFeNiAl), with no cracks visible at the indentation site on the surface, section 4.1.4. The B2 phase is found to be the matrix phase by XRD observation in section 4.1.1, and in this phase the large atomic radius of Al can increase the lattice distortion in this alloy, which will increase solid solution strengthening [64,90]. The Al can also form fine phases, possibly the Al-Ni intermetallic phase, as shown in section 4.3.2 which will also increase strength.

The Cu addition slightly increases the hardness in CoCrFeNiCu compared with CoCrFeNi, to a lesser extent than CoCrFeNiAl and CoCrFeNiSn. The hardness value of CoCrFeNiCu increases from 126 HV0.5 (CoCrFeNi) to 154 HV0.5 (CoCrFeNiCu), section 4.1.4. Cracks are observed in the interdendritic region where the Cu-rich phase is found. Cracks appear to have formed in the Cu-rich phase and propagate within this phase, as shown in SEM

images (Figure 4.8c). It is suggested in literature that the increase in the hardness value of CoCrFeNiCu stems from the Cu segregation and the grain-size reduction [68]. The Cu rich phase is an FCC phase, and so can display ductile behavior (even though interfacial cracking is seen) [68].

The increase in hardness of CoCrFeNiSn is shown in section 4.1.4. The Sn addition can contribute to increased hardness values from 126 HV0.5 (CoCrFeNi) to 517 HV0.5 (CoCrFeNiSn). Figure 4.10 shows an SEM image of an indent in CoCrFeNiSn with EDS analysis, which confirms that the lighter phase is the Ni-Sn-rich phase. Despite having high hardness [190,191], the Ni-Sn-rich phase has lower toughness and is the phase where cracking occurs. Crack propagation appears to be resisted by the CoCrFeNi phase (which has an FCC structure and greater ductility), as many cracks terminate at the interface between the two phases. The microstructure of the CoCrFeNiSn alloy therefore has the potential to show improvements in hardness over CoCrFeNi, due to the presence of the high hardness Ni-Sn phase, and for improvements in toughness over the Ni-Sn-rich phase alone, due to the presence of the ductile CoCrFeNi phase.

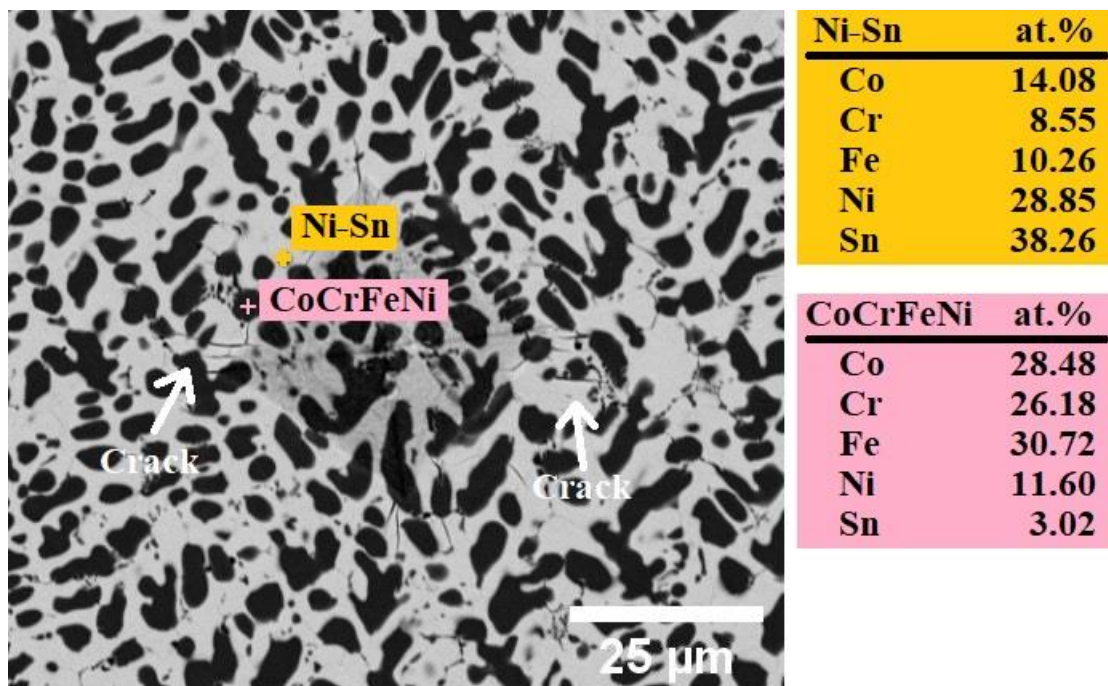


Figure 4.10: EDS analysis showing the chemical composition of CoCrFeNiSn indent.

The volume fraction of the phases is a one of the essential variables for both of these behaviours. It was found that the amount of Ni-Sn phase (56.7%) is greater than the FCC phase (43.3%), consistent with the much greater hardness of CoCrFeNiSn compared to CoCrFeNi. These volume fractions are at a level where each phase existing as a percolating, interconnected

network is possible. This evidence shows that Sn has a transformative effect on the microstructure, and hence hardness, in the CoCrFeNiSn system. The formation of a matrix of Ni-Sn-rich phase, which is a hexagonal structure, is the main factor in raising the hardness [190,191], while the minor phase FCC solid solution CoCrFeNi phase (which is still present in a large amount) introduces some crack propagation resistance.

4.3 Results: characterization of CoCrFeNi and HEA samples after corrosion testing

4.3.1 Corrosion analysis in 0.6 M NaCl solution

To understand the corrosion behaviour of all experimental samples in 0.6 M NaCl solution, the Potentiostat/Galvanostat electrochemical instrument was conducted, Figure 4.11 and Table 4.7.

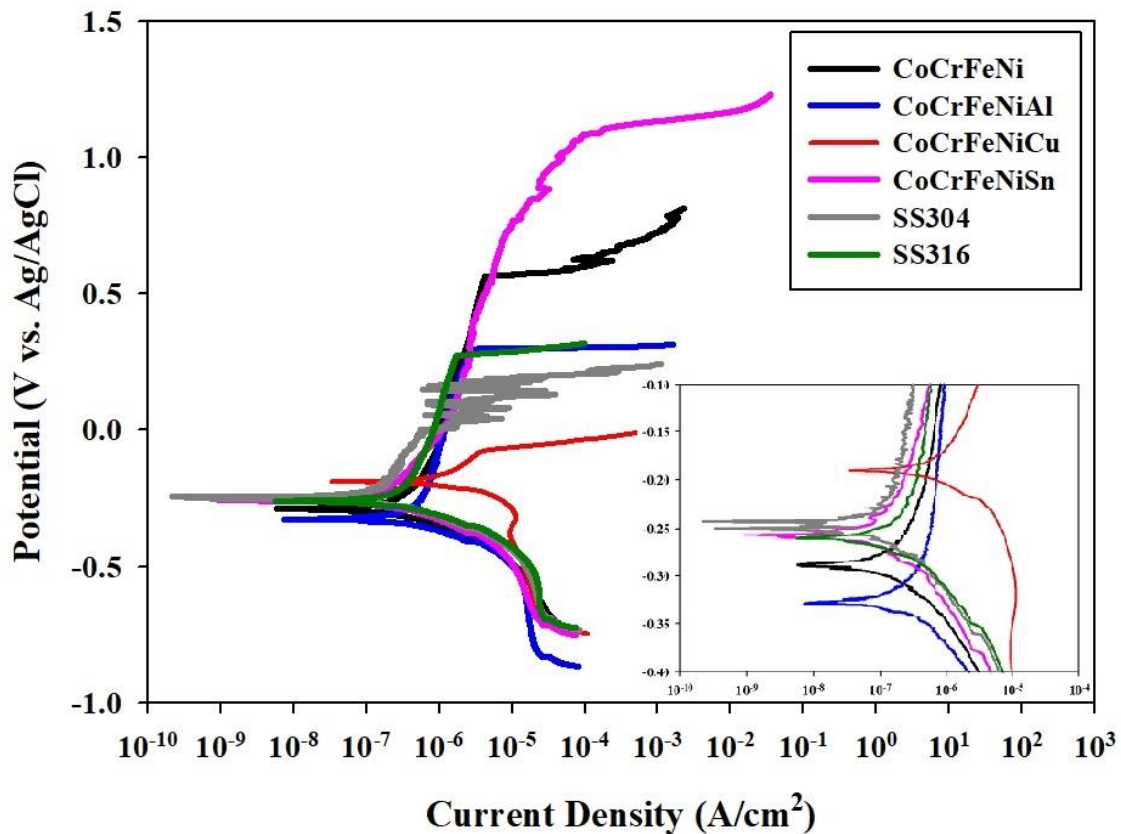


Figure 4.11: Linear polarization curves of four alloy and two stainless steel samples immersed in 0.6 M NaCl solution at room temperature.

The corrosion behaviour of samples immersed in 0.6 M NaCl solution at room temperature is analyzed by linear polarization plots. Figure 4.11 shows the plot of current density (i ; A/cm²) against potential (E ; V vs. Ag/AgCl). Some of the HEA systems show good

corrosion properties when compared with conventional stainless steels, as seen in Figure 4.11. From these curves, the corrosion parameters such as corrosion potential (E_{corr}), pitting potential (E_p) and passivation potential ($\Delta E_p = E_p - E_{corr}$) can be extracted, as given in Table 4.7. Both E_p and ΔE_p are measured to indicate the extent of passive region under medium chloride conditions. These parameters help to reveal the corrosion-resisting capability of the oxide films during the electrochemical operation.

Table 4.7: The corrosion properties of four alloy and two stainless steel samples immersed in 0.6 M NaCl solution at room temperature.

Alloys	E_{corr} (mV _{Ag/AgCl})	E_p (mV _{Ag/AgCl})	ΔE_p (mV _{Ag/AgCl})
CoCrFeNi	-257±13	556±27	813±30
CoCrFeNiAl	-322±10	297±40	619±43
CoCrFeNiCu	-180±13	-69±9	111±21
CoCrFeNiSn	-252±5	1099±14	1351±12
SS304	-246±13	199±12	445±17
SS316	-254±7	267±35	521±42

The CoCrFeNiSn system shows the best corrosion resistance compared to the other alloys since it shows the highest pitting potential and the largest passive region. The full values for this HEA, Table 4.7, show it has the highest ΔE_p , indicating the good stability of the passive film in the pitting-corrosion region of the polarization test. The enhancement of the passive region must stem from the Sn addition, which could form a stable passive film at the surface and contributes to protecting the sample surface from chloride-ion attack. It can be observed that the alloy with the addition of Sn shows the widest passive region as seen in Figure 4.11. As shown in Figure 4.12, the corrosion behavior of CoCrFeNiSn in the transpassive region is observed. CoCrFeNiSn has a high pitting potential (E_p ; 1,099 mV), indicating oxide-film breakdown will occur in the potential range of oxygen evolution. This behavior may stem from complex oxide film, containing, for example Cr and Sn, that could have a high stability and increase in the pitting potential value. Many previous works indicate the possible breakdown of oxide films in the potential range of oxygen evolution in various multi-component alloys, such as 2205 duplex stainless steel [192], Al_{0.1}CoCrFeNi [193], and CoCrFeNi and CoCrFeNiAl [164], as seen here for the alloys under study. In addition, oxygen evolution might be affected or inhibited by differences in the oxide composition, similar to exchange current densities for the cathodic reactions. Thus, a more stable oxide (with Sn) and a potential

limitation of oxygen evolution may give such an observed behaviour. However, none of these reports offer a clear explanation for the mechanism [164,193,194], and while it may be due to effects of a complex oxide film, and possible changes to oxide behavior, such as electrical conductivity, as a result, further work would be required to reach a conclusion on this. In addition, CoCrFeNiSn shows the highest E_p and ΔE_p when compared with other alloys as seen in Table 4.7. This further indicates the formation of a stable oxide film in the CoCrFeNiSn system, which is resistant to corrosion attack and oxide-film breakdown.

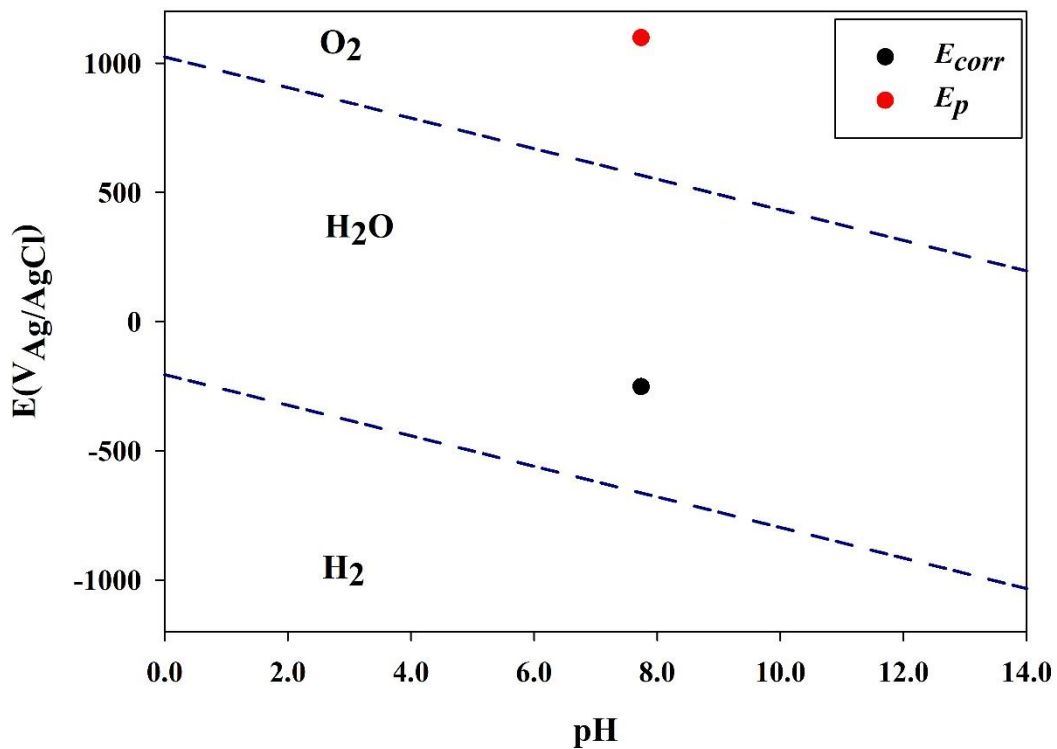


Figure 4.12: E_{corr} and E_p of CoCrFeNiSn immersed in 0.6 M NaCl solution at room temperature plotted on the E-pH diagram of water at room temperature.

In contrast, the lowest E_p and ΔE_p values are found in the alloy with Cu; this HEA has the highest E_{corr} , and was observed to have the narrowest passive region of the alloys examined here, Figure 4.11 and Table 4.7. The Cu addition has the most negative effect on the corrosion properties, as evidenced by showing the lowest E_p and ΔE_p . Furthermore, CoCrFeNiCu and CoCrFeNiAl have lower corrosion resistance than the stainless steels, SS304 and SS316. The other two alloys, CoCrFeNi and CoCrFeNiSn have higher corrosion resistance than the stainless steels, having a large passive region in chloride solution.

4.3.2 Post-corrosion alloy microstructure and composition (0.6 M NaCl solution)

As-polarized samples were examined by SEM after being immersed in the chloride-containing solution. A difference in the sample surfaces can clearly be observed between pre- and post-corrosion testing. The sample surfaces before corrosion testing in all alloy systems show flat surfaces with no corroded areas in the case of both single phase and two phase (as cast) samples, Figure 4.3. On the other hand, BSE images reveal the CoCrFeNi and three HEA microstructures which have been damaged by chloride-ion attack, as shown in Figure 4.13

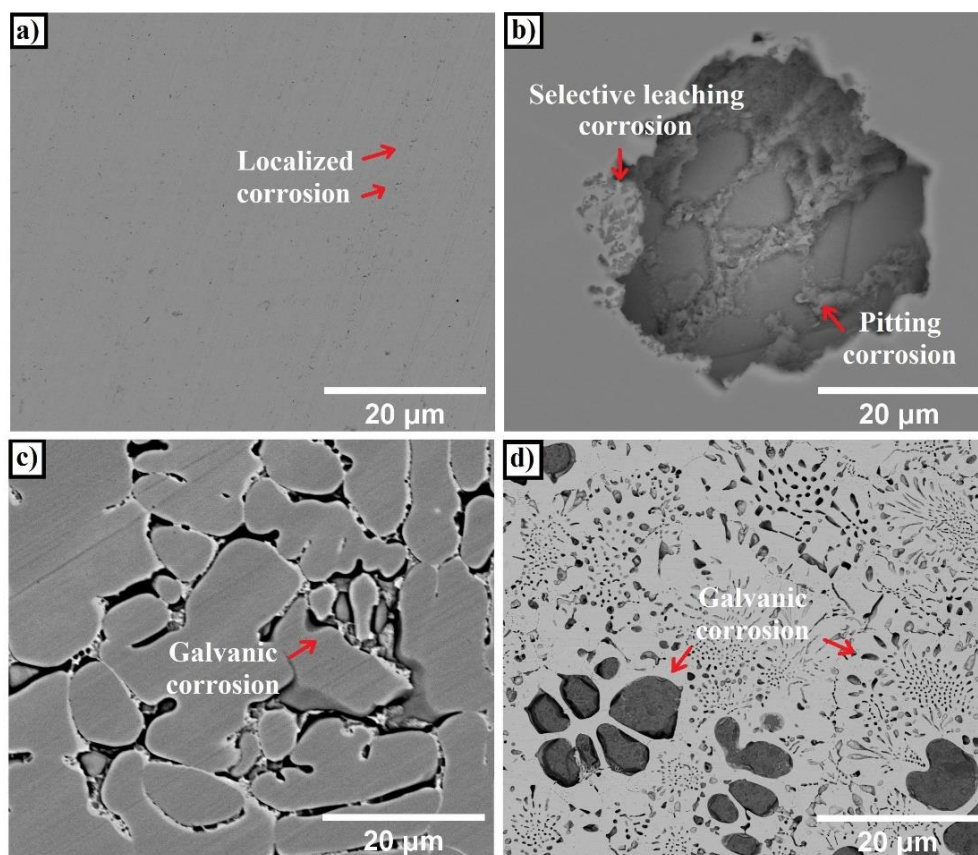


Figure 4.13: BSE images of the surface of HEAs samples after immersion in 0.6 M NaCl solution at room temperature; a) CoCrFeNi, b) CoCrFeNiAl, c) CoCrFeNiCu, and d) CoCrFeNiSn.

Localized corrosion of the CoCrFeNi surface is observed in Figure 4.13a. This may have been initiated by chloride-ion attack in an area having low-Cr content, as some variation in composition in this alloy on an atomic scale has been observed in other work [69]; however, it should be noted that with the sensitivity of the methods applied here no inhomogeneity in element distribution was seen in CoCrFeNi. This shows that the passive films formed are relatively weakly bonded and insufficiently stable for restricting the propagation of corrosion in this system [2,11]. Figure 4.13b shows the CoCrFeNiAl surface structure, exhibiting very large pitting holes, with another material or residue around their outer edge, sometimes filling

the interior of smaller holes. Detailed examination indicates two types of corrosion behaviour, an apparent selective leaching corrosion due to the dissolution of the Al-Ni-rich phase from the major B2 (ordered BCC) phase, leading to pitting corrosion once the product of selective leaching is removed. These corrosion behaviours may be caused by the Al-Ni-rich BCC/B2 ordered BCC dual-phase structure in CoCrFeNiAl. The surface damage after corrosion of the CoCrFeNiCu system is displayed in Figure 4.13c. This alloy contains a matrix-FCC phase and a Cu-rich FCC phase, which leads to the galvanic corrosion driven by the different potential of these phases [2]. Examination of the CoCrFeNiSn system shows a dendritic structure with a finer scale rod-like eutectic formed in the interdendritic regions. The structure consists of a Ni-Sn-rich HCP phase (brighter regions) and a CoCrFeNi-FCC phase (darker regions), Figure 4.13d. Corrosion is seen to take place more significantly on the FCC phase, likely to stem from the different potential values of the two phases in the same manner (though to a lesser extent) as in the CoCrFeNiCu system [69,182]. In addition, micro-galvanic corrosion can occur in alloys containing a second phase or multiple phases, such as duplex stainless steels [194] and WE43 alloy (Mg-4Y-3Gd-1Nd- 0.5Zr) [195]. This corrosion behavior could also be found in CoCrFeNiCu and CoCrFeNiSn due to the presence of two phases in these alloys in the tested condition. The polarization testing in the dual-phase alloys may induce micro-galvanic corrosion behavior on the CoCrFeNiCu and CoCrFeNiSn surfaces. Types of corrosion in this work are considered following the evidence of corrosion morphology in the SEM images (Figures 4.13 and 4.15). However, immersion testing may be a more suitable method to analyze galvanic corrosion due to the ability to assess the effect of immersion time, which is a significant parameter for investigating the change in corrosion morphology and the calculation of the corrosion rate [194,195].

Table 4.8: The results of phase fraction analysis via ImageJ software and the general observation of surface characteristics. Results are for the CoCrFeNi and three HEA surfaces after corrosion testing, with an additional test of CoCrFeNiSn before corrosion testing, which was conducted to better understand the phase makeup of this novel alloy, and whether the apparent dominance of the hexagonal phase seen in the corroded samples was an effect of large changes in visible phases due to the corrosion process.

Alloys	Phase composition	Phase fraction (%)	Surface characteristics
CoCrFeNi	FCC (CoCrFeNi)	100	Low corrosion
CoCrFeNiAl	B2 ordered BCC (CoCrFeNiAl)	(not possible to analyze by this technique - BCC (Al-Ni rich phase too small to resolve)	High corrosion
	BCC (Al-Ni-rich)	(Al-Ni rich phase too small to resolve)	High corrosion (see Figure 4.16)
CoCrFeNiCu	FCC (CoCrFeNi)	86.8 (± 3.3)	Not corroded
	FCC (Cu-rich)	13.2 (± 3.3)	Corroded
CoCrFeNiSn	Hexagonal (Ni-Sn-rich)	56.7	-
	FCC (CoCrFeNi)	43.3	-
Post-corrosion test	Hexagonal (Ni-Sn-rich)	63.8 (± 4.1)	Not corroded
	FCC (CoCrFeNi)	36.2 (± 4.1)	Corroded

The phase fraction and surface characteristics were analyzed from BSE images of the surface of the CoCrFeNi and three HEA samples using ImageJ software indicated the phase fraction of the different phases and the location of the most apparent corrosion as summarised in Table 4.8. In this mode of imaging, in CoCrFeNi it was not possible to distinguish a second phase (in agreement with the earlier results indicating that this is a single phase alloy, section 4.1.1). On the other hand, CoCrFeNiCu and CoCrFeNiSn showed two distinct phases (also in agreement with the earlier results). In the case of CoCrFeNiAl, only one phase could be seen, but from other evidence it is likely to contain a minor Al-Ni-rich (BCC) phase and a B2 (ordered BCC) phase, Figures 4.16. As in Figure 4.17, EDS mapping at high resolution of the CoCrFeNiAl alloy can show the existence of the Al-Ni-rich phase at the nanoscale, but the fine

particle size prevents these being seen in conventional SEM. This difficulty in analyzing the phases also means it is not possible to calculate the phase fraction by ImageJ. Although not carried out here, TEM may be a suitable technique to explore the near-nanoscale Al-Ni-rich phases further. The SEM images on the other hand are suitable to visually estimate the level of corrosion damage on the sample surface in Figures 4.13 and 4.16. In the CoCrFeNiCu alloy, the majority of the structure (more than 85%) was a CoCrFeNi-containing phase (FCC-structured from the XRD results), while the remainder was a phase heavily dominated by Cu. In the alloy of CoCrFeNiSn the dominant phase (more than 60%) was Ni-Sn-rich (likely to be hexagonal from the XRD results), but there was a significant proportion of CoCrFeNi phase present as well. It also reveals the difference in the phase fraction observed at the surface of CoCrFeNiSn between pre- and post-corrosion tests in chloride solution. The proportion of the measured residual CoCrFeNi phase seen at the surface decreases by approximately 7%, from 43% to 36%. It indicates that the percentage of the CoCrFeNi phase has apparently been dissolved by about 16.3%, Table 4.8. This is likely to result from the CoCrFeNi phase being removed and revealing more of the Ni-Sn rich phase at the surface, and indicates that the CoCrFeNi phase has more sensitivity to chloride attack than the Ni-Sn-rich phase. In the three alloys where there were two phases present (CoCrFeNiAl, CoCrFeNiCu, and CoCrFeNiSn), it was also attempted to determine the scale of the microstructure. For the CoCrFeNiAl alloy, a second Al-Ni-rich (BCC) phase remaining in the porous structure, around 77 nm in diameter with fine particles similar to a round shape was found, Figure 4.17. The Cu rich phase in the CoCrFeNiCu alloy occurred at grain boundaries, forming interconnected networks that were typically 1-2 μm in thickness, but extended throughout the alloy. The CoCrFeNiSn appeared to show the CoCrFeNi phase on several scales, firstly in possibly dendritic structures of around 5-10 μm in diameter, and a finer eutectic-like structure at a submicron scale.

The images were also used to identify the extent of corrosion, and, for the two phase samples, whether this was more associated with a particular phase. It was found that CoCrFeNi with a single phase, almost no corroded area could be found. In the CoCrFeNiAl, CoCrFeNiCu, and CoCrFeNiSn systems, two phases are present. In the case of CoCrFeNiAl, Al and Ni seems to be dissolved from the matrix CoCrFeNiAl phase during the corrosion process. Subsequently, a porous Co-Cr-Fe-rich phase is observed. The Cu phase in CoCrFeNiCu is the main phase corroded by chloride attack, while the CoCrFeNi has little apparent damage in this alloy. By contrast, the CoCrFeNi phase in both dendritic and eutectic-like structures shows more extensive corrosion in CoCrFeNiSn, while the Ni-Sn-rich phase does not appear to have been

affected. This indicates that the Ni-Sn-rich phase in the CoCrFeNiSn system probably has the best corrosion resistance of all the separate phases under these conditions of the materials investigated here. These observations correspond with the corrosion properties of alloys in Table 4.7 and the corroded SEM images of alloys in Figure 4.13.

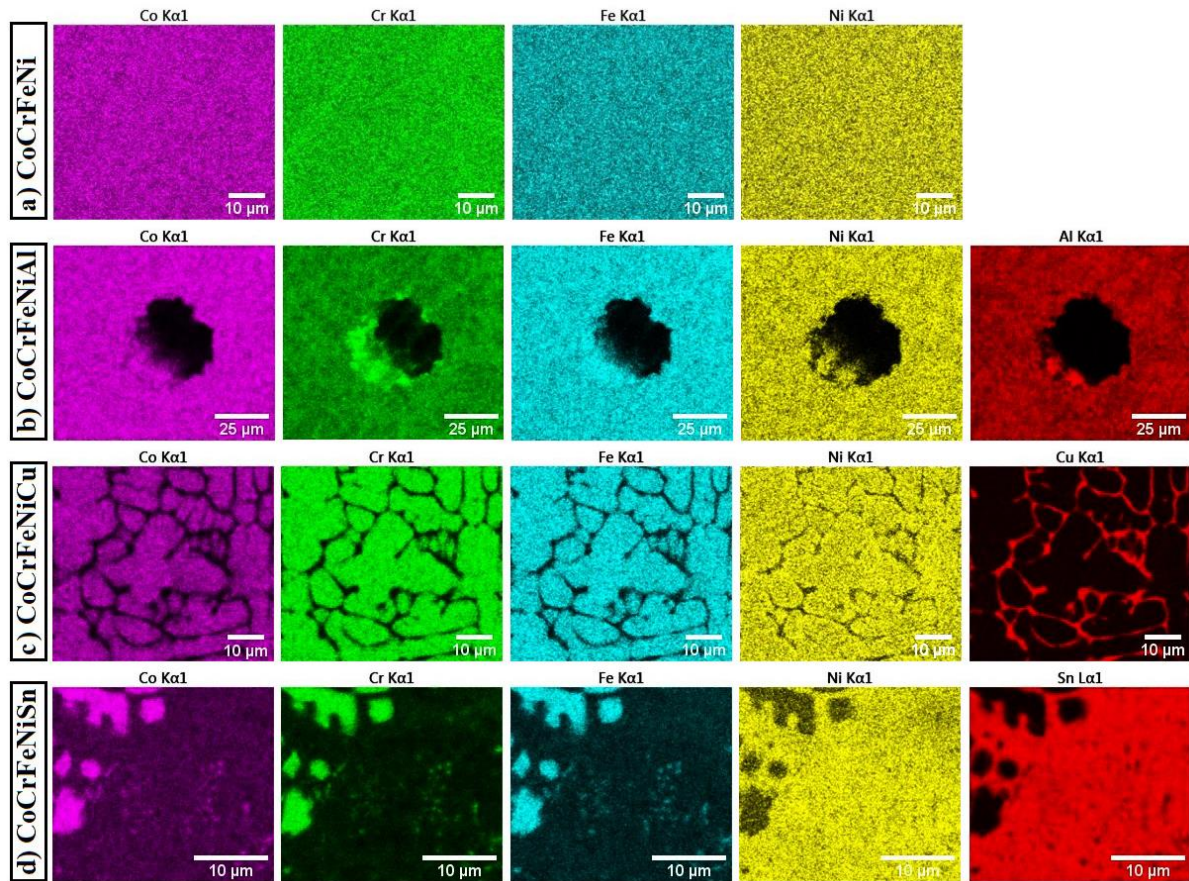


Figure 4.14: EDS mapping images of the surface of HEAs samples after immersion in 0.6 M NaCl solution at room temperature; a) CoCrFeNi, b) CoCrFeNiAl, c) CoCrFeNiCu, and d) CoCrFeNiSn (The contrast and sharpness of these images have been adjusted manually to aid visualization and analysis).

The distribution of elements in the SEM images taken post corrosion testing was determined by EDS mapping, as shown in Figure 4.14. The chemical distributions confirm the phase composition as assessed above and from XRD. It can be seen that there is (as measured by this technique) a homogeneous distribution of the constituent elements in the CoCrFeNi system Figure 4.14a, which will be the single FCC phase similar to the EDS mapping of the as-cast CoCrFeNi sample in Figure 4.5. The CoCrFeNiAl system shows a generally uniform distribution in a major CoCrFeNiAl (B2) phase that it is like the elemental distribution maps of this alloy before corrosion testing, Figure 4.5 (the defect in the center of the image is a corrosion pit), Figure

4.14b, with some slight structure visible in the distribution of Al and Ni elements in the bottom-left region of the pit, indicating a tendency of an Al-Ni phase (possibly an intermetallic) to precipitate in the area surrounding the Co-Cr-Fe-rich phase. It also reveals the possibility of forming a second Al-Ni-rich phase in this system. The addition of Cu or Sn to the main HEA system leads to a non-uniform elemental distribution and the formation of two phases. CoCrFeNiCu, Figure 4.14c, shows strong segregation of Cu way from the other elements, which are well-mixed. The Cu forms at the grain boundary regions, and correlates with the observed corrosion damage. It is also similar to the EDS mapping of the Cu segregation along the interdendritic region in pre-corrosion testing in this alloy, Figure 4.5. In CoCrFeNiSn, the bright region on the BSE image in Figure 4.14d is associated with Ni and Sn, likely to be a hexagonal Ni-Sn-rich phase, in Figure 4.14d while a second region can be confirmed as CoCrFeNi (the FCC phase). Clearly, EDS mapping in the as-cast CoCrFeNiSn sample in Figure 4.5 can reveal the elemental distribution in both the CoCrFeNi and Ni-Sn-rich phases corresponding to these EDS maps. The presence in the Ni-Sn-rich phases is confirmed by XRD analysis in section 4.1.1.

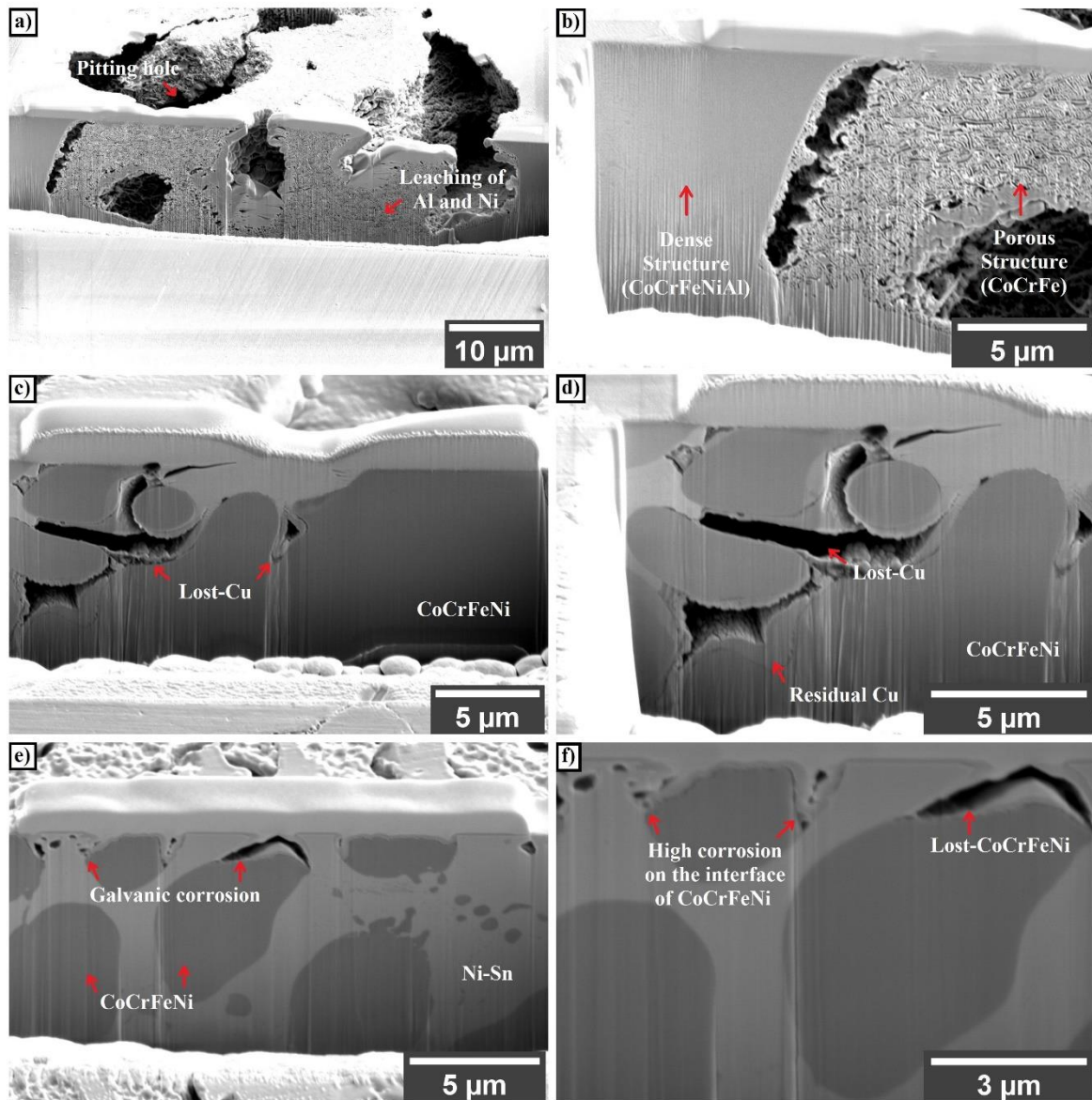


Figure 4.15: Cross-sectional SEM images of FIB cross sections through features observed on the surface of HEA samples immersed in 0.6 M NaCl solution at room temperature; a-b) CoCrFeNiAl, c-d) CoCrFeNiCu, and e-f) CoCrFeNiSn.

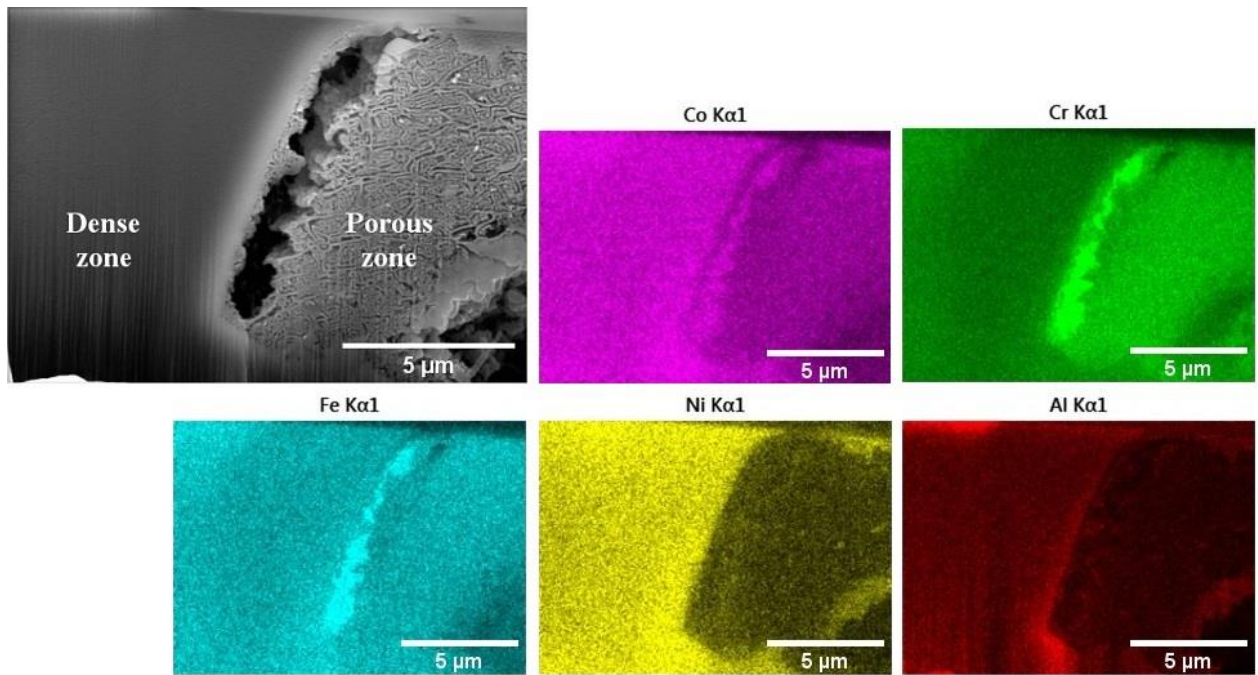


Figure 4.16: EDS mapping images of cross-sectional CoCrFeNiAl immersed in 0.6 M NaCl solution at room temperature.

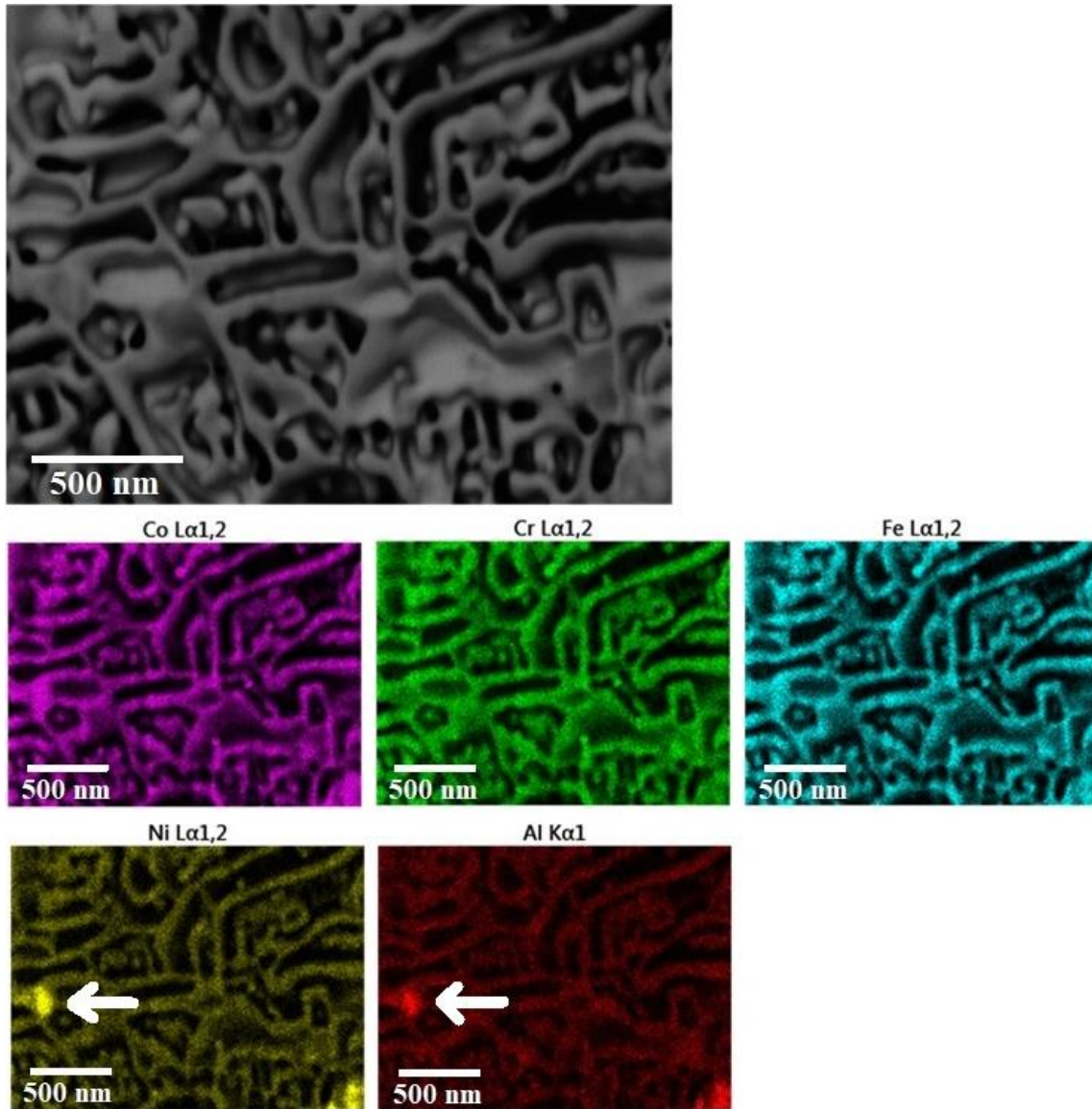


Figure 4.17: EDS mapping images of a cross-section through CoCrFeNiAl at high resolution showing in a porous Co-Cr-Fe-rich structure after corrosion testing in 0.6 M NaCl solution at room temperature.

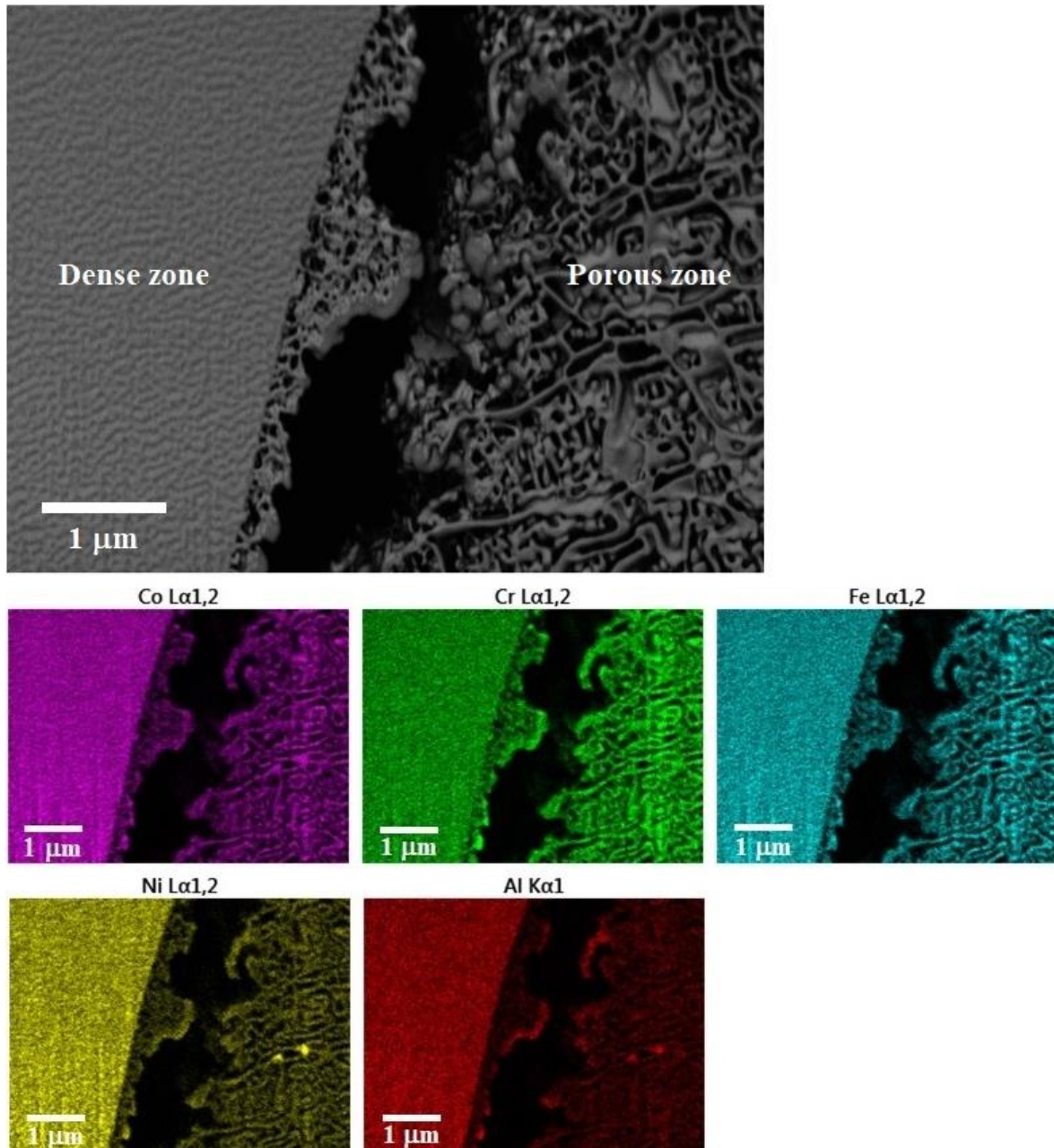


Figure 4.18: EDS mapping images of a cross-section through CoCrFeNiAl at high resolution showing in both the dense and porous regions after corrosion testing in 0.6 M NaCl solution at room temperature.

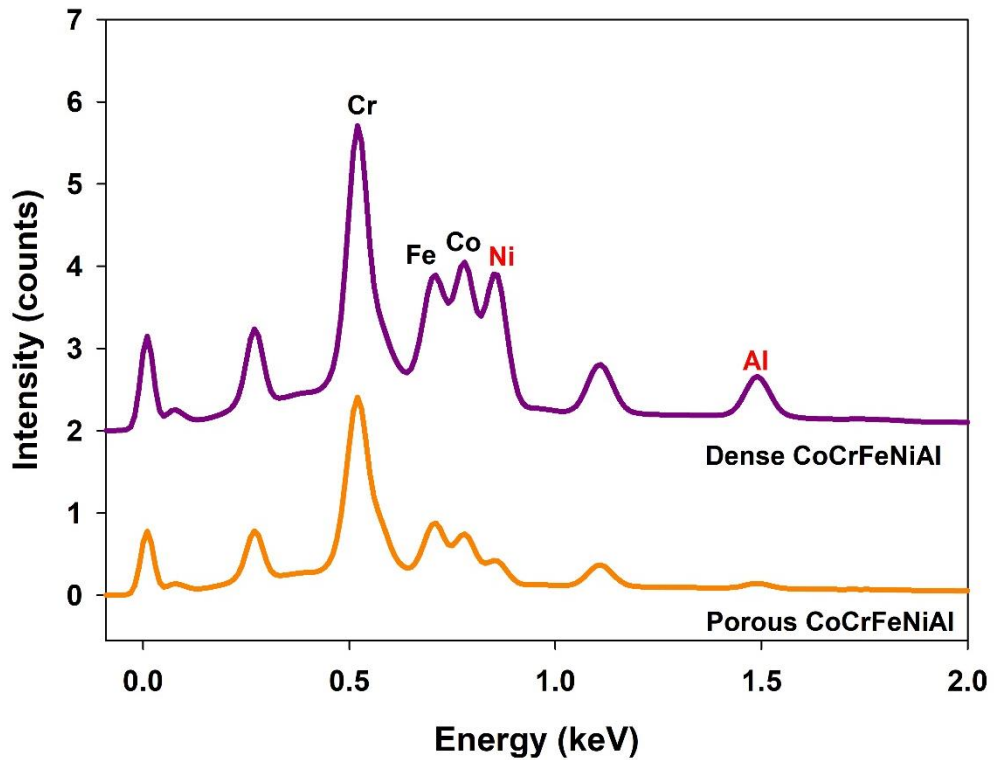


Figure 4.19: A chemical composition comparing dense and porous regions from the EDS data of Figure 4.18.

To explore the corrosion processes further, cross sections around particular features seen after corrosion in some of the samples were made with FIB and were imaged in the SEM, Figure 4.15. CoCrFeNiAl, Figure 4.15a and 4.15b, has two structures; one apparently porous which exists within other, larger cavities in the overall dense, unaffected structure; these larger cavities are also, sometimes vacant. The former of these is the first to be created in the corrosion process, and is likely to be the by-product of the selective leaching of two elements, Al and Ni (as shown by EDS maps, Figure 4.16). The remaining Fe, Co and Cr take up less volume and reorganize into a porous structure during a dealloying process, as confirmed in Figures 4.16-4.18. These EDS results indicate that this alloy may contain two phases. The former is the minor Al-Ni-rich phase, which may dissolve rapidly and is likely to have lower corrosion resistance than the Co-Cr-Fe-rich phase. This corrosion behaviour can be observed in the difference in the chemical compositions in the EDS maps at high resolution, Figures 4.17-4.18. These show that Al and Ni are present in a lower quantity in the porous regions, while high amounts of Co, Cr, and Fe are found in the remaining areas without porosity. The porous Co-Cr-Fe-rich structure may then form subsequently when the corrosion process is in a near-final state and develops to become a pit (Figures 4.16 and 4.18). The other phase in the alloy is the major CoCrFeNiAl (B2) phase shown in the dense zone (Figures 4.16 and 4.18) which is

similar to the EDS mapping of CoCrFeNiAl pre-corrosion testing (Figure 4.5). It shows a uniform distribution of Co, Cr, Fe, Ni, and Al elements in this region. As shown in Figure 4.17, it also reveals a region of porous structure with relatively high Co, Cr, and Fe levels. In addition, there is a possible observation of the Al-Ni-rich intermetallic compound, indicated by white arrows in this figure. Comparison of the chemical composition identified by EDS analysis in Figure 4.18 indicates a decrease in the intensity of the peaks corresponding to Ni and Al in the energy spectra at 0.85 and 1.49 keV, respectively, suggesting that these elements are removed from the alloy in a dealloying-like process, Figure 4.19.

Cross sectional SEM images of particular features identified on the surface of CoCrFeNiAl, CoCrFeNiCu, and CoCrFeNiSn were taken, and are shown in Figure 4.15. The intent of these images was to explore if these features were associated with the underlying microstructure of each of these alloys (it should be noted that the resolution of the analysis used is not sufficient to offer information on the microstructure within the oxide films formed). The cross-sectional image of corrosion features seen on the surface of CoCrFeNi shows the interconnected distribution of the Cu phase, which is corroded to a large extent in comparison to the FCC phase in Figures 4.15c and 4.15d, supporting the interpretation of this corrosion being galvanic in origin. The cross sectional image of CoCrFeNiSn, Figures 4.15e and 4.15f, shows attack of the CoCrFeNi phase in preference to the Ni-Sn phase. This is particularly high at the interface, as shown in Figure 4.15f. It is again likely to be due to micro-galvanic corrosion between FCC CoCrFeNi and the Ni-Sn-rich phase. Such a process could induce the dissolution of the FCC CoCrFeNi phase under a chloride environment. This indicates that the FCC CoCrFeNi phase has lower corrosion resistance in this environment than the Ni-Sn-rich phase.

4.3.3 Post-corrosion surface analysis (0.6 M NaCl solution)

The oxide films formed on the sample surfaces after the electrochemical experiment were analyzed by the XPS technique. This technique can determine chemical composition in the uppermost 5-10 nm of the sample surface and is, therefore, suitable for studying the passive film [136]. It should be noted that the method cannot, of course, elucidate the sub-nanometer structure of the oxide films produced, and a full analysis of this structure to assess the formation mechanisms and behavior during corrosion would require Transmission Electron Microscope observation, which is not performed here. The XPS survey spectra and high resolution XPS spectra in the binding energies range of 40-70 eV of alloy samples are shown in Figure 4.20. The spectra reveal the presence of Co, Cr, Fe, Ni, O and C on all HEA sample surfaces. Figure

4.20b shows the broad peaks of Co, Fe, and Ni elements. This can relate to the overlap of the main peaks in these elements. This figure does not focus on the fifth element present in the alloys, such as Al, Cu, and Sn, which would show main peaks at other binding energies. As in Figure 4.20a, the additional peaks that are seen on the CoCrFeNiAl, CoCrFeNiCu, and CoCrFeNiSn spectra are attributed to the presence of the fifth elements, Al, Cu and Sn. The C, O, and Sn peaks have a high intensity, while a low intensity of Cu and Al are observed. The detection of C is most probably due to adventitious carbon contaminations, as discussed in section 4.1.4. The presence of O suggests that an oxide film is formed on the sample surface, some metals being oxidized.

Table 4.9: The chemical composition on the sample surfaces after corrosion testing in 0.6 M NaCl solution.

Alloys	Relative atomic concentration (at.%)							
	Co	Cr	Fe	Ni	Al	Cu	Sn	O
CoCrFeNi	9.90	27.89	20.90	10.47	-	-	-	30.84
CoCrFeNiAl	7.18	16.42	8.86	10.05	15.11	-	-	42.38
CoCrFeNiCu	9.45	19.78	11.26	12.63	-	3.37	-	43.50
CoCrFeNiSn	3.37	19.36	7.37	5.13	-	-	8.11	56.65

The calculated relative atomic concentrations of the sample surface via XPS analysis are presented in Table 4.9. It is found that Cr is present at the surface in the highest proportion in all alloy systems (without considering the oxygen and carbon contents, but examining the main metallic elements intended to be present in all of the alloys (Co, Cr, Fe, and Ni); CoCrFeNi (27.9 at.%), CoCrFeNiCu (19.8 at.%), CoCrFeNiSn (19.4 at.%), and CoCrFeNiAl (16.4 at.%), while the proportion of the added alloying elements to the base CoCrFeNi are as follows; Al/CoCrFeNiAl (15.1 at.%), Sn/CoCrFeNiSn (8.1 at.%), and Cu/CoCrFeNiCu (3.4 at.%). A large amount of oxygen is detected, in the range of 30.8 at.% to 56.7 at.%. As in Appendix B, unexpectedly high carbon contamination is also seen. In particular, it would be expected that Cr, and possibly the alloying elements, lead to the potential for forming an oxide layer on the sample surface and may participate in such a layer. Thus, they are the vital factor directly relating to the improvement in corrosion properties of alloy samples, and XPS can be further used to examine and compare the oxidation state of these elements at the surface. From this, with the assumption that these are bonding with oxygen, it can be inferred which elements are present in any oxide film that is formed. In the discussion that follows, to be concise we

refer to the elements in their metallic state (e.g. Cr) and in the oxide corresponding to the oxidation state measured (e.g. Cr_2O_3); it must be noted however that the actual films formed are likely to mixtures of oxides of different elements. Detailed analysis of this by Transmission Electron Microscopy will take place in future work.

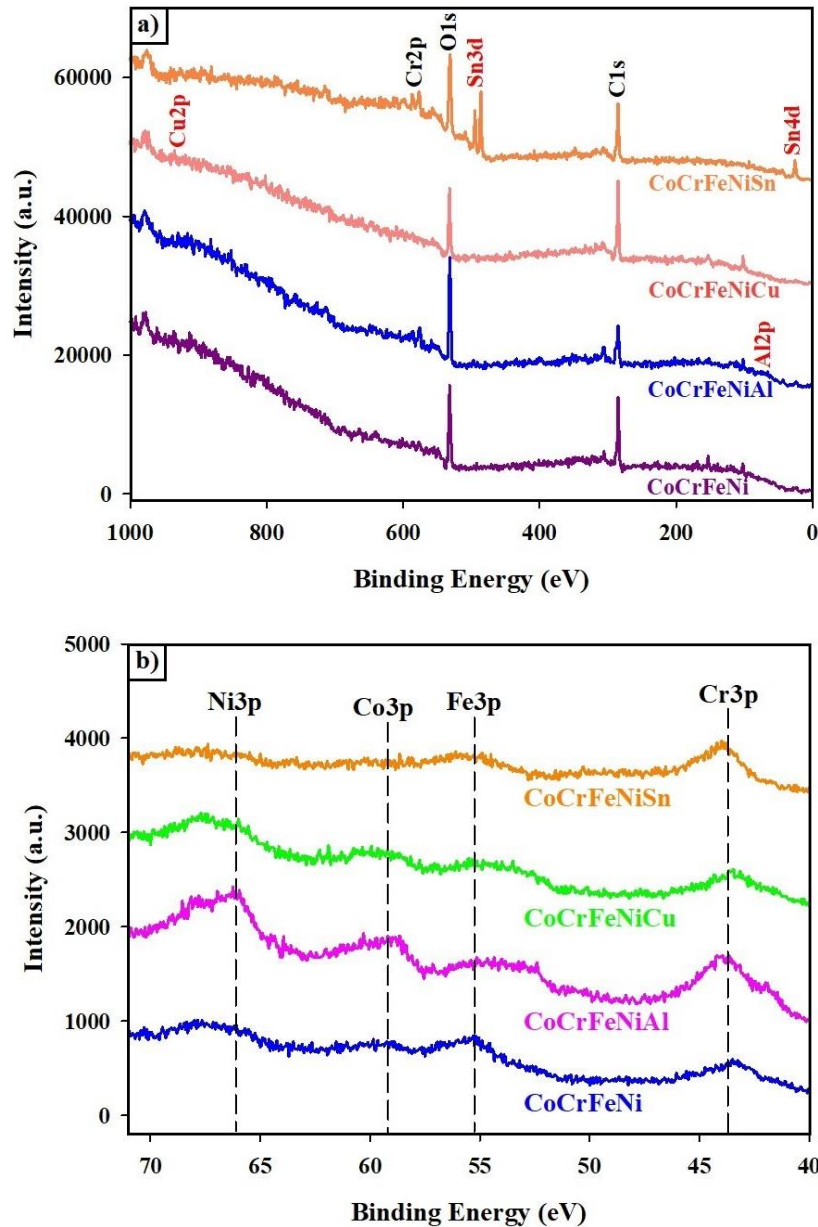


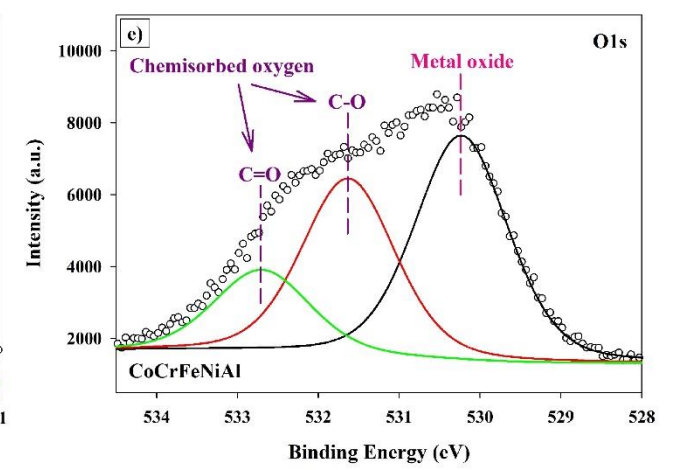
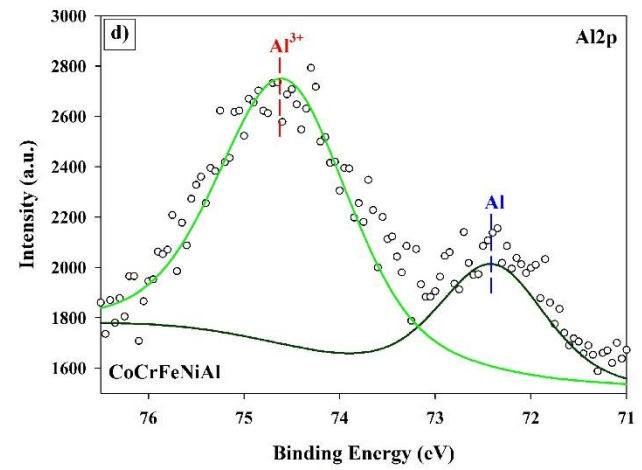
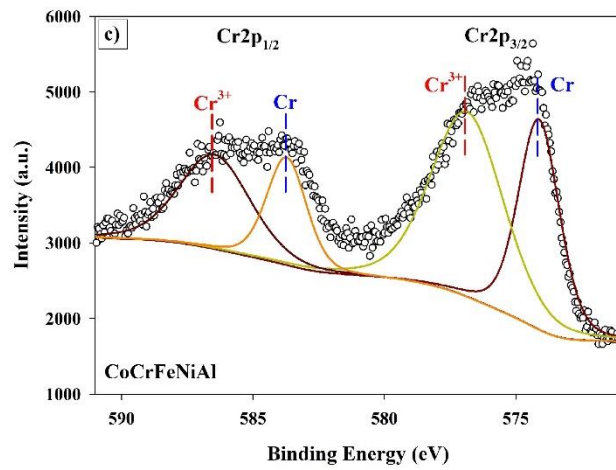
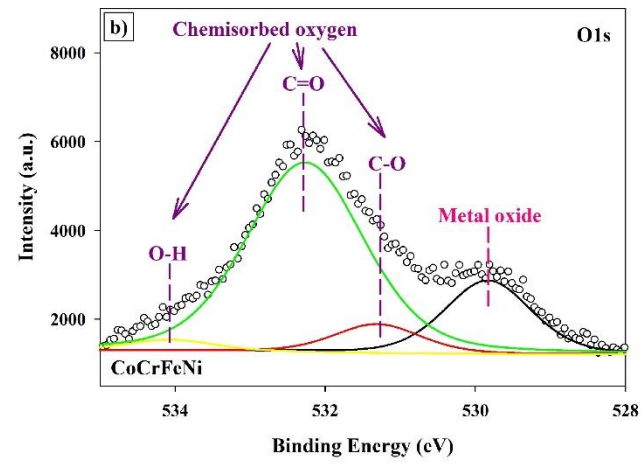
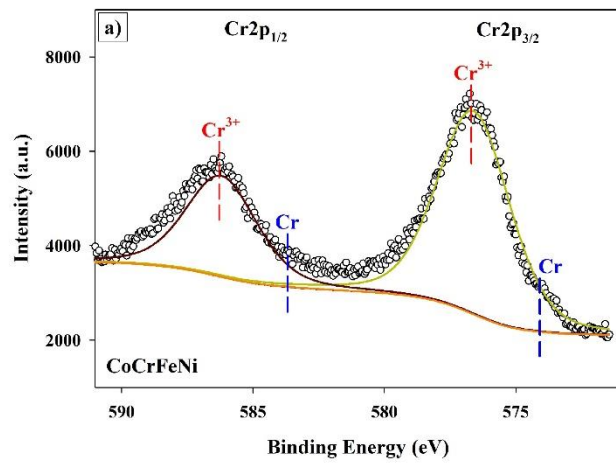
Figure 4.20: a) XPS survey spectra and b) high resolution XPS spectra in the binding energies range of 40-70 eV of alloy samples after corrosion testing.

Figure 4.21 shows the high resolution XPS spectra in the Cr 2p, Al 2p, Cu $2p_{3/2}$, Sn 3d, and O 1s peak regions of alloy samples. The Cr 2p spectra of all the HEA samples exhibit two main spin-orbit peaks, Cr $2p_{3/2}$ and Cr $2p_{1/2}$, separated by approximately 9.6 eV. The Cr $2p_{3/2}$ peaks can be deconvoluted into two components at the binding energies of 574.12 eV and

576.60 eV-576.90 eV which are attributed to Cr and Cr³⁺ (Cr₂O₃), respectively. This indicates that Cr₂O₃ is formed to a large extent on all the alloy samples. The Al 2p peak of the CoCrFeNiAl sample can be fitted into two peaks at the binding energies of 72.39 eV and 74.58 eV corresponding to Al and Al³⁺ (Al₂O₃), respectively. The high Al₂O₃ content of 74.50 at.% is observed. The Cu 2p_{3/2} peak of CoCrFeNiCu sample exhibits two main peaks of Cu and Cu¹⁺ (Cu₂O) at the binding energies of 932.68 eV and 933.70 eV, respectively, showing the low content of Cu₂O (18.26 at.%). The Sn 3d_{5/2} peak of CoCrFeNiSn can be fitted into two peaks at the binding energies of 484.80 eV and 486.39 eV which are attributed to Sn and Sn⁴⁺ (SnO₂), respectively. This suggests that SnO₂ is formed with high content of 86.47 at.%. The oxygen absorption in both metal oxide and chemisorbed oxygen is explained in section 4.1.4. The O 1s peak can be measured at the range of binding energies from 529.83 eV to 530.23 eV for metal oxide, and from 531.31 eV to 534.07 eV for chemisorbed oxygen. The atomic proportions of metal oxides and metals are summarized again in Table 4.10.

Table 4.10: The relative atomic proportion of metal oxides and metals (referred to atomic percentage of the total content of the element at the surface) on the sample surfaces after corrosion testing in 0.6 M NaCl solution.

Alloys	Cr (Cr at.%)		Al (Al at.%)		Cu (Cu at.%)		Sn (Sn at.%)	
	Cr ³⁺	Cr	Al ³⁺	Al	Cu ¹⁺	Cu	Sn ⁴⁺	Sn
CoCrFeNi	99.85	0.15	-	-	-	-	-	-
CoCrFeNiAl	60.85	39.15	74.50	25.50	-	-	-	-
CoCrFeNiCu	83.62	16.38	-	-	18.26	81.74	-	-
CoCrFeNiSn	100.00	0.00	-	-	-	-	86.47	13.53



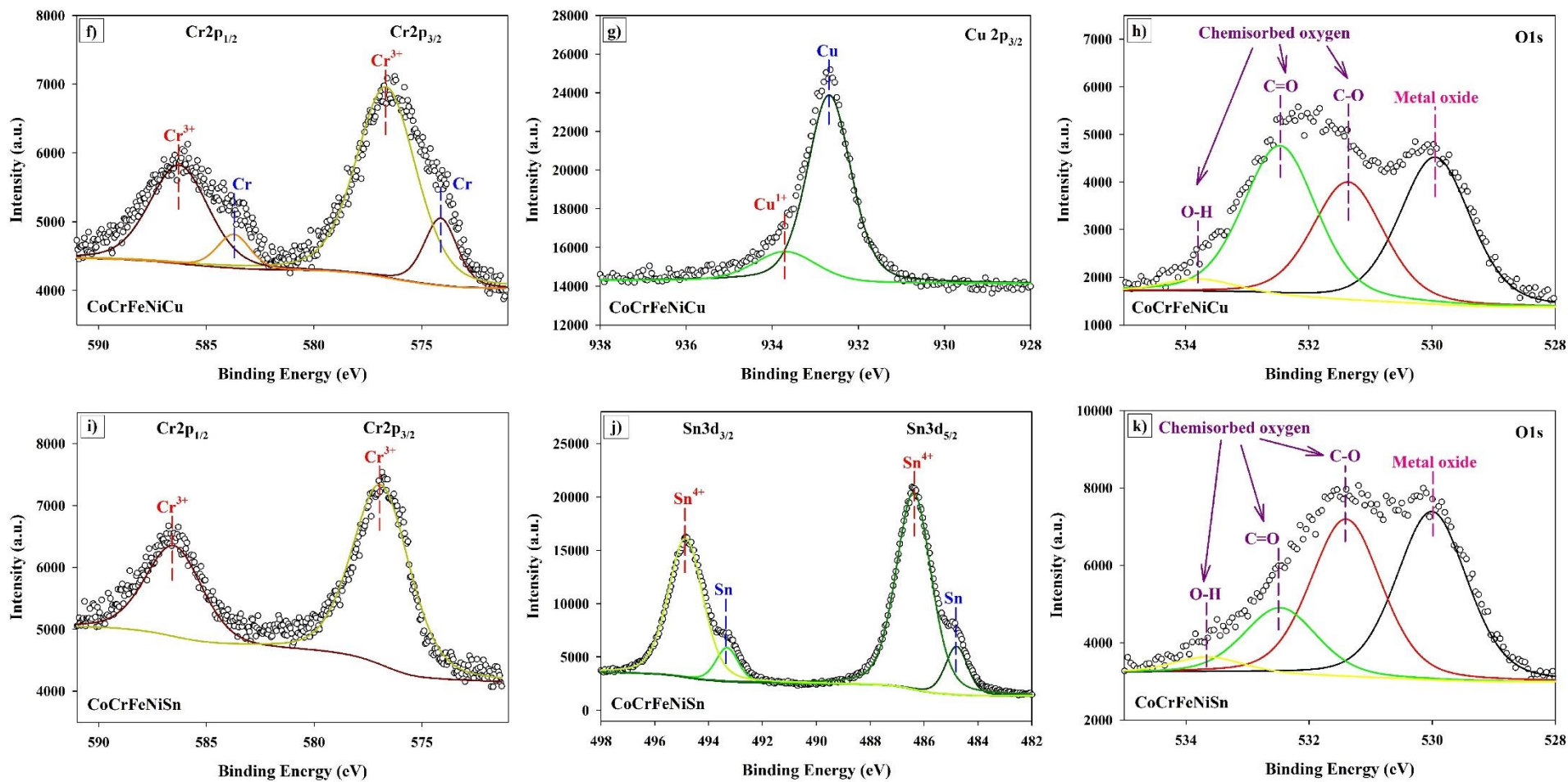


Figure 4.21: High resolution XPS spectra in the; a,c,f,i) Cr 2p, d) Al 2p, g) Cu 2p_{3/2}, j) Sn 3d, and b,e,h,k) O 1s peak regions of CoCrFeNi and three HEA samples after corrosion testing in 0.6 NaCl solution.

It can be seen from the results that the addition of Al and Cu have the effect of reducing the formation of Cr_2O_3 (more of the Cr is in the metallic state), while the oxide films which are generated by these alloying elements, Al_2O_3 and Cu_2O , are at moderate to low intensity Al_2O_3 (74.50 at.%) and Cu_2O (18.26 at.%). These oxide films are weakly bonded and unstable under the tested conditions, and thus lead to the poorer corrosion resistance observed in these alloys, being present at a lower proportion after corrosion testing [2,136]. Al_2O_3 is likely to be relatively weak at preventing chloride-ion attack, owing to chloride-ion adsorption and incorporation in the oxide film [196,197]. Chloride ions are likely to move toward the interface between metal and oxide surfaces. It leads to a lower passive current density with chloride-ion incorporation and oxide thinning prior to pitting potential, thereby blistering and rupturing the oxide film [196,197]. In the case of Cu_2O films, it may stem from the formation of oxide films at a low thickness, approximately 5 nm [198]. The thickness of Cu_2O films is likely to insufficiently resist attack by chloride ions. By contrast to these alloys, the addition of Sn results in an increase in proportion of conversion of metallic form to oxide for both Cr_2O_3 (100 Cr at.%) and SnO_2 (86.47 Sn at.%). This system can therefore form a significant passive film, which is stronger bonding than the other oxides formed on these alloys. XPS analysis confirms that there is the largest proportion of the passive film remaining after corrosion in the CoCrFeNiSn. The Cr_2O_3 is known to be a stable, corrosion-resistant oxide, and there is evidence to suggest that SnO_2 is also a stable film with high potential for protecting against chloride-ion attack [199,200].

4.3.4 Corrosion analysis in 0.6 M H_2SO_4 solution

To understand the corrosion behaviour of all experimental samples in 0.6 M H_2SO_4 solution, the Potentiostat/Galvanostat electrochemical instrument was conducted, Figure 4.22 and Table 4.11.

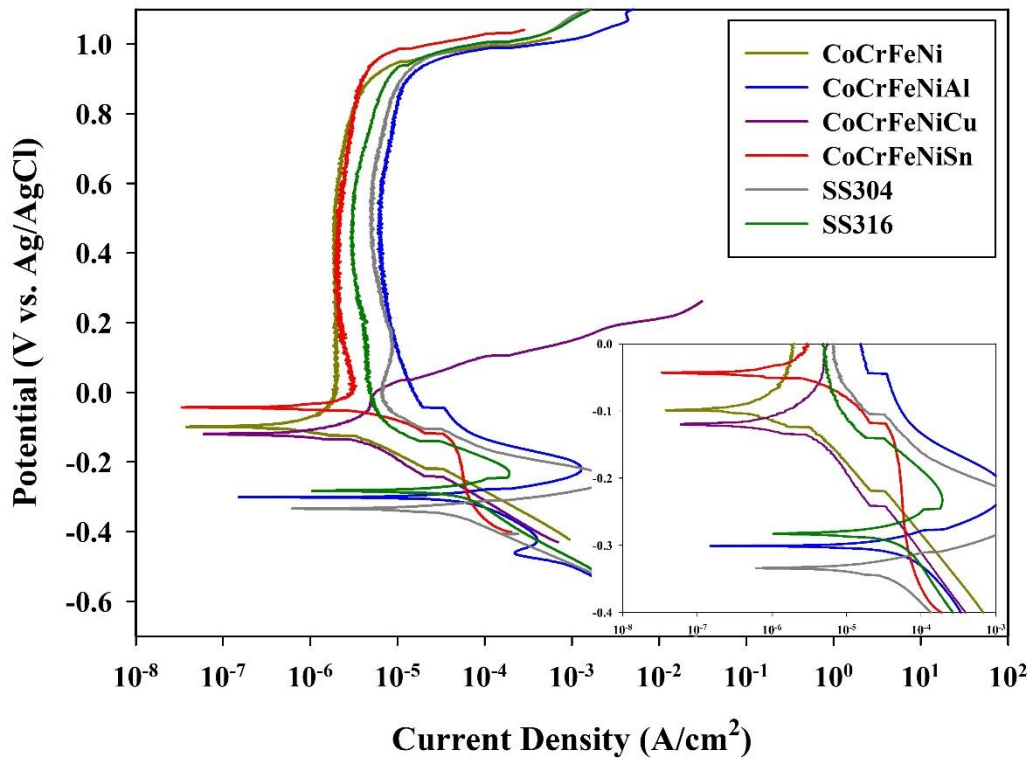


Figure 4.22: Corrosion behaviour of four alloy and two stainless steel samples immersion in 0.6 M H₂SO₄ solution.

The corrosion behaviour of the four alloy and two stainless steel samples in an aggressive acidic solution is displayed in Figure 4.22. This graph indicates the relation between the applied potential and the measured current density under the sulfuric acidic environment. Some of the alloy systems have higher corrosion resistance than conventional stainless steels under these conditions, while some alloys show lower corrosion resistance than the stainless steels tested, as seen in Figure 4.22. Four corrosion parameters, corrosion potential (E_{corr}), corrosion current density (i_{corr}), transpassive potential (E_t), and passivation potential (ΔE_p ; $E_t - E_{corr}$) are presented in Table 4.11. Two important parameters, E_{corr} and E_t , are used to identify the corrosion properties in acidic solution for this work.

Table 4.11: The analytical corrosion data of four alloy and two stainless steel samples in 0.6 M H₂SO₄ solution at room temperature.

Alloys	Solution	Average pH values	E_{corr} (mV _{Ag/AgCl})	i_{corr} (μ A/cm ²)	E_t (mV _{Ag/AgCl})	ΔE_p (mV _{Ag/AgCl})
CoCrFeNi			-98±17	1.70±0.08	935±0.1	1033±18
CoCrFeNiAl			-309±1	76.38±1.57	934±1	1254±1
CoCrFeNiCu	0.6 M	0.45	-121±7	4.40±0.64	9±6	129±6
CoCrFeNiSn	H ₂ SO ₄		-38±8	3.65±0.73	968±1	1006±7
SS304			-355±6	47.79±9.16	936±3	1291±4
SS316			-291±4	52.61±1.14	949±7	1240±7

In acidic solution, some of the (two-phase) alloys in this work have poorer corrosion behaviour than the single-phase alloy of the CoCrFeNi system, while the corrosion resistance of another two-phase alloy in the same experiment is superior to the CoCrFeNi alloy. The addition of Sn to form CoCrFeNiSn yields an alloy with the lowest corrosion sensitivity of all the samples examined here with the highest E_{corr} and E_t . These are increased compared to the main CoCrFeNi alloy from -98 mV (CoCrFeNi) to -38 mV (CoCrFeNiSn) in the case of E_{corr} and from 935 mV (CoCrFeNi) to 968 mV (CoCrFeNiSn) for E_t . In contrast, the Cu addition to form CoCrFeNiCu gives an alloy which shows high corrosion sensitivity with values of E_{corr} and E_t reduced from CoCrFeNi; E_{corr} from -98 mV (CoCrFeNi) to -121 mV (CoCrFeNiCu) and E_t from 935 mV (CoCrFeNi) to 9 mV (CoCrFeNiCu). The lowest E_t value of CoCrFeNiCu system in this work may lead to a poor passivity with the narrowest passive zone (ΔE_p ; 129 mV), Figure 4.22. Furthermore, it was found that some of these alloys have higher corrosion resistance in this acidic solution than stainless steels. CoCrFeNiSn has higher values of E_{corr} and E_t than both SS304 and SS316 samples. The E_{corr} and E_t values of CoCrFeNiAl are lower than SS316.

4.3.5 Post-corrosion microstructure and surface analysis (0.6 M H₂SO₄ solution)

To understand the post-corrosion microstructure and surface chemical composition, SEM and XPS were conducted (Figures 4.23–4.25 and Tables 4.12–4.13).

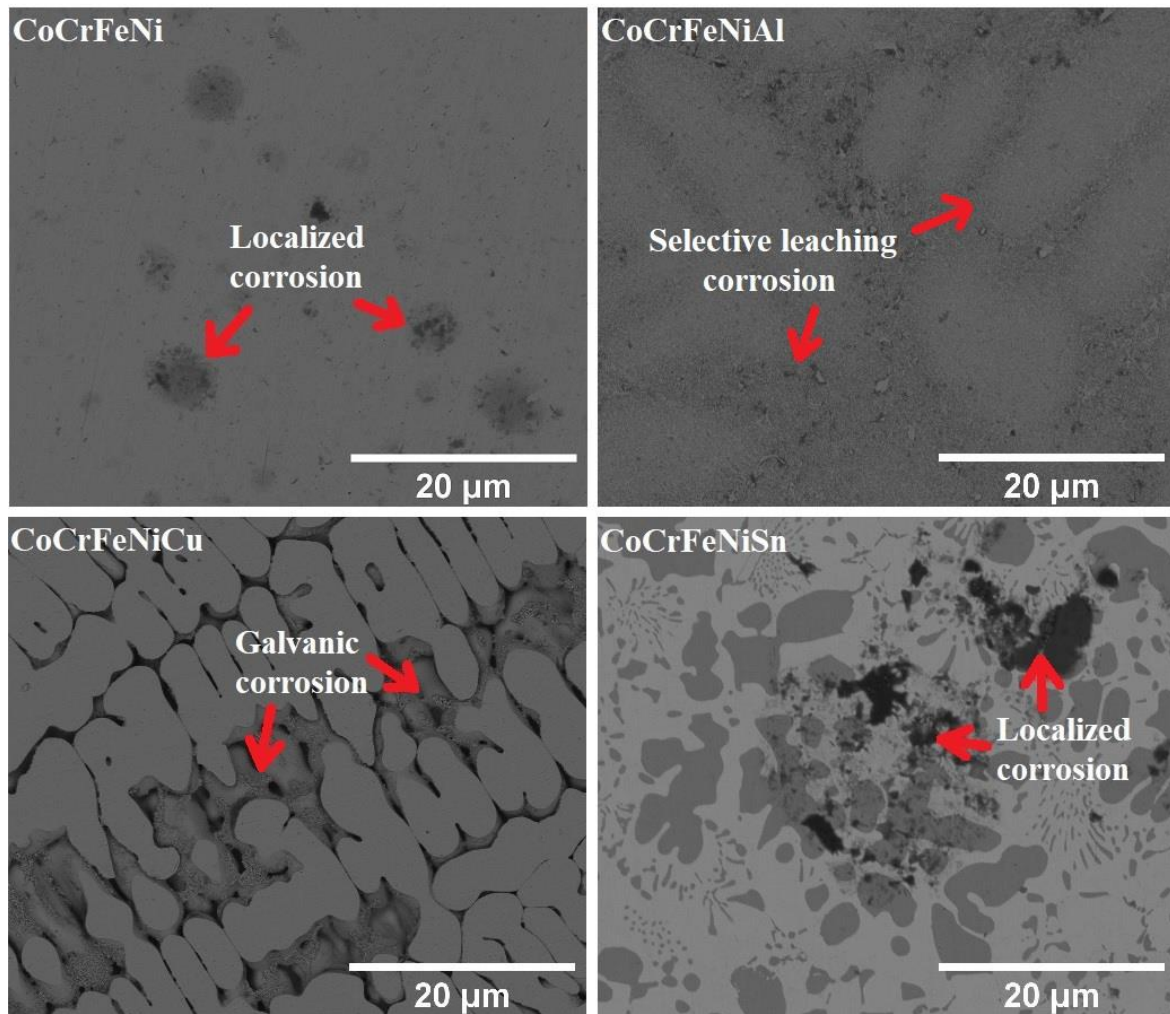


Figure 4.23: BSE micrographs on the corroded surface of four alloy samples after immersion in 0.6 M H_2SO_4 solution.

Sample surfaces after immersion in 0.6 M H_2SO_4 solution were examined by SEM and in all cases surface damage, as shown in Figure 4.23, was observed. In both CoCrFeNi and CoCrFeNiSn localized corrosion is likely to occur. Evidence that could correspond to galvanic corrosion can be found on the surface of CoCrFeNiCu systems, while selective dissolution can be observed at the CoCrFeNiAl surface. In the case of CoCrFeNiAl, preferential dissolution has taken place, revealing features that may be the interdendritic region or grain boundaries. This interdendritic area may contain an Al-Ni-rich second phase, while a major B2 phase is likely to form on the dendritic area, as discussed in sections 4.1.1 and 4.1.2. It could result in a difference in corrosion potential between the two regions, leading to selective dissolution. It can be observed in the removal of the Al-Ni-rich phase. CoCrFeNiCu also presents evidence of a galvanic corrosion process, which could be driven by the different corrosion potential of the Cu-rich and CoCrFeNi phases, preferentially attacking the Cu-rich phase, and indicates

sensitivity to intergranular attack along the lost Cu-rich phase on grain boundaries. This corrosion behaviour seems to be similar to that occurring in this alloy immersed in chloride solution, as reported by Muangtong et al. [172].

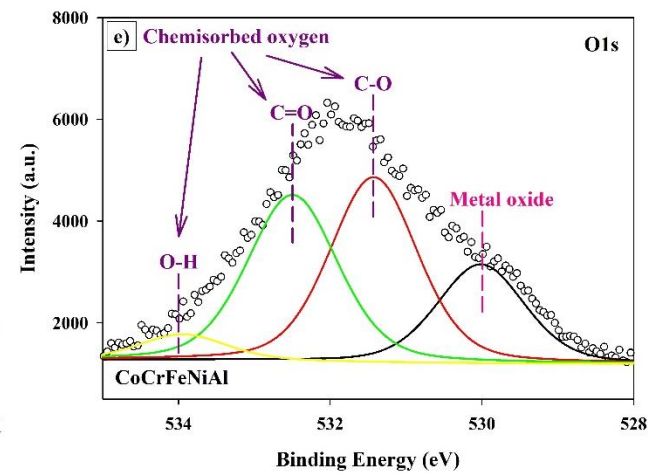
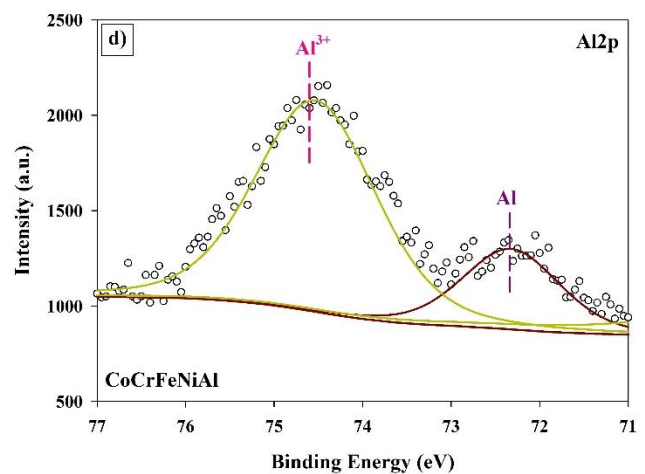
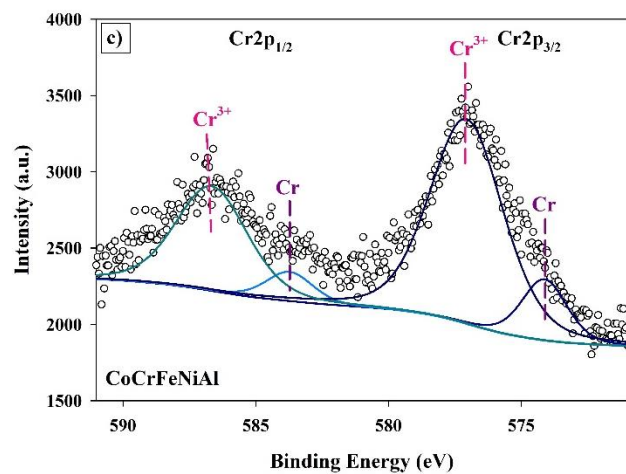
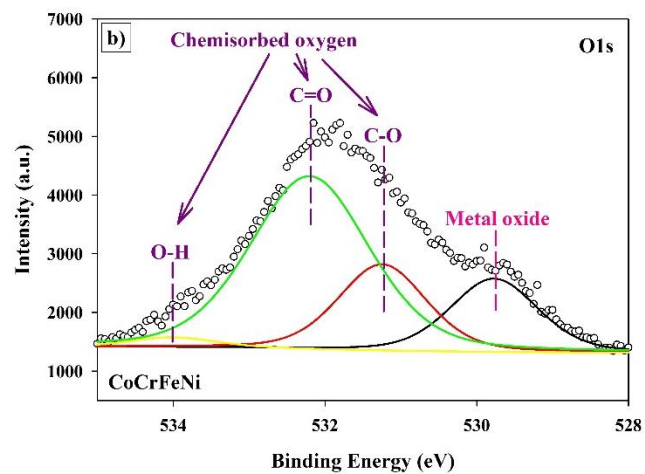
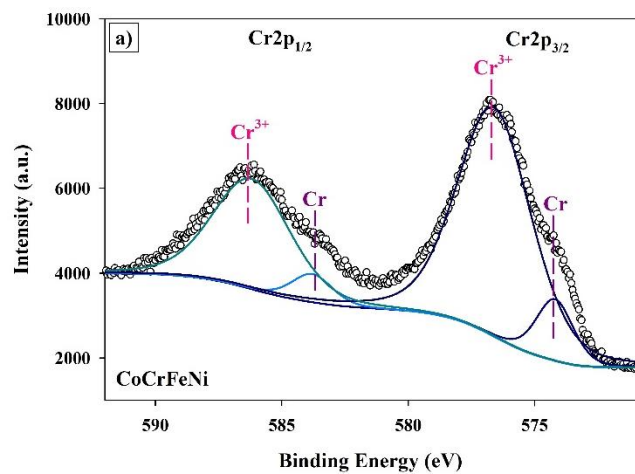
As discussed in section 4.1.4, HEAs formed from several metallic elements are likely to create multi-oxide films on the sample surface when exposed to appropriate environments. Four types of oxide-film (Co_3O_4 , Cr_2O_3 , Fe_2O_3 , and NiO) have been reported to form on the surface of CoCrFeNi [175], but it is likely that there are complex passive films, with multiple elements involved in the formation of complex oxides, present on the samples in this work. As the films are not imaged in detail, it is not possible to verify the precise local film composition and structure on each sample. Instead, XPS has been used, which gives an indication of the oxidation state of particular elements of interest. This investigation has been focussed on the state of the Cr and of the additional element added to the alloys (Al, Cu and Sn), determining if they are in the metallic form or with an oxidation state that would correspond to their most common oxide (Cr_2O_3 , Al_2O_3 , Cu_2O , and SnO_2). This decision has been made as Cr_2O_3 is considered a highly efficient protective film in many solutions [101,125,132,137] and the behaviour of the additional element is likely to be an important factor in determining the differences in the behaviour of the samples. Looking at the state of these individual elements will allow assessment of the extent to which they are involved in the oxide film, but it should be recognised that there are likely to be more complex passive films on the sample surface.

The relative atomic concentration of the elements present at the alloy surfaces was first explored by XPS analysis (the chemical composition without oxygen and carbon content has been assessed for the bulk alloy pre-corrosion testing to be in all cases relatively close to equiatomic, Table 4.2 and [172]). All alloy specimens were measured after corrosion testing in 0.6 M H_2SO_4 solution as summarized in Tables 4.12. This result is similar to the XPS analysis of post-corrosion testing in chloride solution. The presence of Cr in the oxidation state corresponding to Cr_2O_3 is likely to play a vital role in the protective film to resist corrosion attack in acidic solution. It indicates that the proportion of Cr detected is the highest metallic composition in almost all alloy systems (after immersion in acid it is 35.6 at.% in CoCrFeNi , 28.5 at.% in CoCrFeNiSn and 26.1 at.% in CoCrFeNiCu), except for the CoCrFeNiAl alloy, where it is at 11.5 at.% after acid immersion. This dominance of Cr near the surface is likely to be due to its role in protective oxides at the surface. The presence of such a passive film should decrease the corrosion sensitivity of the alloy specimen in an acidic electrolyte solution. In the CoCrFeNiAl alloy, Al is the majority metallic element at the surface, at 22.6 at.% after

acid immersion. Al and Cr in the major CoCrFeNiAl (B2) phase in the CoCrFeNiAl system may for example form a mixed (Cr,Al)₂O₃ layer due to the individual oxides being isostructural, allowing substitution between Al- and Cr-oxides, as discussed in section 4.4.1. In addition, the presence of oxygen and carbon on the sample surface can be detected via the XPS measurement. A high oxygen content, in the range of 32.9 at.% to 44.2 at.%, is found in almost all alloy systems in this experiment, as shown in Table 4.12. The oxygen observation, Table 4.12 and Figure 4.24, relates to the oxidation state, due to the oxide formation from metallic elements on the exposed surface with oxygen in the air, sections 4.1.4 and 4.3.3. This result is similar to the unexpectedly high carbon detection on the sample surface, Fig 4.24, assumed to result from carbon contamination during handling or shipping processes, as discussed in sections 4.1.4 and 4.3.3, and may have a similar origin.

Table 4.12: The relative atomic concentration (at.%) at the sample surfaces for the alloys under study post-corrosion testing in 0.6 M H₂SO₄ solution.

Alloys	Relative atomic concentration (at.%)							
	Co	Cr	Fe	Ni	Al	Cu	Sn	O
CoCrFeNi	8.78	35.62	12.54	10.16	-	-	-	32.89
CoCrFeNiAl	4.87	11.46	6.55	10.89	22.62	-	-	43.61
CoCrFeNiCu	7.39	26.11	9.47	8.22	-	4.59	-	44.21
CoCrFeNiSn	8.85	28.54	6.48	12.97	-	-	6.19	36.95



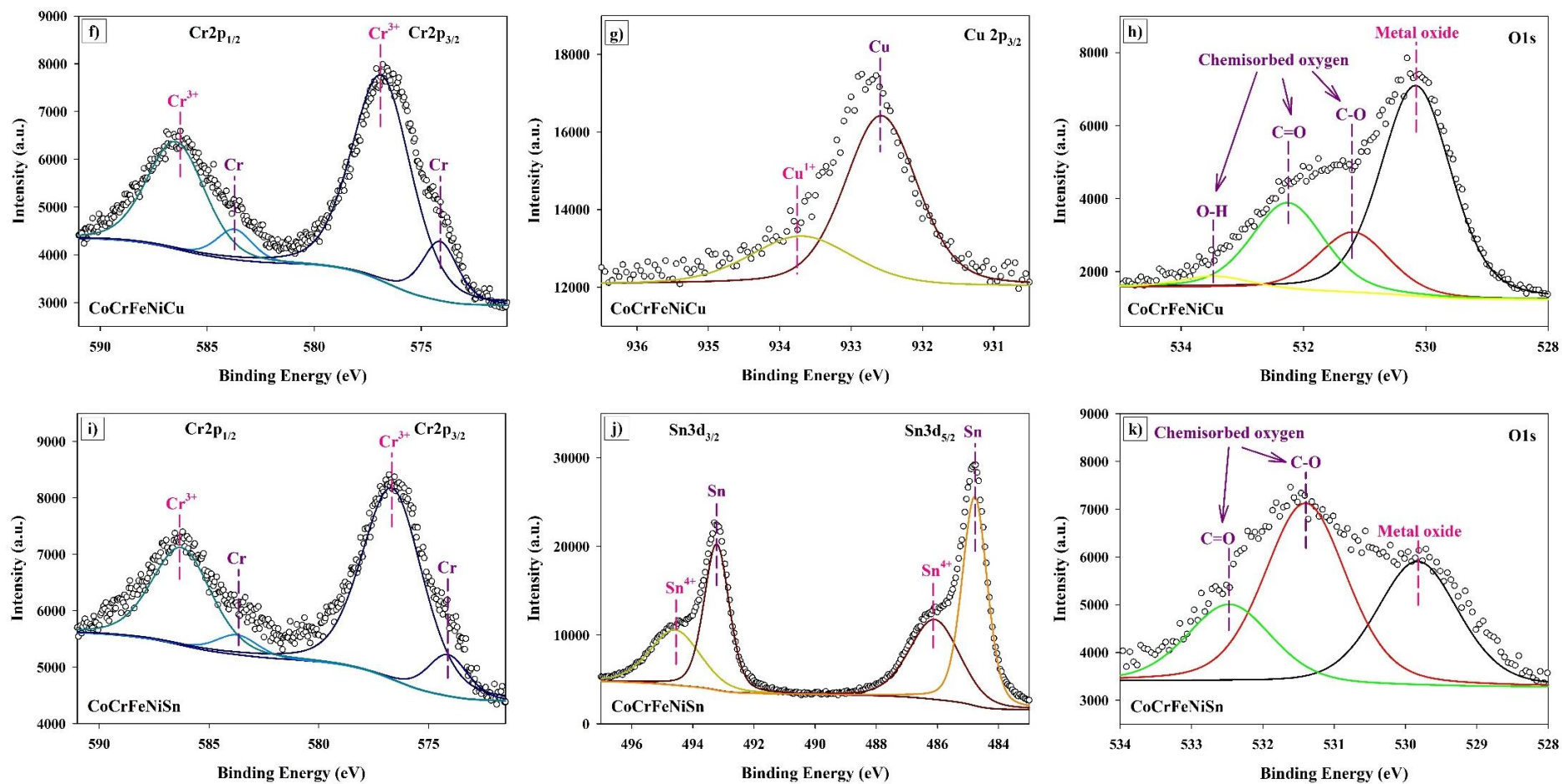


Figure 4.24: The XPS spectra of alloys analysed post-corrosion testing in 0.6 M H₂SO₄ solution to present the metal and metal-oxide regions of; a,c,f,i) Cr 2p, d) Al 2p, g) Cu 2p_{3/2}, j) Sn 3d, and b,e,h,k) O 1s peaks.

Figure 4.24 shows XPS spectra for high-resolution evaluation of the samples after exposure to H₂SO₄ acidic solution. Five elemental XPS spectra; Al 2p, Cr 2p, Cu 2p_{3/2}, Sn 3d, and O 1s, are used to assess the chemical state of the corresponding atomic species (and thus indicate whether these metallic atoms tend to be present in the metallic form or as compounds; likely to be oxides) at the sample surfaces. The XPS technique is suitable for analyzing surface chemistry or observing the interaction between the exposed sample surface and its environment to form an oxide film. Its measured data are in the form of the values of the released binding energy by electrons emitted from samples and the intensity value of each detected binding energy [160]. The XPS depth profile for the conditions used in this work is approximately 5-10 nm. It is typically sufficient to identify the chemical composition of the passive film [136]. While for thin films the interaction depth could be enough to also detect signal from the metal below the film, XPS can typically separate the spectrum of the underlying metal from its oxide film, leading to the definitive identification of passive film on the alloy surface [160]. The results are consistent with a main protective film of Cr₂O₃ formed by the interaction between Cr³⁺ and O²⁻. Cr 2p spin-orbit coupling consisting of Cr 2p_{3/2} and Cr 2p_{1/2} is detected in all alloys analysed. The deconvoluted Cr 2p_{3/2} peak can be found at the binding energies of 574.12 eV-574.20 eV (Cr metal) and 576.60 eV-577.06 eV (Cr oxide). For the three alloying elements which distinguish the samples here (Al, Cu and Sn), the formation of Al₂O₃ with Al³⁺ in the CoCrFeNiAl system was indicated by two peaks of Al 2p spectra at the binding energies of 72.33 eV (Al metal) and 74.53 eV (Al oxide). The Cu 2p_{3/2} peak suggesting the creation of Cu₂O from Cu¹⁺ in the CoCrFeNiCu system was detected from two peaks at the binding energies of 932.58 eV (Cu metal) and 933.70 eV (Cu oxide). Two spin orbitals can be detected in the Sn 3d spectrum; Sn 3d_{5/2} and Sn 3d_{3/2} for the formation of SnO₂ with Sn⁴⁺. The Sn 3d_{5/2} peak can be found at the binding energies of 484.78 eV (Sn metal) and 486.09 eV (Sn oxide). In the case of O 1s peak which referred to the oxidation state for all alloys in this work, it can be detected at the binding energies of 529.77 eV to 530.16 eV (metal oxide) and from 531.18 eV to 534.01 eV (chemisorbed oxygen).

Table 4.13: The relative surface atomic concentration (at.%) of each analysed element at the surface post-corrosion testing in 0.6 M H₂SO₄ solution in metallic and ionized form (taken to indicate the relative involvement of the atoms in either the alloy in metallic form or as metal oxides).

Alloys	Cr (Cr at.%)		Al (Al at.%)		Cu (Cu at.%)		Sn (Sn at.%)	
	Cr	Cr ³⁺	Al	Al ³⁺	Cu	Cu ¹⁺	Sn	Sn ⁴⁺
CoCrFeNi	11.92	88.08	-	-	-	-	-	-
CoCrFeNiAl	15.48	84.51	27.48	72.51	-	-	-	-
CoCrFeNiCu	15.78	84.21	-	-	71.19	28.81	-	-
CoCrFeNiSn	12.56	87.44	-	-	-	-	57.04	42.96

Table 4.13 represents the calculated proportions for each of the analysed elements between the metallic form and as ions (taken to represent oxides) for the alloy systems examined here. The data are collected for the surface of the samples after corrosion assessment in acidic solution. These indicate the quality of the passive-film present (via the extent to which the surface is oxidized, and whether a strong, resistant oxide is formed), which will strongly affect the performance in resisting corrosion attack. The addition of the further alloying elements to the main four component equiatomic alloy system affects the oxide formation on the specimen surface. In acidic solution, the added fifth elements may reduce the proportion of the Cr in a state that suggests it may be participating in oxide. The reduction is least with Sn addition, where CoCrFeNiSn has 87.4 at.% of the Cr oxidized (versus 88.1 at.% in CoCrFeNi), and greatest with Cu added into CoCrFeNiCu where 84.2 at.% of the Cr is oxidized. The additional elements are partially oxidized themselves after acid immersion. On the surface of CoCrFeNiAl 72.5 at.% of the Al is oxidized, but only 28.8 at.% of the Cu on the surface of CoCrFeNiCu, as in Table 4.13. Furthermore, the additional elements in CoCrFeNiSn and CoCrFeNiAl are well involved in the formation of a passive film; of alloying elements; the oxidation states would correspond to SnO₂ and Al₂O₃. In relation to Cr, which may be the optimum oxide to form, CoCrFeNi has the highest ability to generate the Cr oxide in acidic solution where 88.1 at.% of this element at the surface being converted.

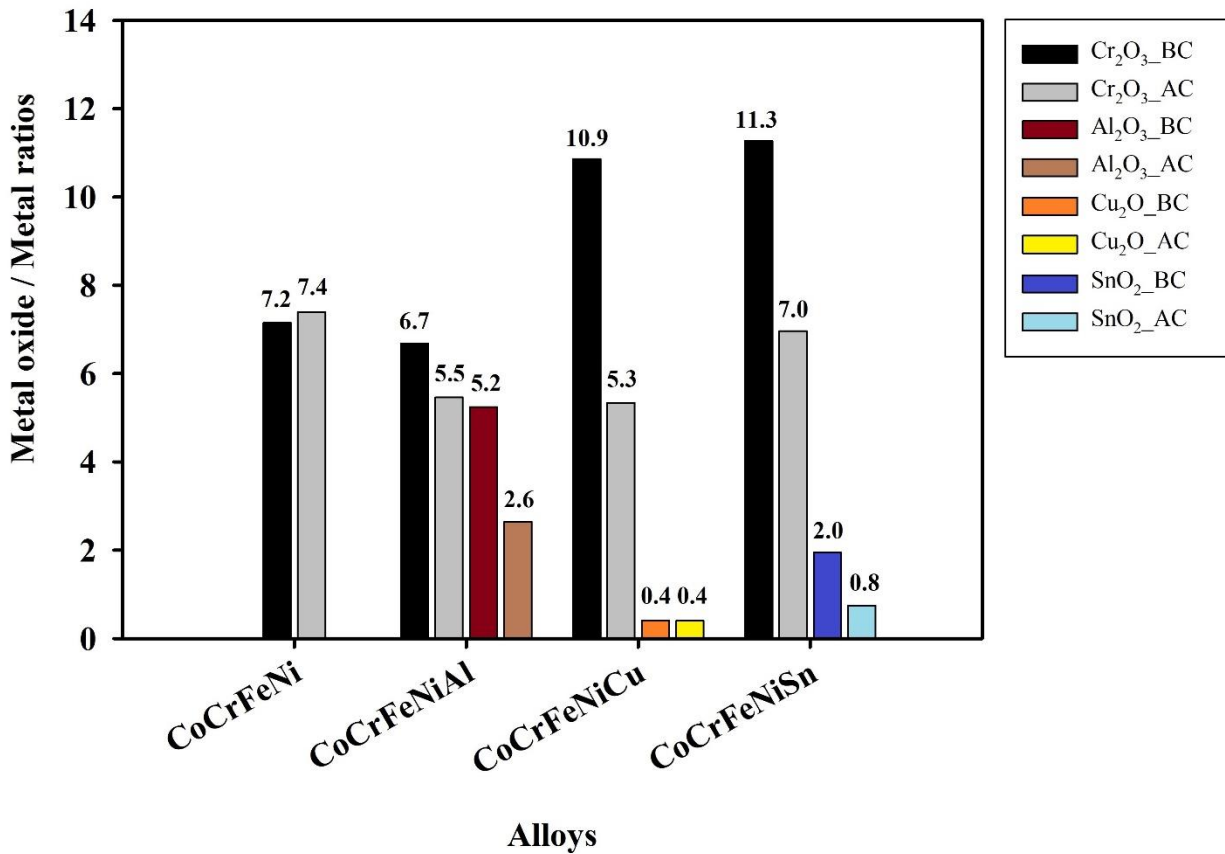


Figure 4.25: The comparison of the extent of oxidation at the sample surface, assessed via the ratio of metal oxide to metal in four alloys in pre- and post-corrosion testing in 0.6 M H₂SO₄ solution (BC refers to before corrosion testing, and AC means after corrosion testing).

Figure 4.25 shows the change in the extent of oxidation on the sample surface via the ratio of metal oxide to metal detected for four alloys, CoCrFeNi, CoCrFeNiAl, CoCrFeNiCu, and CoCrFeNiSn, in pre- and post-corrosion testing in a sulfuric acid environment. The proportion of Cr in the oxidized form in almost all alloys is decreased after corrosion in sulfuric acid; this could correlate with a reduction in the amount of oxide film (containing oxidized Cr) present at the surface. CoCrFeNiCu has the highest proportion decrease in oxidized Cr from 10.9 (pre-corrosion testing) to 5.3 (post-corrosion testing). On the other hand, the lowest amount of oxidized Cr proportion reduction, from 6.7 (pre-corrosion testing) to 5.5 (post-corrosion testing), is found in CoCrFeNiAl. In the case of the additional element, which was also examined as well as Cr, the proportion of Cu in the oxidized form at the CoCrFeNiCu surface after testing in sulfuric acid remains the same as pre-corrosion testing at 0.4. CoCrFeNiAl has a larger decrease in the proportion of Al in the oxidized form, from 5.2 (pre-corrosion testing) to 2.6 (post-corrosion testing), while the proportion of Sn in the oxidized form in CoCrFeNiSn also decreases significantly from 2.0 (pre-corrosion testing) to 0.8 (post-

corrosion testing). If taken to suggest the removal of oxides containing the relevant elements, these results can be said to correspond with the microstructure change seen resulting from corrosion by sulfuric acid in Figure 4.23. In the case of CoCrFeNiAl, it shows that an Al-Ni-rich second phase in CoCrFeNiAl may be easily removed in this solution, possibly by galvanic corrosion attack, as there appears to be a significant reduction of the amount of oxide film. However, a galvanic attack can occur when a sample is exposed without polarisation. In contrast, selective dissolution typically occurs when a sample is polarised, which indicates differences in the electrochemical potentials of both phases. Thus, the CoCrFeNiAl surface should be formed by selective dissolution rather than galvanic corrosion. In the case of CoCrFeNiCu, galvanic corrosion is likely occurring to attack along the interdendritic region of the Cu-rich phase. Some of the adjacent material of the main CoCrFeNi phase may also be removed; this could be responsible for a reduction in oxide containing Cr. In the formation of localized corrosion on the CoCrFeNiSn surface, most of the corroded area occurs in the CoCrFeNi phase. Evidence of corrosion attack is rarely seen in the hexagonal Ni-Sn-rich phase. This may correlate with the large decrease in the proportion of Cr in the oxidized state (and therefore possible oxide film removal) after corrosion testing. CoCrFeNi may show repassivation, reforming oxides containing Cr after localized corrosion attack. This could be inferred from the increase in the proportion of Cr in the oxidized state after corrosion testing, from 7.2 (pre-corrosion testing) to 7.4 (post-corrosion testing).

4.3.6 Corrosion analysis in 0.6 M NaAlO₂ solution

To understand the corrosion behaviour of all experimental samples in 0.6 M NaAlO₂ solution, the Potentiostat/Galvanostat electrochemical instrument was conducted, Figure 4.26 and Table 4.14.

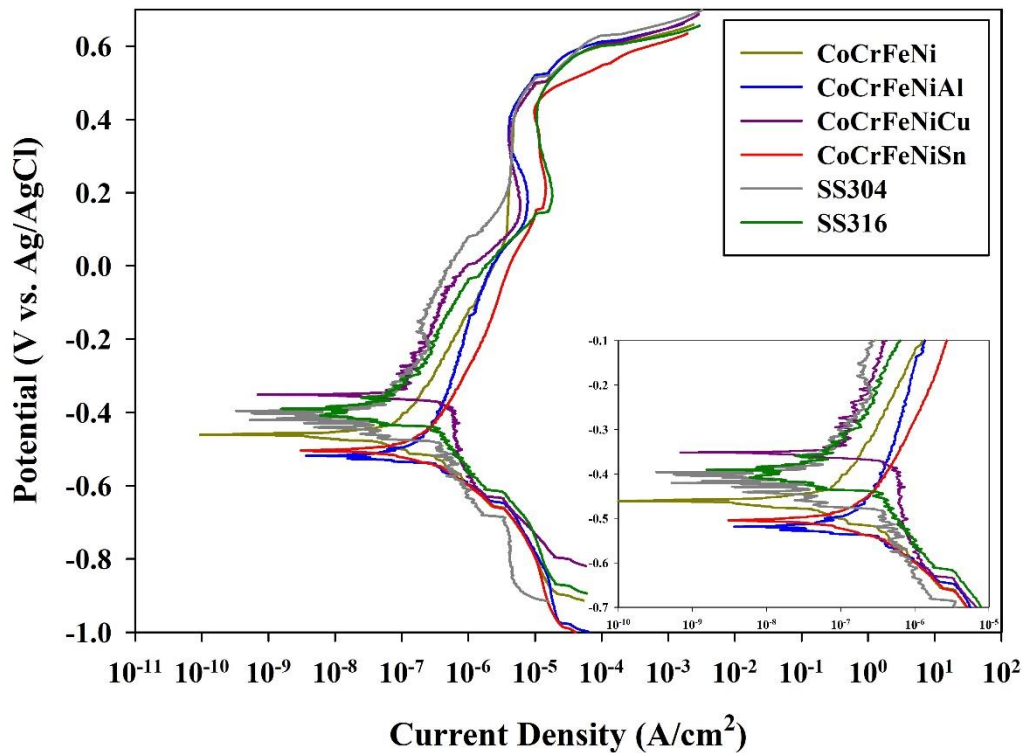


Figure 4.26: Corrosion behaviour of four alloy and two stainless steel samples immersion in 0.6 M NaAlO₂ solution.

As shown in Figure 4.26, the relationship between the potential in $V_{Ag/AgCl}$ and the current density in A/cm^2 indicates the corrosion behaviour of four experimental alloys and two commercial stainless steel samples, all in the as-cast state, in a strongly alkaline solution with a pH of 13.11. The novel alloys all contain CoCrFeNi, with different additional elements, Al, Cu, and Sn, being a significant variable leading to a change in corrosion parameters, Table 4.14. Of the parameters measured and shown in Table 4.14 (corrosion potential (E_{corr}), corrosion current density (i_{corr}), transpassive potential (E_t), and passivation potential (ΔE_p ; $E_t - E_{corr}$) it is E_{corr} and E_t which are used to identify the corrosion properties in this work, as was done in the corrosion experiments in both chloride and sulfuric acid solutions, sections 4.3.1 and 4.3.4. These corrosion parameters may show the effect of the alloying elements on the corrosion resistance of the experimental alloys in this work.

Table 4.14: The analytical corrosion data of four alloy and two stainless steel samples in 0.6 M NaAlO₂ solution at room temperature.

Alloys	Solution	Average pH values	E_{corr} (mV _{Ag/AgCl})	i_{corr} (μ A/cm ²)	E_t (mV _{Ag/AgCl})	ΔE_p (mV _{Ag/AgCl})
CoCrFeNi			-431±8	0.06±0.03	513±2	944±9
CoCrFeNiAl			-504±6	0.23±0.01	510±4	1014±7
CoCrFeNiCu	0.6 M	13.11	-337±34	0.22±0.12	517±13	854±37
CoCrFeNiSn	NaAlO ₂		-491±24	0.20±0.06	458±7	949±29
SS304			-416±15	0.24±0.14	500±1	916±16
SS316			-398±14	0.07±0.02	506±4	904±16

For corrosion testing in alkaline solution, the single phase alloy of CoCrFeNi shows higher corrosion resistance than most of the dual-phase systems tested. However, one two-phase alloy tested in this work is likely to be superior to CoCrFeNi. The Cu addition in CoCrFeNiCu shows the best values of E_{corr} and E_t . E_{corr} and E_t values of CoCrFeNiCu are higher than those of CoCrFeNi; E_{corr} changes from -431 mV (CoCrFeNi) to -337 mV (CoCrFeNiCu) and E_t from 513 mV (CoCrFeNi) to 517 mV (CoCrFeNiCu). Al and Sn added to CoCrFeNi decrease the values of E_{corr} and E_t compared with CoCrFeNi. Their E_{corr} values drop from -431 mV (CoCrFeNi) down to -504 mV (CoCrFeNiAl) and -491 mV (CoCrFeNiSn), while their E_t values drop from 513 mV (CoCrFeNi) down to 510 mV (CoCrFeNiAl) and 458 mV (CoCrFeNiSn). However, Table 4.14 shows that CoCrFeNiAl (ΔE_p ; 1,014 mV) and CoCrFeNiSn (ΔE_p ; 949 mV) have higher passivity than other alloys in this work. In addition, CoCrFeNiCu presents better corrosion behaviour than the stainless steel samples assessed with the higher values of E_{corr} and E_t than SS316 and SS304.

4.3.7 Post-corrosion microstructure and surface analysis (0.6 M NaAlO₂ solution)

To understand the post-corrosion microstructure and surface chemical composition, SEM and XPS were conducted (Figures 4.27–4.29 and Tables 4.15–4.16).

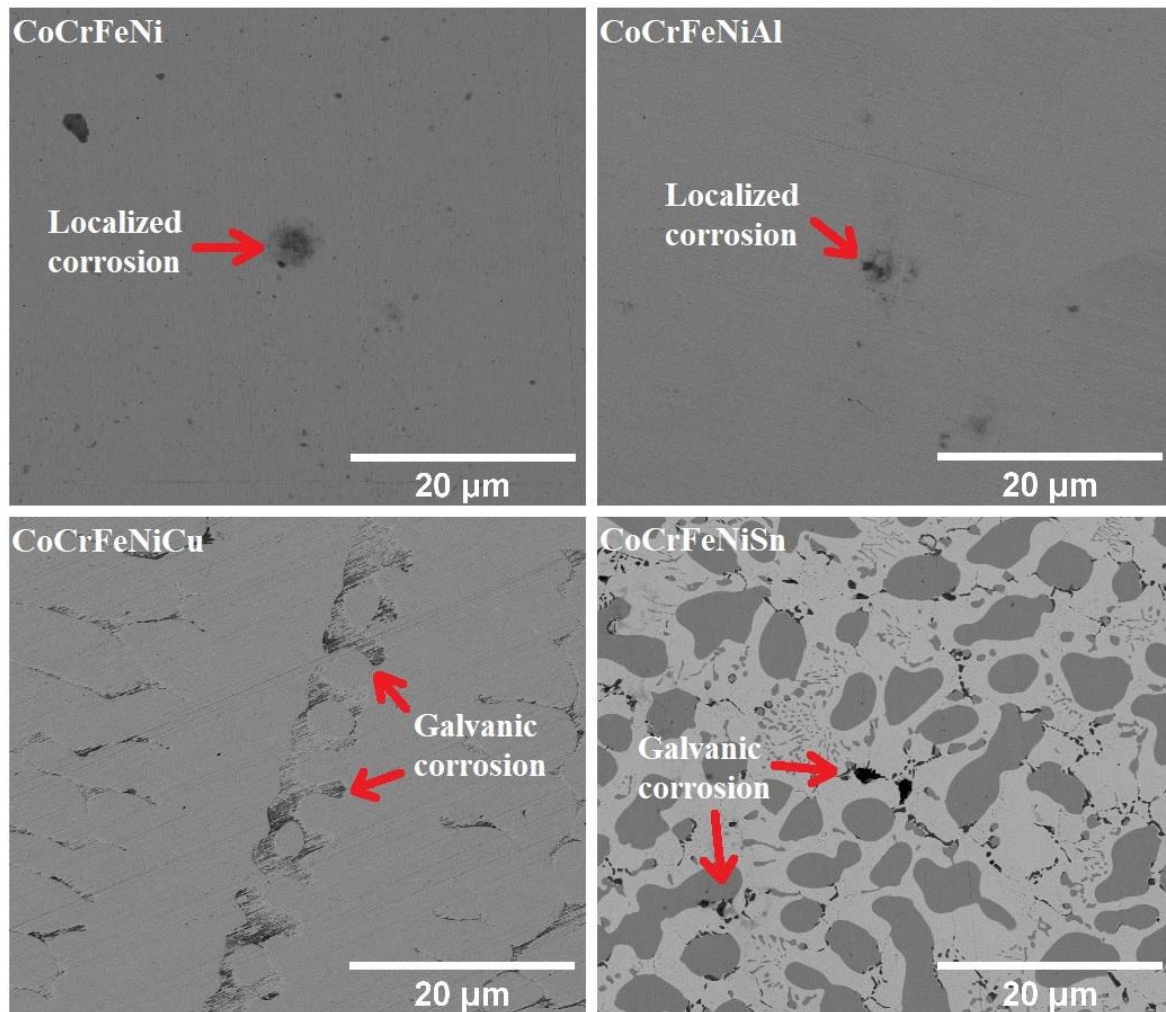


Figure 4.27: BSE micrographs on the corroded surface of four alloy samples after immersion in 0.6 M NaAlO₂ solution.

The appearance of the sample surfaces after exposure to alkaline solution shows some different features to the result of exposure to acidic solution in some of the systems, as presented in Figure 4.27. CoCrFeNi and CoCrFeNiAl show localized corrosion, while galvanic corrosion, with a particular phase being attacked while the other is relatively unchanged, occurs in CoCrFeNiCu and CoCrFeNiSn. CoCrFeNiCu again shows corrosion damage on the segregated Cu-rich phase, though compared to the result of the acidic electrolyte the level of this is low, while it is the CoCrFeNi phase in the microstructure of CoCrFeNiSn where dark regions, likely to be holes formed in the surface, have been found. It can be inferred that there exists a difference in potential between the phases in these alloys which show two phase microstructures and where differences in corrosion behaviour of the phases is found in the BSE images. The corroded Cu in CoCrFeNiCu and the lost CoCrFeNi in CoCrFeNiSn were therefore likely damaged by galvanic corrosion attack, while the CoCrFeNi in CoCrFeNiCu

and the Ni-Sn in CoCrFeNiSn were protected in this solution. In addition, the level of surface damage observed in the four alloy systems appears likely to vary in the different electrolytes. All four alloys appear to have a higher level of surface damage when tested in an acidic solution, as compared with corrosion testing in an alkaline solution, Figures 4.23 and 4.27. This qualitative difference corresponds to the measurement of a higher value of i_{corr} for the four alloy systems measured in corrosion tests in an acidic solution, Tables 4.11 and 4.14.

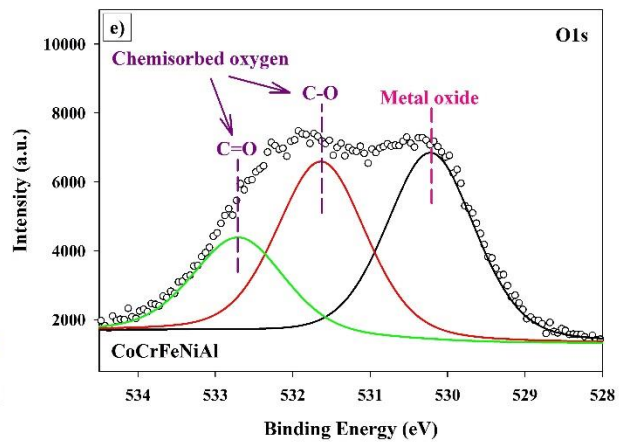
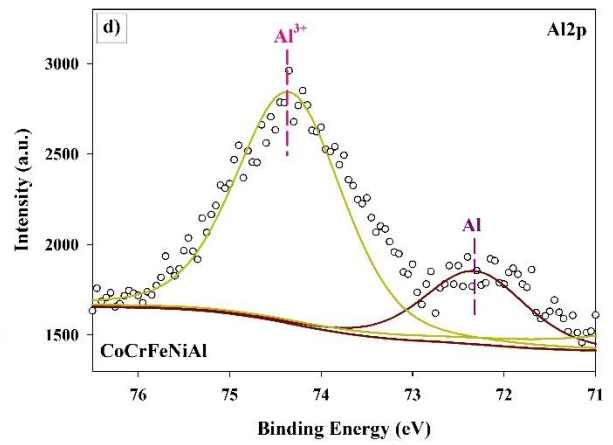
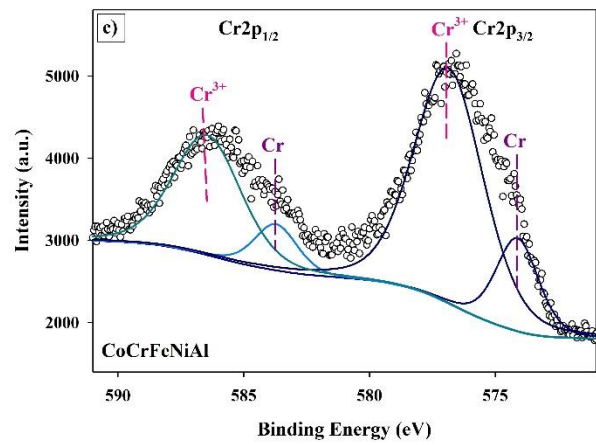
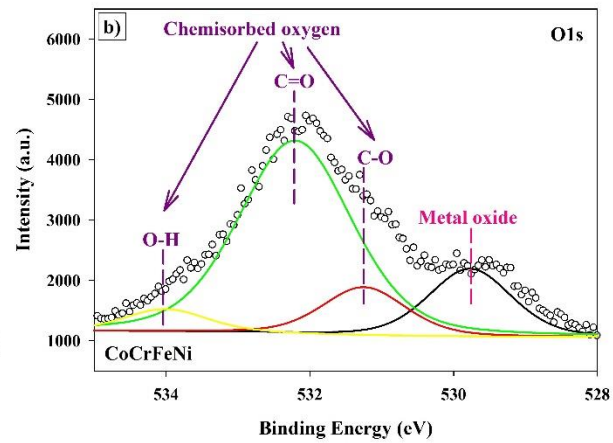
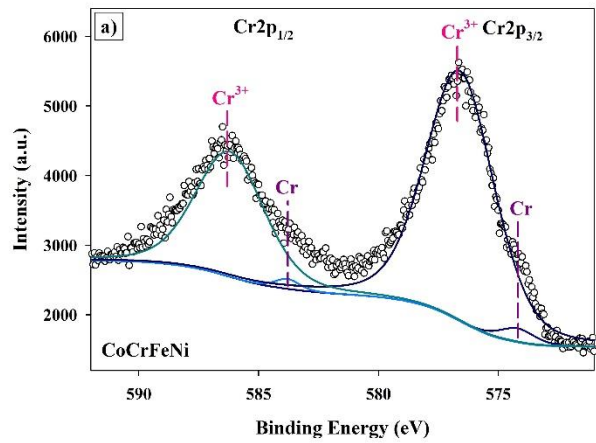
As discussed in sections 4.1.4 and 4.3.5, the evidence found indicates that multiple component alloys probably react with oxygen to form oxides involving several metallic elements on the alloy surface. The surface of CoCrFeNi alloy, as reported in [175], showed four metallic-oxide species, such as Co_3O_4 , Cr_2O_3 , Fe_2O_3 , and NiO. The alloys in this work are therefore also likely to create complex metal oxides from multiple metallic elements. As discussed in section 4.3.5, XPS is a surface chemical analysis, generating signal from emissions that give information on the binding energy of electrons in the metallic sample [160]. The XPS depth profile expected for the conditions used in this work is approximately 5-10 nm, which may mean the signal comes from both the metal oxides on the sample surface, and the metal underneath. The identification of Cr in the oxidation state corresponding to Cr_2O_3 is particularly used in this work as Cr_2O_3 itself is a good protective film to resist general corrosion [101,125,132,137]. The common oxidation states of the additional metallic elements, (i.e. corresponding to Al_2O_3 , Cu_2O , and SnO_2) were also selected for observation as these elements constitute the main differences between the alloys tested.

Table 4.15: The relative atomic concentration (at.%) at the sample surfaces for the alloys under study post-corrosion testing in 0.6 M NaAlO₂ solution.

Alloys	Relative atomic concentration (at.%)							
	Co	Cr	Fe	Ni	Al	Cu	Sn	O
CoCrFeNi	10.62	24.11	16.63	14.94	-	-	-	33.70
CoCrFeNiAl	7.07	12.16	8.83	11.23	16.05	-	-	44.66
CoCrFeNiCu	8.27	19.33	13.50	9.81	-	3.29	-	45.80
CoCrFeNiSn	10.51	19.62	16.53	1.46	-	-	7.13	44.75

As shown in Table 4.15, the relative atomic concentration of the elements present at the alloy surfaces was first explored by XPS analysis (the composition has been evaluated for the bulk alloy pre-corrosion testing to be in all cases relatively close to equiatomic when any measured oxygen and carbon content is neglected, Table 4.2 and [172]). All alloy specimens

were measured after corrosion testing in 0.6 M NaAlO₂ solution as summarized in Table 4.15. This indicates that the proportion of Cr detected is the highest in almost all alloy systems after in alkaline immersion. It is 24.1 at.% in CoCrFeNi, 19.6 at.% in CoCrFeNiSn, 19.3 at.% in CoCrFeNiCu. The exception is in CoCrFeNiAl, where it is 12.2 at.% after alkaline immersion. These results are similar to corrosion testing in 0.6 M H₂SO₄ solution. The presence of Cr is potentially useful, as it could act as a protective oxide to resist corrosion attack in this solution. On the other hand, Al in the CoCrFeNiAl system is present in the largest proportion at the surface, 16.1 at.%, after corrosion testing.



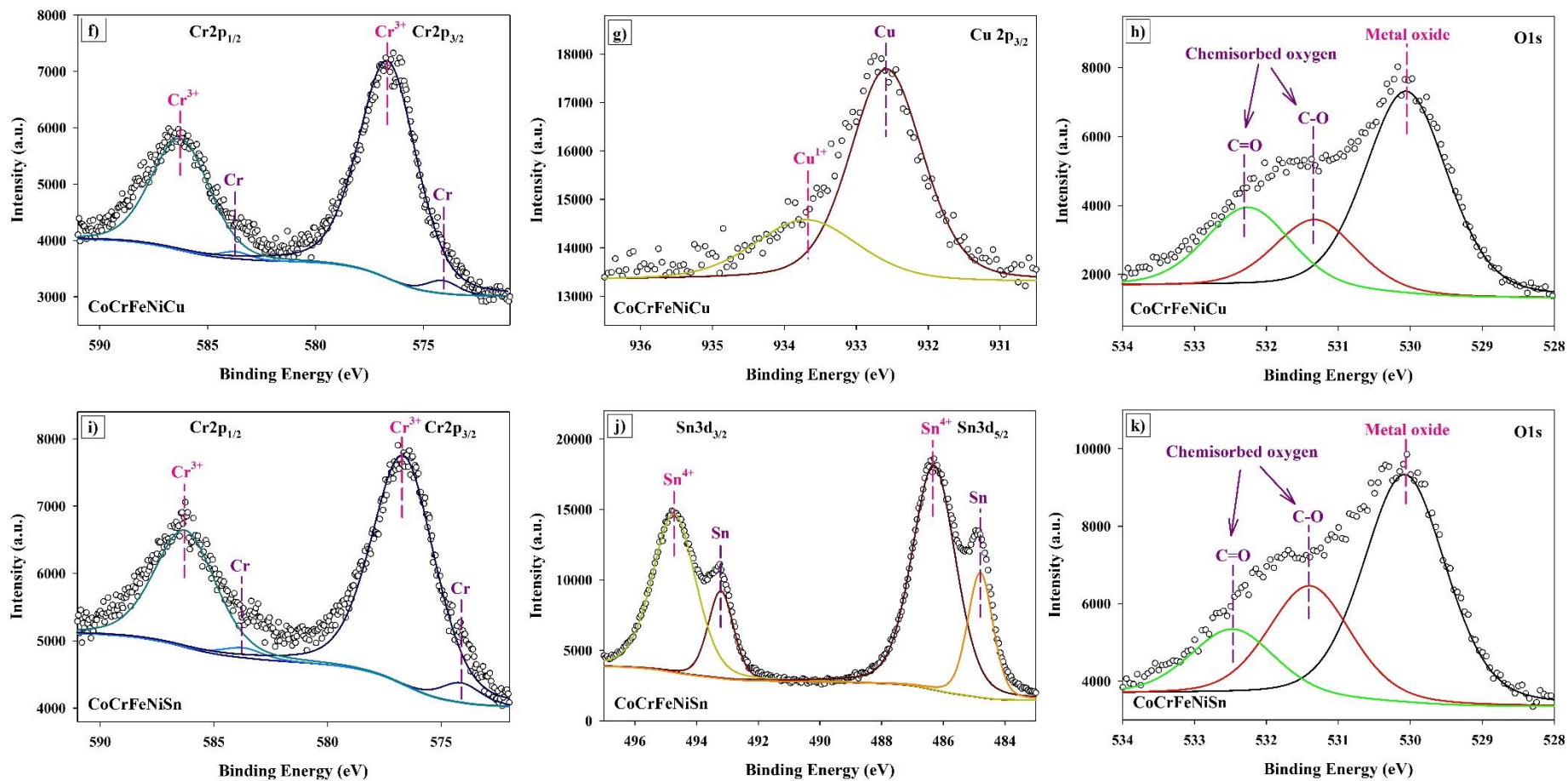


Figure 4.28: The XPS spectra of alloys analysed post-corrosion testing in 0.6 M NaAlO₂ solution to present the metal and metal-oxide regions of; a,c,f,i) Cr 2p, d) Al 2p, g) Cu 2p_{3/2}, j) Sn 3d, and b,e,h,k) O 1s peaks.

Figure 4.28 show XPS spectra for high resolution monitoring of the samples in alkaline solution. Five elemental XPS spectra; Al 2p, Cr 2p, Cu 2p_{3/2}, Sn 3d, and O 1s, are used to assess the chemical state of the corresponding atomic species (and thus indicate whether these metallic atoms tend to be present in the metallic form or as compounds; likely to be oxides when they may have a bond with oxygen) at the sample surfaces. The results are consistent with a main protective film of Cr₂O₃ formed by the interaction between Cr³⁺ and O²⁻. Cr 2p spin-orbit coupling consisting of Cr 2p_{3/2} and Cr 2p_{1/2} is observed in all alloys analysed. The deconvoluted Cr 2p_{3/2} peak can be detected at the binding energies of 574.12 eV-574.20 eV (Cr metal) and 576.60 eV-576.86 eV (Cr oxide). For the three additional elements which distinguish the samples here (Al, Cu and Sn), the formation of Al₂O₃ with Al³⁺ in the CoCrFeNiAl system was indicated by two peaks of Al 2p spectra at the binding energies of 72.33 eV (Al metal) and 74.35 eV (Al oxide). The Cu 2p_{3/2} peak suggesting the creation of Cu₂O from Cu¹⁺ in the CoCrFeNiCu system was observed via two peaks at the binding energies of 932.58 eV (Cu metal) and 933.70 eV (Cu oxide). Two spin orbitals can be detected in the Sn 3d spectrum; Sn 3d_{5/2} and Sn 3d_{3/2} for the formation of SnO₂ with Sn⁴⁺. The Sn 3d_{5/2} peak can be found at the binding energies of 484.80 eV (Sn metal) and 486.30 eV (Sn oxide).

Table 4.16: The relative surface atomic concentration (at.%) of each analysed element at the surface post-corrosion testing in 0.6 M NaAlO₂ solution in metallic and ionized form (taken to indicate the relative involvement of the atoms in either the alloy in metallic form or as metal oxides).

Alloys	Cr (Cr at.%)		Al (Al at.%)		Cu (Cu at.%)		Sn (Sn at.%)	
	Cr	Cr ³⁺	Al	Al ³⁺	Cu	Cu ¹⁺	Sn	Sn ⁴⁺
CoCrFeNi	2.75	97.26	-	-	-	-	-	-
CoCrFeNiAl	19.57	80.43	34.54	65.45	-	-	-	-
CoCrFeNiCu	3.24	96.76	-	-	71.23	28.77	-	-
CoCrFeNiSn	5.31	94.68	-	-	-	-	24.50	75.51

Table 4.16 represents the calculated proportions for each of the analysed elements between the metallic form and as ions (taken to represent oxides) for the alloy systems examined here. The data are collected for the surface of the samples after corrosion assessment in alkaline solutions. These indicate the quality of the passive-film present (via the extent to which the surface is oxidized, and whether a strong, resistant oxide is formed), which will strongly affect the performance in resisting corrosion attack. The addition of the further

alloying elements to the main four component equiatomic alloy system affects the oxide formation on the specimen surface. The equivalent results in acidic immersion following immersion in alkaline solution are shown in Table 4.16. Here the alloying additions also reduce the proportion of Cr participating in the oxide. The reduction is least in CoCrFeNiCu, where 96.8 at.% of the Cr is oxidized (compared to 97.3 at.% in CoCrFeNi) and greatest in CoCrFeNiAl where 80.4 at.% of the Cr is in ionised form. In both solutions, the fifth additional elements in CoCrFeNiSn and CoCrFeNiAl are well involved in the formation of an oxide film; of alloying elements; the oxidation states would correspond to SnO₂ and Al₂O₃. In relation to Cr, which may be the optimum oxide to form, CoCrFeNi has the highest ability to generate the Cr oxide in alkaline solutions; 97.3 at.% of this element at the surface being converted.

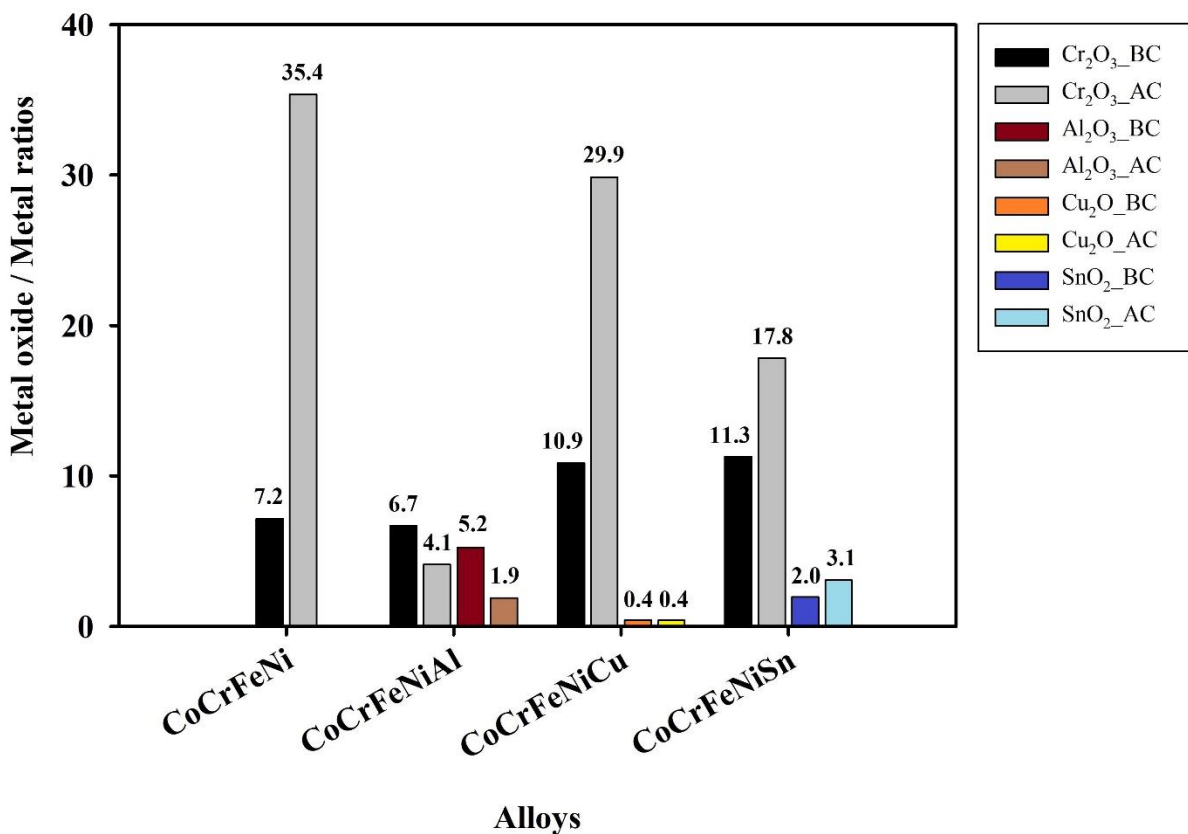


Figure 4.29: The comparison of the extent of oxidation at the sample surface, assessed via the ratio of metal oxide to metal in four alloys in pre- and post-corrosion testing in 0.6 M NaAlO₂ solution (BC refers to before corrosion testing, and AC means after corrosion testing).

As discussed above, the depth of penetration of the XPS analysis may involve detection of signal from the oxide layer and from the bulk. If we make the assumption that the depth of analysis and the thickness of the oxide are comparable in all cases, we can use the ratio between the signal for the different metallic elements analyzed in each state as a measure of the extent

to which the surface is covered by oxide film. If the oxide is not of consistent thickness, then this ratio is likely to be linked to the amount of oxide (a higher ratio for a thicker film). In either case the ratio of metal oxide to metal signal is an indicator of how significant the surface oxidation is, and as we look at this across different species, it can gauge to what extent these are involved in film formation. The ratio of metal oxide to metal on the sample surface pre- and post-corrosion testing in 0.6 M NaAlO₂ (alkaline) solution for the four experimental alloys, CoCrFeNi, CoCrFeNiAl, CoCrFeNiCu, and CoCrFeNiSn, is shown in Figure 4.29. The change in predominant oxide on the alloy surface observed in this work remains the Cr in the oxidized form, as for the acidic experiment in Figure 4.25. Almost all alloys show a high repassivation tendency with an increase in the proportion of Cr in the oxidized form after corrosion in an alkaline solution. The formation of chromium oxide is highly likely to reoccur on the sample surface after the protective-film breakdown. It indicates that Cr acts as an important metallic element to resist alkaline attack. An increasing proportion of Cr in the oxidized form post-corrosion tests is seen in CoCrFeNi (28.2), CoCrFeNiCu (19.0), and CoCrFeNiSn (6.5). On the other hand, a reduction of oxidized Cr proportion is found in CoCrFeNiAl at 2.6. This alloy also has the lowest proportion of Cr in the oxidized form in all samples after corrosion testing, which could be due to competition for oxygen with Al. The oxidation of the fifth element was also investigated. The proportion of Cu in the oxidized form at the CoCrFeNiCu surface is at 0.4 in pre- and post-corrosion testing; an absence of change which was also seen under acidic conditions, Figure 4.25. CoCrFeNiSn has a slightly increased proportion of Sn in the oxidized form, from 2.0 (pre-corrosion testing) to 3.1 (post-corrosion testing), while the proportion of Al in the oxidized form in CoCrFeNiAl has a decreased from 5.2 (pre-corrosion testing) to 1.9 (post-corrosion testing). This result indicates that Sn in the oxidized form is likely to promote and/or coordinate with Cr being the protective oxide film to resist alkaline corrosion. This is consistent with the high passivity (ΔE_p ; 949 mV) seen in CoCrFeNiSn, Table 4.14. On the other hand, CoCrFeNiAl has the highest passivity (ΔE_p ; 1,014 mV) in Table 4.14, despite showing a decreasing proportion of Al and Cr in the oxidized form. This may arise due to the difference between the analytical methods. The polarization technique measures the passive region (passivation potential) resulting from whatever oxide is present, which may involve the elements analyzed, or others, separately or together. XPS on the other hand focusses in on the oxidation of a particular element only. This would suggest that other oxides (Co, Fe, and Ni in the oxidized form at the CoCrFeNiAl surface), are involved in the film and likely to increase the protective nature of that film.

In addition, comparison between XPS data and SEM images may suggest the removal of oxides containing the relevant elements. Generally, alkaline species have a high sensitivity to dissolve in water and ionize as O_2^- and/or OH^- . These ionized species are highly active, forming metal oxides or metal hydroxides with metal at the sample surface [201]. This may be behind the increase in the proportion of Cr in the oxidized form in almost all alloys, CoCrFeNi, CoCrFeNiCu, and CoCrFeNiSn, after corrosion testing in an alkaline solution in Figure 4.29. In contrast, CoCrFeNiAl is likely to form a mixed $(Cr, Al)_2O_3$ oxide, as discussed in sections 4.4.1. As shown in section 2.2.2, the potential-pH equilibrium diagram for aluminum and water at 25 °C indicates that Al has an unstable oxide film which easily dissolves in strongly alkaline solutions, and this could also be the case for Al and Cr in the form of a mixed oxide. CoCrFeNi and CoCrFeNiAl are likely to form localized corrosion, and some byproducts in oxide and/or hydroxide may form on the active area in Figure 4.28. This is consistent with the increasing proportion of Cr in the oxidized state, Figure 4.29. In the cases of CoCrFeNiCu and CoCrFeNiSn, galvanic corrosion is observed via SEM images, Figure 4.27. The Cu-rich phase in CoCrFeNiCu is likely to be corroded according to the low proportion of Cu in the oxidized state at 0.4 (pre- and post-corrosion testing), Figure 4.29. The dendritic CoCrFeNi phase in CoCrFeNiSn has a high sensitivity to be dissolved in an alkaline solution, while the repassivation process of Cr in the oxidized form is insufficient to resist corrosion attack from the alkaline solution as shown in Figures 4.27 and 4.29.

4.4 Discussion: characterization of CoCrFeNi and HEA samples after corrosion testing

4.4.1 Effect of alloying element on the corrosion properties of alloy samples in 0.6 M NaCl solution

Following the evidence presented and discussed above, it is possible to propose a series of mechanisms for the corrosion in chloride solution of the alloys examined in this work. In the CoCrFeNiAl system, it is found that pitting corrosion occurs, with a suggested mechanism for this, consistent with the observations here and what is known about the alloy shown in Figures 4.30a-4.30c. A mixed-oxide film with both Cr and Al cations, in some proportion between Cr_2O_3 and Al_2O_3 , is likely to be formed on the major CoCrFeNiAl (B2) phase. These are the most reactive of the elements present with oxygen, and the two oxides are isostructural with Al and Cr substituting with each other in varying proportions. The metal ions in the +3 oxidation states can form in a type of mixed-cation M_2O_3 oxide [202]. The second Al-Ni-rich phase may create Al_2O_3 film when the sample surface is in contact with atmospheric oxygen,

as shown in Figure 4.30a. Subsequently, during the corrosion process in Figure 4.30b, there are three stages to the evolution of pitting; the first is the selective dissolution of Al and Ni from an area happening to be (Al-Ni)-rich (some tendency for this was seen in Figure 4.14b). These areas form as the atomic pair of Al-Ni have the strongest enthalpy of formation in this system [43,155]. Both Al and Ni are dissolved and transfer electrons to become metal cations, Al^{3+} and Ni^{2+} , in the electrolyte. Subsequently, Ni (II) ions are likely to move to deposit on the alloy surface, replacing Al. EDS data shows the change of chemical composition in pre- and post-corrosion testing of Al and Ni. The decrease in the amount of Al is higher than Ni in Figures 4.18 and 4.19. As reported in [203], micro-galvanic corrosion may induce the dissolution of these elements. CoCrFeNiAl tested in 1 M H_2SO_4 solution saw the dissolution of the Al-Ni-rich phase and formation of a nanoporous Cr-Fe-rich phase, likely under a selective leaching process [203]. In this case, corrosion would proceed by dealloying as Al has the lowest standard electrode potential and the Al_2O_3 is unstable. The second propagation step after passive film breakdown is increasing damage in the region of the pits from small to large corrosion holes [136,204]. The anodic reaction occurs on the alloy surface exposed to the electrolyte while the cathode is the passivated surrounding surface. Pits will grow along the area where Al and Ni are depleted. The final stage is when the CoCrFe residue from dealloying is removed resulting in pit growth, leaving behind the large corrosion pits seen. As indicated in Figure 4.30c, repassivation of the oxide films may occur on the pitting holes after chloride-ion attack.

For the CoCrFeNiCu system, two oxide films are formed, Cr_2O_3 and Cu_2O , Figure 4.30d. Cr_2O_3 is known to be a strong film, resistant to chloride attack, while Cu_2O is a weak film which easily breaks down in the presence of chloride ions. Figure 4.30e shows the chloride ions attacking the Cu-rich areas, leading to the removal of Cu^{1+} from the main Cu phase. Galvanic corrosion of the segregated Cu phase occurs, stemming from its differing potential from the main FCC phase, which forms the cathode, with the Cu-rich phase acting as the anode [2]. The Cu-rich phase is heavily corroded compared to the FCC phase. After corrosion, oxide layers may be regenerated on the sample surface, especially in the areas with Cr, Figure 4.30f.

The corrosion behavior of CoCrFeNiSn is depicted in Figures 4.30g-4.30i. The bulk microstructure of this alloy is composed of two phases, a Ni-Sn intermetallic and CoCrFeNi, which form two passive films, SnO_2 and Cr_2O_3 respectively. Both of these are noble oxide films and will inhibit corrosion in chloride solution, as presented in Figure 4.30g. Galvanic corrosion

is observed on the FCC phase (indicating the Ni-Sn phase has a higher corrosion potential than the CoCrFeNi phase), particularly at the interface where the damage is relatively high, and as a result there is dissolution of some ions, Co^{3+} , Cr^{3+} , Fe^{2+} , and Ni^{2+} , as shown in Figure 4.30h. Then the two passive films can regenerate, as shown in Figure 4.30i.

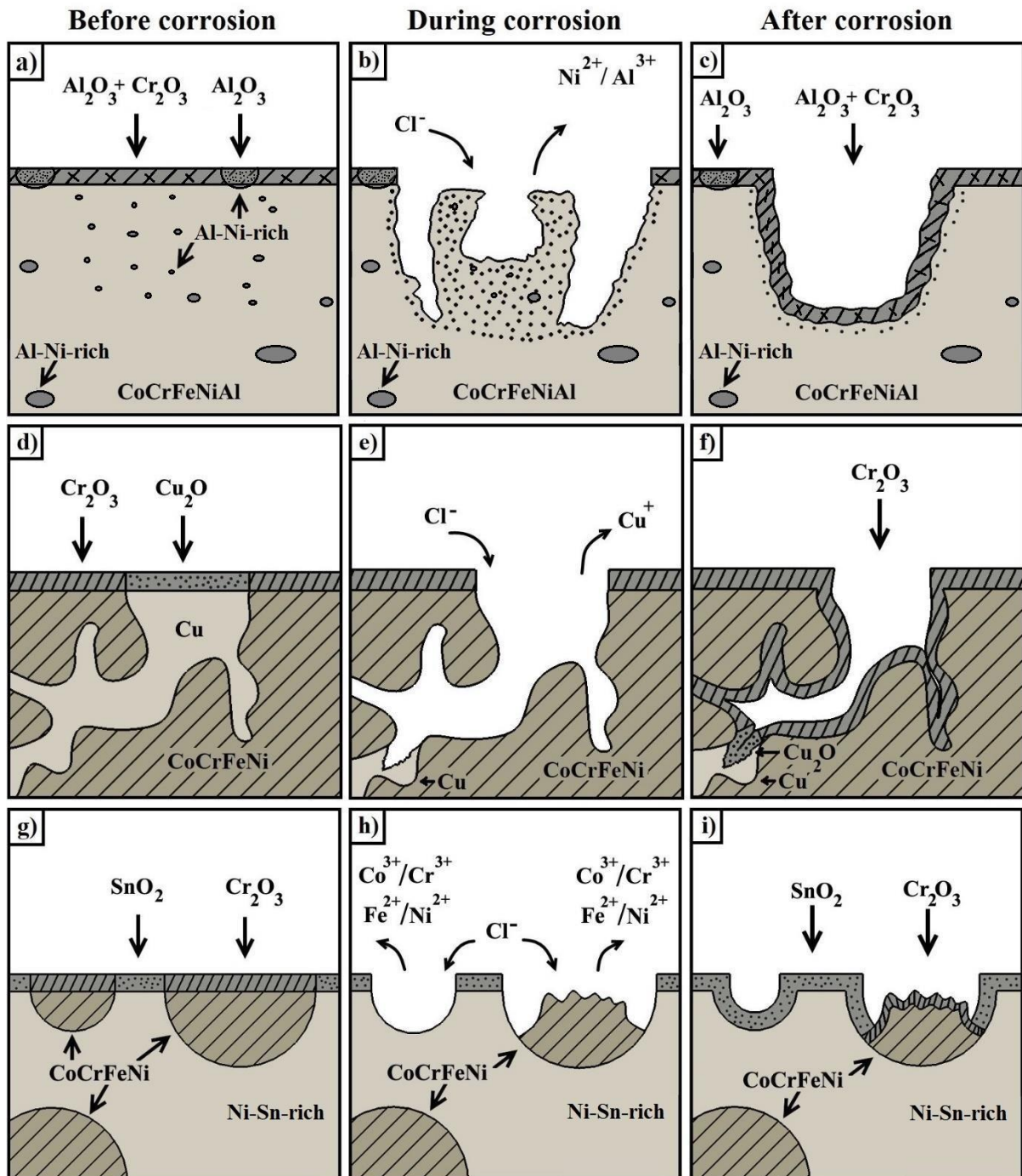


Figure 4.30: A schematic diagram of the proposed processes occurring during the corrosion of three HEA samples examined in this work when tested in 0.6 M NaCl solution at room temperature; a-c) CoCrFeNiAl, d-f) CoCrFeNiCu, and g-i) CoCrFeNiSn.

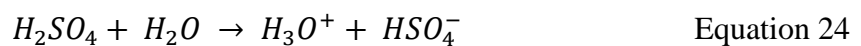
In general, it should be noted that the mechanisms proposed for corrosion depicted in Figure 4.30 are all based on the assumption that the oxide films have a simple structure of good uniformity; local variations and defects (which have not been explored here) could contribute to additional behaviors.

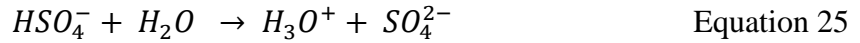
To sum up, the addition of Sn has a positive effect on the rise in corrosion resistance of equiatomic CoCrFeNi in a medium chloride-containing solution, while Al and Cu as alloying elements lead to the decline in corrosion properties under the same conditions.

4.4.2 Effect of alloying element on the corrosion properties of alloy samples in 0.6 M H₂SO₄ solution

It is well known that the nature of the passive film, which forms on a specimen surface, plays a vital role in resisting corrosion attack. Many metallic elements are likely to interact with oxygen to produce different oxide films; for example, the presence of Co₃O₄, Cr₂O₃, Fe₂O₃, and NiO has been reported on CoCrFeNi [175]. Here these oxides plus others involving (where added) the fifth element, Al₂O₃, Cu₂O, and SnO₂, in CoCrFeNiAl, CoCrFeNiCu, and CoCrFeNiSn may be anticipated. However, this implies that there could be different oxides in different surface areas. This is one possibility, but it could also be the case that mixed, complex oxides are formed. The results obtained in this work are not able to make this distinction in the form of oxide that makes up the film, so instead we focus on identifying the presence of Cr, Al, Cu and Sn in their oxidised states (corresponding to Cr₂O₃, Al₂O₃, Cu₂O, and SnO₂) as the chromium frequently participates in films with a good protective effect, and the other elements will help understand the effect on alloy behaviour of the additional elements. This information will be used to investigate possible corrosion mechanisms in all alloy systems. As discussed above, the corrosion properties seen here show different corrosion behaviour in sulfuric acidic solution. The corrosion mechanisms of the alloys examined in this work has been suggested based on the experimental results involving morphology by SEM and chemical composition on the sample surface via XPS.

The morphology is analyzed by SEM after corrosion testing in 0.6 M H₂SO₄ solution in Figure 4.23. There are likely to be two corrosion types occurring in the samples; localized corrosion (CoCrFeNi and CoCrFeNiSn) and galvanic corrosion (CoCrFeAl and CoCrFeNiCu). Sulfuric acid generally dissolves in water to ionize as cations (H₃O⁺) and anions (HSO₄⁻ and SO₄²⁻), as in the equations below [205];





H^+ is used as a shorthand for H_3O^+ when H^+ ions from an acid react with water. It is highly effective at pulling electrons away from the active metallic phase with a lower corrosion potential in a galvanic couple (galvanic corrosion) and a micro-galvanic couple (localized corrosion). Hydrogen gas (H_2) is likely to be produced after this reaction ($2H^+ + 2e^- \rightarrow H_2$). The cathodic reaction occurs due to H^+ cations receiving electron, and the active phase in a galvanic or micro-galvanic couple gives electrons in the anodic reaction [100], according to the equations in section 2.2.2.

In the case of localized corrosion, the micro-galvanic couple may be formed on the CoCrFeNi surface. CoCrFeNi is a single FCC phase with a flat surface before corrosion testing in Figure 4.3a. In post-corrosion testing, localized corrosion is likely to have taken place on its surface, as found in Figure 4.23. To explain this, it could be the case that Cr-depleted regions may occur in a small local area. It should be noted however that no Cr depleted regions have been observed in EDS; it could be that such variation is slight, and is not detected, or it is occurring in a specific region of the sample, different to that explored in SEM. This region with low corrosion potential is likely to be an anode, while a cathode may be found in the nearby area with high corrosion potential. The Cr in the oxidized state in an oxide like Cr_2O_3 form probably plays the main role of protective film, and could regenerate the oxide film on the CoCrFeNi surface to resist corrosion. Such behaviour would correspond to the slight increase in the proportion of Cr in the oxidized form seen in Figure 4.25. Subsequently, the Cr-depleted region may dissolve when the protective oxide film breaks down. The appearance of surface damage is likely to correlate to places without or with reduced oxide protection. Corrosion holes and corrosion products, various metal oxide and hydroxide species, can be found in such areas, Figure 4.23.

Localized corrosion is likely to occur by the same mechanism in CoCrFeNiSn as CoCrFeNi. In this case however, there is a difference in the microstructure, with CoCrFeNiSn being a dual-phase alloy (FCC CoCrFeNi phase and a hexagonal Ni-Sn-rich phase in pre-corrosion tests, as discussed in sections 4.1.1 and 4.1.2). As shown in Figure 4.23, the morphology of corroded regions in CoCrFeNiSn appears similar to CoCrFeNi. Localized corrosion may therefore take place in this alloy. The corroded area in this alloy is rarely found on the anodic region, which is distinct from the behavior in CoCrFeNiAl and CoCrFeNiCu where galvanic corrosion occurs. The different chemical composition in each phase may be the main cause that leads to the formation of the micro-galvanic couple between FCC CoCrFeNi

and hexagonal Ni-Sn-rich phases. This is likely to form an anode at the CoCrFeNi phase, while a cathode may occur in the Ni-Sn-rich phase. This has been assumed according to the occurrence of corrosion characteristics. The Cr₂O₃ and SnO₂ (or other oxides containing these elements in these oxidation states) may also be important protective films for the corrosion resistance in this solution. When the breakdown of oxide films occurs, the acidic solution can directly interact with the surface, and this leads to dissolution. Several cation species, Co, Cr, Fe, and Ni, in the anodic area are likely to be released and may give rise to metal oxides being observed in post-corrosion tests. These corrosion products, including Cr oxide, may cover the anodic area, as shown in Figures 4.23 and 4.24.

Selective dissolution is likely to occur in CoCrFeNiAl. The two-phase composition in these alloy systems may be the main reason leading to the appearance of selective dissolution on their surface, similar to the corrosion behaviour in 0.6 M NaCl solution (section 4.4.1). Initially, the mechanism of micro-galvanic corrosion may form a micro-galvanic couple on the CoCrFeNiAl surface. An anode, which is the lower corrosion potential in a micro-galvanic couple, is likely to form at the second Al-Ni-rich phase. In contrast, the major B2 phase with high corrosion potential may become the cathode. If it is present in a simple state, the Cr in the oxidized form (Cr₂O₃) would be likely to be a higher stability oxide film than the Al in the oxidized state (Al₂O₃) or a mixed (Cr, Al)₂O₃ film. This is consistent with the high decrease in the proportion of Al in the oxidized state, as presented in Figure 4.25. This could result in the breakdown of the passive film at the CoCrFeNiAl surface during the corrosion process, allowing the sulfuric acid solution to dissolve the Al-Ni-rich phase, leading to the release of cation species, Al³⁺ and Ni²⁺, in this solution. It can be indicated that micro-galvanic corrosion may induce the dissolution of these elements.

The formation of galvanic corrosion is found in the CoCrFeNiCu system. A galvanic couple in this system may form between the Cu-rich phase (anode) and the FCC CoCrFeNi phase (cathode). If considered in terms of simple oxides, Cr₂O₃ would be the most effective corrosion protective film, while Cu₂O would be relatively unstable. The small proportion of Cu in the oxidized state may be insufficient to resist the corrosion reaction, as shown in Figures 4.23 and 4.25, leading to dissolution of the Cu-rich phase and the nearby area.

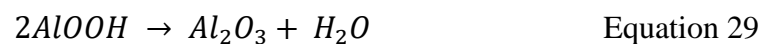
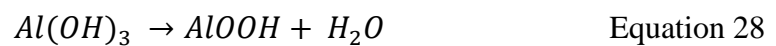
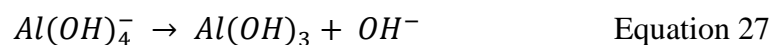
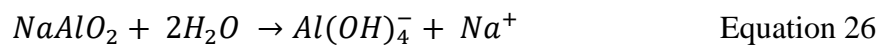
In addition, a conventional alloy, SS304, is used for comparison with the corrosion properties of the novel alloys in this work. In the optimized condition [125] SS304 shows higher corrosion resistance (-0.10 V_{Ag/AgCl} in E_{corr} and 11.60 $\mu\text{A}/\text{cm}^2$ in i_{corr}) than when tested in a remelted and as-cast form in this work (-0.36 V_{Ag/AgCl} in E_{corr} and 47.79 $\mu\text{A}/\text{cm}^2$ in i_{corr}).

This may be due to the microstructural changes induced, or from a change in composition (particularly of Cr) due to remelting, although the composition has not been reassessed. To compare directly the SS304 properties, to the new alloys, we can take the literature values as being more representative of this material in the usual condition (though it should be noted that the new alloys are being tested without any optimization of their microstructure or heat treatment). The tests here show that CoCrFeNi and CoCrFeNiSn have higher corrosion resistance than SS304, as discussed in sections 4.3.4 and 4.3.5. On the other hand, CoCrFeNiAl and CoCrFeNiCu have poorer corrosion behaviour than the commercial grade of SS304. This may indicate, as discussed above, that the oxide films, perhaps a mixed (Cr, Al)₂O₃ oxide and Cu₂O, or more complex oxides containing these elements, occurring in these alloys, are less stable, sections 4.3.4 and 4.3.5.

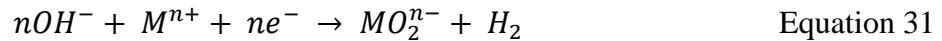
4.4.3 Effect of alloying element on the corrosion properties of alloy samples in 0.6 M NaAlO₂ solution

As discussed in sections 4.4.1 and 4.4.2, the metal oxides forming on the sample surface play a vital role as a protective film for resisting the corrosive environment. While it is not certain to form simply here, Cr₂O₃ is frequently observed to be a highly effective protective layer in the observation of corrosion behaviour. The presence of Cr in this oxidation state was again assessed along with the additional elements in their common oxidation states (Al₂O₃, Cu₂O, and SnO₂). Differences were seen in alloy systems, likely due to different corrosion forms in alkaline solutions. This is discussed according to the evidence of morphology and the composition of metals and metal oxides at the sample surface in this work.

In the investigation of corrosion behaviour in alkaline solution, as in acidic solution, it is also found that two feasible corrosion forms are localized corrosion (CoCrFeNi and CoCrFeNiAl) and galvanic corrosion (CoCrFeCu and CoCrFeNiSn). The interaction between sodium aluminate and water can result in cations (Na⁺) and anions ($Al(OH)_4^-$ and OH^-), including the formation of oxide (Al₂O₃) and hydroxide (AlOOH). It is also likely to generate a strong aggressive alkaline solution, as in the equations below [206];



Metal (M) with low corrosion potential may form an anode (Equation 30), and a cathode may occur by OH⁻ and metal cations gaining electrons (ne⁻). OH⁻ is likely to react with metal ions (Mⁿ⁺) to form metal hydroxide (MO₂ⁿ⁻), Equation 31. A different potential between anode and cathode is likely to generate a micro-galvanic couple (localized corrosion) and a galvanic couple (galvanic corrosion).



As assumed in the corrosion mechanism in an alkaline solution, localized corrosion is likely to occur on the CoCrFeNi and CoCrFeNiAl surfaces. The surface of CoCrFeNi (single FCC phase) before corrosion testing in Figure 4.3a shows a change in the surface damage from localized corrosion attack covering the sample surface with corrosion products after corrosion testing, Figure 4.27. This indicates that a micro-galvanic couple may form on the CoCrFeNi surface. A small local area depleted in, for example, Cr and thus having low corrosion potential may produce an anodic area, while the nearby region with a higher Cr content and high corrosion potential would be likely to become a cathodic area. A different potential between the two areas may cause localized corrosion. The predominant film, which contains Cr in the oxidized state, protects the CoCrFeNi surface from this aggressive alkaline solution, though this can break down. Subsequently, the unprotected alloy surface is directly in contact with an alkaline solution, and the anodic area with a low corrosion potential may dissolve. Corrosion holes and corrosion products are likely to be produced in this area, Figure 4.27. In addition, corrosion products, such as Cr₂O₃, Cr(OH)₃, and other metal oxide and hydroxide species, are likely to form on the CoCrFeNi surface. This is consistent with the increase in the proportion of Cr in the oxidized form observed (Figure 4.29) and the formation of hydroxide species (Figure 4.28) in post-corrosion tests.

In the case of CoCrFeNiAl, localized corrosion similar to CoCrFeNi is likely, as presented in Figure 4.27. The mechanism may be the same as CoCrFeNi, despite CoCrFeNiAl being a two-phase alloy. A small local anode may occur in the interdendritic Al-Ni-rich phase with low corrosion potential. It is likely to lose electrons and become a corroded area. A cathode may be produced at the dendritic B2 phase with high corrosion potential. The main protective film also contains Cr in the oxidized form (such as Cr₂O₃). It suggests that Al in the oxidized state (for example Al₂O₃ or a mixed (Cr, Al)₂O₃ film) is likely to have less stability than Cr in the oxidized form. This corresponds to a large decrease in the proportion of Al in

the oxidized state after corrosion testing in Figure 4.29. Dissolution is found in the anodic area after the breakdown of passive films. Al^{3+} , Ni^{2+} , and other cation species at the anode are likely to be released in an alkaline solution.

The occurrence of galvanic corrosion is observed in CoCrFeNiCu and CoCrFeNiSn. The galvanic-corrosion mechanism in sodium aluminate solution may be similar to the sulfuric acid solution in the previous section. The dissimilar phases present in both CoCrFeNiCu and CoCrFeNiSn may be the main reason for the formation of galvanic corrosion. A galvanic couple in the CoCrFeNiCu is likely to occur between the anode (Cu-rich phase) with low corrosion potential and the cathode (FCC CoCrFeNi phase) with high corrosion potential. The anodic region at the Cu-rich phase may emit electrons and corrode this region, while the FCC CoCrFeNi phase becomes a cathodic area due to a higher corrosion potential. The protective film may incorporate Cr and be able to regenerate, as observed in Figure 4.29. In contrast, the unstable Cu_2O film may be an initial point of oxide-film breakdown, so the Cu-rich phase at an anodic area is attacked and dissolves in this solution, as in Figure 4.27.

CoCrFeNiSn is likely to produce a galvanic couple between the FCC CoCrFeNi phase (low corrosion potential) and the hexagonal Ni-Sn-rich phase (high corrosion potential) resulting from the different corrosion potential between these phases. Cr in the oxidized form also seems to be present in the protective film, while Sn in the oxidized state (such as SnO_2) may be a secondary oxide film, or participant in a complex oxide film, to further promote corrosion resistance. The film is likely to regenerate after the oxide-film breakdown, as presented in Figure 4.29. The corroded area occurs in the FCC CoCrFeNi phase (anode) to release some metal ions, Co^{3+} , Cr^{3+} , Fe^{2+} , and Ni^{2+} , from this area, Figure 4.27.

No evidence is currently available on the corrosion behaviour of SS304 in sodium aluminate solution, or the effect of a re-melting process of SS304 on the corrosion resistance compared to commercial SS304 in this solution. Thus, there is insufficient data to make a clear comparison of the relative behavior of the novel alloys tested here and conventional materials, such as SS304.

4.5 Results: characterization of CoCrFeNi and CoCrFeNiSn after tribocorrosion testing in 0.6 M NaCl solution

Characterization of CoCrFeNi and CoCrFeNiSn after tribocorrosion testing in 0.6 M NaCl solution is the last experimental section of my doctoral thesis. It is a continuation of

research in two sections: 4.1: characterization of as-cast CoCrFeNi and HEA samples; and 4.3: characterization of CoCrFeNi and HEA samples after corrosion testing. The first section reveals that CoCrFeNiSn has the highest hardness (517 HV0.5; 5.07 GPa) of all alloys in this work (Figure 4.7). The second section shows that CoCrFeNiSn shows the best corrosion resistance compared to the other alloys since it shows the highest pitting potential (E_p ; 1,099 mV) and the largest passive region (ΔE_p ; 1,351 mV) in Table 4.7. It indicates the good stability of the passive film in 0.6 M NaCl solution of the polarization test. As mentioned above, excellent properties in the CoCrFeNiSn alloy are observed in both high hardness and high passivity in NaCl solution. This potential leads to it being the selected candidate alloy for tribocorrosion testing, which combines wear and corrosion tests together, in the last section. As hardness is a complementary property to wear behaviour, CoCrFeNiSn is additionally analyzed in nanoindentation to measure hardness in each phase and in Electrical Impedance Spectroscopy (EIS) testing to identify the tribocorrosion mechanism between passive layers on the contact surface and oxide-film properties formed on the interface, including tribocorrosion testing. To compare with CoCrFeNiSn, CoCrFeNi was chosen for testing to observe the influence of tin on tribocorrosion properties.

4.5.1 Hardness observation

As presented in section 4.1.4, the Sn addition can increase the hardness of CoCrFeNiSn. The hardness value of the CoCrFeNiSn alloy determined during the tribocorrosion tests is significantly higher than that of the CoCrFeNi alloy; 517 HV0.5 (5.07 GPa) and 126 HV0.5 (1.24 GPa) respectively, as in Figure 4.7. The Ni-Sn-rich phase may cause enhanced hardness due to its hexagonal structure, and due to its possible nature as an ordered compound (although this is not certain). A further indication of this phase being the origin of the high hardness is from the nanoindentation data in Figure 4.31 and Table 4.17. CoCrFeNiSn was tested with a Berkovitch diamond nanoindenter at an applied load of 2,000 μN on two different areas on a polished surface, in the Ni-Sn-rich and FCC CoCrFeNi phases, as presented in the load-displacement curves (Figure 4.31). The mechanical properties can be obtained from analysis of the nanoindentation curves. The hardness value can be calculated by dividing the indentation load by the contact area (with corrections applied for the additional area in the measurement due to the elastic contact), while the elastic modulus value is derived from the slope of the unloading curve [207]. The hardness of the hexagonal Ni-Sn-rich phase is higher than that of the FCC CoCrFeNi phase, 10.23 GPa compared to 5.14 GPa. In contrast, the FCC CoCrFeNi phase has higher elastic modulus (173.34 GPa) than the hexagonal Ni-Sn-rich phase (162.43

GPa). These hardness observations also correspond to the deformation seen in an SEM image of a microscale indent in the as-cast CoCrFeNiSn in Figure 4.8d. This indent size is small with no bowed edges. Cracks are observed in the hexagonal Ni-Sn-rich areas indicating a brittle phase, while they seem less likely to propagate in the FCC CoCrFeNi areas suggesting a ductile phase. The cracking mechanism of CoCrFeNiSn is discussed in section 4.2.2.

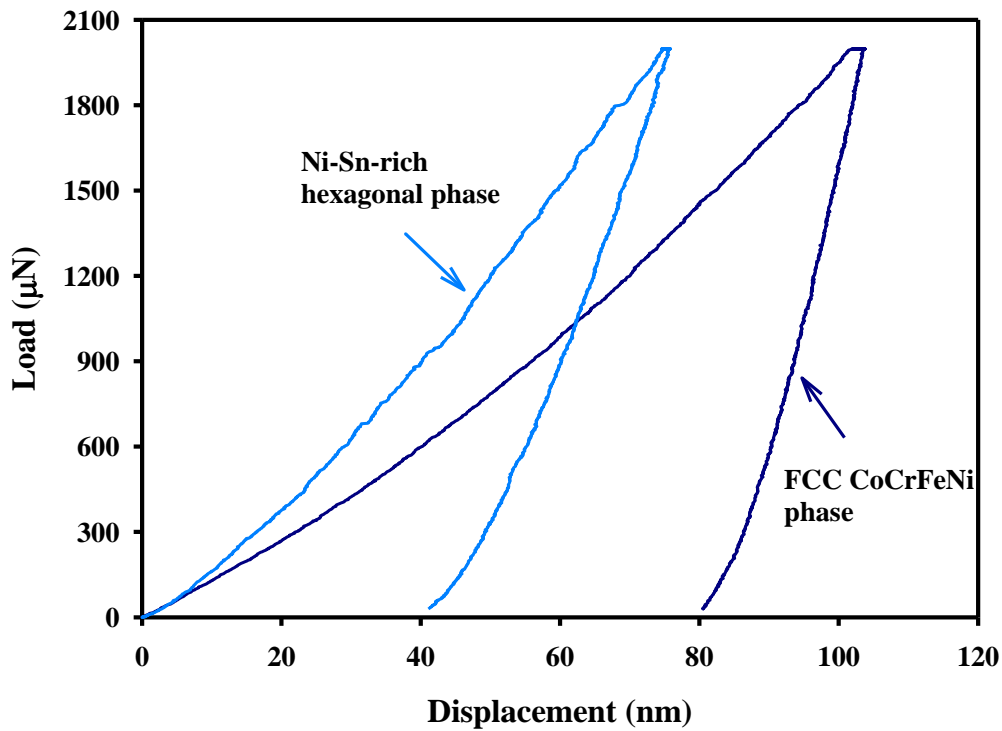


Figure 4.31: Load-displacement curves for nanoindentation testing in CoCrFeNiSn showing a different indentation deformation behaviour between FCC CoCrFeNi and Ni-Sn-rich hexagonal phases.

Table 4.17: The mechanical properties, hardness and modulus, and contact depth during nanoindentation testing of two phases in the CoCrFeNiSn alloy.

Phase	Hardness (GPa)	Modulus (GPa)	Contact depth (nm)
FCC CoCrFeNi	5.14 ± 0.18	173.34 ± 9.82	90.92 ± 2.05
Ni-Sn-rich hexagonal	10.23 ± 0.81	162.43 ± 5.69	56.86 ± 3.20

4.5.2 Corrosion analysis in 0.6 M NaCl solution

Figure 4.32 presents the potentiodynamic curves for the CoCrFeNi and CoCrFeNiSn alloys immersed in 0.6 M NaCl solution at ambient temperature. The passive region ΔE_p , which is the difference between E_p and E_{corr} , of CoCrFeNiSn (1,028 mV) is about twice as wide as

that for CoCrFeNi (491 mV). Adding Sn to CoCrFeNi has therefore significantly increased the passivity of alloy, possibly because of the formation of oxides based on SnO₂ at the surface in addition to the main Cr₂O₃ and other oxide films [172], which appears to increase the protective oxide layer stability. However, there is only a relatively small enhancement in the corrosion parameters, shown in Table 4.18, for CoCrFeNiSn compared to the alloy without Sn. We find that i_{corr} is decreased by approximately 20% and the linear polarization resistance R_p increased by approximately 21% for CoCrFeNiSn compared to CoCrFeNi. In addition, both CoCrFeNi and CoCrFeNiSn have higher corrosion resistance than the commercial 316L stainless steel, Table 4.18. They show higher E_{corr} values (-140 mV (CoCrFeNiSn), -171 mV (CoCrFeNi), and -530 mV (SS316L)) and lower i_{corr} values (0.04 $\mu\text{A}/\text{cm}^2$ (CoCrFeNiSn), 0.05 $\mu\text{A}/\text{cm}^2$ (CoCrFeNi), and 77.70 $\mu\text{A}/\text{cm}^2$ (SS316L)).

Table 4.18: The corrosion parameters, obtained via the electrochemical analysis of CoCrFeNi and CoCrFeNiSn alloys in 0.6 M NaCl solution at ambient temperature.

Alloy system	i_{corr} ($\mu\text{A}/\text{cm}^2$)	E_{corr} (mV _{SCE})	E_p (mV _{SCE})	ΔE_p (mV _{SCE})	R_p ($\Omega \text{ cm}^2$) $\times 10^6$
CoCrFeNi	0.05 \pm 0.01	-170.59 \pm 2.35	320.07 \pm 3.67	490.66 \pm 6.02	0.53 \pm 0.01
CoCrFeNiSn	0.04 \pm 0.003	-140.16 \pm 43.71	887.47 \pm 192.13	1,027.63 \pm 235.83	0.64 \pm 0.05
SS316L [208]	77.70	-530	-	-	-

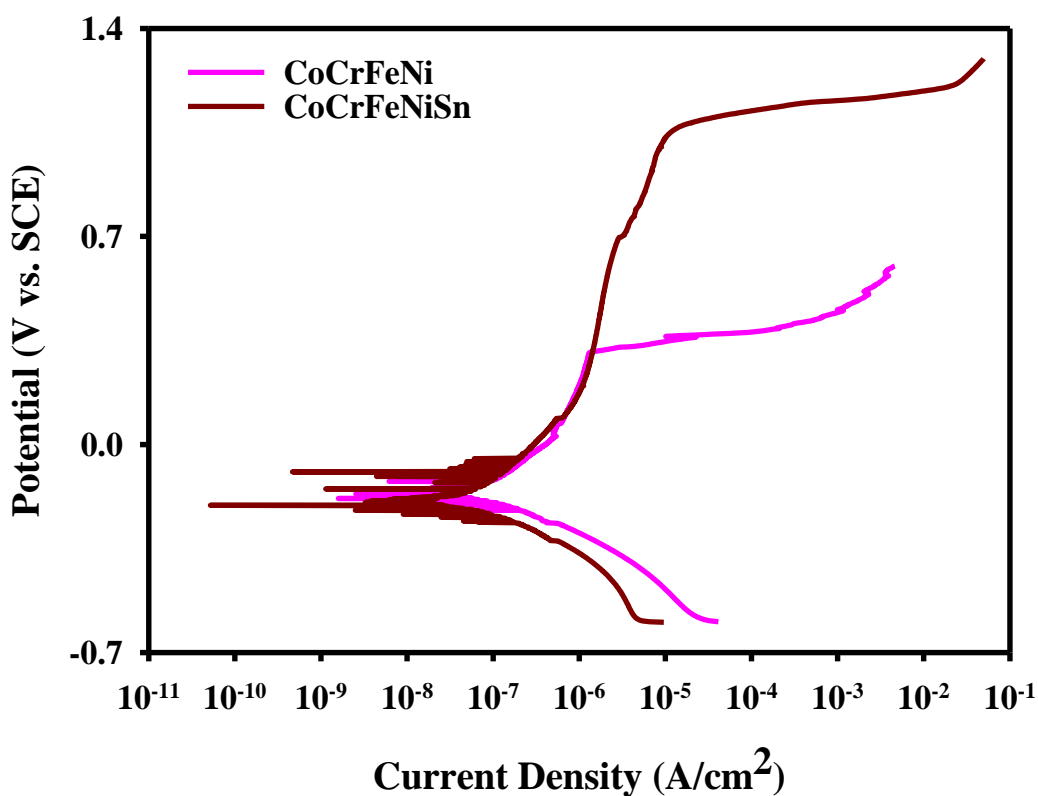


Figure 4.32: The potentiodynamic curves of CoCrFeNi and CoCrFeNiSn alloys in 0.6 M NaCl solution at ambient temperature.

The EIS spectra for CoCrFeNi and CoCrFeNiSn samples immersed in chloride solution at room temperature in both Nyquist and Bode plots formats are shown in Figures 4.34: and 4.35 respectively. For all tests, the Nyquist plots show a semicircle with the centre depressed below the x-axis, clearly revealing the non-perfect capacitive behaviour of the surface layer. The semicircles intersect the x-axis at high frequencies giving the solution resistance R_s . At very low frequencies (which cannot be reached experimentally but can be extracted by using electric equivalent circuit modelling), the semicircle should intersect the x-axis again to give the solution resistance plus the total surface resistance (R_s+R_t). At intermediate frequencies, the imaginary part starts to increase, indicating the capacitive behaviour of the surface. A significant increase in the semicircle size can be observed due to the adding of Sn to CoCrFeNi. An increase in the semicircle size of CoCrFeNiSn can indicate an increase in the polarization resistance of this alloy in chloride solution [209]. It is consistent with R_{ads} and R_{oxide} of CoCrFeNiSn being higher than CoCrFeNi in Table 4.19.

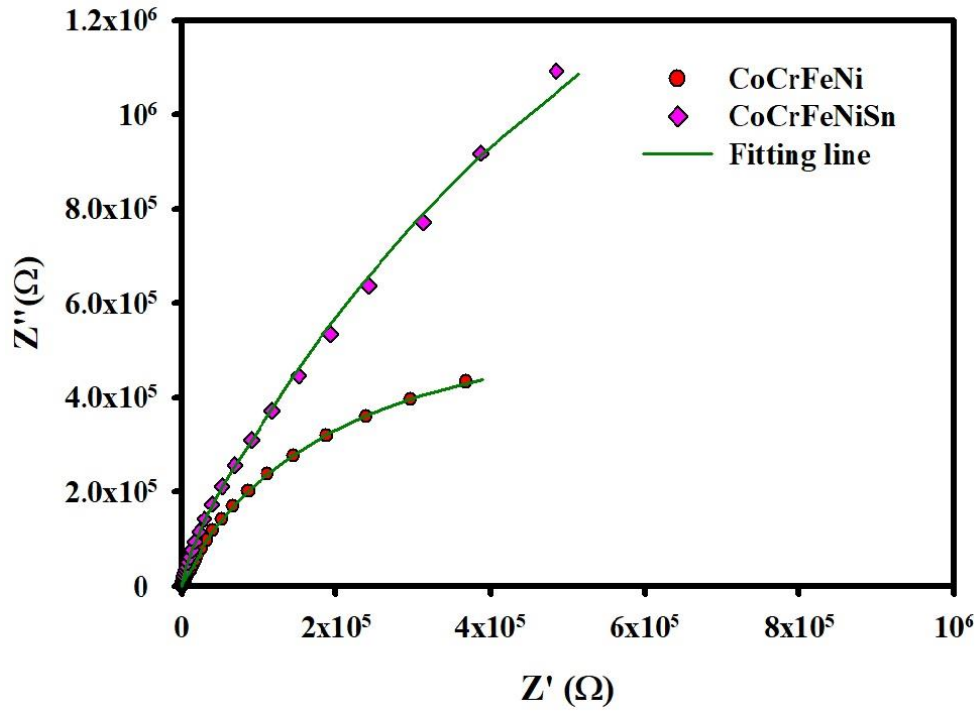
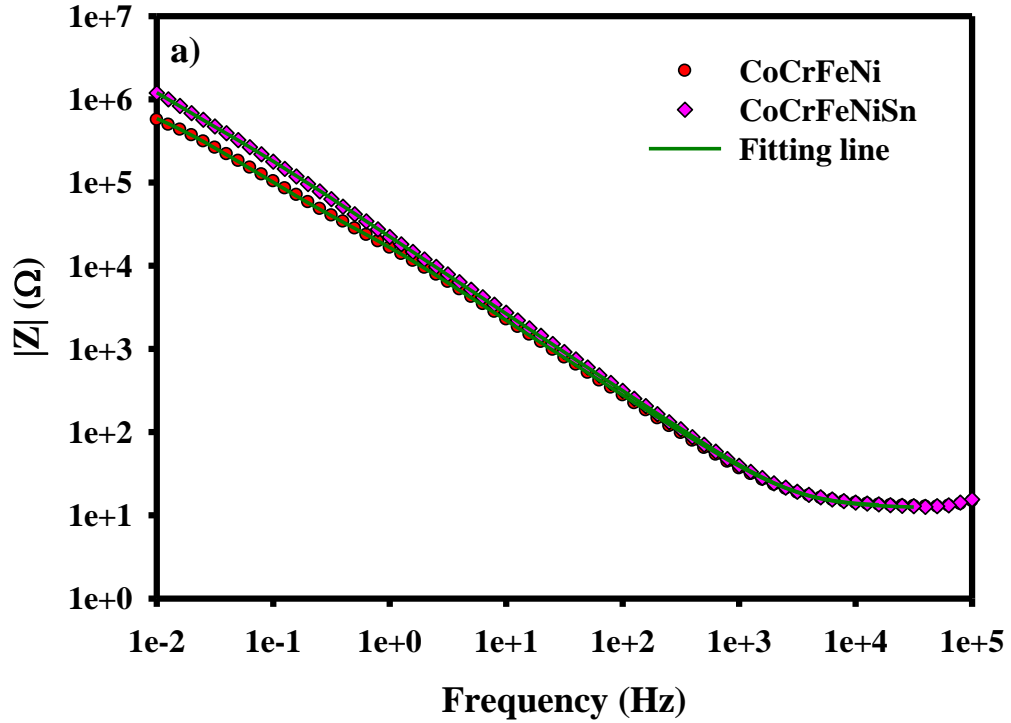


Figure 4.33: The Nyquist plots of CoCrFeNi and CoCrFeNiSn alloys in 0.6 M NaCl solution at ambient temperature.



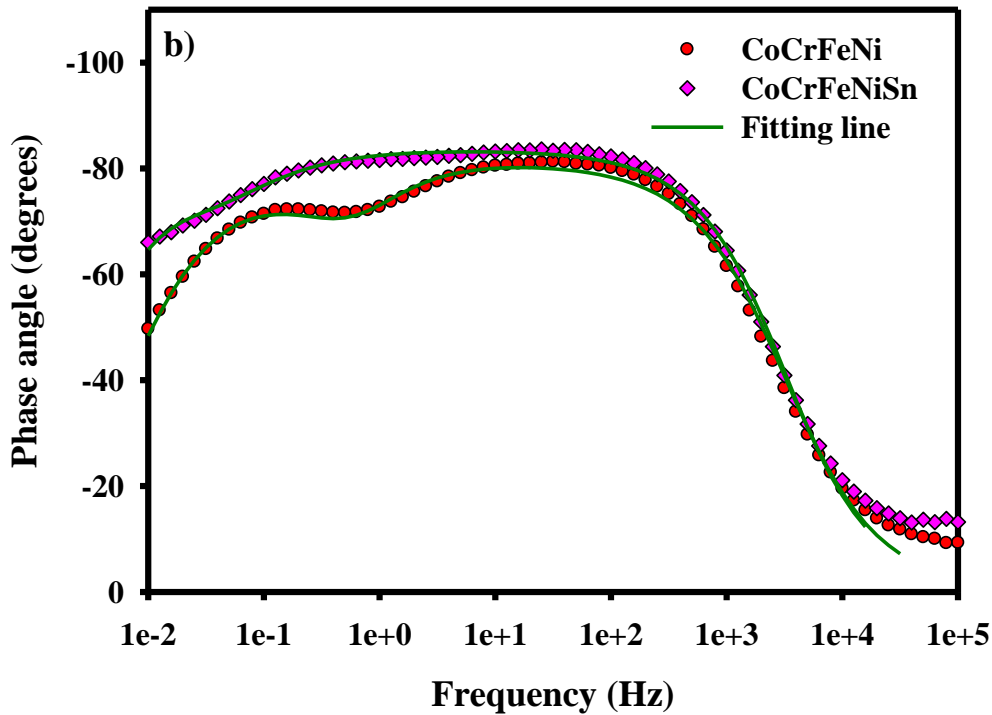


Figure 4.34: a) The Bode plots and b) Bode phase plots of CoCrFeNi and CoCrFeNiSn alloys in 0.6 M NaCl solution at ambient temperature.

The Bode plot in Figure 4.34a, and the Bode phase plot in Figure 4.34b, show that the material exhibits a plateau at high and low frequencies, giving R_s and (R_s+R_t) respectively. At intermediate frequencies, the curve is a fitting line with a slope close to -1 in all cases. The phase shift Bode plot, Figure 4.34b gives the same indication as the phase peaks at intermediate frequencies, due to the increase in the imaginary component of the impedance. Two time constants can be clearly distinguished from the figure for both tested alloys. The first one at high frequencies, attributed to the oxide layer (pink regions), and a second one at low frequencies, which is attributed to a surface adsorbed layer (light purple regions). Based on this hypothesis, the Electric Equivalent Circuit (EEC) shown in Figure 4.35 was used to model the EIS data. An EEC of this type has previously been used in modelling EIS data for passive metallic materials [210-212]. This circuit applies two RQ elements (resistance and capacitance) in series with R_s . R_s is serialized with two parallels of the constant phase element (CPE) and the resistance (R) with a first parallel of the adsorbed layer (CPE_{ads} and R_{ads}) and a second parallel of the oxide film (CPE_{oxide} and R_{oxide}) [210-212]. CPE is used as a substitute for a capacitor and can describe the non-ideal behaviour of the double layer at the surface [211].

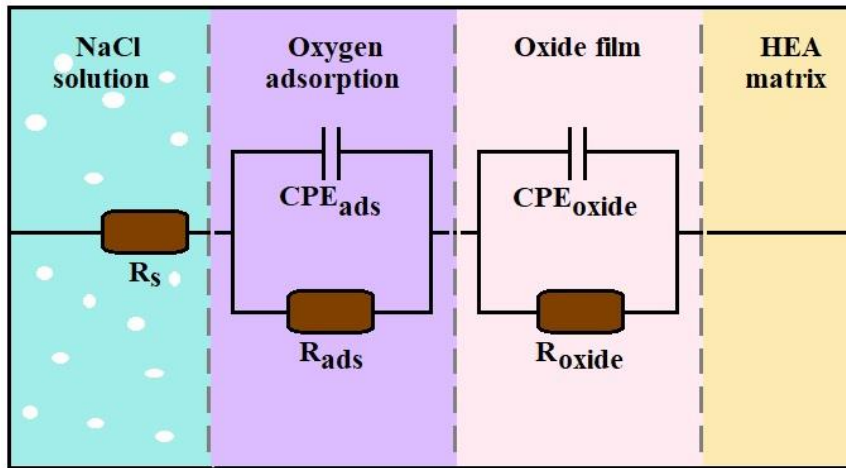


Figure 4.35: The equivalent circuit model of alloys for fitting in 0.6 M NaCl solution at ambient temperature.

All the parameters resulting from the fitting to the EIS data are tabulated in Table 4.19. It shows that CoCrFeNiSn (R_{ads} ; 18.1 k Ω cm² and R_{oxide} ; 1.4 M Ω cm²) has higher R_{ads} and R_{oxide} values than CoCrFeNi (R_{ads} ; 1.7 k Ω cm² and R_{oxide} ; 0.4 M Ω cm²). On the other hand, CoCrFeNi (Q_{ads} ; 160 μ F cm⁻¹s ^{α -1} and Q_{oxide} ; 49 μ F cm⁻¹s ^{α -1}) has higher Q_{ads} and Q_{oxide} values than CoCrFeNiSn (Q_{ads} ; 126 μ F cm⁻¹s ^{α -1} and Q_{oxide} ; 37 μ F cm⁻¹s ^{α -1}), as in Table 4.19. This indicates that CoCrFeNiSn is superior corrosion resistance (in terms of the electrical transport), while it is inferior in capacitance compared to CoCrFeNi. Thus, adding Sn to CoCrFeNi has a significant impact on R_{oxide} which is possibly because of the formation of Ni-Sn-rich phase with high passivity and the stable SnO₂ films with dense structure [172]. Additionally, R_{ads} exhibited an increase by more than an order of magnitude for CoCrFeNiSn compared to the alloy without Sn. Furthermore, the comparison of passive film properties between the commercial SS316L and two alloys, CoCrFeNi and CoCrFeNiSn, in this work shows that SS316 (0.01 M Ω cm²) has the lowest R_{oxide} value, Table 4.19.

4.5.3 Tribocorrosion analysis in 0.6 M NaCl solution

To understand the tribocorrosion behaviour, a tribocorrosion tester was conducted, Figures 4.36–4.38 and Tables 4.19–4.20.

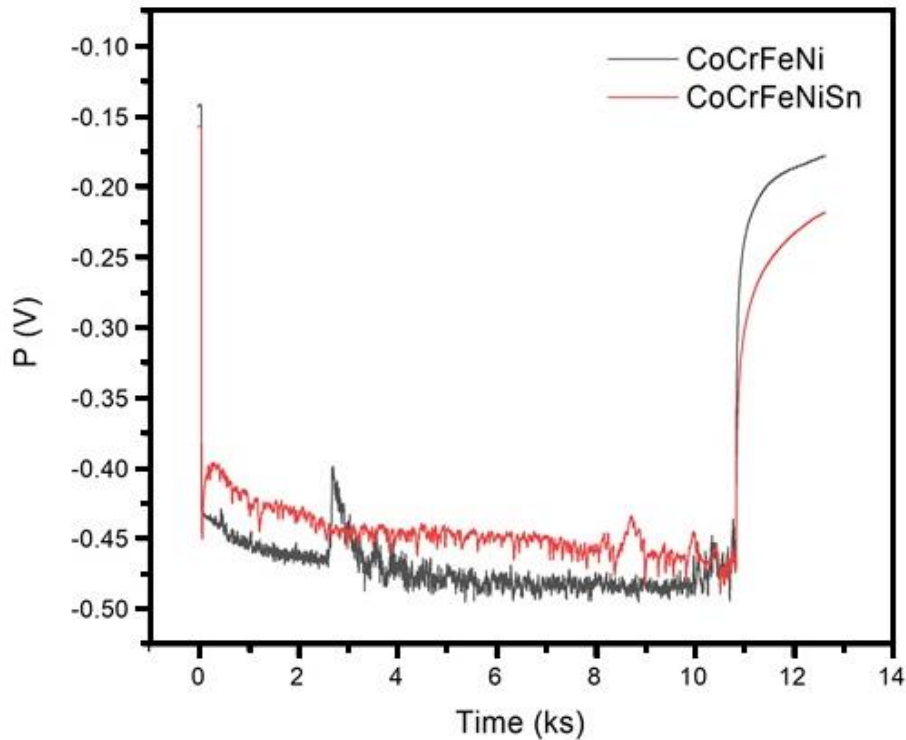


Figure 4.36: Sliding potential for CoCrFeNi and CoCrFeNiSn alloys tested in 0.6 M NaCl solution at ambient temperature.

Figure 4.36 shows the sliding potential versus time for CoCrFeNi and CoCrFeNiSn alloys. It reveals the stability of the passive film in chloride solution with the OCP measurement. CoCrFeNiSn shows that rubbing started on its surface at -0.45 V (0 s), and rubbing stopped at -0.47 V (10,856 s). In the case of CoCrFeNi, rubbing started on its surface at -0.44 V (0 s), and stopped at -0.46 V (10,858 s). However, CoCrFeNiSn is likely to see less OCP shifting of the potential than CoCrFeNi. Rubbing resulted in a drop of the potential by 150-200 mV for the two alloys. The potential value of CoCrFeNiSn is likely to be higher than CoCrFeNi, as in Figure 4.36. It could imply a more stable passive film in CoCrFeNiSn than CoCrFeNi. This is likely to be the typical tribocorrosion behaviour shown by passive metals and alloys [213].

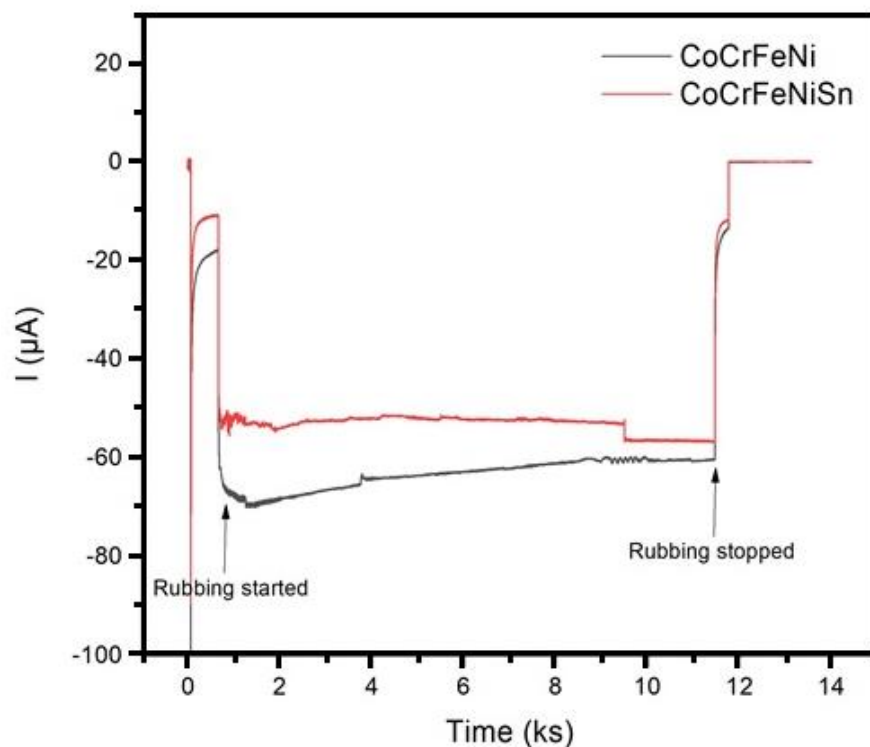


Figure 4.37: Cathodic current flowing in tribocorrosion testing for CoCrFeNi and CoCrFeNiSn alloys tested in 0.6 M NaCl solution at ambient temperature.

Figure 4.37 shows the measured current versus time for the two tested alloys at cathodic potential. When the cathodic potential was first applied, the current exhibited a sudden cathodic drop, followed by stabilization over time to $\approx 19 \mu\text{A}$ for CoCrFeNi and $\approx 11 \mu\text{A}$ for CoCrFeNiSn. The current exhibited a cathodic shift of more than $60 \mu\text{A}$ when rubbing started on the CoCrFeNi surface. Its cathodic current is likely to decrease after 9,000 s when rubbing stopped. Slightly less cathodic shifting of the current was seen for CoCrFeNiSn. This is possibly because of the mechanical removal of the oxide layer due to abrasion of the surface and better mass transfer provided by agitation during rubbing. As shown in Figure 4.39b, most of the area assessed in the wear trace in CoCrFeNiSn is in the Ni-Sn-rich phase, where it is believed from the earlier XPS results that Sn participates in the surface oxide. In contrast, the current in tests on CoCrFeNi (which evidently does not have any Sn on the oxide) is less stable than CoCrFeNiSn, increasing continuously from when rubbing is started to 10,000 s, Figure 4.37.



Figure 4.38: Tribocorrosion testing parameters for CoCrFeNi and CoCrFeNiSn tested in 0.6 M NaCl solution at ambient temperature.

All the results of tribological and tribocorrosion tests are tabulated in Table 4.20. COF did not show any significant differences dependant on the alloy system being studied. A significant decrease in K was noticed as a result of the addition of Sn to the CoCrFeNi alloy under OCP and cathodic conditions. Figure 4.38 shows the tribocorrosion parameters; W_0 , ΔW_C , and ΔC_W . W_0 exhibited a slight decrease for CoCrFeNiSn compared to CoCrFeNi by about 12%. However, adding Sn to CoCrFeNi caused a reduction in ΔC_W to less than one fifth of the original value and ΔW_C to about one third. As a result, the total material loss T measured for CoCrFeNiSn was one third of that for CoCrFeNi, as in Table 4.20.

It would be instructive to compare the results to known materials, such as SS316L for the same conditions, though no evidence has been reported for the tribocorrosion testing of SS316L at the same as applied load of 0.5 N in chloride solution. The closest tests in the same solution [214] measure SS316L at a normal load of 5N, rather than the load of 0.5 N used for tribocorrosion testing in this work. From the report, the volume loss (V) of SS316 is $2.3 \times 10^{-3} \text{ mm}^3$. Though this is higher compared to CoCrFeNi and CoCrFeNiSn in both OCP and cathodic tests, Table 4.20, direct comparison is not possible due to the different testing loads.

Table 4.19: EIS model parameters for CoCrFeNi and CoCrFeNiSn alloys in 0.6 M NaCl solution at ambient temperature.

Alloy system	R_s ($\Omega \text{ cm}^2$)	R_{ads} ($\text{k}\Omega \text{ cm}^2$)	Q_{ads} ($\mu\text{F cm}^{-1}\text{s}^{\alpha-1}$)	n_{ads}	R_{oxide} ($\text{M}\Omega \text{ cm}^2$)	Q_{oxide} ($\mu\text{F cm}^{-1}\text{s}^{\alpha-1}$)	n_{oxide}	$Chi-Sqr$	$Sum-Sqr$
CoCrFeNi	3.90±0.45	1.70±0.10	160.33±36.24	0.98	0.36±0.04	49.21±4.03	0.89	0.0014	0.18
CoCrFeNiSn	3.35±0.26	18.10±12.36	126.26±20.45	0.88	1.35±0.18	37.13±1.98	0.95	0.0019	0.23
SS316L [208]	76.00	-	-	-	0.01	290.00	0.75	0.0350	-

Table 4.20: Tribological and tribocorrosion parameters for CoCrFeNi and CoCrFeNiSn alloys tested in 0.6 M NaCl solution at ambient temperature.

Alloy system	Condition	Averaged COF	V (mm^3) $\times 10^{-4}$	SA (mm^2)	K ($\text{mm}^3/\text{N m}$) $\times 10^{-6}$	$E_{sliding}$ (V)	i_{wr} (mA/cm^2) $\times 10^{-2}$	W_0 (mm/y)	ΔW_C (mm/y)	ΔC_W (mm/y)	T (mm/y)
CoCrFeNi	OCP	0.34±0.02	8.18±0.5	0.482±0.04	7.57±0.4	-0.47	5.6	0.42±0.08	3.86	0.62±0.03	4.91±0.05
	Cathodic	0.43±0.01	0.26±0.04	0.17±0.02	0.24±0.03						
CoCrFeNiSn	OCP	0.31±0.015	1.92±0.1	0.338±0.002	1.77±0.1	-0.46	1	0.37±0.001	1.17	0.11±0.01	1.66±0.09
	Cathodic	0.38±0.02	0.16±0.02	0.126±0.01	0.14±0.02						

SEM images, as in Figure 4.39, reveal the wear morphology of the alloy samples. It was observed that the CoCrFeNi surface experiences high damage and there are many cracks or tear features along the direction of the wear tracks in Figure 4.39a. On the other hand, Figure 4.39b shows the wear morphology of CoCrFeNiSn alloy, with no apparent sign of damage or cracks on the sample surface. Thus, this evidence helps to confirm that the CoCrFeNiSn alloy has higher tribocorrosion resistance than CoCrFeNi alloy and it also corresponds with the data analysis in Table 4.20.

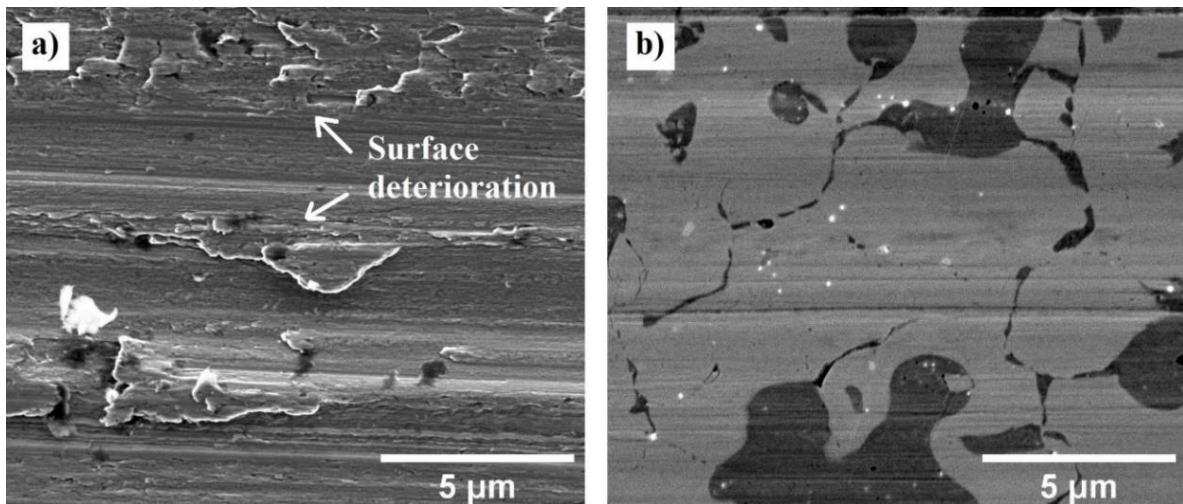


Figure 4.39: SEM micrographs showing the wear morphology after tribocorrosion testing of (a) CoCrFeNi and (b) CoCrFeNiSn.

4.6 Discussion: characterization of CoCrFeNi and CoCrFeNiSn after tribocorrosion testing in 0.6 M NaCl solution

4.6.1 Effect of the Sn addition on the tribocorrosion properties of CoCrFeNiSn testing in 0.6 M NaCl solution

As seen in the results above, the Sn addition to the CoCrFeNi alloy may be an important factor in the increase in tribocorrosion resistance seen in this work. This could be through the presence of a second phase in CoCrFeNiSn (a major hexagonal Ni-Sn-rich - confirmed by XRD in section 4.1.1, and also consistent with the XRD analysis from Hao et al. [215] - and a minor CoCrFeNi phase) rather than a single FCC phase in CoCrFeNi. Hao et al. [215] indicate that increasing the Sn proportion will increase the proportion of the hexagonal Ni₃Sn₂ phase in CoCrFeNiSn. This leads to an increase in hardness from CoCrFeNiSn_{x=0} to CoCrFeNiSn_{x=1} [215]. CoCrFeNiSn has higher hardness than CoCrFeNi, as shown in Figure 4.31 and Table 4.17. The occurrence of a hard Ni-Sn-rich phase could promote an increase in wear resistance at the CoCrFeNiSn surface. As presented in Figure 4.38, all wear rates in CoCrFeNiSn appear

to be lower compared to CoCrFeNi, and this also corresponds with the observed wear morphology of alloys. CoCrFeNiSn has no apparent sign of damage or cracks on the sample surface, while surface degradation can be detected at the CoCrFeNi surface, as in Figure 4.39. CoCrFeNiSn has been found to have a lower wear rate compared to CoCrFeNiSn₀ and CoCrFeNiSn_{0.5} alloys across a range of applied loads from 1 N to 5 N [215]. The presence of Sn in the oxidation state of SnO₂ seems likely to promote the stability of oxide films and increase corrosion resistance, Table 4.20. It also seems to increase stability in both sliding potential and cathodic current in Figures 4.37 and 4.38. This is consistent with the increased tendency to form SnO₂ at higher Cr proportion, as seen in the XPS analysis in [215].

To sum up, this research indicates that Sn addition to the main CoCrFeNi alloy has a vital role in raising the tribocorrosion properties, due to the formation of two phases, a major phase of hexagonal Ni-Sn-rich with high strength and a minor phase of FCC CoCrFeNi which shows greater ductility and imparts an increased degree of toughness. It also includes the promotion of corrosion resistance and the stability of oxide films resulting from the presence of Sn in the oxidation state.

CHAPTER 5

Overall conclusions and recommendations

5.1 Overall conclusions

The aim of this PhD research was to investigate the effect of specific alloying elements, Al, Cu, Sn, on the development of corrosion properties, hardness, and tribocorrosion resistance in the main CoCrFeNi HEA system. It can be concluded that;

- With the addition of these alloying elements, the microstructure and phase composition of the main CoCrFeNi system, which is a single phase of FCC CoCrFeNi, can be transformed to different structures. The formation of two phases in CoCrFeNiAl, CoCrFeNiCu and CoCrFeNiSn from the addition of Al, Cu and Sn. Two phases in CoCrFeNiAl, a major ordered B2 phase and a minor Al-Ni-rich phase, is generated when Al is added. CoCrFeNiCu consists of the FCC CoCrFeNi phase and the segregation of Cu, while the addition of Sn into CoCrFeNi can form a dual phase structure of FCC CoCrFeNi phase and hexagonal Ni-Sn-rich phase. These changes have the potential to lead to the improvement of the properties of these alloys, such as hardness, corrosion resistance, and tribocorrosion properties.
- The corrosion behaviour of the alloys studied was compared with two grades of stainless steels, SS304 and SS316, in different solutions. CoCrFeNiSn is found to have the highest passivity of all the tested specimens in 0.6M NaCl solution, resulting from good formation of oxide films based on Cr₂O₃ and SnO₂, while CoCrFeNiCu shows the poorest resistance to the corrosive effect of chloride solution, due to an unstable passive film which decreases the passive region. In addition, comparing corrosion behaviour between two stainless steels (SS304 and SS316) and experimental alloys in chloride solution indicates that the stainless steels, in the as cast condition tested here, have higher corrosion resistance than CoCrFeNiCu and CoCrFeNiAl. In contrast, they have poorer corrosion behaviour than CoCrFeNi and CoCrFeNiSn. In acidic and alkaline solutions, the lowest corrosion sensitivity with the highest corrosion and transpassive potentials (E_{corr} and E_t) are found in CoCrFeNiSn for 0.6M H₂SO₄ solution and CoCrFeNiCu for 0.6M NaAlO₂ solution, in both cases occurring as a consequence of the existence of protective oxide films containing Cr in the oxidation state of Cr₂O₃ and, in the

case of CoCrFeNiSn, Sn in the oxidation state of SnO₂ on the alloy surfaces (these may occur as simple oxides, or more complex oxides with multiple cations, with the likely participation of other elements from the alloy to some extent). It can be observed that CoCrFeNiAl has the highest passivity under both conditions, with likely formation of oxide layers based on mixed (Cr, Al)₂O₃ and/or Al₂O₃ films (with possible involvement of other metallic elements) on the specimen surface in both acidic and alkaline solutions. CoCrFeNiSn has high E_{corr} and E_t values and thus better corrosion behaviour than both SS304 and SS316 samples in a sulfuric acidic solution. The corrosion behaviour of CoCrFeNiCu in sodium aluminate solution has similar to CoCrFeNiSn in an acidic solution, in that it has high E_{corr} and E_t values, and so higher corrosion resistance than these stainless steels.

- CoCrFeNiSn has higher hardness than CoCrFeNi, due to the dual phase structure of CoCrFeNiSn. This consists of the Ni-Sn-rich phase, which is itself of high hardness, and the ductile CoCrFeNi phase, which seems to provide a degree of toughness improvement and resists crack propagation during hardness testing.
- CoCrFeNiSn showed good corrosion resistance in chloride solution and high hardness, and this alloy also has a good performance in tribocorrosion resistance in medium chloride conditions, compared with the main CoCrFeNi system. The dual phase structure with hexagonal Ni-Sn-rich and FCC CoCrFeNi phases is significant for this. Wear resistance is increased by the high hardness and ductile ability from the dual phase structure, and corrosion properties are aided by the stable protective film from Cr₂O₃ and SnO₂.

5.2 Recommendations

This PhD research has been designed based on the experimental assessment of the corrosion behaviour of different alloys under different solutions (NaCl, H₂SO₄, and NaAlO₂ solutions). In doing this, the emphasis was placed on electrochemical analysis via Potentiostat technique, as this is a reliable and rapid method that allows the differences in corrosion behaviour of all samples to be demonstrated. However, the understanding in this field is not complete without further evidence to address the exact composition and form of the oxide films which form on the specimen surfaces, as presented in chapter 4. These films could be single metallic element oxides in different locations on the surface, or mixed oxides with complex structure. The exact oxide will be important for complete explanation of the corrosion mechanism of all alloy systems in this work under the different electrolytes. Transmission

Electron Microscopy (TEM) analysis of the surface films on the alloy specimens would be needed to reveal the exact nature (structure and composition) of the passive films forming on each phase present in the microstructures. This technique would also resolve some remaining questions from this work, such as the identification of the crystal structure in the new Ni-Sn-rich phase observed in CoCrFeNiSn, and the change in microstructure and phase composition in pre- and post-corrosion testing. In addition, the chemical composition of all alloys after corrosion testing in both sulfuric acid and sodium aluminate solutions should analyze by EDS to indicate the change in alloy components and the emission of metal ions in the corrosion mechanism at the anodic area.

The promising properties of CoCrFeNiSn, at least for tribocorrosion resistance, are worth investigating further. There are many areas where both wear and corrosion occur, such as in bearings in marine wind turbines, for example, and better materials will mean reduced costs from maintenance and repair, and down time of the equipment. To make an assessment of suitability here however, it would be necessary to understand other properties of the alloy. While the hardness has been assessed in this work, the tensile properties have not, and, with the high volume fraction of the brittle Ni-Sn-rich phase it is perhaps likely that the alloy will show limited ductility and toughness, both of which would be limiting if it could not be used as a very thin surface layer. Following proper assessment of the actual mechanical properties of larger specimens, some alloy design work may be possible. In this study we have explored equiatomic HEAs only, but of course many compositions within the CoCrFeNiSn system are possible and by reducing the Sn content (CoCrFeNiSn_{x<1}), it should be possible to alter the fraction of the brittle reinforcing phase and possibly tune the mechanical behavior. Thermomechanical treatments could also be effective through microstructure control, and this could also be explored.

REFERENCES

- [1] Alaneme, K.K., Bodunrin, M.O. and Oke, S.R. (2016) ‘Processing, alloy composition and phase transition effect on the mechanical and corrosion properties of high entropy alloys: a review’, *Journal of materials research and technology*, 5(4), pp. 384–393. doi:10.1016/j.jmrt.2016.03.004.
- [2] Shi, Y., Yang, B. and Liaw, P.K. (2017) ‘Corrosion-resistant high-entropy alloys: A review’, *Metals*, 7(2), p. 43. doi:10.3390/met7020043.
- [3] Zheng, Z.Y., Li, X.C., Zhang, C. and Li, J.C. (2015) ‘Microstructure and corrosion behaviour of FeCoNiCuSn_x high entropy alloys’, *Materials science and technology*, 31(10), pp. 1148–1152. doi:10.1179/1743284714Y.0000000730.
- [4] Wang, W.R., Wang, W.L. and Yeh, J.W. (2014) ‘Phases, microstructure and mechanical properties of Al_xCoCrFeNi high-entropy alloys at elevated temperatures’, *Journal of alloys and compounds*, 589, pp. 143–152. doi:10.1016/j.jallcom.2013.11.084.
- [5] Murty, B.S., Yeh, J.W. and Ranganathan, S. (2014) “Chapter 1 and 2” in *High-entropy alloys*. London, England: Elsevier: Butterworth-Heinemann.
- [6] Yeh, J.W., Chen, S.K., Lin, S.J., Gan, J.Y., Chin, T.S., Shun, T.T., Tsau, C.H. and Chang, S.Y. (2004) ‘Nanostructured high-entropy alloys with multiple principal elements: novel alloy design concepts and outcomes’, *Advanced engineering materials*, 6(5), pp. 299–303. doi:10.1002/adem.200300567.
- [7] Davis, J.R. (2000) “Chapter 1” in *Corrosion [electronic resource]: understanding the basics*. Materials Park, Ohio: ASM International.
- [8] Tang, Z., Huang, L., He, W. and Liaw, P.K. (2014) ‘Alloying and processing effects on the aqueous corrosion behavior of high-entropy alloys’, *Entropy (Basel, Switzerland)*, 16(2), pp. 895–911. doi:10.3390/e16020895.
- [9] G2MT Laboratories, [Online] [Cited: 9 April 2020] <http://www.g2mtlabs.com/cost-of-corrosion/>
- [10] Kao, Y.F., Lee, T.D., Chen, S.K. and Chang, Y.S. (2010) ‘Electrochemical passive properties of Al_xCoCrFeNi (x = 0, 0.25, 0.50, 1.00) alloys in sulfuric acids’, *Corrosion science*, 52(3), pp. 1026–1034. doi:10.1016/j.corsci.2009.11.028.
- [11] Hsu, Y.J., Chiang, W.C. and Wu, J.K. (2005) ‘Corrosion behavior of FeCoNiCrCu_x high-entropy alloys in 3.5% sodium chloride solution’, *Materials chemistry and physics*, 92(1), pp. 112–117. doi:10.1016/j.matchemphys.2005.01.001.
- [12] Fujieda, T., Shiratori, H., Kuwabara, K., Hirota, M., Kato, T., Yamanaka, K., Koizumi, Y., Chiba, A. and Watanabe, S. (2017) ‘CoCrFeNiTi-based high-entropy alloy with superior tensile strength and corrosion resistance achieved by a combination of additive manufacturing using selective electron beam melting and solution treatment’, *Materials letters*, 189, pp. 148–151. doi:10.1016/j.matlet.2016.11.026.
- [13] Fujieda, T., Chen, M., Shiratori, H., Kuwabara, K., Yamanaka, K., Koizumi, Y., Chiba, A. and Watanabe, S. (2019) ‘Mechanical and corrosion properties of CoCrFeNiTi-based high-entropy alloy additive manufactured using selective laser melting’, *Additive manufacturing*, 25, pp. 412–420. doi:10.1016/j.addma.2018.10.023.

- [14] Ji, W., Fu, Z., Wang, W., Wang, H., Zhang, J., Wang, Y. and Zhang, F. (2014) ‘Mechanical alloying synthesis and spark plasma sintering consolidation of CoCrFeNiAl high-entropy alloy’, *Journal of alloys and compounds*, 589, pp. 61–66. doi:10.1016/j.jallcom.2013.11.146.
- [15] Murty, B.S., Yeh, J.W. and Ranganathan, S. (2014) “Chapter 1-5” in *High-entropy alloys*. London, England: Elsevier: Butterworth-Heinemann.
- [16] Alshataif, Y.A., Sivasankaran, S., Al-Mufadi, F.A., Alaboodi, A.S. and Ammar, H.R. (2020) ‘Manufacturing Methods, Microstructural and Mechanical Properties Evolutions of High-Entropy Alloys: A Review’, *Metals and materials international*, 26(8), pp. 1099–1133. doi:10.1007/s12540-019-00565-z.
- [17] Otto, F., Yang, Y., Bei, H. and George, E.P. (2013) ‘Relative effects of enthalpy and entropy on the phase stability of equiatomic high-entropy alloys’, *Acta materialia*, 61(7), pp. 2628–2638. doi:10.1016/j.actamat.2013.01.042.
- [18] Miracle, D.B. and Senkov, O.N. (2017) ‘A critical review of high entropy alloys and related concepts’, *Acta materialia*, 122, pp. 448–511. doi:10.1016/j.actamat.2016.08.081.
- [19] Calvo-Dahlborg, M. and Brown, S.G.R. (2017) ‘Hume-Rothery for HEA classification and self-organizing map for phases and properties prediction’, *Journal of alloys and compounds*, 724, pp. 353–364. doi:10.1016/j.jallcom.2017.07.074.
- [20] Yeh, J.W. (2006) ‘Recent progress in high-entropy alloys’, *European journal of control*, 31(6), pp. 633–648. doi:10.3166/acsm.31.633-648.
- [21] Geanta, V., Voiculescu, I., Vizureanu, P. and Sandu, A.V. (2019) “High entropy alloys for medical applications” in *Engineering steels and high entropy-alloys*. London: IntechOpen Press.
- [22] Brandani, G.B., Schor, M., MacPhee, C.E., Grubmüller, H., Zachariae, U. and Marenduzzo, D. (2013) ‘Quantifying disorder through conditional entropy: an application to fluid mixing’, *PloS one*, 8(6), pp. e65617–e65617. doi:10.1371/journal.pone.0065617.
- [23] Hoffmann, H.J. (2014) ‘Entropy and entropy of mixing’, *Materialwissenschaft und Werkstofftechnik*, 45(3), pp. 137–168. doi:10.1002/mawe.201400208.
- [24] Zhang, Y., Zhou, Y.J., Lin, J.P., Chen, G.L. and Liaw, P.K. (2008) ‘Solid-solution phase formation rules for multi-component alloys’, *Advanced engineering materials*, 10(6), pp. 534–538. doi:10.1002/adem.200700240.
- [25] Guo, S. and Liu, C.T. (2011) ‘Phase stability in high entropy alloys: formation of solid-solution phase or amorphous phase’, *Progress in natural science*, 21(6), pp. 433–446. doi:10.1016/S1002-0071(12)60080-X.
- [26] Guo, S., Hu, Q., Ng, C. and Liu, C.T. (2013) ‘More than entropy in high-entropy alloys: forming solid solutions or amorphous phase’, *Intermetallics*, 41, pp. 96–103. doi:10.1016/j.intermet.2013.05.002.
- [27] Chen, S., Cai, Z., Lu, Z., Pu, J., Chen, R., Zheng, S., Mao, C. and Chen, S. (2019) ‘Tribo-corrosion behavior of VAlTiCrCu high-entropy alloy film’, *Materials characterization*, 157, p. 109887. doi:10.1016/j.matchar.2019.109887.

- [28] Zhu, Z.G., Ma, K.H., Wang, Q. and Shek, C.H. (2016) ‘Compositional dependence of phase formation and mechanical properties in three CoCrFeNi-(Mn/Al/Cu) high entropy alloys’, *Intermetallics*, 79, pp. 1–11. doi:10.1016/j.intermet.2016.09.003.
- [29] Liang, S.M. and Schmid-Fetzer, R. (2017) ‘Evaluation of calphad approach and empirical rules on the phase stability of multi-principal element alloys’, *Journal of phase equilibria and diffusion*, 38(4), pp. 369–381. doi:10.1007/s11669-017-0577-0.
- [30] Guo, S., Ng, C., Lu, J. and Liu, C.T. (2011) ‘Effect of valence electron concentration on stability of fcc or bcc phase in high entropy alloys’, *Journal of applied physics*, 109(10), pp. 103505–103505–5. doi:10.1063/1.3587228.
- [31] Calvo-Dahlborg, M., Mehraban, S., Lavery, N.P., Brown, S.G.R., Cornide, J., Cullen, J., Cieslak, J., Leong, Z., Goodall, R. and Dahlborg, U. (2021) ‘Prediction of phase, hardness and density of high entropy alloys based on their electronic structure and average radius’, *Journal of alloys and compounds*, 865, p. 158799. doi:10.1016/j.jallcom.2021.158799.
- [32] Zhang, Y. and Peng, W.J. (2012) ‘Microstructural control and properties optimization of high-entropy alloys’, *Procedia engineering*, 27, pp. 1169–1178. doi:10.1016/j.proeng.2011.12.568.
- [33] Ren, M., Li, B. and Fu, H. (2013) ‘Formation condition of solid solution type high-entropy alloy’, *Transactions of nonferrous metals society of China*, 23(4), pp. 991–995. doi:10.1016/S1003-6326(13)62557-1.
- [34] Cui, L., Ma, B., Feng, S.Q. and Wang, X.L. (2014) ‘Microstructure and Mechanical Properties of High-Entropy Alloys CoCrFeNiAl by Welding’, *Advanced materials research*, 936, pp. 1635–1640.
- [35] Ji, W., Wang, W., Wang, H., Zhang, J., Wang, Y., Zhang, F. and Fu, Z. (2015) ‘Alloying behavior and novel properties of CoCrFeNiMn high-entropy alloy fabricated by mechanical alloying and spark plasma sintering’, *Intermetallics*, 56, pp. 24–27. doi:10.1016/j.intermet.2014.08.008.
- [36] Liu, H., Zhang, T., Sun, S., Zhang, G., Tian, X. and Chen, P. (2021) ‘Microstructure and dislocation density of AlCoCrFeNiSi_x high entropy alloy coatings by laser cladding’, *Materials letters*, 283, p. 128746. doi:10.1016/j.matlet.2020.128746.
- [37] Yeh, J.W., Liaw, P.K. and Zhang, Y. (2016) “Chapter 5: Fabrication Routes” in *High-entropy alloys: fundamentals and applications*. Switzerland: Springer.
- [38] Web of Science, [Online] [Cited: 17 April 2023] <https://www.webofscience.com/wos/woscc/basic-search>
- [39] Butler, T.M. and Weaver, M.L. (2016) ‘Oxidation behavior of arc melted AlCoCrFeNi multi-component high-entropy alloys’, *Journal of alloys and compounds*, 674, pp. 229–244. doi:10.1016/j.jallcom.2016.02.257.
- [40] Munitz, A., Salhov, S., Hayun, S. and Frage, N. (2016) ‘Heat treatment impacts the microstructure and mechanical properties of AlCoCrFeNi high entropy alloy’, *Journal of alloys and compounds*, 683, pp. 221–230. doi:10.1016/j.jallcom.2016.05.034.
- [41] Aristeidakis, I.S. and Tzini, M.I.T. (2016) *High Entropy Alloys*. University of Thessaly.
- [42] Wang, Y.P., Li, B.S., Ren, M.X., Yang, C. and Fu, H.Z. (2008) ‘Microstructure and compressive properties of AlCrFeCoNi high entropy alloy’, *Materials science & engineering*.

A, *Structural materials: properties, microstructure and processing*, 491(1), pp. 154–158. doi:10.1016/j.msea.2008.01.064.

[43] Qiu, Y., Gibson, M.A., Fraser, H.L. and Birbilis, N. (2015) ‘Corrosion characteristics of high entropy alloys’, *Materials science and technology*, 31(10), pp. 1235–1243. doi:10.1179/1743284715Y.0000000026.

[44] Muangtong, P. (2017) *Porous High Entropy Alloys: 1st Year Confirmation Report*. University of Sheffield.

[45] Bishop-Moser, J. (2018) “Manufacturing High Entropy Alloys: Pathway to Industrial Competitiveness”. Michigan: MForesight: Alliance for Manufacturing Foresight Press.

[46] Miracle, D.B., Miller, J.D., Senkov, O.N., Woodward, C., Uchic, M.D. and Tiley, J. (2014) ‘Exploration and development of high entropy alloys for structural applications’, *Entropy (Basel, Switzerland)*, 16(1), pp. 494–525. doi:10.3390/e16010494.

[47] Miracle, D.B. (2019) ‘High entropy alloys as a bold step forward in alloy development’, *Nature communications*, 10(1), pp. 1805. doi:10.1038/s41467-019-09700-1.

[48] Löbel, M., Lindner, T., Mehner, T. and Lampke, T. (2017) ‘Microstructure and wear resistance of AlCoCrFeNiTi high-entropy alloy coatings produced by HVOF’, *Coatings (Basel, Switzerland)*, 7(9), p. 144. doi:10.3390/coatings7090144.

[49] Liu, Y. and Janssen, G.C.A.M. (2017) ‘Impact wear of structural steel with yield strength of 235 MPa in various liquids’, *Coatings (Basel, Switzerland)*, 7(12), p. 237. doi:10.3390/coatings7120237.

[50] Gao, M.C., Miracle, D.B., Maurice, D., Yan, X., Zhang, Y. and Hawk, J.A. (2018) ‘High-entropy functional materials’, *Journal of materials research*, 33(19), pp. 3138–3155. doi:10.1557/jmr.2018.323.

[51] Guo, J., Wang, H., von Rohr, F., Wang, Z., Cai, S., Zhou, Y., Yang, K., Li, A., Jiang, S., Wu, Q., Cava, R.J. and Sun, L. (2017) ‘Robust zero resistance in a superconducting high-entropy alloy at pressures up to 190 GPa’, *Proceedings of the National Academy of Sciences - PNAS*, 114(50), pp. 13144–13147. doi:10.1073/pnas.1716981114.

[52] Chemistry LibreTextsTM: High Temperature Superconductors, [Online] [Cited: 15 October 2020] [https://chem.libretexts.org/Bookshelves/General_Chemistry/Map%3A_General_Chemistry_\(Petrucci_et_al.\)/23%3A_The_Transition_Elements/23.9%3A_High_Temperature_Superconductors](https://chem.libretexts.org/Bookshelves/General_Chemistry/Map%3A_General_Chemistry_(Petrucci_et_al.)/23%3A_The_Transition_Elements/23.9%3A_High_Temperature_Superconductors)

[53] Ma, N., Liu, S., Liu, W., Xie, L., Wei, D., Wang, L., Li, L., Zhao, B. and Wang, Y. (2020) ‘Research progress of titanium-based high entropy alloy: methods, properties, and applications’, *Frontiers in bioengineering and biotechnology*, 8, pp. 603522–603522. doi:10.3389/fbioe.2020.603522.

[54] Castro, D., Jaeger, P., Baptista, A.C. and Oliveira, J.P. (2021) ‘An overview of high-entropy alloys as biomaterials’, *Metals (Basel, Switzerland)*, 11(4), p. 648. doi:10.3390/met11040648.

[55] Akmal, M., Hussain, A., Afzal, M., Lee, Y.I. and Ryu, H.J. (2021) ‘Systematic study of (MoTa)_xNbTiZr medium- and high-entropy alloys for biomedical implants- In vivo biocompatibility examination’, *Journal of materials science & technology*, 78, pp. 183–191. doi:10.1016/j.jmst.2020.10.049.

- [56] Yang, W., Liu, Y., Pang, S., Liaw, P.K. and Zhang, T. (2020) ‘Bio-corrosion behavior and in vitro biocompatibility of equimolar TiZrHfNbTa high-entropy alloy’, *Intermetallics*, 124, p. 106845. doi:10.1016/j.intermet.2020.106845.
- [57] Wang, S., Wu, D., She, H., Wu, M., Shu, D., Dong, A., Lai, H. and Sun, B. (2020) ‘Design of high-ductile medium entropy alloys for dental implants’, *Materials science & engineering. C, Materials for biological applications*, 113, p. 110959. doi:10.1016/j.msec.2020.110959.
- [58] Murty, B.S., Yeh, J.W. and Ranganathan, S. (2014) “Appendix1” in *High-entropy alloys*. London, England: Elsevier: Butterworth-Heinemann.
- [59] Yeh, J.W. (2013) ‘Alloy design strategies and future trends in high-entropy alloys’, *JOM (1989)*, 65(12), pp. 1759–1771. doi:10.1007/s11837-013-0761-6.
- [60] He, F., Wang, Z., Han, B., Wu, Q., Chen, D., Li, J., Wang, J., Liu, C.T. and Kai, J.J. (2018) ‘Solid solubility, precipitates, and stacking fault energy of micro-alloyed CoCrFeNi high entropy alloys’, *Journal of alloys and compounds*, 769, pp. 490–502. doi:10.1016/j.jallcom.2018.07.336.
- [61] Wang, J., Guo, T., Li, J., Jia, W. and Kou, H. (2018) ‘Microstructure and mechanical properties of non-equilibrium solidified CoCrFeNi high entropy alloy’, *Materials chemistry and physics*, 210, pp. 192–196. doi:10.1016/j.matchemphys.2017.06.037.
- [62] Liu, W.H., Lu, Z.P., He, J.Y., Luan, J.H., Wang, Z.J., Liu, B., Liu, Y., Chen, M.W. and Liu, C.T. (2016) ‘Ductile CoCrFeNiMo_x high entropy alloys strengthened by hard intermetallic phases’, *Acta materialia*, 116, pp. 332–342. doi:10.1016/j.actamat.2016.06.063.
- [63] Baker, H. and Okamoto, H. (1992) *ASM Handbook. Vol. 3. Alloy Phase Diagrams*, ASM International, Materials Park, Ohio 44073-0002, USA, 1992. 501 pp.
- [64] Li, C., Li, J.C., Zhao, M. and Jiang, Q. (2010) ‘Effect of aluminum contents on microstructure and properties of Al_xCoCrFeNi alloys’, *Journal of alloys and compounds*, 504, pp. S515–S518. doi:10.1016/j.jallcom.2010.03.111.
- [65] Uporov, S., Bykov, V., Pryanichnikov, S., Shubin, A. and Uporova, N. (2017) ‘Effect of synthesis route on structure and properties of AlCoCrFeNi high-entropy alloy’, *Intermetallics*, 83, pp. 1–8. doi:10.1016/j.intermet.2016.12.003.
- [66] Hsu, C.Y., Juan, C.C., Chen, S.T., Sheu, T.S., Yeh, J.W. and Chen, S.K. (2013) ‘Phase diagrams of high-entropy alloy system Al-Co-Cr-Fe-Mo-Ni’, *JOM (1989)*, 65(12), pp. 1829–1839. doi:10.1007/s11837-013-0773-2.
- [67] Kao, Y.F., Chen, T.J., Chen, S.K. and Yeh, J.W. (2009) ‘Microstructure and mechanical property of as-cast, -homogenized, and -deformed Al_xCoCrFeNi (0 ≤ x ≤ 2) high-entropy alloys’, *Journal of alloys and compounds*, 488(1), pp. 57–64. doi:10.1016/j.jallcom.2009.08.090.
- [68] Verma, A., Tarate, P., Abhyankar, A.C., Mohape, M.R., Gowtam, D.S., Deshmukh, V.P. and Shanmugasundaram, T. (2019) ‘High temperature wear in CoCrFeNiCu_x high entropy alloys: The role of Cu’, *Scripta materialia*, 161, pp. 28–31. doi:10.1016/j.scriptamat.2018.10.007.
- [69] Cornide, J., Calvo-Dahlborg, M., Chambreland, S., Asensio Dominguez, L., Leong, Z., Dahlborg, U., Cunliffe, A., Goodall, R. and Todd, I. (2015) ‘Combined atom probe tomography and TEM investigations of CoCrFeNi, CoCrFeNi-Pd_x (x=0.5, 1.0, 1.5) and CoCrFeNi-Sn’, *Acta physica Polonica, A*, 128(4), pp. 557–560. doi:10.12693/APhysPolA.128.557.

- [70] *Fundamentals of modern manufacturing: materials, processes, and systems*. 3rd ed. (2007). Hoboken, N.J.: Wiley.
- [71] Broitman, E. (2017) ‘Indentation hardness measurements at macro-, micro-, and nanoscale: a critical overview’, *Tribology letters*, 65(1), pp. 1–18. doi:10.1007/s11249-016-0805-5.
- [72] Herrmann, K. (2011) “Chapter 1” in *Hardness testing; principles and applications*. Materials Park, Ohio: ASM International.
- [73] International Organization for Standardization. (2002) “ISO 14577: Metallic Materials-Instrumented Indentation Test for Hardness and Materials Parameters”. Geneva: International Organization for Standardization Press.
- [74] Rahim, R.A.A. and Elbahrawy, E.M.S. (2017) ‘The indentation size effect and its role in microhardness measurements of two viscoelastic materials under different loads and times’, *Al-Azhar Journal of Dental Science*, 20(1), pp. 45–51. doi: 10.21608/ajdsm.2017.107489
- [75] Kavetsky, T., Borcc, J., Sangwal, K. and Tsmots, V. (2010) ‘Indentation size effect and Vickers microhardness measurement of metal-modified arsenic chalcogenide glasses’, *Journal of optoelectronics and advanced materials*, 12(10), pp. 2082–2091.
- [76] Zuback, J.S. and DebRoy, T. (2018) ‘The hardness of additively manufactured alloys’, *Materials*, 11(11), p. 2070. doi:10.3390/ma11112070.
- [77] Maskery, I., Aboulkhair, N.T., Corfield, M.R., Tuck, C., Clare, A.T., Leach, R.K., Wildman, R.D., Ashcroft, I.A. and Hague, R.J.M. (2016) ‘Quantification and characterisation of porosity in selectively laser melted Al–Si10–Mg using X-ray computed tomography’, *Materials characterization*, 111, pp. 193–204. doi:10.1016/j.matchar.2015.12.001.
- [78] Chou, R., Milligan, J., Paliwal, M. and Brochu, M. (2015) ‘Additive manufacturing of Al-12Si alloy via pulsed selective laser melting’, *JOM (1989)*, 67(3), pp. 590–596. doi:10.1007/s11837-014-1272-9.
- [79] Zhang, H., Zhu, H., Qi, T., Hu, Z. and Zeng, X. (2016) ‘Selective laser melting of high strength Al–Cu–Mg alloys: processing, microstructure and mechanical properties’, *Materials science & engineering. A, Structural materials : properties, microstructure and processing*, 656, pp. 47–54. doi:10.1016/j.msea.2015.12.101.
- [80] Cormier, D., Harrysson, O. and West, H. (2004) ‘Characterization of H13 steel produced via electron beam melting’, *Rapid prototyping journal*, 10(1), pp. 35–41. doi:10.1108/13552540410512516.
- [81] Simchi, A. and Asgharzadeh, H. (2004) ‘Densification and microstructural evaluation during laser sintering of M2 high speed steel powder’, *Materials science and technology*, 20(11), pp. 1462–1468. doi:10.1179/026708304X3944.
- [82] Jamshidinia, M., Sadek, A., Wang, W. and Kelly, S. (2015) ‘Additive manufacturing: of steel alloys using laser powder-bed fusion’, *Advanced materials & processes*, 173(1), pp. 20–24.
- [83] Zhang, K., Liu, W.J. and Shang, X.F. (2007) ‘Characteristics of laser aided direct metal powder deposition process for nickel-based superalloy’, *Materials science forum*, 534-536, pp. 457–460.

- [84] Wang, Z., Guan, K., Gao, M., Li, X., Chen, X. and Zeng, X. (2012) ‘The microstructure and mechanical properties of deposited-IN718 by selective laser melting’, *Journal of alloys and compounds*, 513, pp. 518–523. doi:10.1016/j.jallcom.2011.10.107.
- [85] Kanagarajah, P., Brenne, F., Niendorf, T. and Maier, H.J. (2013) ‘Inconel 939 processed by selective laser melting: effect of microstructure and temperature on the mechanical properties under static and cyclic loading’, *Materials science & engineering. A, Structural materials: properties, microstructure and processing*, 588, pp. 188–195. doi:10.1016/j.msea.2013.09.025.
- [86] Poondla, N., Srivatsan, T.S., Patnaik, A. and Petraroli, M. (2009) ‘A study of the microstructure and hardness of two titanium alloys: Commercially pure and Ti–6Al–4V’, *Journal of alloys and compounds*, 486(1), pp. 162–167. doi:10.1016/j.jallcom.2009.06.172.
- [87] Hernandez, J., Li, S.J., Martinez, E., Murr, L.E., Pan, X.M., Amato, K.N., Cheng, X.Y., Yang, F., Terrazas, C.A., Gaytan, S.M., Hao, Y.L., Yang, R., Medina, F. and Wicker, R.B. (2013) ‘Microstructures and hardness properties for β -phase Ti-24Nb-4Zr-7.9Sn alloy fabricated by electron beam melting’, *Journal of materials science & technology*, 29(11), pp. 1011–1017. doi:10.1016/j.jmst.2013.08.023.
- [88] Huang, W., Zhang, Y., Dai, W. and Long, R. (2019) ‘Mechanical properties of 304 austenite stainless steel manufactured by laser metal deposition’, *Materials science & engineering. A, Structural materials: properties, microstructure and processing*, 758, pp. 60–70. doi:10.1016/j.msea.2019.04.108.
- [89] Tucho, W.M., Lysne, V.H., Austbø, H., Sjolyst-Kverneland, A. and Hansen, V. (2018) ‘Investigation of effects of process parameters on microstructure and hardness of SLM manufactured SS316L’, *Journal of alloys and compounds*, 740, pp. 910–925. doi:10.1016/j.jallcom.2018.01.098.
- [90] Wang, W.R., Wang, W.L., Wang, S.C., Tsai, Y.C., Lai, C.H. and Yeh, J.W. (2012) ‘Effects of Al addition on the microstructure and mechanical property of $\text{Al}_x\text{CoCrFeNi}$ high-entropy alloys’, *Intermetallics*, 26, pp. 44–51. doi:10.1016/j.intermet.2012.03.005.
- [91] Jiang, H., Han, K., Qiao, D., Lu, Y., Cao, Z. and Li, T. (2018) ‘Effects of Ta addition on the microstructures and mechanical properties of CoCrFeNi high entropy alloy’, *Materials chemistry and physics*, 210, pp. 43–48. doi:10.1016/j.matchemphys.2017.05.056.
- [92] Tsau, C.H. and Tsai, M.C. (2018) ‘The effects of Mo and Nb on the microstructures and properties of CrFeCoNi(Nb,Mo) alloys’, *Entropy (Basel, Switzerland)*, 20(9), p. 648. doi:10.3390/e20090648.
- [93] Shun, T.T., Chang, L.Y. and Shiu, M.H. (2012) ‘Microstructures and mechanical properties of multiprincipal component CoCrFeNiTi_x alloys’, *Materials science & engineering. A, Structural materials: properties, microstructure and processing*, 556, pp. 170–174. doi:10.1016/j.msea.2012.06.075.
- [94] Salishchev, G.A., Tikhonovsky, M.A., Shaysultanov, D.G., Stepanov, N.D., Kuznetsov, A.V., Kolodiy, I.V., Tortika, A.S. and Senkov, O.N. (2014) ‘Effect of Mn and V on structure and mechanical properties of high-entropy alloys based on CoCrFeNi system’, *Journal of alloys and compounds*, 591, pp. 11–21. doi:10.1016/j.jallcom.2013.12.210.
- [95] Erdogan, A., Döleker, K.M. and Zeytin, S. (2020) ‘Effect of laser re-melting on electric current assistive sintered CoCrFeNiAl_xTi_y high entropy alloys: formation, micro-hardness and

wear behaviors’, *Surface & coatings technology*, 399, p. 126179. doi:10.1016/j.surfcoat.2020.126179.

[96] Lee, C.F. and Shun, T.T. (2016) ‘Effect of Fe content on microstructure and mechanical properties of $\text{Al}_{0.5}\text{CoCrFe}_x\text{NiTi}_{0.5}$ high-entropy alloys’, *Materials characterization*, 114, pp. 179–184. doi:10.1016/j.matchar.2016.02.018.

[97] Ma, S.G. and Zhang, Y. (2012) ‘Effect of Nb addition on the microstructure and properties of AlCoCrFeNi high-entropy alloy’, *Materials science & engineering. A, Structural materials: properties, microstructure and processing*, 532, pp. 480–486. doi:10.1016/j.msea.2011.10.110.

[98] Dong, Y., Zhou, K., Lu, Y., Gao, X., Wang, T. and Li, T. (2014) ‘Effect of vanadium addition on the microstructure and properties of AlCoCrFeNi high entropy alloy’, *Materials & design*, 57, pp. 67–72.

[99] Jiang, L., Cao, Z.Q., Jie, J.C., Zhang, J.J., Lu, Y.P., Wang, T.M. and Li, T.J. (2015) ‘Effect of Mo and Ni elements on microstructure evolution and mechanical properties of the $\text{CoFeNi}_x\text{VMo}_y$ high entropy alloys’, *Journal of alloys and compounds*, 649, pp. 585–590. doi:10.1016/j.jallcom.2015.07.185.

[100] Neto, M.Q. (2019) *Understanding the Wear and Tribocorrosion Processes and Mechanisms of Titanium Alloys in Bovine Serum Solution*. University of Sheffield.

[101] Jiang, S., Lin, Z., Xu, H. and Sun, Y. (2018) ‘Studies on the microstructure and properties of $\text{Al}_x\text{CoCrFeNiTi}_{1-x}$ high entropy alloys’, *Journal of alloys and compounds*, 741, pp. 826–833. doi:10.1016/j.jallcom.2018.01.247.

[102] Chatterjee, B. (2015) ‘Science and industry of electropolishing’, *Jahrbuch Oberflächentechnik*, 71, pp. 77–93.

[103] Amin, M.A., El-Bagoury, N., Saracoglu, M. and Ramadan, M. (2014) ‘Electrochemical and corrosion behavior of cast re-containing inconel 718 alloys in sulphuric acid solutions and the effect of Cl^- ’, *International journal of electrochemical science*, 9(9), pp. 5352–5374.

[104] American Society for Testing and Materials, (2004) “ASTM-G102-89: Standard Practice for Calculation of Corrosion Rates and Related Information from Electrochemical Measurements”. West Conshohocken: ASTM International Press.

[105] Ahmad, Z. and Institution of Chemical Engineers (2006) *Principles of corrosion engineering and corrosion control [electronic resource]*. 1st ed. Amsterdam; Boston, Mass.: Elsevier/BH.

[106] Davis, J.R. (2000) “Chapter 3” in *Corrosion [electronic resource]: understanding the basics*. Materials Park, Ohio: ASM International.

[107] Tan, Y. (2013) *Heterogeneous electrode processes and localized corrosion [electronic resource]*. Hoboken, N.J.: Wiley.

[108] Cramer, S.D. and Covino, B.S. (2003) *ASM Handbook Vol. 13A Corrosion: Fundamentals, Testing, and Protection*, ASM Handbook Vol. 13A Corrosion: Fundamentals, Testing, and Protection.

[109] Cicek, V. (2014) *Corrosion engineering*. Beverly, Massachusetts; Hoboken, New Jersey: Scrivener Publishing: Wiley.

- [110] Moncmanova, A. (2007) *Environmental deterioration of materials*. Slovak Republic: WIT Press.
- [111] Garcia, E.M., Santos, J.S., Pereira, E.C. and Freitas, M.B.J.G. (2008) ‘Electrodeposition of cobalt from spent Li-ion battery cathodes by the electrochemistry quartz crystal microbalance technique’, *Journal of power sources*, 185(1), pp. 549–553. doi:10.1016/j.jpowsour.2008.07.011.
- [112] Huang, L., Yu, C.H., Hopke, P.K., Shin, J.Y. and Fan, Z. (2014) ‘Trivalent chromium solubility and its influence on quantification of hexavalent chromium in ambient particulate matter using EPA method 6800’, *Journal of the Air & Waste Management Association (1995)*, 64(12), pp. 1439–1445. doi:10.1080/10962247.2014.951745.
- [113] Singh, P., Sunder, M., Campbell, E. and Palmer, L. (2020). ‘A case study of nickel dendritic growth on printed-circuit boards’, in *Conference: 2020 Pan Pacific Microelectronics Symposium (Pan Pacific)*. doi:10.23919/PanPacific48324.2020.9059398.
- [114] Zohdy, K.M., El-Sherif, R.M. and El-Shamy, A.M. (2021) ‘Corrosion and Passivation Behaviors of Tin in Aqueous Solutions of Different pH’, *Journal of Bio- and Tribo- Corrosion*, 7(2). doi:10.1007/s40735-021-00515-6.
- [115] Becker, W.T. and Shipley, R.J. (2002) *ASM Handbook Vol. 11 Failure Analysis and Prevention*, ASM Handbook Vol. 11 Failure Analysis and Prevention.
- [116] Elayaperumal, K. and Raja, V.S. (2015) *Corrosion failures: theory, case studies, and solutions*. Hoboken, New Jersey: John Wiley & Sons, Inc.
- [117] Ali, A.M. (2021) ‘Investigation the effect of friendly environment material on aluminum corrosion resistant’, *Journal of Mechanical Engineering Research and Developments*, 44(1).
- [118] Shi, J.M., He, C.L., Li, G.P., Chen, H.Z., Fu, X.Y., Li, R., Ma, G.F. and Wang, J.M. (2018) ‘Corrosion behaviorsof pure copper and Cu-Ni-Zn alloy in NaCl solution and artificial salt water’, in *2nd International Conference on New Material and Chemical Industry (NMCi2017)*. Bristol: Iop Publishing Ltd. doi:10.1088/1757-899X/292/1/012004.
- [119] EL Ibrahim, B., Bazzi, L. and EL Issami, S. (2020) ‘The role of pH in corrosion inhibition of tin using the proline amino acid: theoretical and experimental investigations’, *RSC advances*, 1(5), pp. 29696–2974. doi:10.1039/d0ra04333h.
- [120] Badawy, W.A., Ismail, K.M. and Fathi, A.M. (2006) ‘Corrosion control of Cu–Ni alloys in neutral chloride solutions by amino acids’, *Electrochimica acta*, 51(20), pp. 4182–4189. doi:10.1016/j.electacta.2005.11.037.
- [121] Shalabi, K., El-Gammal, O.A. and Abdallah, Y.M. (2021) ‘Adsorption and inhibition effect of tetraaza-tetradentate macrocycle ligand and its Ni (II), Cu (II) complexes on the corrosion of Cu10Ni alloy in 3.5% NaCl solutions’, *Colloids and surfaces. A, Physicochemical and engineering aspects*, 609, p. 125653. doi:10.1016/j.colsurfa.2020.125653.
- [122] Mosayebi, S., Rezaei, M. and Mahidashti, Z. (2020) ‘Comparing corrosion behavior of Ni and Ni-Mo electroplated coatings in chloride mediums’, *Colloids and surfaces. A, Physicochemical and engineering aspects*, 594, p. 124654. doi:10.1016/j.colsurfa.2020.124654.
- [123] Sharma, A., Oh, M.C., Kim, J.T., Srivastava, A.K. and Ahn, B. (2020) ‘Investigation of electrochemical corrosion behavior of additive manufactured Ti–6Al–4V alloy for medical

implants in different electrolytes', *Journal of alloys and compounds*, 830, p. 154620. doi:10.1016/j.jallcom.2020.154620.

[124] Liu, J., Liu, H., Chen, P. and Hao, J. (2019) 'Microstructural characterization and corrosion behaviour of AlCoCrFeNiTi_x high-entropy alloy coatings fabricated by laser cladding', *Surface & coatings technology*, 361, pp. 63–74. doi:10.1016/j.surfcoat.2019.01.044.

[125] Ye, Q., Feng, K., Li, Z., Lu, F., Li, R., Huang, J. and Wu, Y. (2017) 'Microstructure and corrosion properties of CrMnFeCoNi high entropy alloy coating', *Applied surface science*, 396, pp. 1420–1426. doi:10.1016/j.apsusc.2016.11.176.

[126] Zhou, C., Hu, S., Shi, Q., Tao, H., Song, Y., Zheng, J., Xu, P. and Zhang, L. (2020) 'Improvement of corrosion resistance of SS316L manufactured by selective laser melting through subcritical annealing', *Corrosion science*, 164, p. 108353. doi:10.1016/j.corsci.2019.108353.

[127] Porcayo-Calderon, J., Rodriguez-Diaz, R.A., Porcayo-Palafox, E., Colin, J., Molina-Ocampo, A. and Martinez-Gomez, L. (2015) 'Effect of Cu addition on the electrochemical corrosion performance of Ni₃Al in 1.0 M H₂SO₄', *Advances in materials science and engineering*, 2015. doi:10.1155/2015/209286.

[128] Wasekar, N.P., Verulkar, S., Vamsi, M.V.N. and Sundararajan, G. (2019) 'Influence of molybdenum on the mechanical properties, electrochemical corrosion and wear behavior of electrodeposited Ni-Mo alloy', *Surface & coatings technology*, 370, pp. 298–310. doi:10.1016/j.surfcoat.2019.04.059.

[129] Valle-Quitana, J.C., Dominguez-Patiño, G.F. and Gonzalez-Rodriguez, J.G. (2014) 'Corrosion inhibition of carbon steel in 0.5 M H₂SO₄ by phtalocyanine blue', *ISRN Corrosion* [Preprint]. doi:10.1155/2014/945645.

[130] Galal, A., Atta, N.F. and Al-Hassan, M.H.S. (2005) 'Effect of some thiophene derivatives on the electrochemical behavior of AISI 316 austenitic stainless steel in acidic solutions containing chloride ions II. Effect of temperature and surface studies', *Materials chemistry and physics*, 89(1), pp. 28–37. doi:10.1016/j.matchemphys.2004.08.018.

[131] Halim, J., Abdel-Karim, R., El-Raghy, S., Nabil, M. and Waheed, A. (2012) 'Electrodeposition and characterization of nanocrystalline Ni-Mo catalysts for hydrogen production', *Journal of nanomaterials*, 2012, pp. 1–9. doi:10.1155/2012/845673.

[132] Qiu, X. (2019) 'Corrosion behavior of Al₂CrFeCo_xCuNiTi high-entropy alloy coating in alkaline solution and salt solution', *Results in physics*, 12, pp. 1737–1741. doi:10.1016/j.rinp.2019.01.090.

[133] Wang, J., Li, W., Yang, H., Huang, H., Ji, S., Ruan, J. and Liu, Z. (2020) 'Corrosion behavior of CoCrNi medium-entropy alloy compared with 304 stainless steel in H₂SO₄ and NaOH solutions', *Corrosion science*, 177, p. 108973. doi:10.1016/j.corsci.2020.108973.

[134] Rahman, T., Ebert, W.L. and Indacochea, J.E. (2018) 'Effect of molybdenum additions on the microstructures and corrosion behaviours of 316L stainless steel-based alloys', *Corrosion Engineering, Science and Technology*, 53(3), pp. 226-233. doi: 10.1080/1478422X.2018.1443991.

[135] Szewczyk-Nykiel, A. (2015) 'The influence of molibdenum on corrosion resistance of sintered austenitic stainless steels', *Technical Transactions*, 112(4-M), pp. 131–142. doi: 10.4467/2353737XCT.15.344.4865.

- [136] Shi, Y., Collins, L., Feng, R., Zhang, C., Balke, N., Liaw, P.K. and Yang, B. (2017) ‘Corrosion of $\text{Al}_x\text{CoCrFeNi}$ high-entropy alloys: Al-content and potential scan-rate dependent pitting behavior’, *Corrosion science*, 119, pp. 33–45. doi:10.1016/j.corsci.2017.02.019.
- [137] Wang, W., Wang, J., Yi, H., Qi, W. and Peng, Q. (2018) ‘Effect of molybdenum additives on corrosion behavior of $(\text{CoCrFeNi})_{100-x}\text{Mo}_x$ high-entropy alloys’, *Entropy (Basel, Switzerland)*, 20(12), p. 908. doi:10.3390/e20120908.
- [138] Ren, B., Liu, Z.X., Li, D.M., Shi, L., Cai, B. and Wang, M.X. (2012) ‘Corrosion behavior of CuCrFeNiMn high entropy alloy system in 1 M sulfuric acid solution’, *Materials and corrosion*, 63(9), pp. 828–834. doi:10.1002/maco.201106072.
- [139] Chou, Y.L., Yeh, J.W. and Shih, H.C. (2010) ‘The effect of molybdenum on the corrosion behaviour of the high-entropy alloys $\text{Co}_{1.5}\text{CrFeNi}_{1.5}\text{Ti}_{0.5}\text{Mo}_x$ in aqueous environments’, *Corrosion science*, 52(8), pp. 2571–2581. doi:10.1016/j.corsci.2010.04.004.
- [140] Mathew, M.T., Srinivasa Pai, P., Pourzal, R., Fischer, A. and Wimmer, M.A. (2009) ‘Significance of tribocorrosion in biomedical applications: overview and current status’, *Advances in tribology*, 2009, pp. 1–12. doi:10.1155/2009/250986.
- [141] Nair, R.B., Arora, H.S., Ayyagari, A., Mukherjee, S. and Grewal, H.S. (2018) ‘High entropy alloys: prospective materials for tribo-corrosion applications’, *Advanced engineering materials*, 20(6), p. 1700946–n/a. doi:10.1002/adem.201700946.
- [142] López-Ortega, A., Arana, J.L. and Bayón, R. (2018) ‘Tribocorrosion of passive materials: a review on test procedures and standards’, *International journal of corrosion*, 2018, pp. 1–24. doi:10.1155/2018/7345346.
- [143] Hutchings, I.M. (2017) *Tribology: friction and wear of engineering materials*. 2nd edition. Kidlington, Oxford, United Kingdom: Butterworth-Heinemann, an imprint of Elsevier.
- [144] Igual Muoz, A. and Espallargas, N. (2011) “Tribocorrosion mechanisms in sliding contacts” in *Tribocorrosion of Passive Metals and Coatings*. Cambridge: Woodhead Publishing Press.
- [145] Davis, J.R. (2000) *Corrosion [electronic resource]: understanding the basics*. Materials Park, Ohio: ASM International.
- [146] Sun, Y. and Rana, V. (2011) ‘Tribocorrosion behaviour of AISI 304 stainless steel in 0.5 M NaCl solution’, *Materials chemistry and physics*, 129(1), pp. 138–147. doi:10.1016/j.matchemphys.2011.03.063.
- [147] Yan, Y., Neville, A., Dowson, D. and Williams, S. (2006) ‘Tribocorrosion in implants-assessing high carbon and low carbon Co–Cr–Mo alloys by in situ electrochemical measurements’, *Tribology international*, 39(12), pp. 1509–1517. doi:10.1016/j.triboint.2006.01.016.
- [148] Chen, J., Zhang, Q., Li, Q., Fu, S. and Wang, J. (2014) ‘Corrosion and tribocorrosion behaviors of AISI 316 stainless steel and Ti6Al4V alloys in artificial seawater’, *Transactions of nonferrous metals society of China*, 24(4), pp. 1022–1031. doi:10.1016/S1003-6326(14)63157-5.
- [149] Wood, R.J.K. (2007) ‘Tribo-corrosion of coatings: a review’, *Journal of physics. D, Applied physics*, 40(18), pp. 5502–5521. doi:10.1088/0022-3727/40/18/S10.

- [150] Argade, G.R., Joshi, S.S., Ayyagari, A.V., Mukherjee, S., Mishra, R.S. and Dahotre, N.B. (2019) 'Tribocorrosion performance of laser additively processed high-entropy alloy coatings on aluminum', *Applied physics. A, Materials science & processing*, 125(4), pp. 1–9. doi:10.1007/s00339-019-2573-1.
- [151] Zeng, Q. and Xu, Y. (2020) 'A comparative study on the tribocorrosion behaviors of AlFeCrNiMo high entropy alloy coatings and 304 stainless steel', *Materials today communications*, 24, p. 101261. doi:10.1016/j.mtcomm.2020.101261.
- [152] Kitano, M., Ishii, H., Shirai, Y. and Ohmi, T. (2011) 'High-corrosion-resistant Al₂O₃ passivation-film formation by selective oxidation on austenitic stainless steel containing Al', *Journal of vacuum science & technology. A, Vacuum, surfaces, and films*, 29(2), p. 21002. doi:10.1116/1.3543709.
- [153] Ni, S., Lv, X., Li, T., Yang, X. and Zhang, L. (2013) 'Preparation of Cu₂O–Cu anode for high performance Li-ion battery via an electrochemical corrosion method', *Electrochimica acta*, 109, pp. 419–425. doi:10.1016/j.electacta.2013.07.088.
- [154] Wan, C., Zhang, L. and Liu, X. (2020) 'Corrosion assessment of Sn-Ni alloy coatings using neutral salt spray tests and electrochemical methods', *International journal of electrochemical science*, 15(1), pp. 26–38. doi:10.20964/2020.01.20.
- [155] Takeuchi, A. and Inoue, A. (2005) 'Classification of bulk metallic glasses by atomic size difference, heat of mixing and period of constituent elements and its application to characterization of the main alloying element', *Materials transactions*, 46(12), pp. 2817–2829. doi:10.2320/matertrans.46.2817.
- [156] Gordy, W. and Thomas, W.J.O. (1956) 'Electronegativities of the elements' *The Journal of Chemical Physics*, 24, pp. 439–444.
- [157] Xiao, D.H., Zhou, P.F., Wu, W.Q., Diao, H.Y., Gao, M.C., Song, M. and Liaw, P.K. (2017) 'Microstructure, mechanical and corrosion behaviors of AlCoCuFeNi-(Cr,Ti) high entropy alloys', *Materials & design*, 116, pp. 438–447. doi:10.1016/j.matdes.2016.12.036.
- [158] METTLER TOLEDO, "Operating Instructions: NewClassic Balances-ML Models", Switzerland: Mettler-Toledo AG Press.
- [159] Greczynski, G. and Hultman, L. (2021) 'Towards reliable X-ray photoelectron spectroscopy: sputter-damage effects in transition metal borides, carbides, nitrides, and oxides', *Applied surface science*, 542, p. 148599. doi:10.1016/j.apsusc.2020.148599.
- [160] Watts, J.F. and Wolstenholme, J. (2003) *An Introduction to Surface Analysis by XPS and AES*. Chichester West Sussex England: J. Wiley.
- [161] Moulder, J.F. and Chastain, J. (1992) *Handbook of X-ray photoelectron spectroscopy: a reference book of standard spectra for identification and interpretation of XPS data*. Eden Prairie, Minn, Physical Electronics Division, Perkin-Elmer Corp.
- [162] Shi, Y., Collins, L., Balke, N., Liaw, P.K. and Yang, B. (2018) 'In-situ electrochemical-AFM study of localized corrosion of Al_xCoCrFeNi high-entropy alloys in chloride solution', *Applied surface science*, 439, pp. 533–544. doi:10.1016/j.apsusc.2018.01.047.
- [163] Tokarewicz, M., Grądzka-Dahlke, M., Rećko, K., Łepicka, M. and Czajkowska, K. (2022) 'Investigation of the structure and corrosion resistance of novel high-entropy alloys for potential biomedical applications', *Materials*, 15(11), p. 3938. doi:10.3390/ma15113938.

- [164] Nascimento, C.B., Donatus, U., Ríos, C.T. and Antunes, R.A. (2020) ‘Electronic properties of the passive films formed on CoCrFeNi and CoCrFeNiAl high entropy alloys in sodium chloride solution’, *Journal of materials research and technology*, 9(6), pp. 13879–13892. doi:10.1016/j.jmrt.2020.10.002.
- [165] Ayyagari, A., Hasannaemi, V., Grewal, H., Arora, H. and Mukherjee, S. (2018) ‘Corrosion, erosion and wear behavior of complex concentrated alloys: a review’, *Metals (Basel, Switzerland)*, 8(8), p. 603. doi:10.3390/met8080603.
- [166] Gamry Instruments: basics of electrochemical impedance spectroscopy [Online] [Cited: 20 April 2023] <https://www.gamry.com/application-notes/EIS/basics-of-electrochemical-impedance-spectroscopy/>
- [167] Espallargas, N., Johnsen, R., Torres, C. and Muñoz, A.I. (2013) ‘A new experimental technique for quantifying the galvanic coupling effects on stainless steel during tribocorrosion under equilibrium conditions’, *Wear*, 307(1-2), pp. 190–197. doi:10.1016/j.wear.2013.08.026.
- [168] Vieira, A.C., Rocha, L.A., Papageorgiou, N. and Mischler, S. (2012) ‘Mechanical and electrochemical deterioration mechanisms in the tribocorrosion of Al alloys in NaCl and in NaNO₃ solutions’, *Corrosion science*, 54(1), pp. 26–35. doi:10.1016/j.corsci.2011.08.041.
- [169] Papageorgiou, N. and Mischler, S. (2012) ‘Electrochemical simulation of the current and potential response in sliding tribocorrosion’, *Tribology letters*, 48(3), pp. 271–283. doi:10.1007/s11249-012-0022-9.
- [170] Mischler, S. (2013) “Sliding Tribo-Corrosion of Passive Metals: Mechanisms and Modeling” in *Tribo-Corrosion: Research, Testing, and Applications*. West Conshohocken: ASTM International Press.
- [171] Chaplygina, A.A., Chaplygin, P.A. and Starostenkov, M.D. (2018) ‘Structural transformations in the NiAl alloys with deviations from the stoichiometric composition during stepwise cooling’, *IOP Conference Series: Materials Science and Engineering*, 447(1), p. 12054. doi:10.1088/1757-899X/447/1/012054.
- [172] Muangtong, P., Rodchanarowan, A., Chaysuwan, D., Chanlek, N. and Goodall, R. (2020) ‘The corrosion behaviour of CoCrFeNi-x (x = Cu, Al, Sn) high entropy alloy systems in chloride solution’, *Corrosion science*, 172, p. 108740. doi:10.1016/j.corsci.2020.108740.
- [173] Wang, X.F., Zhang, Y., Qiao, Y. and Chen, G.L. (2007) ‘Novel microstructure and properties of multicomponent CoCrCuFeNiTi_x alloys’, *Intermetallics*, 15(3), pp. 357–362. doi:10.1016/j.intermet.2006.08.005.
- [174] Mu, Y.K., Jia, Y.D., Xu, L., Jia, Y.F., Tan, X.H., Yi, J., Wang, G. and Liaw, P.K. (2019) ‘Nano oxides reinforced high-entropy alloy coatings synthesized by atmospheric plasma spraying’, *Materials research letters*, 7(8), pp. 312–319. doi:10.1080/21663831.2019.1604443.
- [175] Qiu, Y., Thomas, S., Fabijanic, D., Barlow, A.J., Fraser, H.L. and Birbilis, N. (2019) ‘Microstructural evolution, electrochemical and corrosion properties of Al_xCoCrFeNiTi_y high entropy alloys’, *Materials & design*, 170. doi:10.1016/j.matdes.2019.107698.
- [176] Wang, W., Qi, W., Xie, L., Yang, X., Li, J. and Zhang, Y. (2019) ‘Microstructure and corrosion behavior of (CoCrFeNi)₉₅Nb₅ high-entropy alloy coating fabricated by plasma spraying’, *Materials*, 12(5), p. 694. doi:10.3390/ma12050694.

- [177] Schwarz, H., Uhlig, T., Rösch, N., Lindner, T., Ganss, F., Hellwig, O., Lampke, T., Wagner, G. and Seyller, T. (2021) ‘CoCrFeNi high-entropy alloy thin films synthesised by magnetron sputter deposition from spark plasma sintered targets’, *Coatings (Basel, Switzerland)*, 11(4), p. 468. doi:10.3390/coatings11040468.
- [178] Freindl, K., Partyka-Jankowska, E., Karaś, W., Zając, M., Madej, E., Spiridis, N., Ślęzak, M., Ślęzak, T., Wiśnios, D. and Korecki, J. (2013) ‘Oxygen on an Fe monolayer on W(110): from chemisorption to oxidation’, *Surface science*, 617(100), pp. 183–191. doi:10.1016/j.susc.2013.07.011.
- [179] Milosan, I., Florescu, M., Cristea, D., Voiculescu, I., Pop, M.A., Cañadas, I., Rodriguez, J., Bogatu, C.A. and Bedo, T. (2020) ‘Evaluation of heat-treated AISI 316 stainless steel in solar furnaces to be used as possible implant material’, *Materials*, 13(3), p. 581. doi:10.3390/ma13030581.
- [180] Wang, B., He, H., Naeem, M., Lan, S., Harjo, S., Kawasaki, T., Nie, Y., Kui, H.W., Ungár, T., Ma, D., Stoica, A.D., Li, Q., Ke, Y., Liu, C.T. and Wang, X.L. (2018) ‘Deformation of CoCrFeNi high entropy alloy at large strain’, *Scripta materialia*, 155, pp. 54–57. doi:10.1016/j.scriptamat.2018.06.013.
- [181] Zaddach, A.J., Niu, C., Koch, C.C. and Irving, D.L. (2013) ‘Mechanical properties and stacking fault energies of NiFeCrCoMn high-entropy alloy’, *JOM (1989)*, 65(12), pp. 1780–1789. doi:10.1007/s11837-013-0771-4.
- [182] Liu, L., Zhu, J.B., Zhang, C., Li, J.C. and Jiang, Q. (2012) ‘Microstructure and the properties of FeCoCuNiSn_x high entropy alloys’, *Materials science & engineering. A, Structural materials: properties, microstructure and processing*, 548, pp. 64–68. doi:10.1016/j.msea.2012.03.080.
- [183] Ke, G.Y., Chen, G.Y., Hsu, T. and Yeh, J.W. (2006) ‘FCC and BCC equivalents in as-cast solid solutions of Al_xCo_yCr_zCu_{0.5}Fe_vNi_w high-entropy alloys’, *European journal of control*, 31(6), pp. 669–684. doi:10.3166/acsm.31.669-684.
- [184] Alexandrov, B.T., Lippold, J., Tatman, J. and Murray, G. (2009) ‘Non-equilibrium phase transformation diagrams in engineering alloys’, *ASM Proceedings of the International Conference: Trends in Welding Research*, pp. 467–476. doi: 10.1361/cp2008twr467.
- [185] Balart, M.J., Patel, J.B., Gao, F. and Fan, Z. (2016) ‘Grain refinement of deoxidized copper’, *Metallurgical and materials transactions. A, Physical metallurgy and materials science*, 47(10), pp. 4988–5011. doi:10.1007/s11661-016-3671-8.
- [186] Oar-Arteta Gonzalez, L., Wezendonk, T.A., Sun, X., Kapteijn, F. and Gascon, J. (2017) ‘Metal organic frameworks as precursors for the manufacture of advanced catalytic materials’, *Materials chemistry frontiers*, 1(9), pp. 179–1745. doi:10.1039/c7qm00007c.
- [187] Wagman, D.D., Evans, W.H., Parker, V.B., Schumm, R.H., Halow, I., Bailey, S.M., Churney, K.L. and Nuttall, R.L. (1982) ‘The NBS tables of chemical thermodynamic properties: selected values for inorganic and C1 and C2 organic substances in SI units’, *The Journal of Physical Chemistry*, 11.
- [188] Sabat, K.C., Paramguru, R.K. and Mishra, B.K. (2017) ‘Reduction of oxide mixtures of (Fe₂O₃ + CuO) and (Fe₂O₃ + Co₃O₄) by low-temperature hydrogen plasma’, *Plasma chemistry and plasma processing*, 37(4), pp. 979–995. doi:10.1007/s11090-017-9818-6.

- [189] He, Z., Li, Z., Jiang, X., Wu, C., Liu, Y., Song, X., Yu, Z., Wang, Y., Lan, Z. and Sun, K. (2021) ‘Surface investigation of Ni₈₁Fe₁₉ thin film: using ARXPS for thickness estimation of oxidation layers’, *Metals (Basel, Switzerland)*, 11(12), p. 2061. doi:10.3390/met11122061.
- [190] Rosoiu, S.P., Pantazi, A.G., Petica, A., Cojocaru, A., Costovici, S., Zanella, C., Visan, T., Anicai, L. and Enachescu, M. (2019) ‘Comparative study of Ni-Sn alloys electrodeposited from choline chloride-based ionic liquids in direct and pulsed current’, *Coatings (Basel, Switzerland)*, 9(12), p. 801. doi:10.3390/coatings9120801.
- [191] Chen, Z., He, M., Balakrishnan, B. and Chum, C.C. (2006) ‘Elasticity modulus, hardness and fracture toughness of Ni₃Sn₄ intermetallic thin films’, *Materials science & engineering. A, Structural materials: properties, microstructure and processing*, 423(1-2), pp. 107–110. doi:10.1016/j.msea.2005.12.038.
- [192] Luo, H., Dong, C.F., Cheng, X.Q., Xiao, K. and Li, X.G. (2012) ‘Electrochemical behavior of 2205 duplex stainless steel in NaCl solution with different chromate contents’, *Journal of materials engineering and performance*, 21(7), pp. 1283–1291. doi:10.1007/s11665-011-0030-1.
- [193] Wang, K., Lan, A.D. and Qiao, J.W. (2021) ‘Corrosion behavior of Al_{0.1}CoCrFeNi high entropy alloy in various chloride-containing solutions’, *Frontiers in materials*, 7, pp.1–9. doi.org/10.3389/fmats.2020.533843
- [194] Shaik, L.A. and Thamida, S.K. (2016) ‘Surface evolution of a corroding metal as a moving boundary problem by random assignment of anodic and cathodic sites’, *Journal of electroanalytical chemistry (Lausanne, Switzerland)*, 780, pp. 264–270. doi:10.1016/j.jelechem.2016.09.048.
- [195] Feng, B., Liu, G., Yang, P., Huang, S., Qi, D., Chen, P., Wang, C., Du, J., Zhang, S. and Liu, J. (2021) ‘Different role of second phase in the micro-galvanic corrosion of WE43 Mg alloy in NaCl and Na₂SO₄ solution’, *Journal of magnesium and alloys*, 10(6), pp. 1598–1608. doi:10.1016/j.jma.2020.12.013.
- [196] Natishan, P.M. and O’Grady, W.E. (2014) ‘Chloride ion interactions with oxide-covered aluminum leading to pitting corrosion: a review’, *Journal of the electrochemical society*, 161(9), pp. C421–C432. doi:10.1149/2.1011409jes.
- [197] McCafferty, E. (2003) ‘Semiconductor aspects of the passive oxide film on aluminum as modified by surface alloying’, *Corrosion science*, 45(2), pp. 301–308. [https://doi.org/10.1016/S0010-938X\(02\)00095-1](https://doi.org/10.1016/S0010-938X(02)00095-1).
- [198] Lopesino, P., Alcántara, J., de la Fuente, D., Chico, B., Jiménez, J.A. and Morcillo, M. (2018) ‘Corrosion of copper in unpolluted chloride-rich atmospheres’, *Metals (Basel, Switzerland)*, 8(11), p. 866. doi:10.3390/met8110866.
- [199] Cachet, H., Zenia, F. and Froment, M. (1999) ‘Corrosion-induced activation of SnO₂ films promoted by the electrochemical oxidation of chloride ions’, *Journal of the electrochemical society*, 146, pp. 977–983. doi:10.1149/1.1391708.
- [200] Zhong, X., Zhang, G., Qiu, Y., Chen, Z., Guo, X. and Fu, C. (2013) ‘The corrosion of tin under thin electrolyte layers containing chloride’, *Corrosion science*, 66, pp. 14–25. doi:10.1016/j.corsci.2012.08.040.
- [201] Verma, C. (2021) “Chapter 7” in *Handbook of Science & Engineering of Green Corrosion Inhibitors: Modern Theory, Fundamentals & Practical Applications*. Elsevier Press.

- [202] Le, H.L.T., Goniakowski, J. and Noguera, C. (2019) '(0001) Interfaces between M_2O_3 corundum oxides ($M = Al, Ti, V, Cr, Fe$)', *Surface science*, 679, pp. 17–23. doi:10.1016/j.susc.2018.08.015.
- [203] Kong, K., Hyun, J., Kim, Y., Kim, W. and Kim, D. (2019) 'Nanoporous structure synthesized by selective phase dissolution of AlCoCrFeNi high entropy alloy and its electrochemical properties as supercapacitor electrode', *Journal of power sources*, 437, p. 226927. doi:10.1016/j.jpowsour.2019.226927.
- [204] Qiu, Y., Thomas, S., Gibson, M.A., Fraser, H.L. and Birbilis, N. (2017) 'Corrosion of high entropy alloys', *Npj Materials degradation*, 1(1), pp. 1–18. doi:10.1038/s41529-017-0009-y.
- [205] Bianco, R. and Hynes, J.T. (2004) 'A theoretical study of the $H_2SO_4 + H_2O \rightarrow H_5O_4^- + H_3O^+$ reaction at the surface of aqueous aerosols', *Theoretical chemistry accounts*, 111(2-6), pp. 182–187. doi:10.1007/s00214-003-0524-5.
- [206] Domínguez-Jaimes, L.P., Arenas, M.A., Conde, A., Escobar-Morales, B., Álvarez-Méndez, A. and Hernández-López, J.M. (2022) 'Growth of anodic layers on 304L stainless steel using fluoride free electrolytes and their electrochemical behavior in chloride solution', *Materials*, 15(5), p. 1892. doi:10.3390/ma15051892.
- [207] Guan, B., Wang, H., Xu, R., Zheng, G., Yang, J., Liu, Z., Cao, M., Wu, M., Song, J., Li, N., Li, T., Cai, Q., Yang, X., Li, Y. and Zhang, X. (2016) 'Establishing antibacterial multilayer films on the surface of direct metal laser sintered titanium primed with phase-transited lysozyme', *Scientific reports*, 6(1), pp. 36408–36408. doi:10.1038/srep36408.
- [208] Talha, M., Wang, Q., Xu, M., Ma, Y., Li, Z. and Lin, Y. (2021) 'Improved corrosion protective performance of hybrid silane coatings reinforced with nano ZnO on 316 L stainless steel', *Colloid and interface science communications*, 42, p. 100411. doi:10.1016/j.colcom.2021.100411.
- [209] Mulimbayan, F.M. and Mena, M.G. (2015) 'Investigation of the effects of solution temperature on the corrosion behavior of austenitic low-nickel stainless steels in citric acid using impedance and polarization measurements', in *2015 4th International Conference on Engineering and Innovative Materials (ICEIM 2015)*. CEDEX A: E D P Sciences, p. 2006. doi:10.1051/mateconf/20152702006.
- [210] Kocijan, A., Milošev, I., Merl, D.K. and Pihlar, B. (2004) 'Electrochemical study of Co-based alloys in simulated physiological solution', *Journal of applied electrochemistry*, 34(5), pp. 517–524. doi:10.1023/B:JACH.0000021868.10122.96.
- [211] Vidal, C.V. and Muñoz, A.I. (2009) 'Effect of thermal treatment and applied potential on the electrochemical behaviour of CoCrMo biomedical alloy', *Electrochimica acta*, 54(6), pp. 1798–1809. doi:10.1016/j.electacta.2008.10.018.
- [212] Namus, R., Nutter, J., Qi, J. and Rainforth, W.M. (2020) 'The influence of protein concentration, temperature and cathodic polarization on the surface status of CoCrMo biomedical grade alloys', *Applied surface science*, 499, p. 143908. doi:10.1016/j.apsusc.2019.143908.
- [213] Namus, R. (2018) *CoCrMo alloys in hip and knee replacements application*. University of Sheffield.

[214] Tan, L., Wang, Z., Ma, Y., Yan, Y. and Qiao, L. (2021) 'Tribocorrosion investigation of 316L stainless steel: the synergistic effect between chloride ion and sulfate ion', *Materials research express*, 8(8), p. 86501. doi:10.1088/2053-1591/ac1825.

[215] Hao, X., Zhen, J., Zhao, X., Ma, J., Chen, H., Guo, S., Wang, C. and Wang, C. (2022) 'Effect of Sn addition on the tribological behaviors of CoCrFeNi high entropy alloys', *Journal of alloys and compounds*, 909, p. 164657. doi:10.1016/j.jallcom.2022.164657.

APPENDIX A

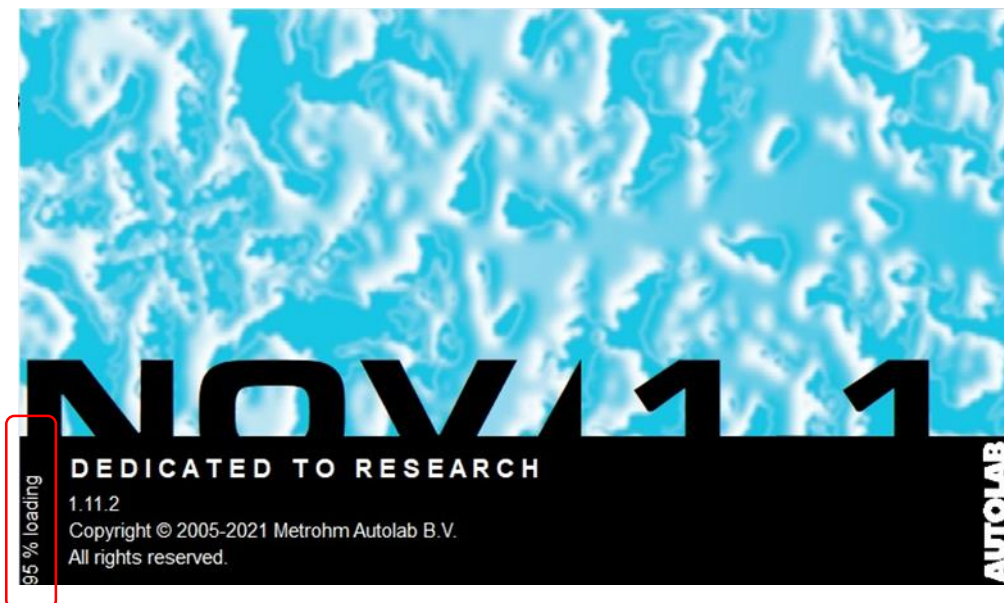
Protocol for the analysis of corrosion parameters by NOVA 1.11.2 software

The corrosion parameters reported in this thesis were obtained from the raw data obtained from tests using the PGSTAT302N Autolab instrument. To extract parameters from this data, an analysis procedure was used, which was performed using NOVA 1.11.2 software installed on a PC. The steps involved in this process are detailed below.

- 1) Launch the Nova 1.11.2 software (icon below).

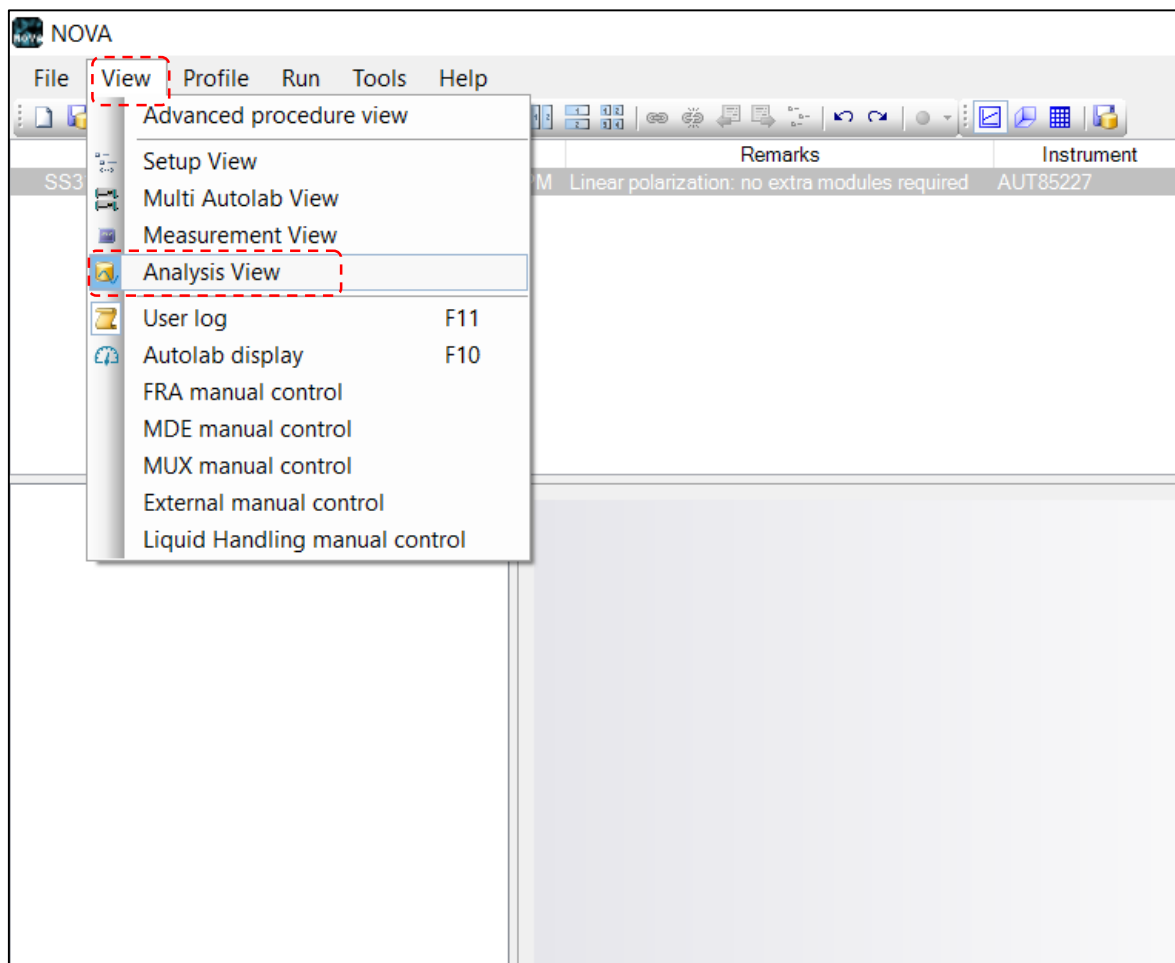


- 2) The Nova 1.11.2 software will be load.



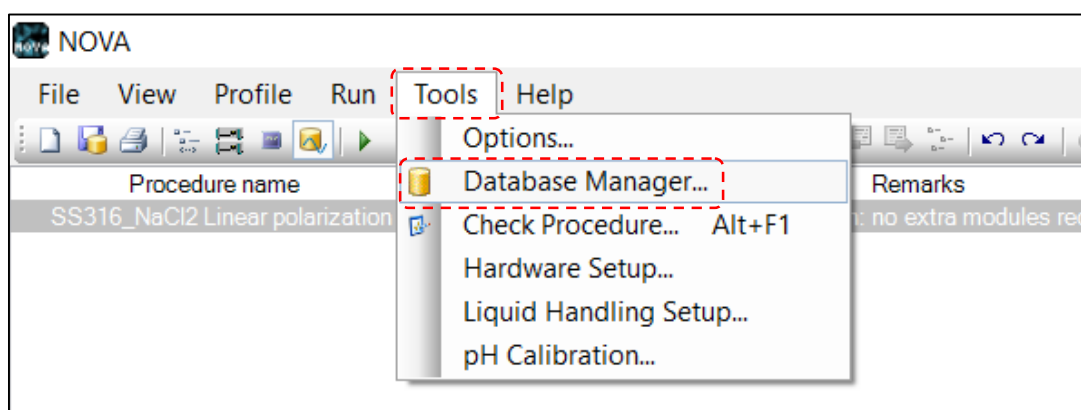
3) When the software is fully opened a starting window will be displayed. Select “View”.

4) Select and double click “Analysis View” to display the window for analyzing the corrosion data.

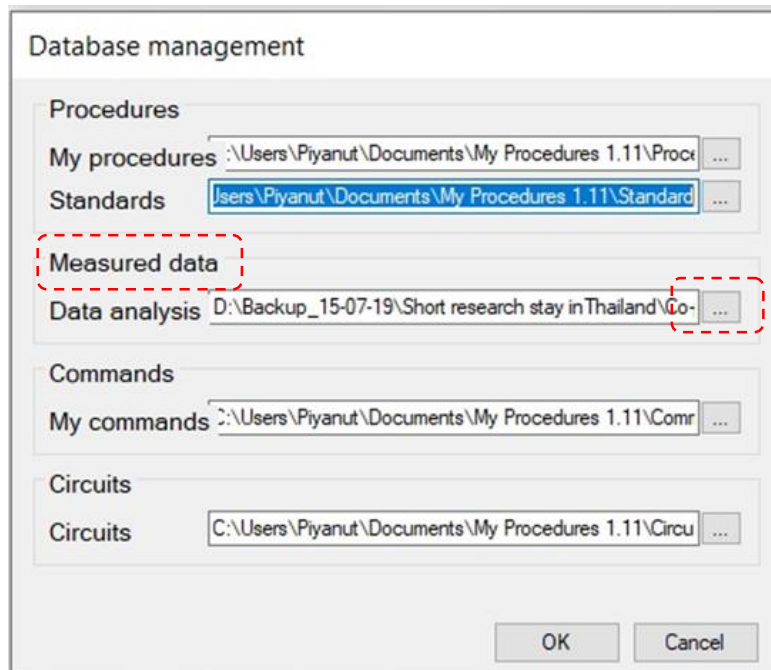


5) Select “Tools”.

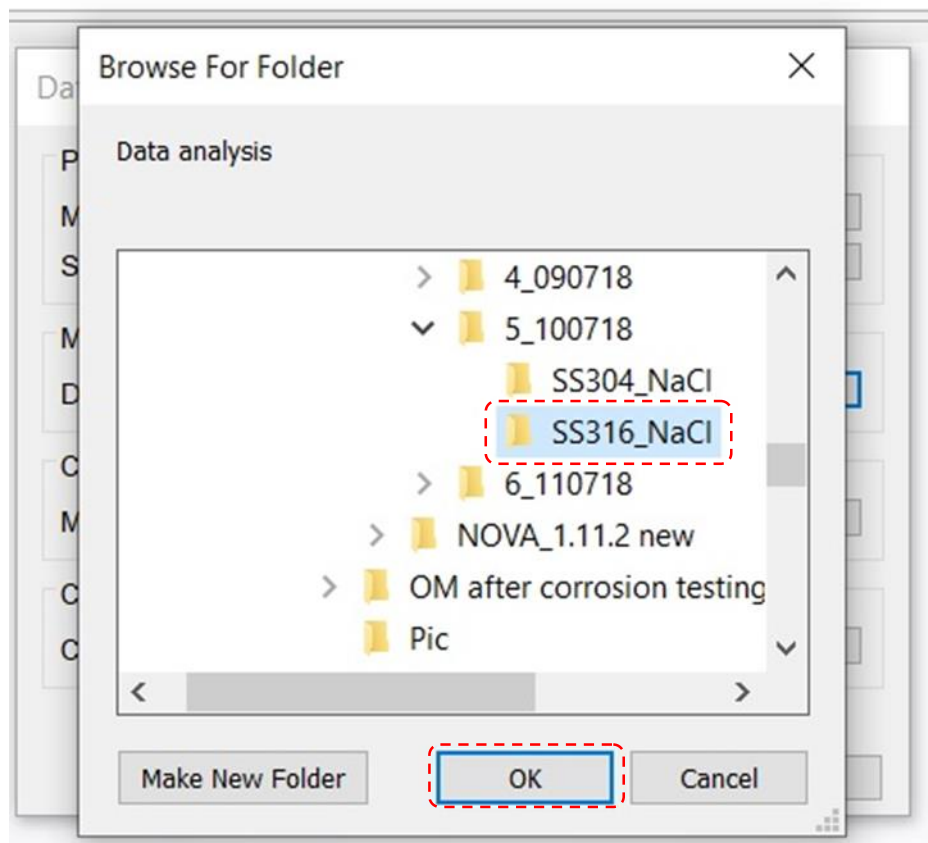
6) Select and double click “Database Management” to open the raw experimental data for corrosion analysis.



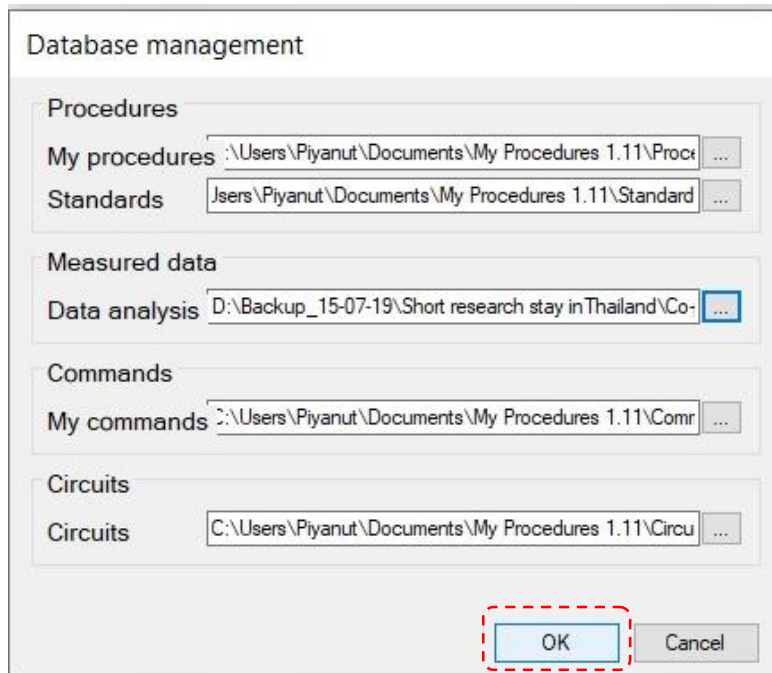
7) Select “Measured data” and double-click “...” at Data analysis to search for the location of the raw data.



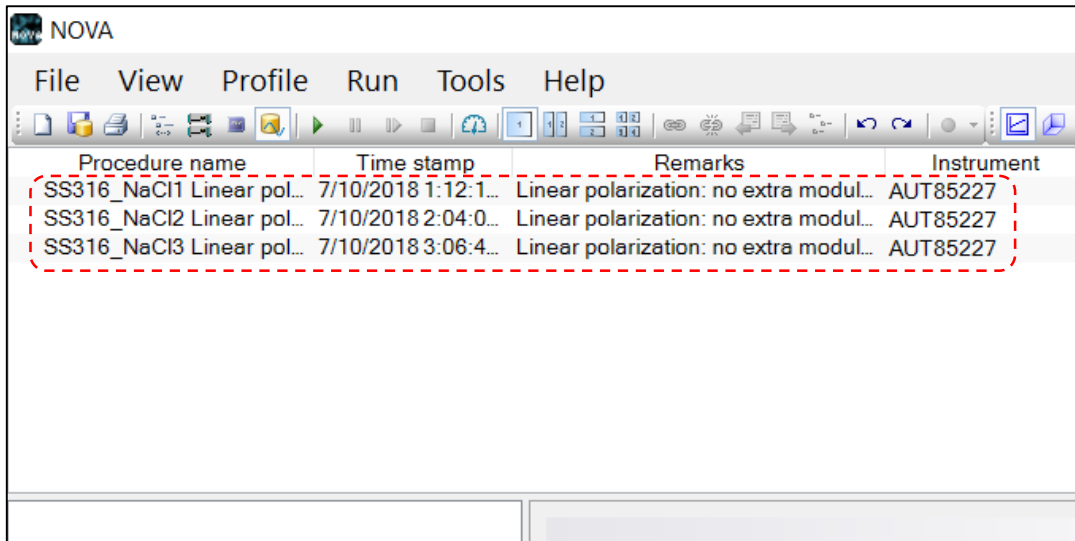
8) Select a folder containing the relevant raw data and click “OK”.



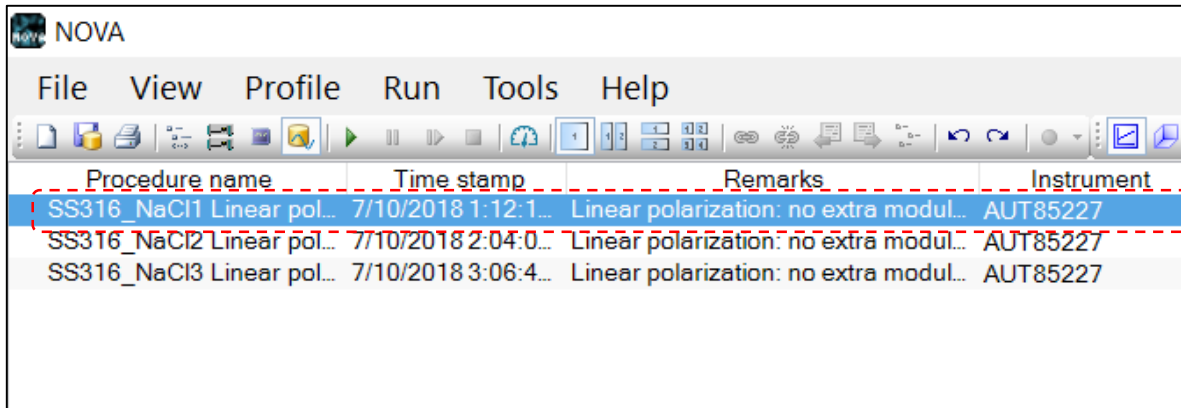
9) Click “OK” again on the Database Management window.



10) The raw data files will appear in the main window.

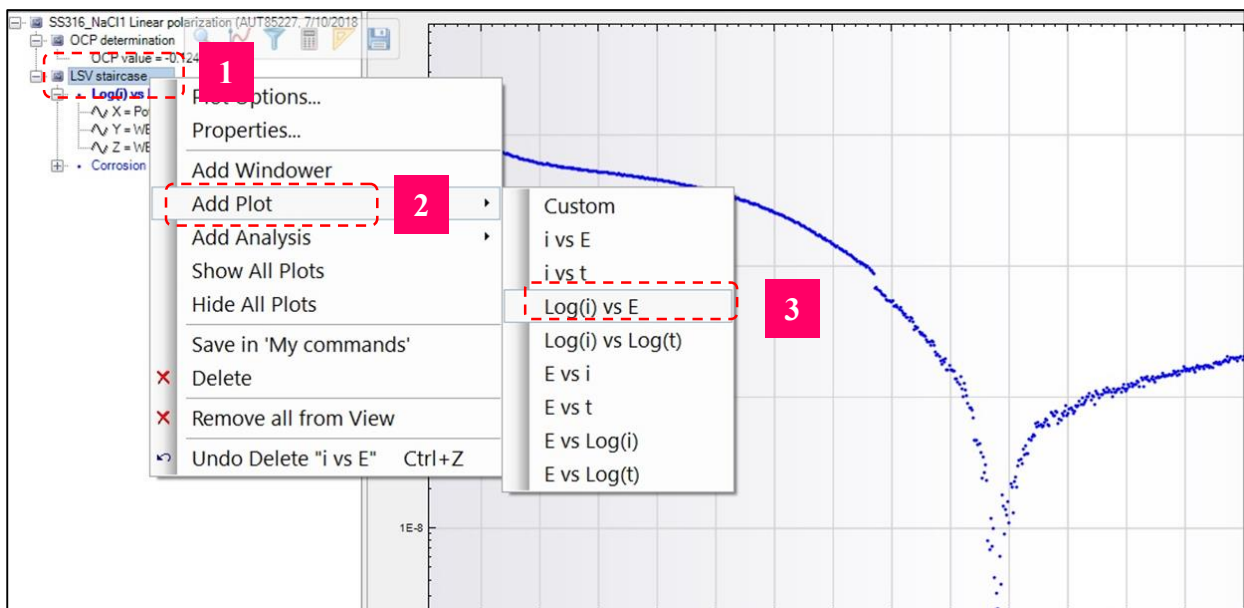


11) Select and double-click a raw data file. It will be highlighted in blue.



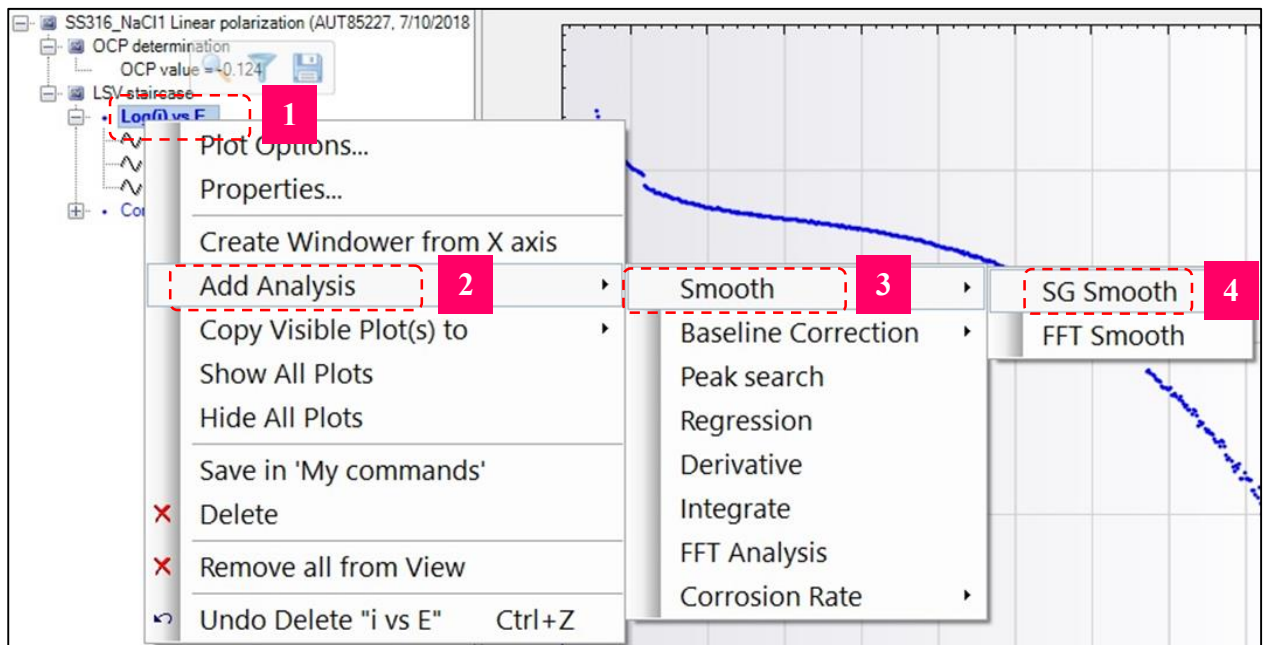
Procedure name	Time stamp	Remarks	Instrument
SS316_NaCl1 Linear pol...	7/10/2018 1:12:1...	Linear polarization: no extra modul...	AUT85227
SS316_NaCl2 Linear pol...	7/10/2018 2:04:0...	Linear polarization: no extra modul...	AUT85227
SS316_NaCl3 Linear pol...	7/10/2018 3:06:4...	Linear polarization: no extra modul...	AUT85227

12) Once the data are loaded into the program, the next step is to create a plot for analysis. Click on the right-hand side of the “LSV staircase” menu (1), select “Add Plot” (2), and choose “Log(i) vs. E” to display the data on x-y axes.

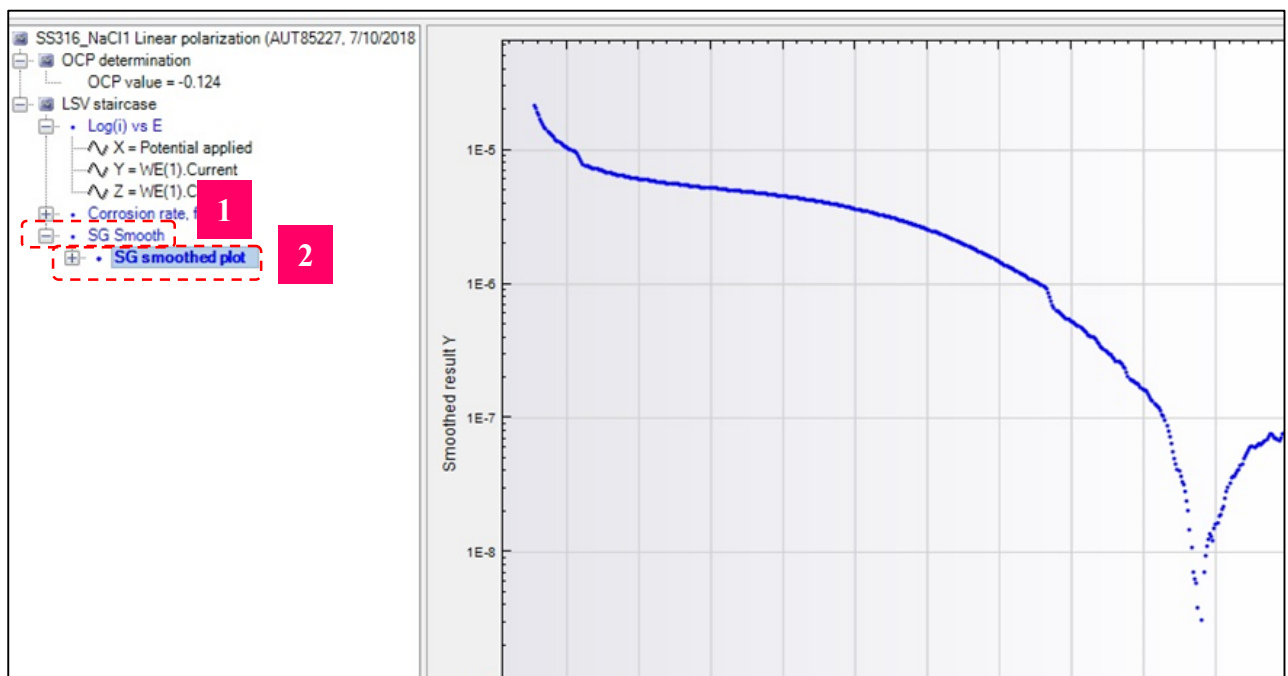


13) In order to avoid scatter in the data and remove noise having an undue effect on the analysis, smoothing the data can be beneficial, and the Nova software contains functions to do this. The Savitzky-Golay (SG) smoothing mode is a fundamental and simple tool used for noise removal during data analysis. It leads to an increase in the ratio of signal and noise in experimental data. On the other hand, a specific frequency or frequency range from a set of experimental data can eliminate to attenuate the impact of the selected frequency or frequency range and enhance the ratio of signal and noise. It can carry out through the fast Fourier transform (FFT) smoothing mode. Thus, the SG Smoot is usually the first selected tool for

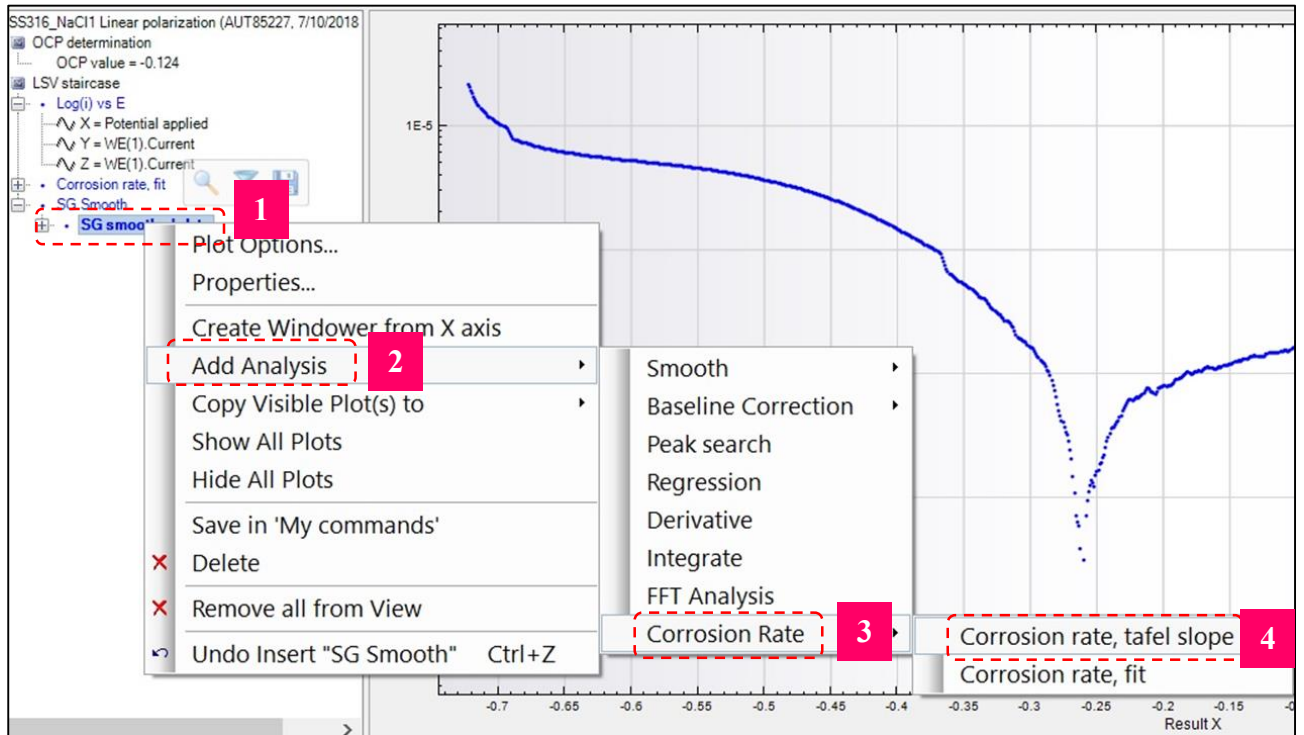
smoothing the data set with an uncomplicated technique. Click on the right-hand side of the “Log(i) vs. E” menu (1), select “Add Analysis” (2), “Smooth” (3), and “SG Smooth” (4).



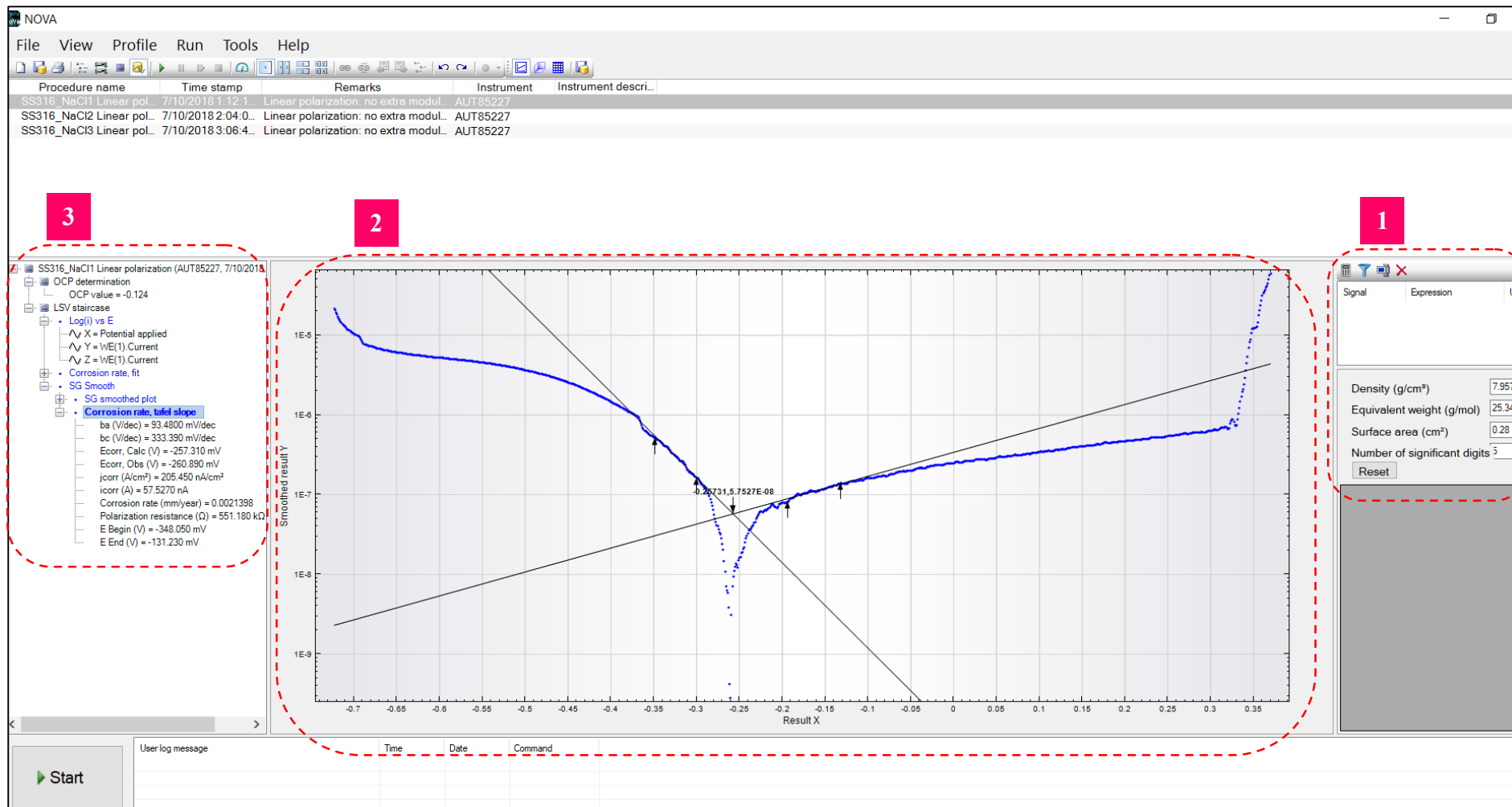
14) Click “SG Smooth” (1) and select “SG Smoothed plot” (2). The function is applied to the data and the plot shows a smoother trace.



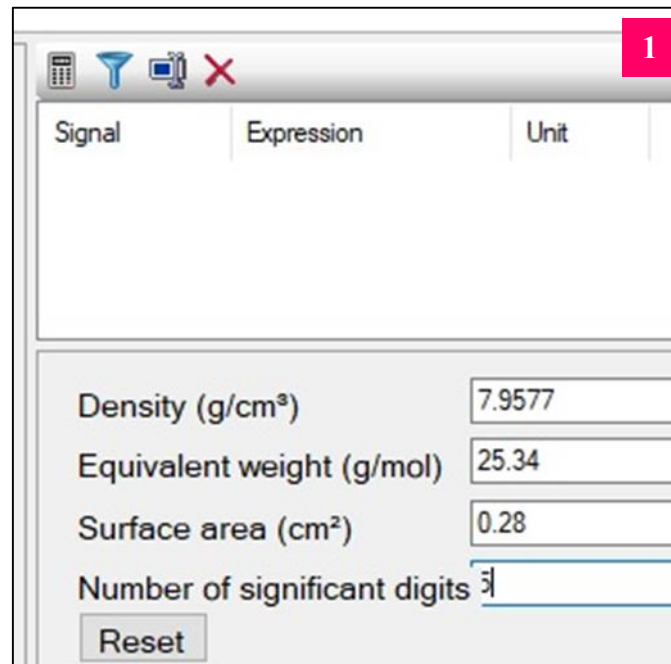
15) Next the click on the right-hand side of the “SG Smoothed plot” menu (1), select “Add Analysis” (2), “Corrosion Rate” (3), and “Corrosion rate, Tafel slope” (4). The Tafel slope technique is used to calculate the corrosion rate and corrosion parameters (the anodic (b_a) and cathodic (b_c) Tafel coefficient, corrosion potential, the exchange current density, and polarization resistance).



16) The main window consists of three parts to operate corrosion software. The first part is to input fundamental data for the calculation of corrosion parameters. The second part is to draw the line of Tafel slopes and create the point of intersection between these two lines to calculate corrosion parameters. Finally, the third part is to present the corrosion rate and corrosion parameters after analyzing the technique of the Tafel slope. Each of these stages is discussed in more detail in the steps below.



17) In the first part, three fundamental items of data concerning the tested samples are required; density, equivalent weight, and surface area. These values were determined for the samples as outlined in Section 3.5.1, 3.6.1.2 and 3.6.4. Density and equivalent weight are variables to calculate the value of corrosion rate as in Equation 11, while surface area uses to analyse the value of exchange current density (j_{corr}). They are inputted to calculate corrosion parameters.

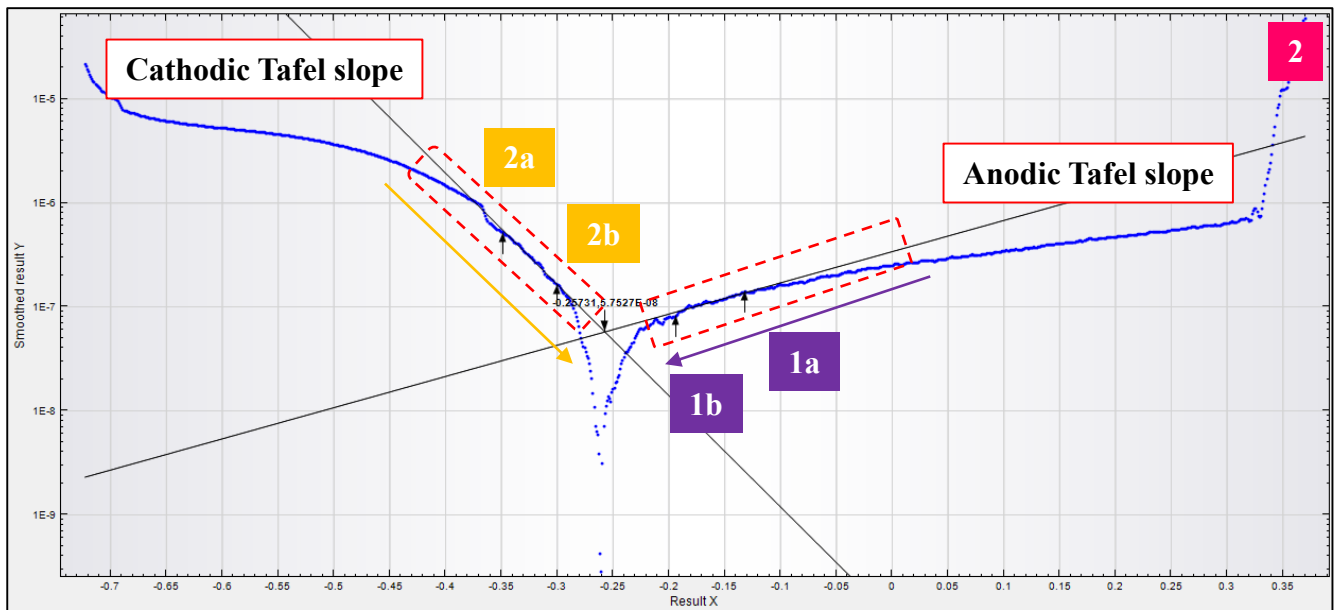


The image shows a software window with a title bar containing icons for a calculator, a funnel, a printer, and a close button. A red square with the number '1' is in the top right corner. Below the title bar is a table with three columns: 'Signal', 'Expression', and 'Unit'. The table is currently empty. Below the table are four input fields with labels and units: 'Density (g/cm³)' with the value '7.9577', 'Equivalent weight (g/mol)' with the value '25.34', 'Surface area (cm²)' with the value '0.28', and 'Number of significant digits' with the value '3'. A 'Reset' button is located at the bottom left of the input area.

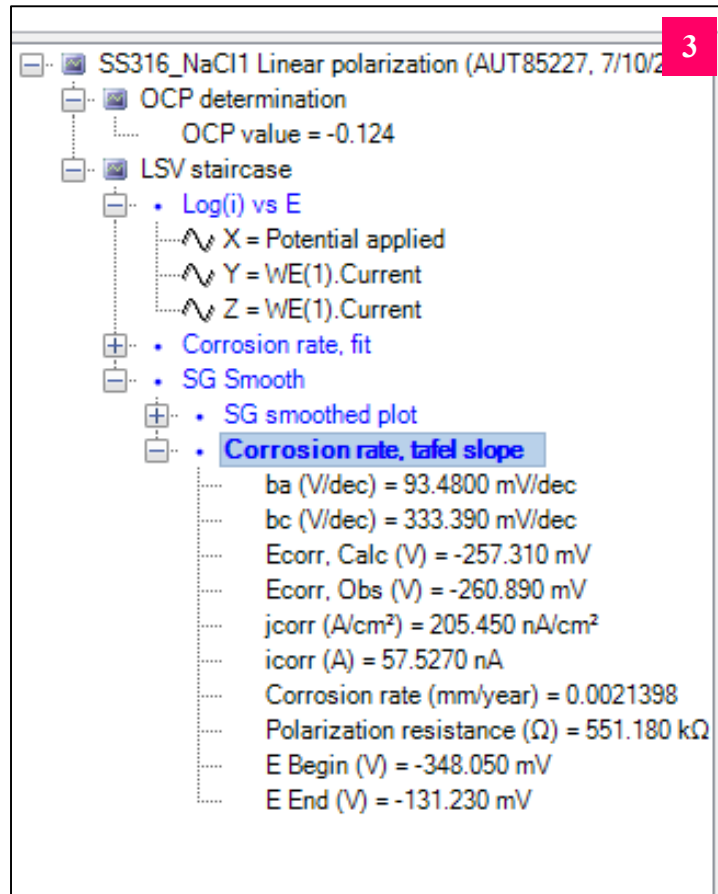
Signal	Expression	Unit
Density (g/cm ³)		7.9577
Equivalent weight (g/mol)		25.34
Surface area (cm ²)		0.28
Number of significant digits		3

Reset

18) In the second part, the Tafel slope technique (discussed in section 2.2.2 and 3.6.4) is used to obtain the corrosion parameters. Initially, two lines of best fit to portions of the curve are required, which define the Tafel slopes. The user identifies two points (indicated as, 1a and 1b for anodic and 2a and 2b for cathodic in the image below) on the anodic and cathodic parts of the curve, and the software identifies the slope of the linear line of best fit to the data between these points. The selection of the points was made based on the systematic approach. Two points of the Tafel slopes (1b and 2b) are around ± 100 mV or 0.1 V away from the value of $E_{corr. Obs}$. From these the Anodic and Cathodic Tafel slopes are obtained.



19) In the third part, the NOVA 1.11.2 software calculates the analytical values of corrosion rate and corrosion parameters, as shown in the figure below. As a check, it was verified that the value of $E_{corr. Calc}$ should be close to the value of $E_{corr. Obs}$ to obtain an accurate value of the corrosion potential.



APPENDIX B

Supplementary data for XPS analysis in pre- and post-corrosion testing

Table A-B: the relative atomic concentration (at.%) in pre- and post-corrosion testing by XPS analysis; CoCrFeNi, CoCrFeNiAl, CoCrFeNiCu, and CoCrFeNiSn alloys.

Test conditions	Alloys	Relative atomic concentration (at.%)								
		Co	Cr	Fe	Ni	Al	Cu	Sn	O	C
Pre-corrosion testing (as-cast samples)	CoCrFeNi	9.97	15.17	11.45	13.54	-	-	-	42.47	7.40
	CoCrFeNiAl	4.21	11.55	6.35	4.37	8.38	-	-	44.18	21.09
	CoCrFeNiCu	2.68	7.82	4.47	2.77	-	4.20	-	23.39	54.68
	CoCrFeNiSn	6.68	13.77	6.66	8.97	-	-	17.59	36.24	10.8
Post-corrosion testing in 0.6 M NaCl solution	CoCrFeNi	7.80	21.98	16.47	8.25	-	-	-	33.15	12.34
	CoCrFeNiAl	6.11	13.97	7.54	10.05	12.86	-	-	36.06	14.92
	CoCrFeNiCu	5.40	11.31	6.44	7.22	-	7.10	-	24.87	37.67
	CoCrFeNiSn	1.93	11.07	4.22	2.94	-	-	11.02	32.45	36.36
Post-corrosion testing in 0.6 M H ₂ SO ₄ solution	CoCrFeNi	4.75	19.24	6.77	5.49	-	-	-	17.76	46.00
	CoCrFeNiAl	3.16	7.43	4.25	10.89	14.66	-	-	28.26	35.19
	CoCrFeNiCu	5.65	19.98	7.14	6.29	-	5.12	-	33.83	21.99
	CoCrFeNiSn	5.02	16.17	3.67	7.35	-	-	11.49	20.94	36.36
Post-corrosion testing in 0.6 M NaAlO ₂ solution	CoCrFeNi	6.16	13.99	9.65	8.67	-	-	-	19.55	41.99
	CoCrFeNiAl	5.58	9.59	6.96	11.23	12.66	-	-	35.23	21.12
	CoCrFeNiCu	5.76	13.48	9.42	6.84	-	4.01	-	31.94	28.55
	CoCrFeNiSn	5.44	15.01	5.33	5.64	-	-	4.18	34.23	30.16

APPENDIX C

Supplementary data for corrosion analysis in different solutions

Table A-C1: The density and equivalent weight of as-cast samples and stainless steels.

Alloys	Density (g/cm ³)	Equivalent weight (g/mol)
CoCrFeNi	8.2038	22.55
CoCrFeNiAl	7.0703	19.42
CoCrFeNiCu	8.3223	24.08
CoCrFeNiSn	8.4453	28.68
SS304	7.9224	25.27
SS316	7.9577	25.34

Table A-C2: The corrosion parameters of alloys and stainless steels in 0.6 M NaCl solution at room temperature.

Alloys	E_{corr} (mV _{Ag/AgCl})	i_{corr} ($\mu\text{A}/\text{cm}^2$)	b_a (mV/dec)	$ b_c $ (mV/dec)	E_p (mV _{Ag/AgCl})	ΔE_p (mV _{Ag/AgCl})	R_p ($\Omega \text{ cm}^2$)	CR (mm/year)
CoCrFeNi	-257±13	$2.05(\pm 0.67) \times 10^{-1}$	111±7	258±12	556±27	813±30	$1.93(\pm 0.89) \times 10^5$	$1.83(\pm 0.59) \times 10^{-3}$
CoCrFeNiAl	-322±10	$6.44(\pm 1.03) \times 10^{-1}$	128±2	827±3	297±40	619±43	$7.69(\pm 1.19) \times 10^4$	$5.77(\pm 0.94) \times 10^{-3}$
CoCrFeNiCu	-180±13	$1.47(\pm 0.29) \times 10^0$	147±10	200±3	-69±9	111±21	$2.58(\pm 0.48) \times 10^4$	$1.39(\pm 0.27) \times 10^{-2}$
CoCrFeNiSn	-252±5	$1.60(\pm 0.33) \times 10^{-1}$	118±0.4	353±7	1099±14	1351±12	$2.52(\pm 0.55) \times 10^5$	$1.77(\pm 0.37) \times 10^{-3}$
SS304	-246±13	$1.21(\pm 0.34) \times 10^{-1}$	88±6	529±1	199±12	445±17	$2.88(\pm 0.64) \times 10^5$	$1.27(\pm 0.33) \times 10^{-3}$
SS316	-254±7	$2.23(\pm 0.46) \times 10^{-1}$	95±4	465±1	267±35	521±42	$1.62(\pm 0.39) \times 10^5$	$2.33(\pm 0.45) \times 10^{-3}$

where E_{corr} is corrosion potential, i_{corr} is corrosion current density, b_a is the Tafel slope of anodic reaction, b_c is the Tafel slope of cathodic reaction, E_p is pitting potential, ΔE_p is passivation potential, R_p is polarization resistance, and CR is corrosion rate.

Table A-C3: The corrosion parameters of alloys and stainless steels in 0.6 M H₂SO₄ solution at room temperature.

Alloys	E_{corr} (mV _{Ag/AgCl})	i_{corr} (μ A/cm ²)	b_a (mV/dec)	$ b_c $ (mV/dec)	E_t (mV _{Ag/AgCl})	ΔE_p (mV _{Ag/AgCl})	R_p (Ω cm ²)	CR (mm/year)
CoCrFeNi	-98±17	1.70±0.08	109±20	2607±5	935±0.1	1033±18	2.66(±0.34) ×10 ⁴	1.53(±0.07) ×10 ⁻²
CoCrFeNiAl	-309±1	76.38±1.57	56±3	130±5	934±1	1254±1	2.22(±0.10) ×10 ²	6.86(±0.14) ×10 ⁻¹
CoCrFeNiCu	-121±7	4.40±0.64	162±6	1196±16	9±6	129±6	1.43(±0.15) ×10 ⁴	4.16(±0.61) ×10 ⁻²
CoCrFeNiSn	-38±8	3.65±0.73	107±9	917±19	968±1	1006±7	1.17(±0.16) ×10 ⁴	4.05(±0.81) ×10 ⁻²
SS304	-355±6	47.79±9.16	119±8	50±3	936±3	1291±4	3.33(±0.01) ×10 ²	4.99(±0.96) ×10 ⁻¹
SS316	-291±4	52.61±1.14	164±1	151±12	949±7	1240±7	6.49(±0.004) ×10 ²	5.48(±0.12) ×10 ⁻¹

where E_{corr} is corrosion potential, i_{corr} is corrosion current density, b_a is the Tafel slope of anodic reaction, b_c is the Tafel slope of cathodic reaction, E_t is transpassive potential, ΔE_p is passivation potential, R_p is polarization resistance, and CR is corrosion rate.

Table A-C4: The corrosion parameters of alloys and stainless steels in 0.6 M NaAlO₂ solution at room temperature.

Alloys	E_{corr} (mV _{Ag/AgCl})	i_{corr} (μ A/cm ²)	b_a (mV/dec)	$ b_c $ (mV/dec)	E_t (mV _{Ag/AgCl})	ΔE_p (mV _{Ag/AgCl})	R_p (Ω cm ²)	CR (mm/year)
CoCrFeNi	-431±8	0.06±0.03	133±11	283±15	513±2	944±9	8.68(±3.52) ×10 ⁵	4.98(±2.37) ×10 ⁻⁴
CoCrFeNiAl	-504±6	0.23±0.01	159±14	572±10	510±4	1014±7	2.31(±0.25) ×10 ⁵	2.11(±0.10) ×10 ⁻³
CoCrFeNiCu	-337±34	0.22±0.12	313±17	489±10	517±13	854±37	4.77(±1.85) ×10 ⁵	2.10(±1.18) ×10 ⁻³
CoCrFeNiSn	-491±24	0.20±0.06	132±12	345±14	458±7	949±29	2.32(±0.84) ×10 ⁵	2.20(±0.62) ×10 ⁻³
SS304	-416±15	0.24±0.14	247±14	1052±22	500±1	916±16	4.67(±1.89) ×10 ⁵	2.52(±1.45) ×10 ⁻³
SS316	-398±14	0.07±0.02	158±15	423±8	506±4	904±16	7.40(±1.72) ×10 ⁵	7.53(±2.13) ×10 ⁻⁴

where E_{corr} is corrosion potential, i_{corr} is corrosion current density, b_a is the Tafel slope of anodic reaction, b_c is the Tafel slope of cathodic reaction, E_t is transpassive potential, ΔE_p is passivation potential, R_p is polarization resistance, and CR is corrosion rate.

APPENDIX D

Supplementary data for XPS analysis in different solutions

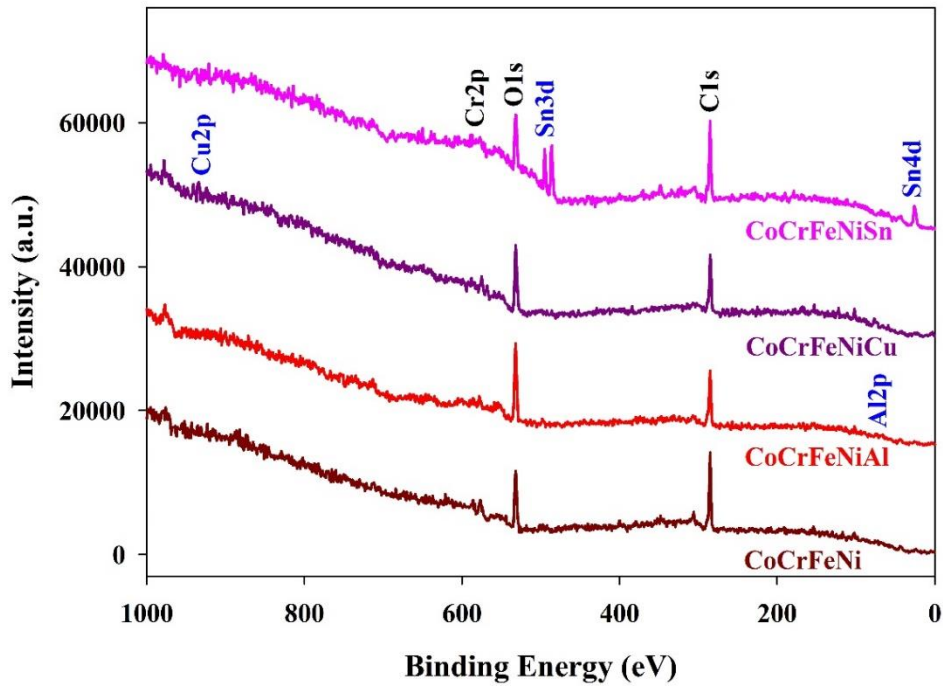


Figure A-D1: The wide scan of XPS spectra in the binding energies range of 0-1,000 eV of alloys for post-corrosion test in 0.6 M H_2SO_4 solution.

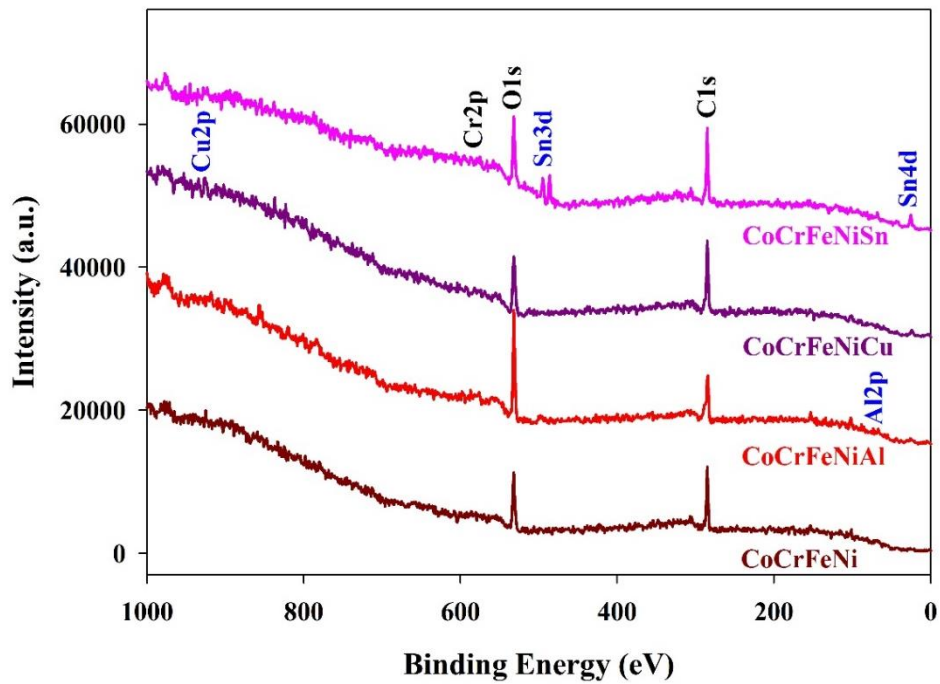


Figure A-D2: The wide scan of XPS spectra in the binding energies range of 0-1,000 eV of alloys for post-corrosion test in 0.6 M NaAlO_2 solution.

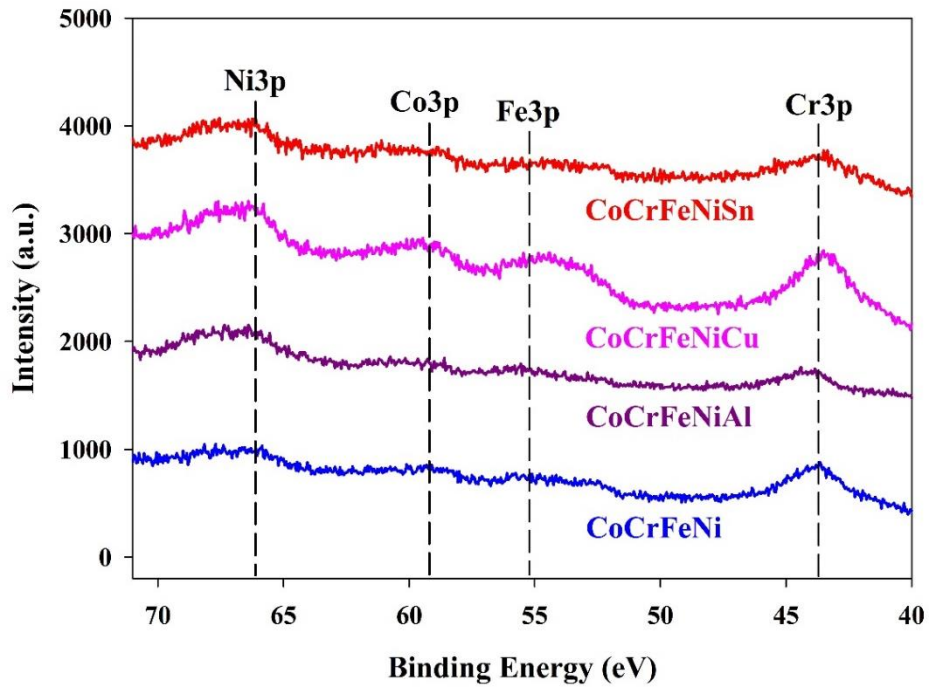


Figure A-D3: XPS spectra at high resolution in the binding energies range of 40-70 eV of alloys for post-corrosion test in 0.6 M H₂SO₄ solution.

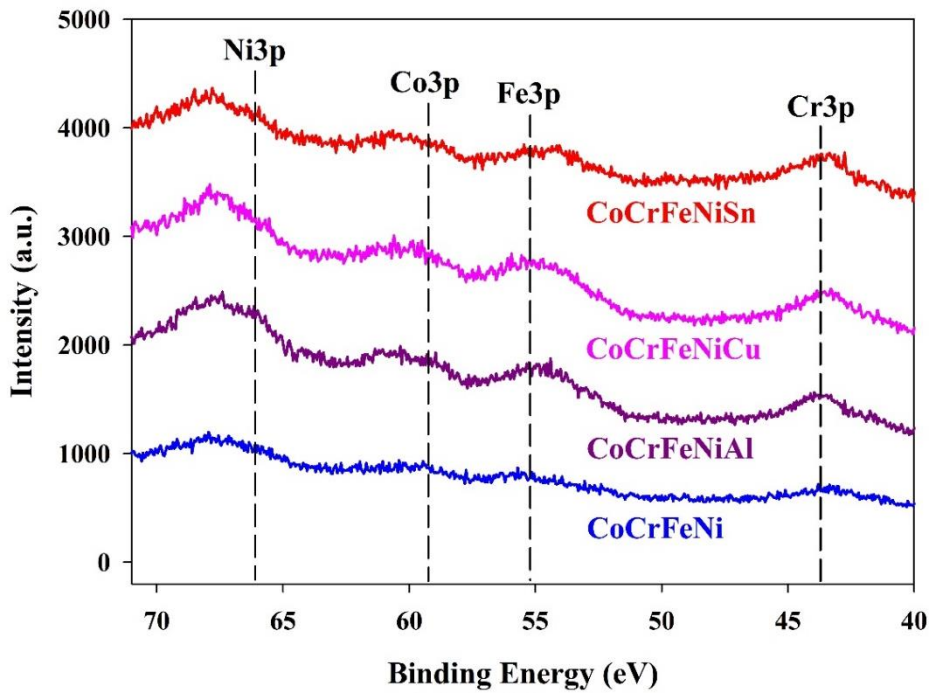


Figure A-D4: XPS spectra at high resolution in the binding energies range of 40-70 eV of alloys for post-corrosion test in 0.6 M NaAlO₂ solution.